AWARD NUMBER: W81XWH-15-1-0574

TITLE: Long-Term Follow-up of the Delayed Effects of Acute Radiation Exposure in Primates

PRINCIPAL INVESTIGATOR: J. Mark Cline, DVM, PhD

CONTRACTING ORGANIZATION: Wake Forest University Health Sciences
Winston Salem, NC 27157

REPORT DATE: October 2017

TYPE OF REPORT: Annual

PREPARED FOR: U.S. Army Medical Research and Materiel Command
Fort Detrick, Maryland 21702-5012

DISTRIBUTION STATEMENT: Approved for Public Release;
Distribution Unlimited

REPORT DOCUMENTATION PAGE

Form Approved
OMB No. 0704-0188

1. REPORT DATE	2. REPORT TYPE	3. DATES COVERED
October 2017	Annual	30 Sep 2016 - 29 Sep 2017

4. TITLE AND SUBTITLE

Long-Term Follow-up of the Delayed Effects of Acute Radiation Exposure in Primates

5a. CONTRACT NUMBER

5b. GRANT NUMBER
W81XWH-15-1-0574

5c. PROGRAM ELEMENT NUMBER

6. AUTHOR(S)

J. Mark Cline, DVM, PhD

jmcline@wakehealth.edu

5d. PROJECT NUMBER

5e. TASK NUMBER

5f. WORK UNIT NUMBER

7. PERFORMING ORGANIZATION NAME(S) AND ADDRESS(ES)
.
Wake Forest University Health Sciences
Winston, NC 27157

8. PERFORMING ORGANIZATION REPORT NUMBER

9. SPONSORING / MONITORING AGENCY NAME(S) AND ADDRESS(ES)
U.S. Army Medical Research and Materiel Command
Fort Detrick, Maryland 21702-5012

10. SPONSOR/MONITOR'S ACRONYM(S)

11. SPONSOR/MONITOR'S REPORT NUMBER(S)

12. DISTRIBUTION / AVAILABILITY STATEMENT
Approved for Public Release; Distribution Unlimited

13. SUPPLEMENTARY NOTES

14. ABSTRACT

The overarching goal of this program is to explore our recent clinically relevant observations of DEARE in a unique cohort of non-human primates (NHP), termed the Radiation Survivor Cohort (RSC). This work consists of 4 projects: 1. Studies of type 2 diabetes mellitus
(T2DM); 2. Radiation-induced heart disease (RIHD); 3. Chronic immune impairment with restriction of the antigenic response repertoire; and 4. Genomic and transcriptomic studies of the molecular pathogenesis of T2DM, RIHD, and immune impairment in the context of DEARE.

15. SUBJECT TERMS-

None provided

16. SECURITY CLASSIFICATION OF:			17. LIMITATION OF ABSTRACT	18. NUMBER OF PAGES	19a. NAME OF RESPONSIBLE PERSON
a. REPORT	b. ABSTRACT	c. THIS PAGE			USAMRMC
U	U	U	UU	137	19b. TELEPHONE NUMBER *(include area code)*

TABLE OF CONTENTS

1. **INTRODUCTION:** Narrative that briefly (one paragraph) describes the subject, purpose and scope of the research.

The **subject** of this research is the phenomenon of Delayed Effects of Acute Radiation Exposure (DEARE). The **purpose** and overarching goal of this program is to explore our recent clinically relevant observations of DEARE in a unique cohort of non-human primates (NHP), termed the Radiation Survivor Cohort (RSC), and a smaller more controlled group of NHP exposed to radiation prospectively, termed the Prospective Radiation Cohort (PRC). The **scope** of this work work consists of 4 projects making use of these unique NHP resources: 1. Studies of type 2 diabetes mellitus (T2DM); 2. Radiation-induced heart disease (RIHD); 3. Chronic immune impairment with restriction of the antigenic response repertoire; and 4. Genomic and transcriptomic studies which will inform us regarding the molecular pathogenesis of T2DM, RIHD, and immune impairment in the context of DEARE. Work during the first two years of this program has proceeded as planned, with slight logistical modifications but no major changes or delays.

2. **KEYWORDS:** Provide a brief list of keywords (limit to 20 words).

Radiation; delayed effects; late effects; heart; immune system; type 2 diabetes mellitus; genomics; transcriptomics; *Mus musculus*; *Macaca mulatta*.

3. ACCOMPLISHMENTS:

What were the major goals of the project?

Major goals are listed below by project, including relevant dates and percentage completion as indicated.

Core Primate Studies (Cline)

SA1: Provide NHP Investigative Platform

Major Task 1: Regulatory Approval (months 1-6)
Milestone: Local Institutional Animal Care and Use Committee (IACUC) and DOD Animal Care and Use Review Office (ACURO) approvals in place (100%)

Major Task 2: Access to Long Term Radiation Survivor Cohort (months 1-6)
Milestone: Scheduling and meetings in progress (75%)
Sample collections have begun, in support of all projects (planned for months 6-60; 40% complete)

Major Task 3: Acquisition of Prospective Cohort (months 1-6)
Milestone: Animals arrived at Wake Forest 2/9/16 (100% completed).

Major Task 4: Irradiation and Study of Prospective Cohort
Milestone: Irradiations planned for quarter 4 (100% completed in Y2Q1)

SA2: Promote Synergy and Productivity

Major Task 5: Data management/tracking, group interactions (months 1-6)
Milestones: Data management (100% completed for years 1 and 2)
Establish monthly web meetings (100% complete)
Annual strategic retreat to be scheduled (100% complete for year 1)
Publications (months 6-60; 30% complete in the context of 5 year plan, cardiac and metabolic papers submitted and accepted; abstracts presented at the annual Radiation Research Society Meeting and other meetings)

SA3: Facilitate Translation and Therapeutic/Preventive approaches

Major Task 6: Strategize towards clinical implementation and future funding
Milestones: Promote new grant submissions (months 36-60; 20% complete)
Progress update at end of year 2 (70% complete)

Project 1: Diabetes (Kavanagh)

SA1: Document the time course of IR-mediated reduced insulin sensitivity

Major Task 1: PRC - Prospective Cohort
Milestones: Create a longitudinal clinical profile of diabetes mellitus (DM) risk with irradiation (15% achieved in context of 5 year plan)

Local IACUC approval (100% achieved)
ACURO Approval (100% Achieved)

Major Task 2: RSC - Radiation Survivor Cohort
Milestones: Generate comparable clinical data in monkeys with DM as DEARE to compare with the earlier prospectively irradiated monkeys (90% achieved in context of 5 year plan)

SA2: Examine IR-related increases in oxidation of tissue proteins over time

Major Task 3: Redox Proteomics of prospective and long-term irradiated tissue
Milestones: Compare and contrast early and late changes in redox proteomics following irradiation in mice and monkeys. Verify the role of Akt protein in DM. Identify individual or protein clusters with long-term modifications following irradiation. (65% achieved in context of 5 year plan)

SA3: Track extracellular matrix (ECM) remodeling, including fibrosis, in muscle and adipose depots after irradiation

Major Task 4: ECM characterization and magnetic resonance imaging (MRI).
Milestones: Characterize tissue changes in both prospective and long-term IR monkeys and relate these to in vivo insulin sensitivity assessments. Validate the utility of MR imaging to detect qualitative tissue changes (40% achieved in context of 5 year plan)

SA4: Evaluate therapeutic agents that reduce fibrosis and restore fat expansion to mitigate metabolic changes with IR.

Major Task 5: Mouse intervention study
Milestones: Prevent metabolic disease development in IR mice with interventions. Demonstrate reductions in protein modifications and/or tissue remodeling with treatment (60% achieved in context of 5 year plan).

Project 2 – Radiation-Induced Heart Disease (Register)

We proposed 3 inter-related Specific Aims across the 5 Year Grant Period.

SA 1: Determine the Effects of Total Body Irradiation on NHP Cardiac Structure and Function.

Major Task 1: Novel cardiac MRI approaches will be used to evaluate myocardial tissue fibrosis, a key component of RIHD, in order to follow changes in myocardial phenotypes in animals across time. Additional structural and functional cardiac phenotypes to be assessed by echocardiography/MRI include left ventricular (LV) mass, posterior and interventricular wall thickness, right ventricular thickness, and aortic wall thickness. Functional parameters will include systolic and diastolic function, ejection fraction, aortic stiffness/pulse wave velocity, wall motion, and electrocardiography. Grid tag mapping will be also used to assess strain and LV volume.
Scheduled Dates: Months 6-48
Milestones: Percent completion: 40% in the context of 5 year plan
Detailed cardiac ultrasound (US) evaluations were conducted and images acquired on the RSC (year 01, GE instrument) and at baseline and at 20 weeks post exposure (March 2017) in the PRC. Echocardiographic image analysis was conducted using the scanner for images collected in the PRC at Baseline. New US image analysis software (TOMTEC) was installed and Drs. Register, Michalson, and staff were trained in its use. The PRC 20 week cardiac US images were evaluated using this analysis package. Cardiac MRI image analysis is underway and some phenotypes determined. Tissue collections from subjects going to necropsy continue.

SA 2: Identify Novel Molecular Biomarkers of Cardiovascular Injury and RIHD

Major Task 2: Identify and evaluate emerging serum markers of cardiac damage implicated in cardiomyocyte death (microRNAs such as miR133a) and extracellular matrix remodeling (type I and III collagen propeptides and degradation products). Circulating miRNA levels and serum extracellular matrix turnover biomarkers will be evaluated in relation to structural and functional phenotypes and histologic and biomolecular features of myocardial tissues and differentially expressed myocardial mRNA and miRNA which will be identified through expression profiling of heart tissues obtained at necropsy.
Scheduled Dates: Months 6-48
Milestones: Percent completion: 15%
RSC: blood samples obtained and processed; PRC: baseline and immediate post-radiation blood samples were collected, processed, and archived for future biochemical analyses. Ongoing blood collections are underway.

SA 3: Determine the Efficacy of Candidate Mitigating Agents on RIHD.

Major Task 3: Assessment of Mitigating Agents. We propose to retrospectively and prospectively assess cardiac and coronary artery injury in NHP in studies of mitigating agents, using animals in the de novo cohort, the long-term cohort, and from prospective studies of growth factors (e.g. HGH), superoxide dismutase mimetics, and novel therapeutics (e.g. platelet analogs). We will use the pathologic and biomarker approaches noted above, including in vivo assessments. These results will be critical to our understanding of RIHD. The preliminary data suggests that the changes in the heart based on the radiation dose are significantly greater that would have been predicted from prior murine studies.
Scheduled Dates: Months 6-48

Milestones: Percent completion: 25% complete in the context of a 5 year plan (assessed effects of a mitigating agent (superoxide dismutase analogue, hexyl MnSOD) on myocardial gene expression, (manuscript in development), performed histologic staining of coronary arteries in available hearts, collected cardiac tissues from Project 1 rat study and cardiac tissue from rhesus monkeys, planning for ECM and other biomarkers in the radiation survivor cohort; other preparations under way). Analyses of troponin-I and BNP in an ancillary study are partially completed (see data below).

Project 3 – Immune Recovery (Duke Consortium – Chen & Sempowski)

SA 1: Define the roles of thymopoiesis and peripheral expansion in overall T cell reconstitution after radiation-induced injury based on radiation dose.

Major Task 1: NHP Studies (5% complete in context of 5 year plan, first analysis in progress)
Milestones:

1.1. Phenotypic analyses in long-term cohort (60 months, 40% complete)
1.2. sjTREC in long-term cohort (60 months, 30% complete)
1.3. Phenotypic analyses in prospective cohort (60 months, 40% complete)
1.4. sjTREC in prospective cohort (60 months, 30% complete)
1.5. Determine primary immune response to influenza vaccine (36 months, 0% complete)
1.6. Determine primary and recall immune response to influenza vaccines (60 months, 0% complete)

Major Task 2: Murine Studies
Milestones:

2.1. Local IACUC Approval (3 months, 100% complete)
2.2. Determine the roles of thymopoiesis and peripheral expansion in overall T cell recovery in the classic radiation injury model (18 months, 100% complete)
2.3. Determine the roles of thymopoiesis and peripheral expansion in overall T cell recovery in the second radiation injury model (7-24 months, 0% complete)

SA 2: Determine if therapeutic agents identified in our previous studies are able to promote or accelerate overall T cell immunity after radiation injury.

Major Task 3: HGH Mouse Studies
Milestones:

3.1. Determine the effect of HGH on phenotypic T cell reconstitution (25-36 months, 0% complete)
3.2. Determine the effect of HGH on functional T cell recovery (37-48 months, 0% complete)
3.3. Determine the mechanism by which HGH promote T cell reconstitution (49-60 months, 0% complete)

Major Task 4: IGF-1 Mouse Studies
Milestones:

4.1. Determine the effect of IGF-1 on phenotypic T cell reconstitution (25-36 months, 0% complete)
4.2. Determine the effect of IGF-1 on functional T cell recovery (37-48 months, 0% complete)
4.3. Determine the mechanism by which IGF-1 promote T cell reconstitution (49-60 months, 0% complete)

Project 4 - Genomic Sequencing and Stem Cell Lines (Duke Consortium – Dave)

Aim1: Define the genetic mutations and gene expression signatures induced by DEARE

Major Task 1: Exome Sequencing
Milestones:
DNA Sample extraction (months 1-36) - 50% complete
Exome analyisis (months 13-60) - 20% complete
Major Task 2: Transcriptome Sequencing
RNAseq (months 6-48) - 20% complete
RANseq analysis (months 12-60) - 20% complete

Aim 2: Determine the molecular basis of lymphoid immunodeficiency induced by DEARE.

Major Task 1: Generate iPSCs
Milestones: iPSC from controls complete 25% complete
Milestones: iPSC from genetic variants 5% complete

Major Task 2: Differentiate iPSCs into lymphoid lineages
Milestone(s) Achieved: B cell characterization complete 5% complete
Milestone(s) Achieved: T cell characterization complete 0% complete

What was accomplished under these goals?

Core Primate Studies (Cline)

1) Major activities:

Protocol approvals for all animal studies; establishment of subcontracts and accounts; development of a meeting schedule; review of goals and plans with all investigators; hiring/allocation of effort for personnel; acquisition of NHP subjects for the prospective cohort; pre-irradation physical examinations, imaging, and blood sampling for all projects; total body irradiation.
Characteristics of our animal populations are briefly described below.

2) Specific objectives:

As per SOW. Regulatory approvals, establishment of meeting schedule, hiring, planning, animal acquisition, irradiation.

3) Results/key outcomes:

- All animal protocol approvals complete at local and ACURO level
- Subcontracts and accounts established
- Goals and plans reviewed with all investigators
- Monthly web conferences established
- Hiring/effort allocations made as planned
- Secure server folders established for data exchange
- NHP subjects acquired for PRC
- Sampling and data acquisition on schedule
- Slight delay in irradiation date (Sept 2016 Y1Q4 to Oct 2016 Y2Q1)
-

4) Other achievements:

Data presented at the annual national meeting of the Centers for Medical Countermeasures against Radiation and at local Wake Forest and Duke venues.

A brief overview and synopsis of major findings is presented below.

<u>The Radiation Survivor Cohort (RSC)</u>

The population of the RSC is shown graphically in Figure 1 (see next page). Briefly, this cohort consists of rhesus macaques (*Macaca mulatta*) irradiated as juveniles or adults, in the range of 3-8.5 Gy via single total body exposure, at a dose delivery of 60-80 cGy/min. The cohort is supported by the National Institute of Allergy and Infectious Disease (NIAID), which is leveraged by this DOD Focused Program award. Animals were acquired between 2007 and 2016 through an “adoption” strategy from multiple sites. The RSC currently consists of 85 irradiated animals and 15 controls. The population has a 5:1 male:female ratio. Animals are housed socially, primarily in pens, and fed a custom-formulated “Typical American Diet”. All animals receive daily environmental enrichment and are part of a behavioral management program. Approximately one-third of the animals were given mitigating agents (e.g. antibiotics or growth factors) during the acute period of hematopoietic injury. This cohort is studied using a multidisciplinary approach to long-term morbidity/mortality. Notably, some animals are now 13 years out from irradiation, providing a unique view of DEARE.

Animals in the RSC undergo a regular schedule of medical care and assessment, including but not limited to:

Daily
- Twice-daily clinical observations
- Environmental enrichment

Biweekly
- Cognitive testing (subset)

Monthly
- Physical exam
- Blood collection for experimental measures and archive
- Urine collection for experimental measures and archive
- Body weight

Semiannually
- Complete blood counts
- Clinical chemistry panels
- Testing for diabetes mellitus (hemoglobin A1c, glucose, with glucose tolerance testing and mimimal model testing on a subset)
- Anthropometrics (trunk length, waist diameter)

Annually
- Flow cytometry (blood, see Project 3)
- Bone marrow aspirate
- Echocardiography
- Computed tomography scan (whole body)
- Renal ultrasound
- Gastrointestinal endoscopy and biopsy
- Bronchoalveolar lavage
- Cranial MRI (subset, 3 year rotation)
- Ocular exam

All animals are given routine veterinary care, and we have established clinical criteria for identification and management of animals with health abnormalities. Major patterns of morbidity in the RSC are summarized in Table 1, below.

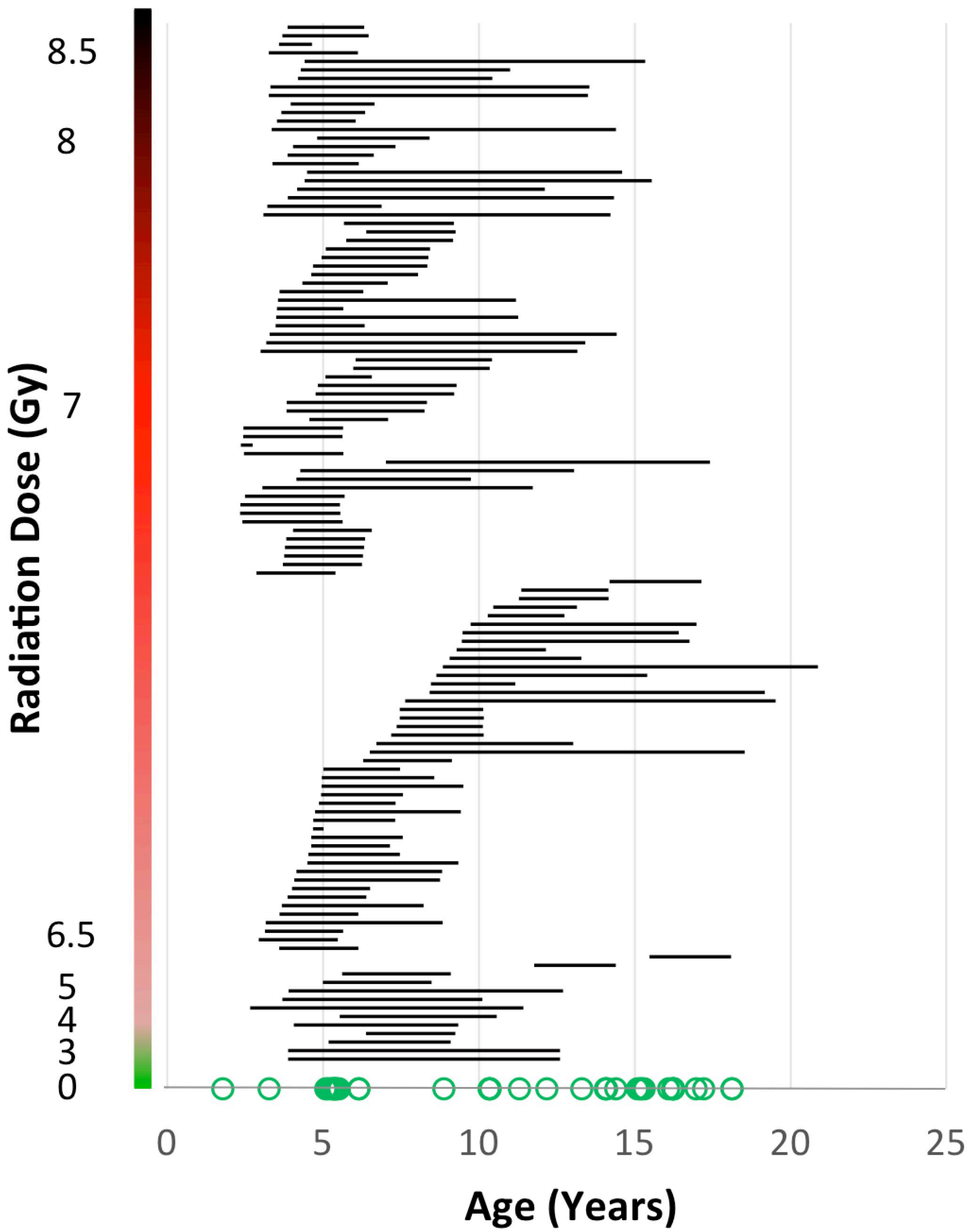

Figure 0.1: Age and dose distribution of the Radiation Survivor Cohort. Each horizontal bar represents a single animal; the left end of the bar is the age at which the animal was irradiated, and the right end of the bar is the animal's current age or age at time of death. Green circles represent the current age of non-irradiated controls. For rhesus monkeys, the typical age a puberty is 3.5 years; typical lifespan is 30 years.

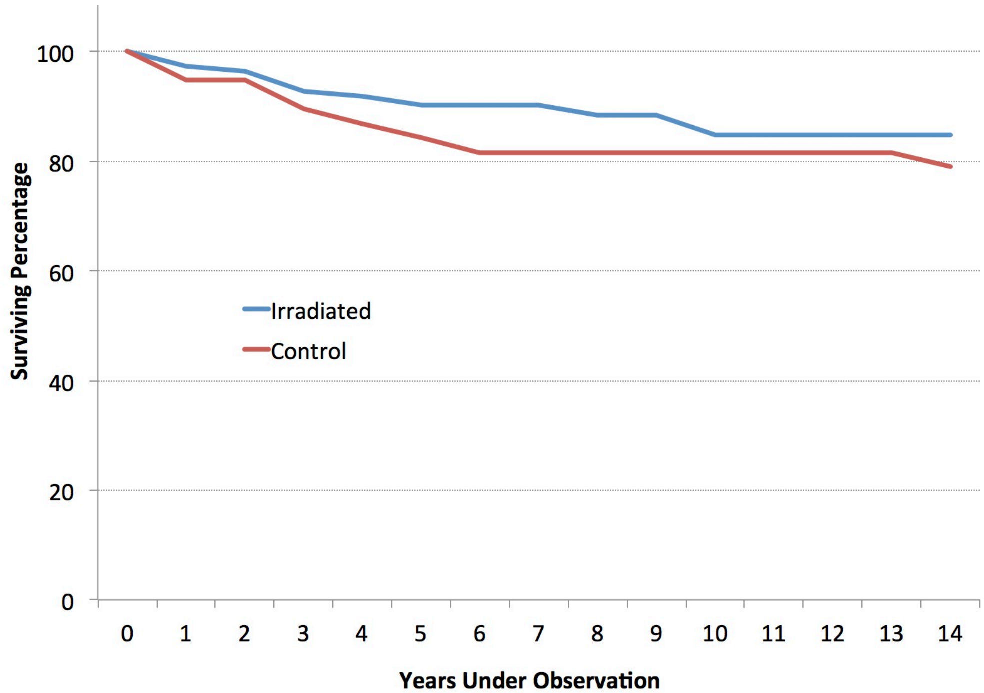

Figure 2: Survival curves by years since irradiation. There is no statistical difference between irradiated and control groups.

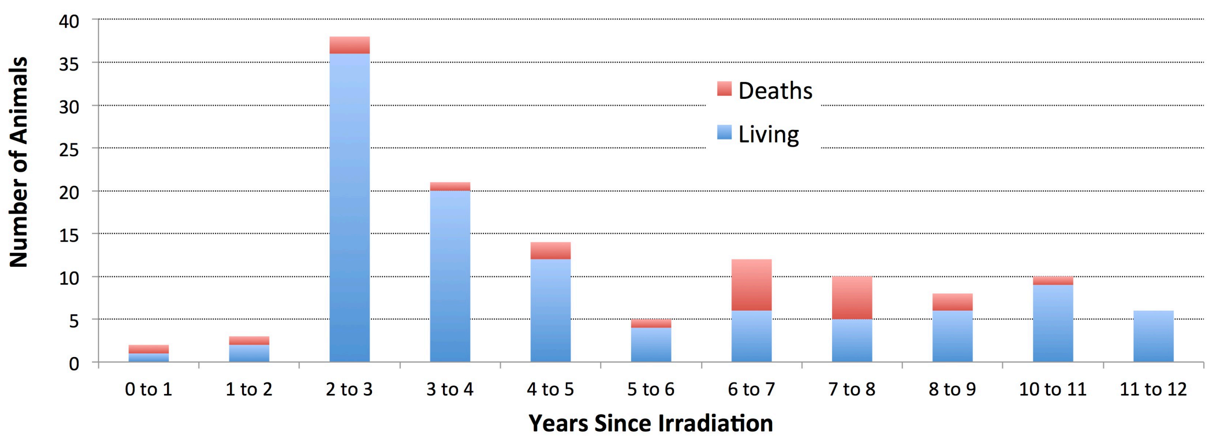

Figure 3: Proportions of irradiated animals euthanized for serious illness, by years since irradiation. Although mortality appears to peak 6-8 years post-irradiation, there no statistically significant time effect.

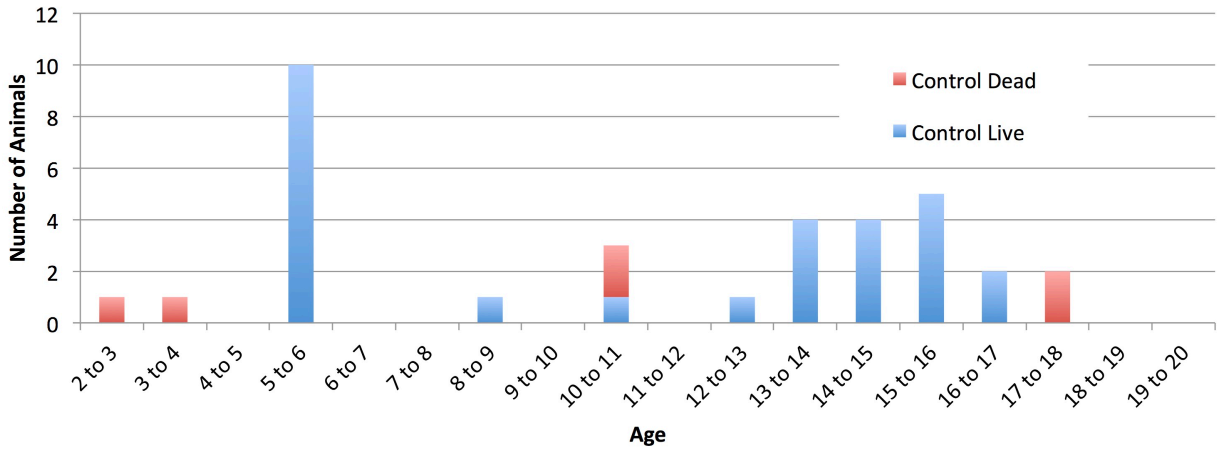

Figure 4: Proportions of control animals euthanized for serious illness, by age. There no statistically significant age effect.

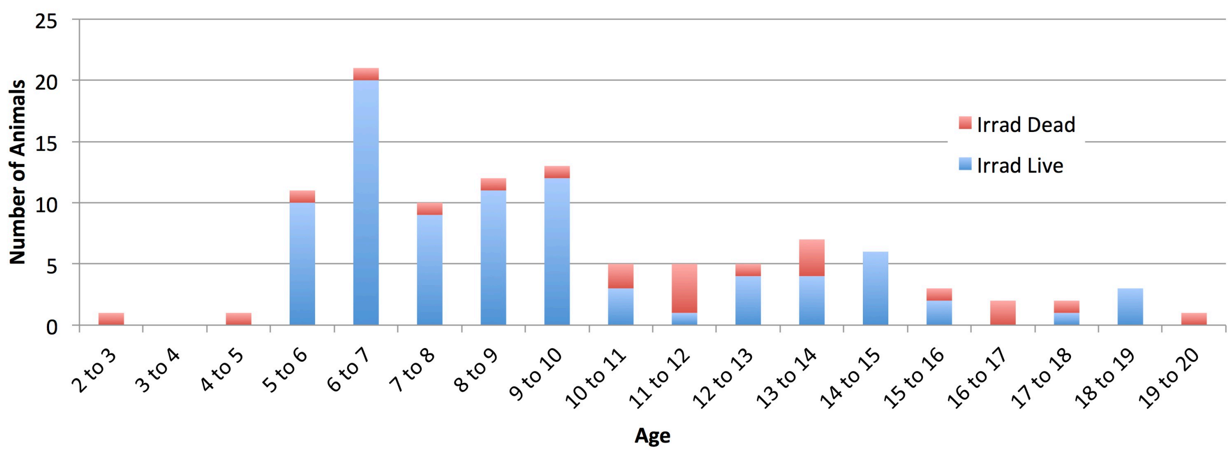

Figure 5: Proportions of irradiated animals euthanized for serious illness, by age. There no statistically significant age effect; the apparent relatively greater mortality in animals aged 10-14 corresponds to the post-irradiation deaths at 6-8 years in Figure

Table 1: Threshold-based determinations of morbidity in the long-term Radiation Survivor Cohort.

Organ or Disease	Irradiated	Control	Fisher's Exact p value	Criteria for Diagnosis of Abnormality
Body Condition Obese	44.4% (20/45)	60% (9/15)	NSD	Waist Circumference > 45 cm or DEXA Body Fat > 30% after 7 years of age
Body Condition Underweight	15.6% (7/45)	13% (2/15)	NSD	Waist Circumference < 25 cm or DEXA Body Fat < 12.3% after 7 years of age
Bone (osteopenia)	34.10% (15/44)	0% (0/13)	0.0129	DEXA BMC < 274g BMD < 0.373 g/cm^3 after 7 years of age CT: Fracture or other abnormality
Brain	12.50% (12/96)	0% (0/15)	NSD	Any MRI lesion Neurologic abnormality
Cardiovascular	25.30% (21/83)	20% (3/15)	NSD	Murmur/valvular insufficiency on echo Stroke volume <5 mls/stroke Cardiac output <0.5 L/min Hypertension MAP > 120 Other
Diabetes	13.10% (16/122)	0% (0/38)	0.013	HbA1c >6.5 Fasting Blood Glucose > 100 mg/dL x 3 Non Fasted Blood Glucose > 200 mg/dL
Gastrointestinal	6.00% (5/83)	6.70% (1/15)	NSD	Any lesion on endoscopy Chronic diarrhea (severity code >2 for >5 days) Other GI signs
Lung	10.80% (9/83)	13.30% (2/15)	NSD	CT densities (any amount) Emphysema >25% of lung volume Hypoxia under sedation (SPO2 < 80%)
Neoplasia	13.10% (16/122)	0% (0/38)	0.0125	Biopsy with histologic diagnosis
Ocular (cataracts)	21.70% (18/83)	0% (0/15)	NSD	Ophthalmologic exam (slit lamp); lens opacity
Renal	35.60% (31/87)	0% (0/24)	< 0.001	Bun > 30 mg/dl Cr > 1.1 mg/dl Loss of renal volume >50% Urolithiasis
Skin	22.90% (19/83)	6.70% (1/15)	NSD	Biopsy diagnosis of dermatitis Other significant disease (e.g. alopecia, depigmentation)
Testicular atrophy	56.70% (17/30)	6.30% (1/16)	0.0253	<10 ml testis volume after 5 years of age

Abbreviations: BUN = blood urea nitrogen; Cr = serum creatinine; CT = computed tomography; DEXA = dual emission x-ray absorptiometry; HbA1c = hemoglobin A1c; MRI = magnetic resonance imaging; NSD = no significan difference; SP02 = oxygen saturation.

The Prospective Radiation Cohort (PRC)
The study design for the PRC is shown below. These specific-pathogen-free animals were acquired and quarantined in year 1 and irradiated in October 2016. Imaging and sample collections are proceeding as per the program statement of work and the needs of the individual projects.

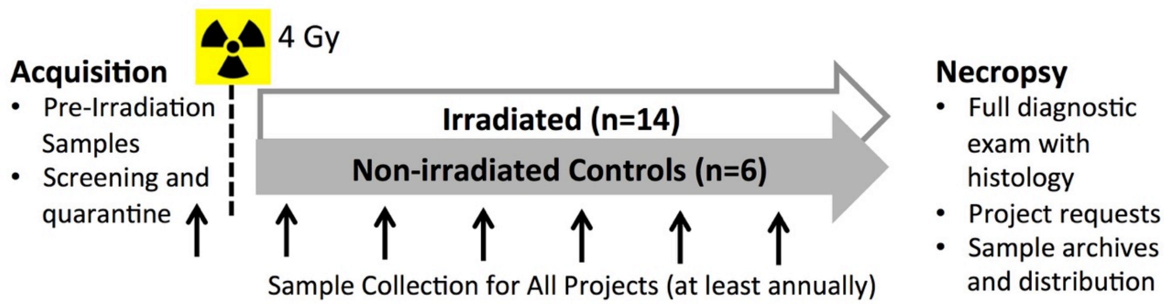

Figure 6: Study design for the Prospective Radiation Cohort (PRC).

Acute Effects in the Prospective Cohort

Irradiation exposures were done as planned, using a 6MV Varian Linear Accelerator and parallel opposed fields to maximize uniformity of dose delivery (total dose 4Gy).

As anticipated, total body irradiation (TBI) produced a rapid and profound hematopoietic injury resulting in lymphopenia, followed by neutropenia, thrombocytopenia and anemia. Eight irradiated animals required transfusions of irradiated blood. The pattern of acute hematopoietic injury is shown in figure 7.

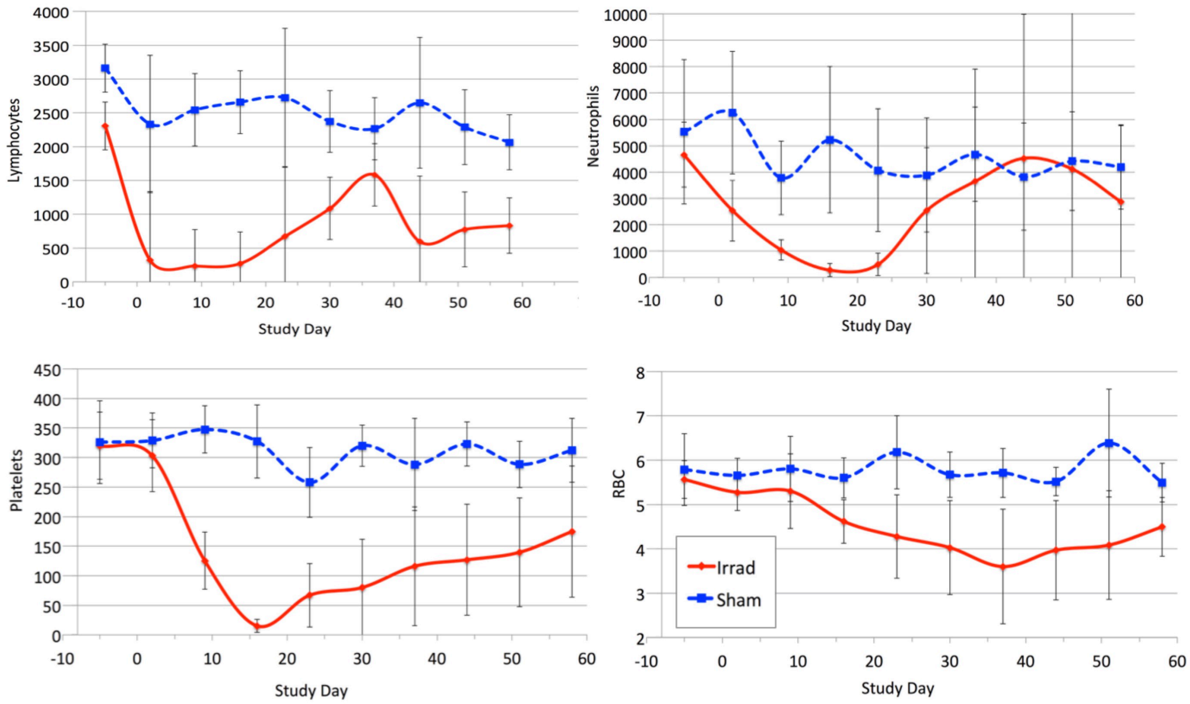

Figure 7: Longitudinal graphs of lymphocyte, neutrophil, platelet and red blood cell counts after 4 Gy TBI.

Three TBI exposed animals in the PRC reached pre-determined endpoints for experimental euthanasia (persistent thrombocytopenia or neutropenia, or evidence of infection such as fever unresponsive to antibiotic treatment). Two of these animals were diagnosed with *Spironucleus* infection, an unusual opportunistic protozoal pathogen of immunosuppressed primates, and one was diagnosed with a disseminated bacterial infection (*Klebsiella)*. All three animals were humanely euthanized and a complete post-mortem tissue collection was done, including terminal samples for Project outcomes.

Spironucleus is a previously reported pathogen of immunodeficiency virus-infected macaques (Bailey et al., 2010, Vet Pathol. 2010; 47:488-94, PMID: 20351359), but has not been reported as a complication of irradiation. Our animals are specific pathogen free and are not infected with immunodeficiency viruses (either type D retroviruses or lentiviruses). We have confirmed the identity of the *Spironucleus* pathogen by PCR, and we intend to publish this novel observation.

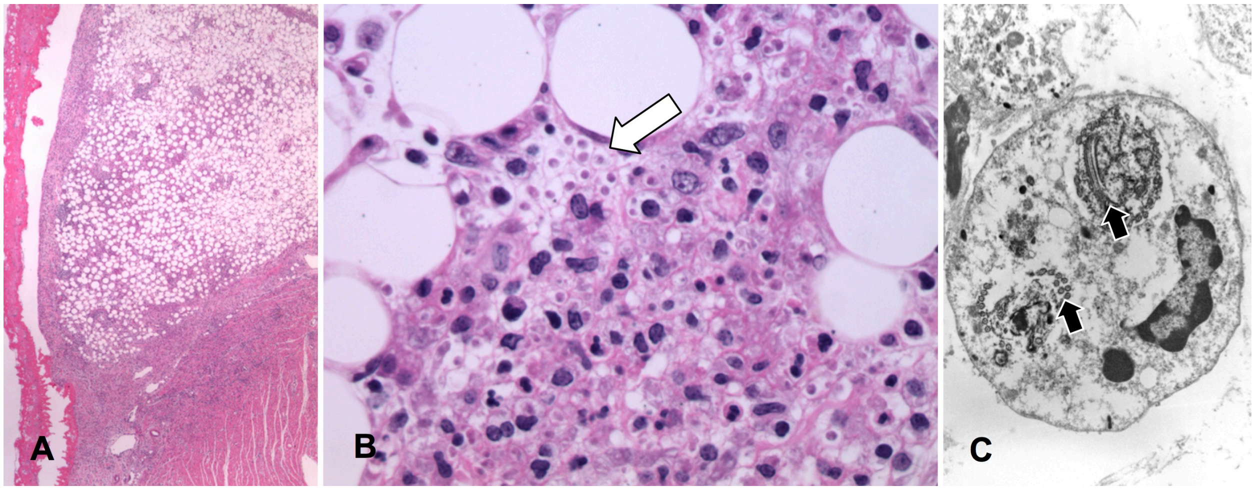

Figure 8: Histologic and ultrastructural appearance of Spironucleus sp. infection. A - myocarditis and epicarditis involving epicardial fat. B - Spironucleus organisms within the lesion (hematoxylin and eosin stain). C - Ultrastructural appearance of the organism confirming characteristic morphology (nucleus and flagellae).

Project 1. Diabetes (Kavanagh)

The overall goal of Project 1 is to identify pathways that track some radiation survivors on a path that results in dysregulated metabolism and increased risk for diabetes. Our studies (**Figures 1.1 and 1.2**) utilize a unique reverse translational flow whereby diabetes has been reported in survivors of radiation exposures, including our nonhuman primates, and we have designed studies to identify the time course, tissue targets, and interventional strategies that will combat diabetogenesis in at-risk individuals. In accordance with this continuum, this annual report is divided into sections that address major accomplishments within the sub-studies named the Radiation Survivor Cohort (RSC), the Prospective Radiation Cohort (PRC), and the Interventional Rodent Studies.

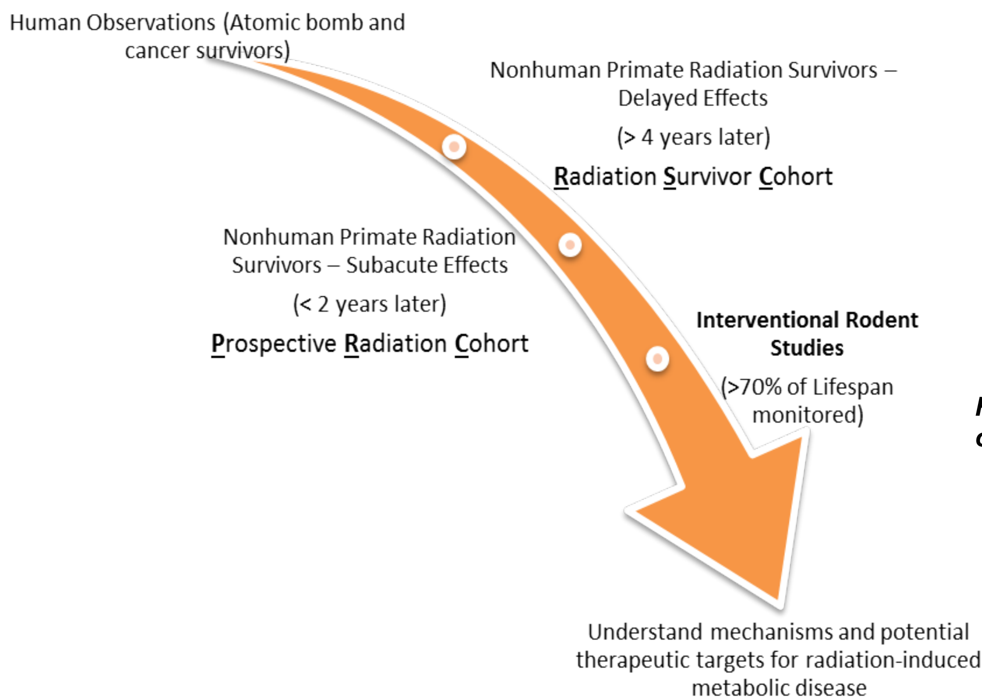

Figure 1. Studies Reported on within Project 1.

A diagram of the monkey cohorts (RSC and PRC) and the assessment points are shown in **Figure 1.1**. We are halfway through the assessment period.

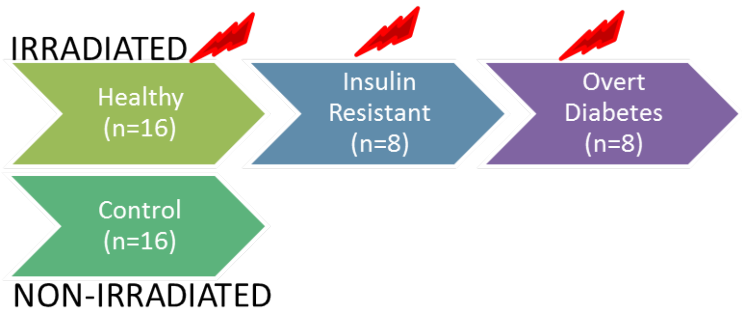

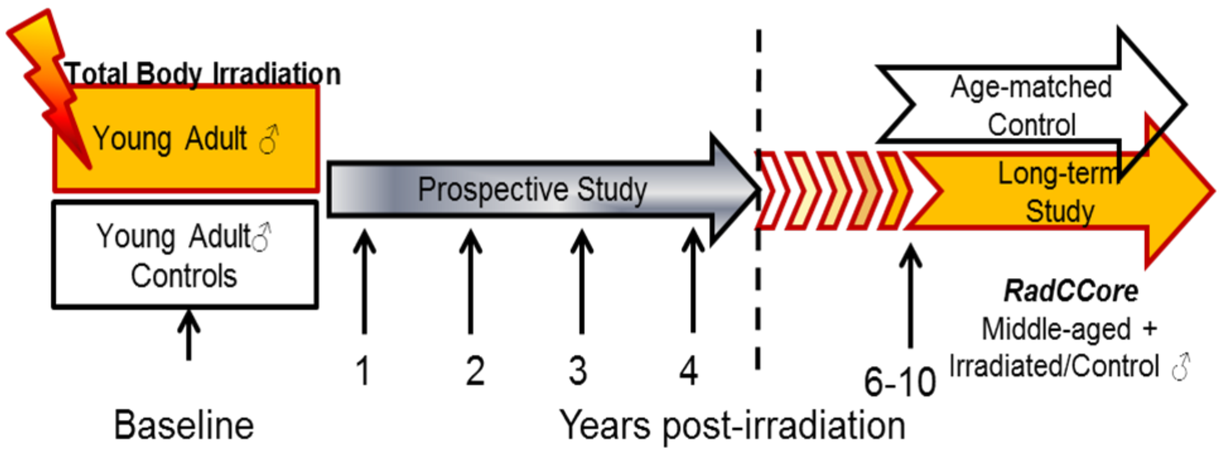

Figure 1.2. RSC monkey groups evaluated within Project 1 (top) and the overlap/continuum achieved with the PRC and RSC

1. **<u>Radiation Survivor Cohort (RSC)</u>**

We have published 2 manuscripts that detail the derangements of metabolism in the RSC monkeys. The most recent publication includes the majority of the data included in the last annual report.

- **Kavanagh K**, Dendinger MD, Davis AT, Register TC, DeBo R., Dugan G, Cline JM. Type II diabetes as a potential delayed late effect of whole body irradiation in nonhuman primates. Radiation Research 2015 183: 398-406.
- Fanning KM, Pfisterer B, Davis AT, Presley TD, Williams IM, Wasserman DH, Cline JM, **Kavanagh K**. Changes in microvascular density differentiate metabolic health outcomes in monkeys with prior radiation exposure and subsequent skeletal muscle ECM remodeling. American Journal of Physiology – Regulatory, Integrative and Comparative Biology 2017 313(3): R290-297.

These studies identified that skeletal muscle maintains an insulin resistant state years after radiation exposure, but animals exhibiting indicators of enhanced capillary perfusion were able to maintain normal overall glucose metabolism and prevent diabetes from developing. In the current year we have selected a new cohort of radiation survivors and age-matched control animals that have not been exposed for ongoing assessment. We have chosen insulin resistant

but non-diabetic representatives so as to get information from animals that have not yet developed diabetes, or are intermediate in their metabolic response (**Figure 1.3**).

The demographics of the new animals (8 healthy irradiated, 8 healthy non-irradiated, and 8 insulin resistant) are shown in **Table 1**. In describing these animals, insulin resistance (IR) is also referred to those with metabolic disease (MetDz). As seen in our publications, radiation results in smaller animals that are non-obese but despite this lean status, show variable metabolic health as measured by glycated HbA1c (%) values and plasma triglycerides (TG). The response to glucose challenge of these individuals is replicate of the profiles published in 2015; the unusual features are that pancreatic responses to glucose in the monkeys with metabolic disease is intact, but fasting hyperinsulinemia is present and glucose disposal is normal (**Figure 1.3**). This further indicates that peripheral tissues are a more important target for health outcomes. HOMA scores are calculated from insulin and glucose in the fasting state and show the expected differences (**Figure 1.4**). The unusual phenotype is the radiation survivor that remains protected from metabolic disease. These animals show significantly lower insulin requirements to metabolize glucose and are suggestive of high insulin responsiveness in the fasting and post-challenge state (**Figure 1.4**). The difference in in insulin response did not reach statistical significance (ANCOVA p=0.17) however we believe this is a biologically interesting phenotype that will be more closely evaluated by quantitating insulin-stimulated tissues for effective receptor activation, as done in our first publication (Kavanagh, Rad Res 2015).

Table 1. Demographics of RSC monkeys newly added to Project 1.

	Dose (Gy)	Time Since Irrad (yrs)	Age @ Irrad (months)	Age (yrs)	BW (kg)	TG (mg/dL)	Glucose (mg/dL)	A1c (%)
Non-Radiated CTL	N/A	N/A	N/A	12.8 (1.36)	14.9 (2.08)	46.4 (2.38)	57 (4)	4.38 (0.09)
Irradiated CTL	6.48 (0.55)	6.26 (0.98)	52.1 (5.94)	10.7 (0.89)	8.51 (0.61)	40.2 (3.57)	54 (4)	4.38 (0.08)
Irradiated IR	6.56 (0.42)	4.33 (1.17)	57.8 (5.60)	9.14 (1.42)	8.62 (0.87)	61.6 (8.69)	74 (9)	5.75 (0.58)
p-value	NS	0.23	0.50	0.13	0.004	0.06	0.12	0.03

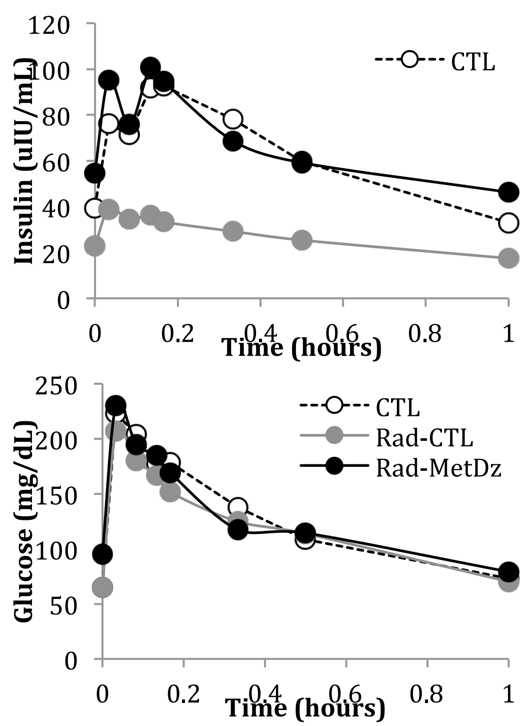

Figure 1.3. Insulin (top) and glucose (bottom) concentrations in response to intravenous glucose challenge. Monkeys with metabolic disease and insulin resistance show similar pancreatic responses and glucose disposal however radiation survivor monkeys that have good health have significantly lower insulin requirements (=better insulin sensitivity in peripheral tissues).

Figure 1.4. HOMA values from monkeys selected from the RSC indicate insulin resistance levels diverge in those selected to study mechanisms of radiation-induced diabetes.

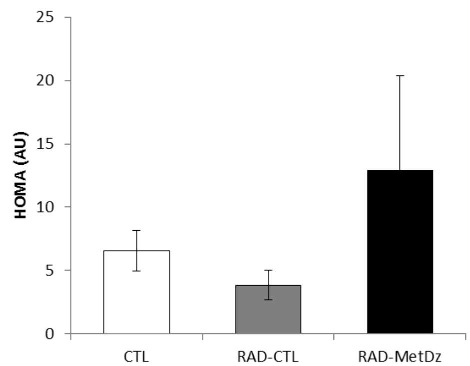

With the addition of these new animals we have strengthened our hypothesis that successful tissue perfusion is key to preventing radiation-induced diabetes years after exposure. Nitric oxide (NO) is the master regulator of vascular tone, and is required for vasorelaxation and thus allowing blood to perfuse further down the capillary tree. Opening of capillaries increases the effective surface area by which glucose can be taken up by muscle cells. Skeletal muscle is responsible for the metabolism of 90% of circulating glucose and thus small reductions in perfusion of this tissue has disproportionately large effects on metabolic health. Plasma NO metabolites (i.e. NO_3) are biomarkers of basal endothelial nitric oxide synthase activity, and levels are deficient in radiation survivor monkeys with insulin resistance (IR) or diabetes. These animals are grouped in **Figure 1.5** as radiation exposed monkeys with metabolic disease (Rad Met Dz). This confirmed that our newly selected monkeys upheld our theory that "super-perfusion" is required to overcome changes in muscle that result of radiation exposure. The second messenger cGMP is what effects smooth muscle relaxation and there is a trend for there to be a reduction in response to radiation which we believe is consistent with underlying changes to skeletal muscle architecture we reported this year (Fanning et al AJP 2017).

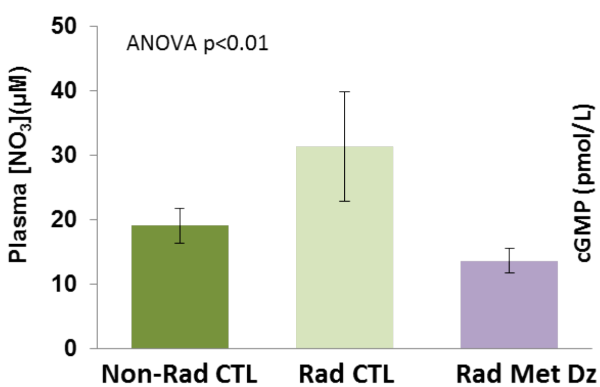

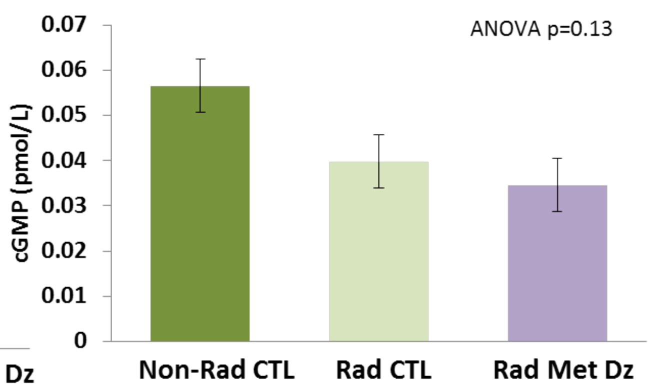

Figure 1.5. Vasorelaxant nitric oxide is high in disease-resistant radiation survivor monkeys. Nitric oxide's second messenger cGMP is lower in radiation survivors.

The primary disturbance in skeletal muscle architecture noted post-radiation was an overabundance of Type 4 collagen, which is an important basement membrane component. Normal extracellular matrix composition allows effective diffusion of NO and cGMP from the endothelium to smooth and skeletal muscle cells, and provides structural integrity for the

signaling of these and other molecules through integrins that connect the extracellular matrix to the cytoskeleton which integrate with intracellular signaling cascades.

We are in process of evaluating the skeletal muscle histology from the newly selected RSC monkeys. We have first confirmed that Type 1 collagen, the most abundant form, is not different with radiation exposure (**Table 2**) and is consistent with our prior report. Currently in process is quantification of the collagen subtypes and capillary density, which we believe is where the interesting findings will be. These data will be combined with proteomics assessments.

Table 2.	Non-Rad (n=7)	Rad (n=11)
% Total Slide Type 1 Collagen	3.23 (0.63)	4.00 (0.59)
% Total Slide Muscle	96.77 (0.63)	96.0 (0.59)

Proteomics assessments have been initiated in the RSC monkeys. This is aimed to provide more granular data about changes in myocellular function and identify pathways that differentiate individuals that track towards developing diabetes from those that remain metabolically healthy. Non-targeted proteomics were performed on tissues retrieved by muscle biopsies, and over 500 proteins were annotated. In non-targeted proteomics, the results reflected the most abundant proteins in muscle, which are primarily reflecting muscle's contractile function. The top 28 abundant proteins in muscle are shown in **Table 3** and illustrate the functional nature of these proteins. In general, prior radiation exposure increased the abundance of these high concentration proteins (286 proteins were increased and 103 proteins were decreased) but none reached statistical cutoffs for significance.

Table 3: Top 29 abundant proteins in muscle	
Titin	Beta-enolase
Creatine kinase M-type	Filamin-C
Glyceraldehyde-3-phosphate dehydrogenase	Myosin regulatory light chain 2, skeletal muscle isoform
Myosin-7	Myosin-4
Glycogen phosphorylase, muscle form	Fructose-bisphosphate aldolase A
Pyruvate kinase PKM	ATP synthase subunit beta, mitochondrial
Serum albumin (Fragment)	Actin, alpha skeletal muscle
Hemoglobin subunit beta	Phosphoglycerate kinase 1
Myosin-6	Tropomyosin alpha-3 chain
Myosin-1	Triosephosphate isomerase
Sarcoplasmic/endoplasmic reticulum calcium ATPase 1	Malate dehydrogenase, mitochondrial
Alpha-actinin-2	ATP-dependent 6-phosphofructokinase, muscle type
Myosin-2	Tropomyosin alpha-1 chain
Sarcoplasmic/endoplasmic reticulum calcium ATPase 2	Heat shock cognate 71 kDa protein
Hemoglobin subunit alpha	

We then moved to targeted proteomics platforms where muscle was fractionated to be able to extract and assess lower abundant proteins in the myocellular matrix. We chose 4 representative animals from each group (Non-radiated control, Radiated control, and Radiated insulin resistant) to evaluate. From these 3 groups, 929 proteins were common with over 1100 proteins identified from each group.

Our first assessment was to evaluate for differences that were related to radiation exposure, not metabolic disease. Consistent with non-targeted proteomics we see that radiation exposure generally upregulated protein abundance. Two proteins that were significant with radiation, but seen in the absence of metabolic disease, were proteasomal subunit type 3 and mitochondrial superoxide dismutase. These are both proteins that have been associated with positive health outcomes which is consistent with the healthy phenotype of these radiation survivors. These have low abundance but were significantly higher in irradiated monkeys. A graph of means and standard deviations of proteins identified in healthy non-radiated and irradiated monkeys is shown in **Figure 1.6**.

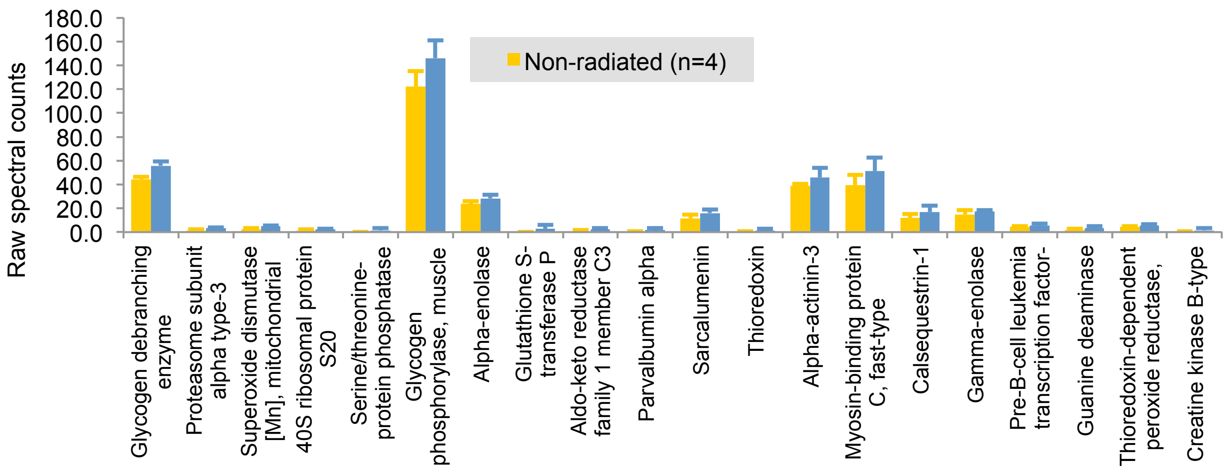

Figure 1.6. Radiation increases protein abundances in monkeys that avoid diabetes as a delayed effect of radiation.

We then compared the differences in protein profiles in those monkeys that succumbed to metabolic disease post-radiation to those that remained healthy (**Figure 1.7**). Monkeys with metabolic disease generally had higher protein abundances. A different set of proteins were identified that separated these cohorts. Proteins to note in these analyses include upregulation of those related to carbohydrate metabolism and oxidation status. Fatty acid binding protein was significantly up-regulated in those animals with metabolic disease. Fatty acid binding protein is a marker of subclinical endotoxemia and inflammation, which was reported as being elevated in a larger sampling of the RSC monkeys (Debo, 2016 Rad Res).

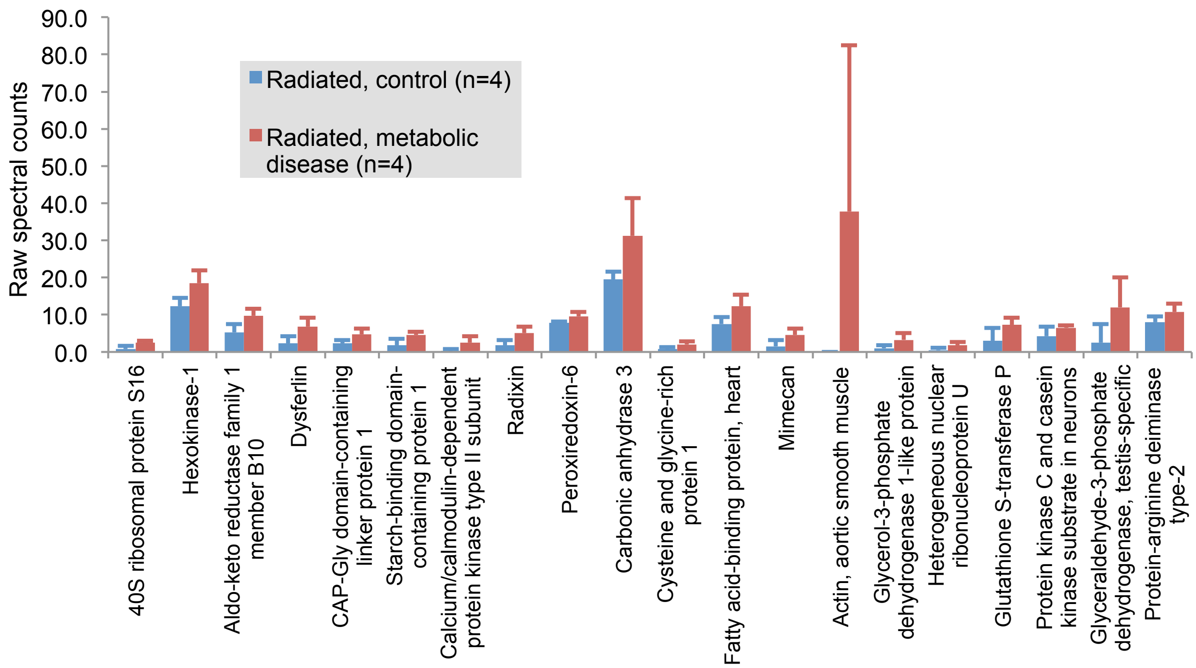

Figure 1.7. Metabolic disease development in radiation survivors is associated protein increases related to carbohydrate metabolism and antioxidant defense.

Parallel reaction monitoring is a proteomics technique for measuring specific proteins of interest. We targeted eNOS, Akt-2, RhoA, and HSP90 for quantitation by this very sensitive measure. Consistent with our PCR results (Fanning, AJP 2017) eNOS was equivalent across our 3 groups. HSP90 amounts were variable and our prior report of lowering following radiation exposure was not confirmed by this method. Prior to this study, Dr. Cristina Furdui had identified Akt-2 in cell culture models as a target that was specifically redox regulated and affected by radiation exposure. We also reported that Akt activation was reduced in response to insulin in radiation survivor monkeys (Kavanagh, 2015 Rad Res). The proteomics shows that Akt-2 is lower in RSC monkeys with metabolic disease and is variable in RSC monkeys without metabolic disease (**Figure 1.8**). Insufficient Akt-2 limits the capacity for insulin to effect glucose disposal and is implicated in NO signaling – both effects would be at least additive in reducing capillary perfusion and glucose metabolism. The next step for this assessment will be redox-specific proteomics to identify the oxidative modifications occurring on Akt-2.

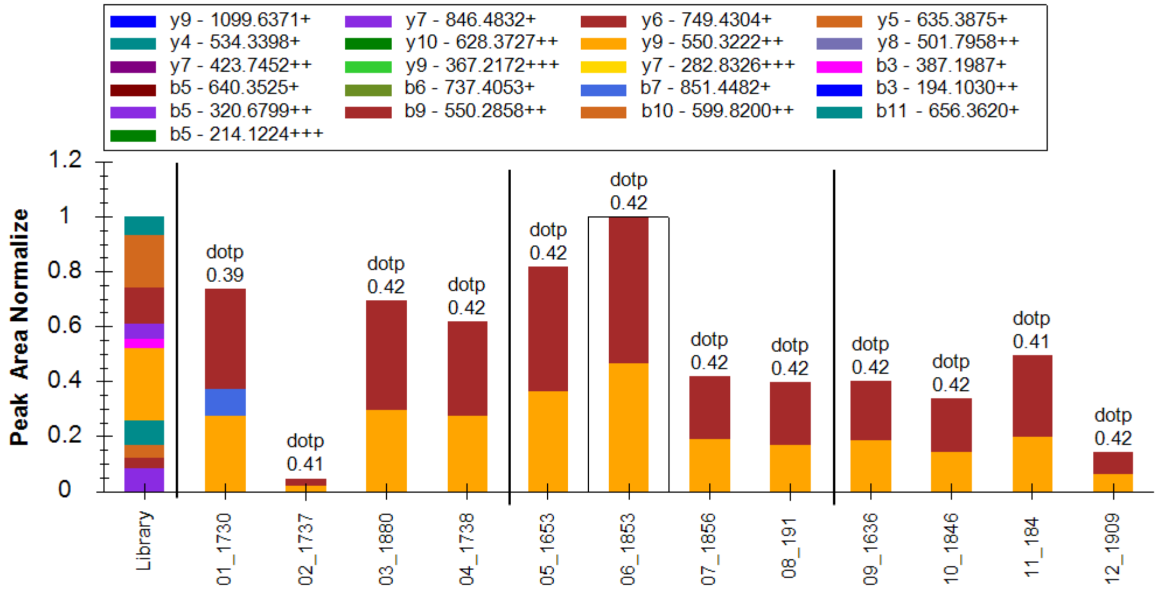

Figure 1.8. Mass spectrometry identification of Akt2 shows that the amount in muscle is variable in healthy radiation survivors, but generally low in those that develop insulin resistance and metabolic disease.

Another protein that was identified in non-targeted proteomics was RhoA (**Figure 1.9**). This is a kinase that is involved in many cellular pathways, but includes important functions with the cellular cytoskeleton. We see that monkeys that remain healthy after radiation exposure have lower amount of RhoA in their muscle. This finding is very exciting as RhoA has important roles in smooth muscle and vascular cell proliferation and migration. RhoA lowering reduces fibrosis in diabetes models and has even been considered as a target for diabetes therapy. Hyperglycemia is known to upregulate RhoA, so the finding in the metabolic diseased animals as compared to their non-diabetic comparators is expected. We will focus on trying to understand the interaction between effective RhoA suppression and the maintenance of normal capillary growth and remodeling as these two characteristics separates the irradiated monkeys based on whether they end up healthy or unhealthy.

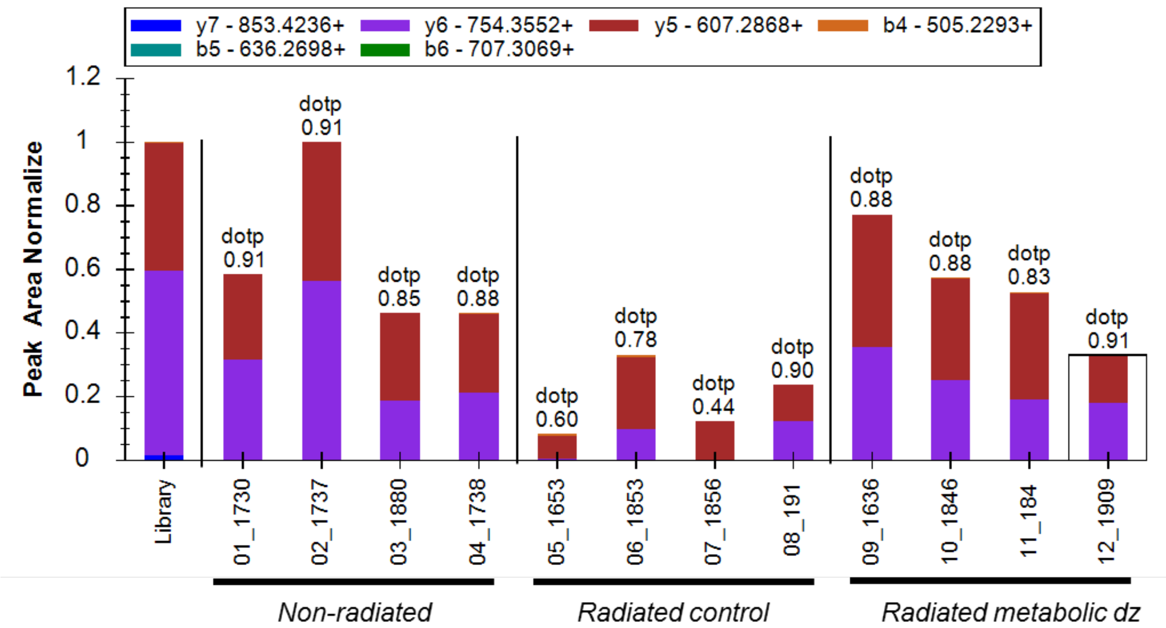

Figure 1.9. Mass spectrometry identification of RhoA shows that the amount in muscle is uniformly low in healthy radiation survivors suggestive of a specific protective response to radiation.

We plan to focus the next publication from the survivor cohort on the intersection between metabolic status, histostructure, and proteomics. To complete this dataset we will complete redox proteomics, quantitation of collagen subtypes, and evaluate muscle samples by electron microscopy to better visualize the interactions of capillaries with the myocyte and ultrastructural details.

2. <u>Prospective Radiation Cohort (PRC)</u>

Twenty monkeys were stratified into a radiation exposed (RAD) and control (CTL) based on bodyweight and cardiovascular risk factors. The study design included a period of acclimation where a Western style diet (high fat, high simple sugar) was fed to all monkeys. Although these 2 groupswere statistically equivalent at baseline, we have seen divergence between groups during this acclimation period such that the control group have worsened glycemic control (A1c%) and higher rates of weight gain (**Table 4 and Figure 1.10**) as compared to the irradiated monkeys.

Table 4.	Control	Radiated	p-value
N	6	11	
BW at radiation	11.30 (0.96)	10.37 (0.86)	0.48
Weight gain (kg/mo)	*0.34 (0.16)*	*0.07 (0.08)*	*0.09*
A1c (%)	4.92 (0.11)	4.65 (0.07)	**0.04**
Glucose (mg/dL)	63.83 (2.96)	66.73 (2.93)	0.51
TG (mg/dL)	50.67 (15.44)	32.91 (5.20)	0.17
TPC (mg/dL)	161 (16.33)	166 (9.70)	0.78
SBP (mmHg)	126 (9.31)	126 (6.76)	0.95
DBP (mmHg)	66 (6.85)	68 (4.97)	0.86
PWV (m/s)	7.7 (0.44)	7.4 (0.44)	0.65

We know from the RSC studies that radiation exposure retards growth and weight gain, thus it was not surprising that at 6 months post-radiation exposure that we saw significant differences in weight and body size (**Table 5**).

Table 5.	Body Weight (kg)	Waist (cm)	Leg Circumference (cm)
CTL (n=6)	12.6 (0.58)	20.5 (0.43)	28.6 (0.72)
RAD (n=9)	11.1 (0.47)	19.1 (0.35)	26.7 (0.59)
ANCOVA p-value	0.03	0.01	0.03

Some of the weight and adiposity (as estimated by waist circumference) difference could be attributed to ongoing recovery from the acute radiation sickness that was observed in the weeks and early months post-exposure in the RAD group. If that is the case, we expect that at 12 months, monkeys will be more equivalent and any differences in metabolism will be more interpretable. At present the greater fatness of the CTL group is causing increases in insulin resistance (**Table 6**, see HOMA scores), with higher values of insulin being required to maintain normoglycemia.

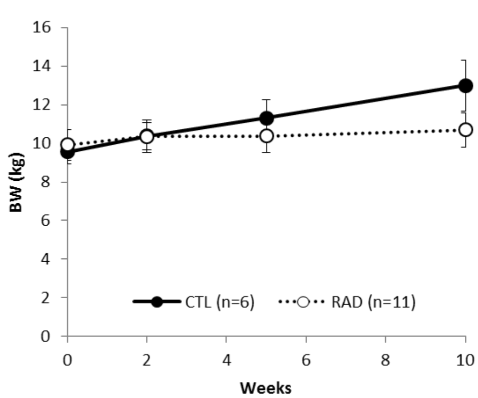

Figure 1.10. Unintended weight gain in control monkeys during the acclimation period prior to study start.

Table 6.	Fasting Glucose (mg/dL)	Fasting Insulin (uIU/mL)	HOMA-IR (AU)	A1c (%)
CTL (n=6)	70.2 (5.14)	61.2 (7.66)	10.8 (1.57)	4.38 (0.15)
RAD (n=9)	60.3 (4.18)	34.0 (6.23)	5.20 (1.27)	4.45 (0.12)
ANCOVA p-value	0.16	0.02	0.02	0.75

This is visually appreciated when you compare glucose tolerance testing curves (**Figure 1.11**) where the insulin excursion in the CTL monkeys is already showing higher values as a result of their more rapid weight gain, and this difference is exaggerated at 6 months. The difference between areas under the curve for insulin (AUCi) did not reach statistical significance however the trend is biologically significant. We are confident that this is adiposity driven, as associations between weight and waist circumference and AUCi were strong and significant at both time points (**Table 7**). One year post-radiation will allow more time for RAD monkeys to "catch-up" and evaluate group differences using the proteomics platform shown above.

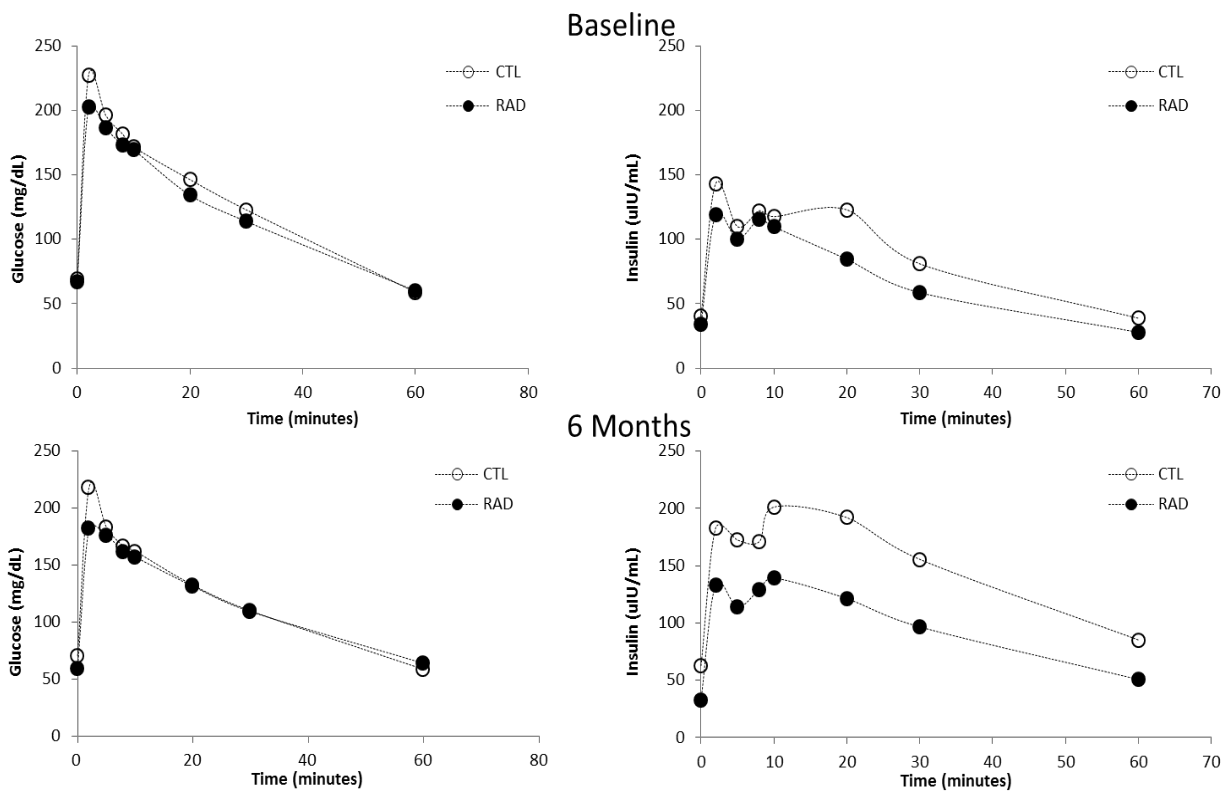

Figure 1.11.Glucose tolerance testing across the first 6 months of study in the PRC. Glucose metabolism (Left panels) is similar between groups over time, however the magnitude of insulin release required to maintain a normal glucose curve is trending higher in the control monkeys. These monkeys have gained more weight over the entire study.

Table 7. AUCi was significantly associated with BW at and waist at both time-points						
	BW			Waist		
BL	R=0.73	p<0.001	n=20	R=0.67	p=0.001	n=20
6mo	R=0.81	p<0.001	n=15	R=0.74	p=0.002	n=15

3. <u>Interventional Rodent Studies</u>

In our first annual report we demonstrated that we had validated a rodent model of sub-lethal irradiation that creates insulin resistance. This model and resultant phenotype are being written up for publication by Dr. Fanning. We have taken that model and are 6 months into an interventional study designed to evaluate potential countermeasures to abrogate radiation-induced insulin resistance (**Figure 1.12**). In this study we are evaluating the effects of inhibiting fibrotic signaling (Transforming Growth Factor beta [TGFb receptor inhibition; IPW-5371 by Innovation Pathways). Briefly, the rationale for this intervention is the observation in the RSC

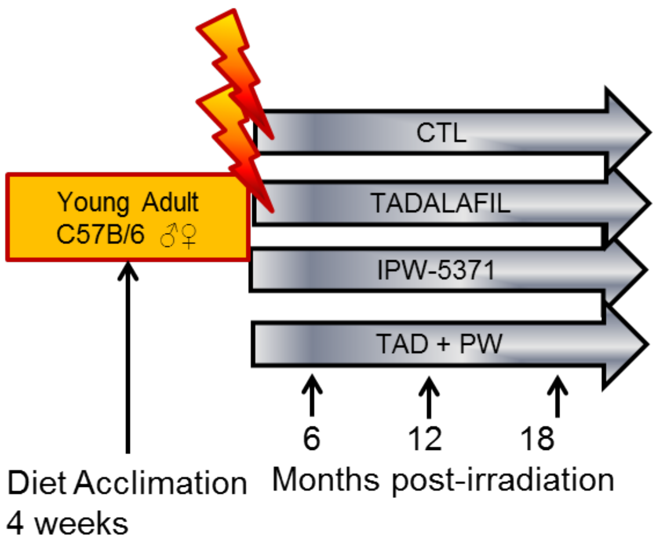

Figure 1.12. Rodent study overview.

that TGFb was increased with radiation (Fanning et al., AJP 2017) and we see an accumulation of collagen subtypes in the muscle tissue. Fibrosis is a well-recognized outcome of radiation exposure and is increasingly important in multiple chronic disease conditions such as heart failure and liver diseases. A related compound in this drug class is already in Phase 2 clinical trials for pulmonary fibrosis, and IPW-5371 has published efficacy in reducing lung fibrosis following radiation in mice. We are also evaluating Tadalafil, a phosphodiesterase-5 inhibitor, marketed as Cialis. This drug has been chosen for emerging evidence that it can enhance perfusion, specifically in skeletal muscle. To date, 3 small clinical trials have demonstrated efficacy and preclinical studies have shown it to reduce heart fibrosis and extracellular matrix accumulation in the context of hyperglycemia. These compounds are studied as single agents and in combination after sub-lethal irradiation.

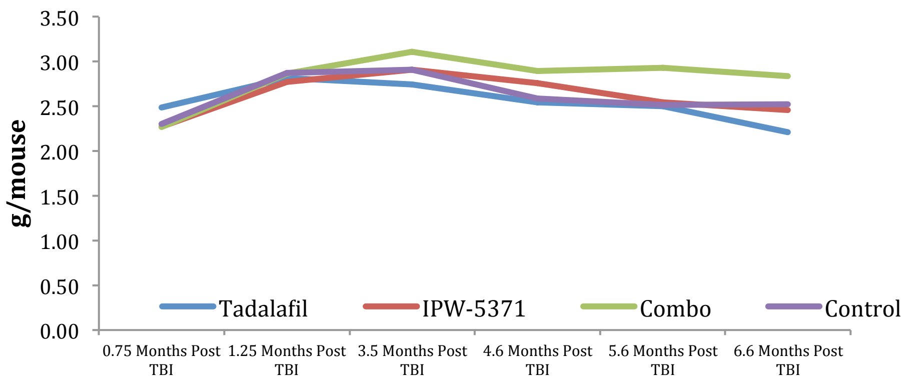

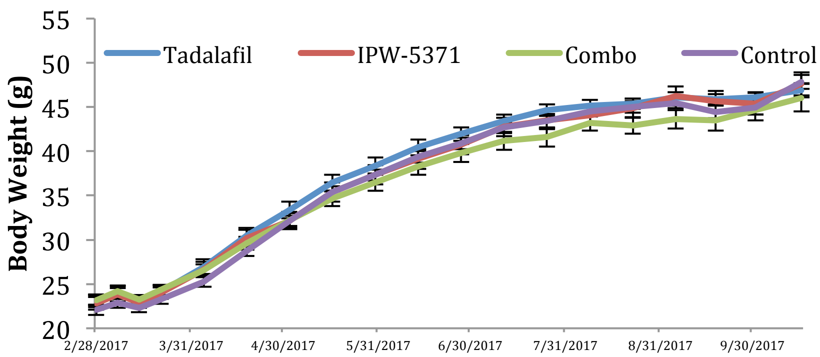

Figure 1.13. Top panel: Food consumption (and estimated drug intake) and body weight over the course of study. Combo (green line) = IPW-5371+Tadalafil.

The IPW-5371 and Tadalafil are administered to the study mice by compounding them in the Western diet being used to drive insulin resistance and obesity. Mice are fed once daily and drug was introduced 2 weeks after irradiation, mimicking what might be possible in the clinical situation. The drug interventions have had no effect on food consumption and weight gain to date (**Figure 1.13**). Due to the Western diet, all groups are considered obese.

IPW-5371 was initially administered as 30mg/kg/d based on prior efficacy for prevention of post-radiation lung fibrosis. At this dose we saw unexpected adverse effects with 9 sudden deaths occurring. These deaths were all in males and 89% of them in the combination treatment group (**Figure 1.14**). One death occurred in the IPW-5371 single agent group. The dose has been reduced to 10mg/kg/d and no further deaths have been observed. The cause of death appears to be great vessel rupture and death with hemorrhage observed in body cavities. A typical example of this lesion's appearance, gross and histological, is shown in **Figure 1.15**. This is a significant and novel finding of a drug interaction with IPW-5371. As drugs of this class are currently in clinical use it highly relevant to the population that is prescribed Tadalafil. We know Tadalafil also has some anti-fibrotic effects, so we hypothesize that the combination of drugs has limited the required amount of extracellular collagen to be deposited at vulnerable sites such as the heart base and aorta. These outflow tracts are subject to high oscillations in pressure and require enough structural integrity to move ejected blood down to the abdomen

and brain. Sudden death by vascular accident is an important side effect as it is difficult to predict or quantitate risk.

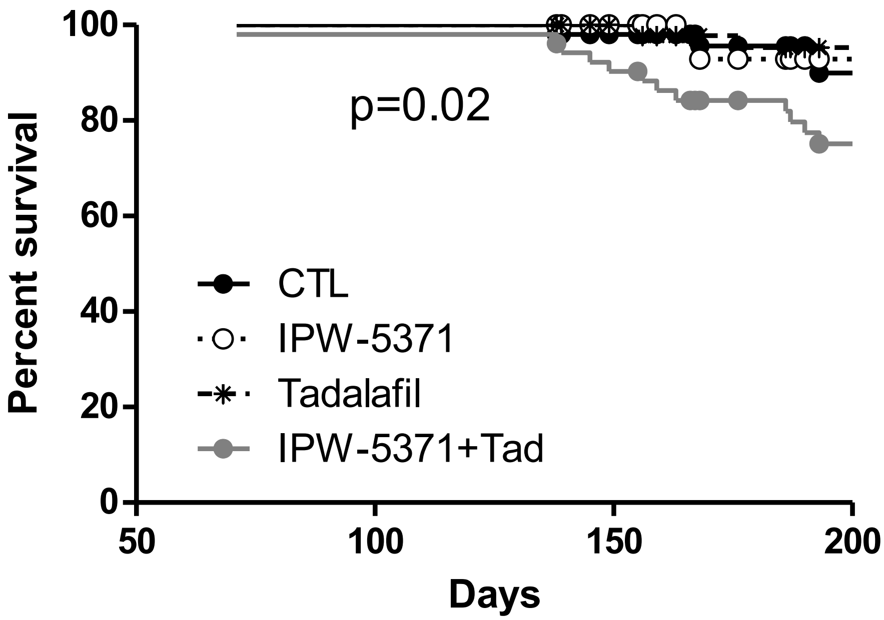

Figure 1.14. Interim survival curve showing significant reduction in survival in mice receiving both IPW-5371 and Tadalafil at 30mg/kg/d and 5mg/kg/d respectively.

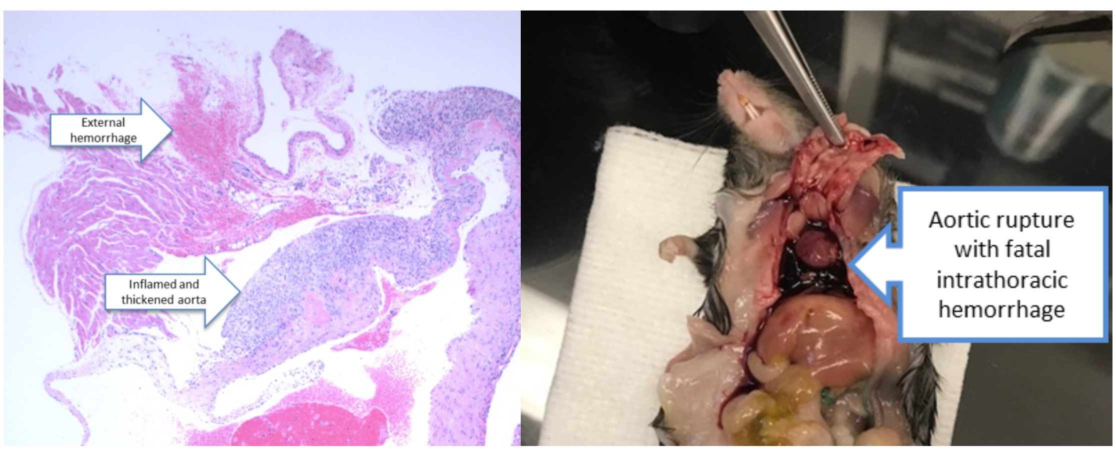

Figure 1.15. Representative histological aortic lesion (Left), with hemorrhage and inflammation indicated by arrows. Typical gross anatomy (Right) of mice suffering aortic lesions and sudden death.

The mechanisms behind why a sex difference in risk exists (males affected) are unknown. We are currently evaluating the same drug combination (Tadalafil + IPW-5371) in non-irradiated male mice to evaluate if radiation-related changes in inflammation and fibrotic signaling are required for this serious side effect to manifest.

Euthanasia has been required in all groups, predominantly for weight loss secondary to neoplasia and possible fatty liver disease. Histological evaluation of all tissues will be done in

the coming year to find subclinical aortic and heart lesions in surviving mice, and confirm the cause of death in those requiring euthanasia.

Organ weights at 6 months post-radiation exposure are shown in **Table 8**. Bodyweights of mice exposed to IPW-5371 were lighter. Organ weights for lung and kidney suggest that mice exposed to IPW-5371 as a single agent or in combination were heavier than controls or Tadalafil only exposed mice.

Table 8.	Greying	BW (g)	Thymus (%BW)	Heart (%BW)	Liver (%BW)	Lung (%BW)	Spleen (%BW)	Kidney (%BW)
Control	1.25 (0.19)	42.7 (0.97)a	0.23 (0.02)	0.32 (0.01)	5.68 (0.41)	0.41 (0.03)a	0.24 (0.03)	0.95 (0.04)a
Tadalafil	0.18 (0.19)	45.0 (1.23)a	0.25 (0.02)	0.34 (0.03)	5.94 (0.72)	0.32 (0.01)b	0.23 (0.02)	0.91 (0.03)a
IPW-5371	1.5 (0.19)	38.0 (2.13)b	0.23 (0.02)	0.40 (0.03)	4.94 (0.27)	0.45 (0.03)a	0.25 (0.02)	1.13 (0.07)b
IPW-5371+Tad	0.92 (0.42)	43.4 (1.78)a	0.22 (0.01)	0.38 (0.04)	5.02 (0.24)	0.46 (0.04)a	0.22 (0.02)	1.11 (0.06)b
p-value	0.18	0.02	0.63	0.24	0.40	0.005	0.79	0.01

We did not see any difference in fasting glucose values at 6 months across the 4 groups (p=0.52) suggesting our interventions are not showing a benefit. Glucose tolerance testing confirms that no benefit is apparent with IPW-5371 and Tadalafil may worsen the metabolism of glucose. Insulin tolerance testing also failed to show clear benefits across the treatment groups (**Figure 1.16**). The improvement in response to insulin in the IPW-5371 will remain cautiously interpreted until repeat assessments are done at 12 months. Analyses of these data are ongoing but at the 6 month post-radiation exposure, we are not seeing an improvement in whole body metabolism with our countermeasures.

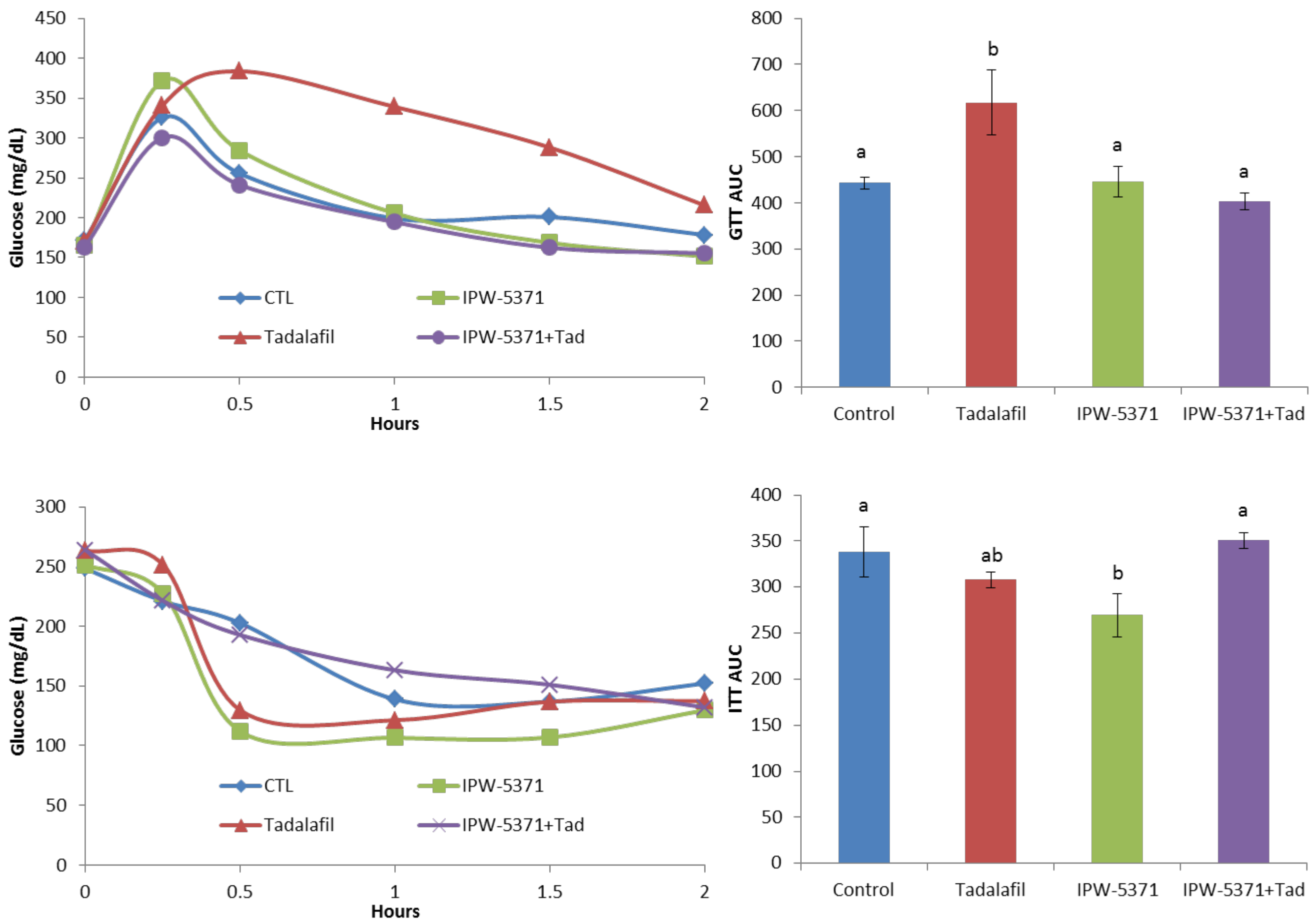

Figure 1.16. Average glucose tolerance curves and calculated areas under the curve (top panels) showing Tadalafil worsened glucose disposal rates. Insulin tolerance mean curves and calculated areas under the curve (bottom panels) show that IPW-5371 improved insulin-stimulated glucose disposal. This finding will be re-evaluated following dose reduction at 12 months.

We do a battery of physical function testing to assess healthspan in these mice. Both experimental agents lessened functional endurance as measured by treadmill time to exhaustion (**Figure 1.17**). Drug effects were not additive in this outcome. This reduction in function is consistent with no change or a detrimental change in glucose metabolism.

Data planned for generation in the next year will be histological assessment of tissues collected at 6 months and repeat assessments of healthspan at 12 months.

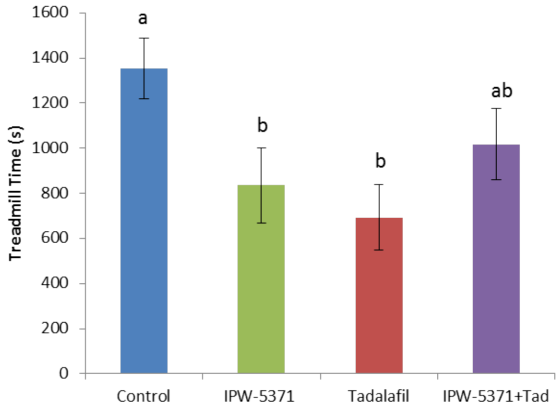

Figure 1.17. Treadmill endurance is a measure of metabolism, cardiovascular and skeletal muscle function. All interventional groups were less able to exercise than control mice, with significant differences observed in both IPW-5371 and Tadalafil treated mice.

Project 2 – Radiation/Heart Disease (Register)

1) Major Activities

a. Blood collections: Collection and processing of blood samples in the prospective cohort during the subacute post-radiation phase for planned serum and plasma biomarker analyses.
b. Monitoring and surveillance of the recoveries of the animals in the prospective cohort post irradiation in order to plan follow-up US and MRI imaging studies of cardiac structure and function.
c. Continued discussions with Duke investigators on cross-project technical collaboration on cell collections, processing, and analysis.
d. PBMC preparations and monocyte isolations and sorting from PRC were conducted in May and again in September-October.
e. Biomarkers: Cardiac biomarkers: Internal Clinical labs began running research samples through automated ultrasensitive clinical analyses for troponin I and BNP.
f. Cardiac tissue analyses: Processing of myocardial and coronary artery tissue blocks (RSC, & past Project with mitigator) for assessment of coronary artery atherosclerosis (CAA) using VVG stain and Visiopharm software. All stained sections have been scanned and stored and have been qualitatively examined, now will undergo quantitative assessment using Visiopharm modules under development.
g. Cardiac Ultrasound Analysis Software: We continue to improve the Cardiac Image Analysis software system (TOMTEC) for customized output to accommodate the smaller NHP heart sizes.
h. Cardiac Ultrasound Data collected from the 20 week post-ARE US images have been assessed to evaluate the effects of radiation and data will be presented at the October Radiation Research Meeting. Additional modification to the data processing and output from the TOMTEC system is ongoing.
j. Cardiac MRI studies on the 16 PRC monkeys were conducted March 28- April 3, 2017. Quantitative analysis of T1 images pre- and post-contrast has been conducted in the Wake Forest Clinical Research Ultrasonography Lab. Statistical analysis of the dataset is underway.
k. Monthly DOD Conference calls have been conducted.

2) Specific objectives

Collections of samples, US, and cMRI images from the prospective cohort as described above. Planning for next cardiac imaging and biomarker assessments.

3) Results/key outcomes

Cardiac MRI: Image analysis has been partially completed for multiple parameters in Baseline and 5 month MRI studies in the PRC. Key MRI measures include left ventricular (LV) mass, posterior and interventricular wall thickness, right ventricular thickness, aortic wall thickness, and the presence of myocardial fibrosis. Functional parameters include systolic and diastolic function, ejection fraction, aortic stiffness/pulse wave velocity (PWV), and electrocardiography (ECG). MR grid tag mapping is being used to assess strain and LV volume, contrast enhanced perfusion MR will be used to assess microvascular function. T1 mapping techniques were used to evaluate myocardial extracellular volume fraction (ECVF), which corresponds to diffuse subclinical myocardial fibrosis, analysis of these was conducted using Medical Image

Processing Software (MIMP) on the baseline and 5 month post-radiation MRI images in the PRC. Measurements were made in collaboration with Dr. Dalane Kitzman and his staff, who have significant expertise in human and nonhuman primate cardiac analyses.

Analyses of these datasets is underway.

Echocardiography: We have evaluated the baseline and 5 month follow-up echocardiographic measures. Key outcomes are shown in **Figures 2.1 and 2.2**. There were no significant differences between groups in any of the baseline echocardiographic measures of CV structure or function (not shown). Over the first 5 months following TBI, no significant changes over time or differences between groups were observed in fractional shortening, ejection fraction, cardiac output, aorta/left atrium ratio (a measure of pulmonary, or M mode measures of chamber size (Fig 2.1).
Figure 2.2 displays echocardiographic measures of diastolic filling of the left ventricle. Early filling velocity of the left ventricle did not change over time and there was no difference between groups. Irradiated monkeys experienced a significant increase in the late filling velocity across the mitral valve (A) compared to baseline and to controls at 5 months (both $p<0.05$), and the E/A ratio showed a non-significant trend towards a reduction ($p=0.11$), which would be indicative of impairment of LV relaxation, though the numbers technically appear to be within the normal range.

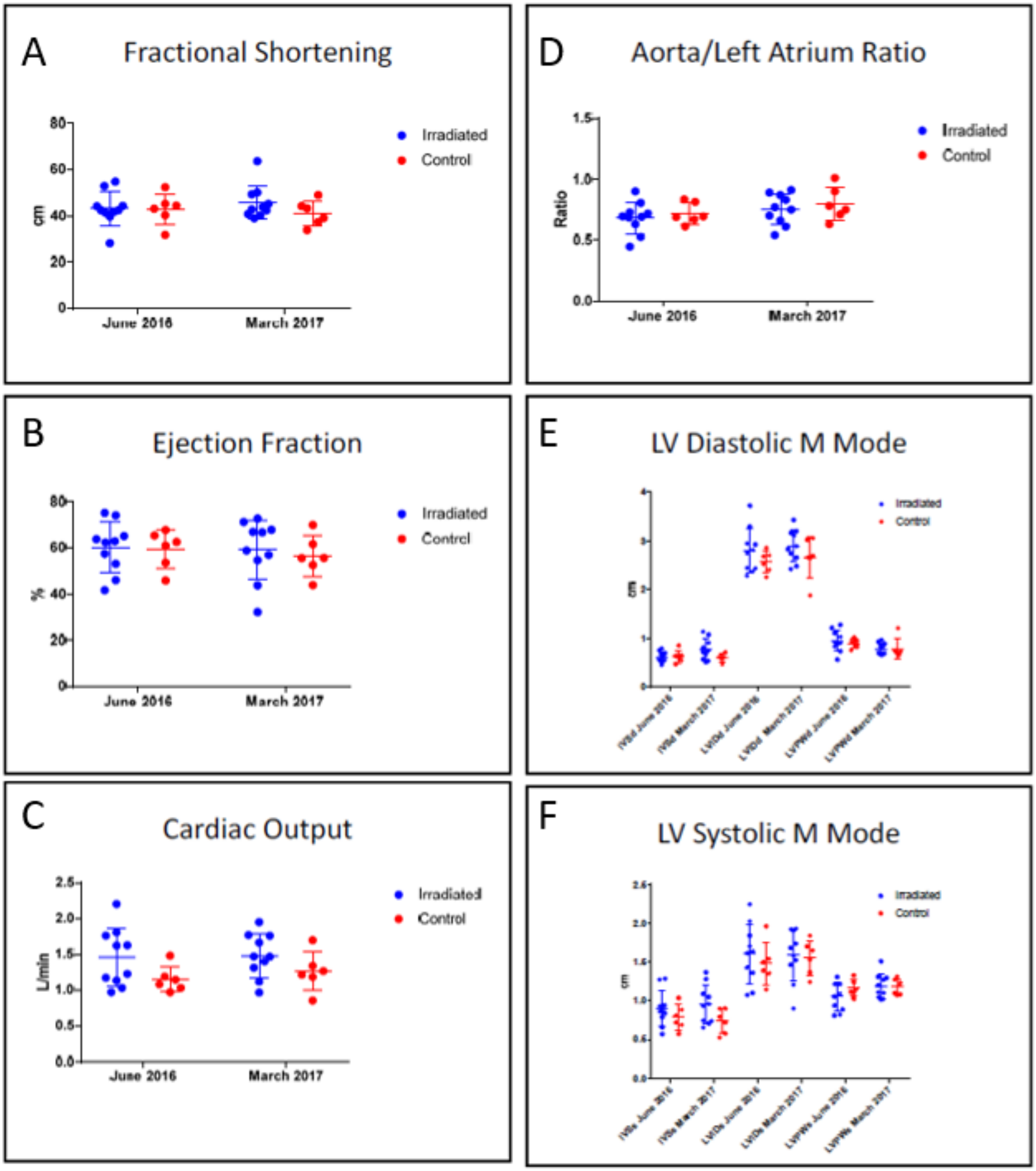

Figure 2.1 Echocardiographic data from the PRC Prior to and 5 months following 4 Gy TBI. No significant changes over time or differences between groups were observed in fractional shortening, ejection fraction, cardiac output, aorta/left atrium ration (a measure of pulmonary hypertension.

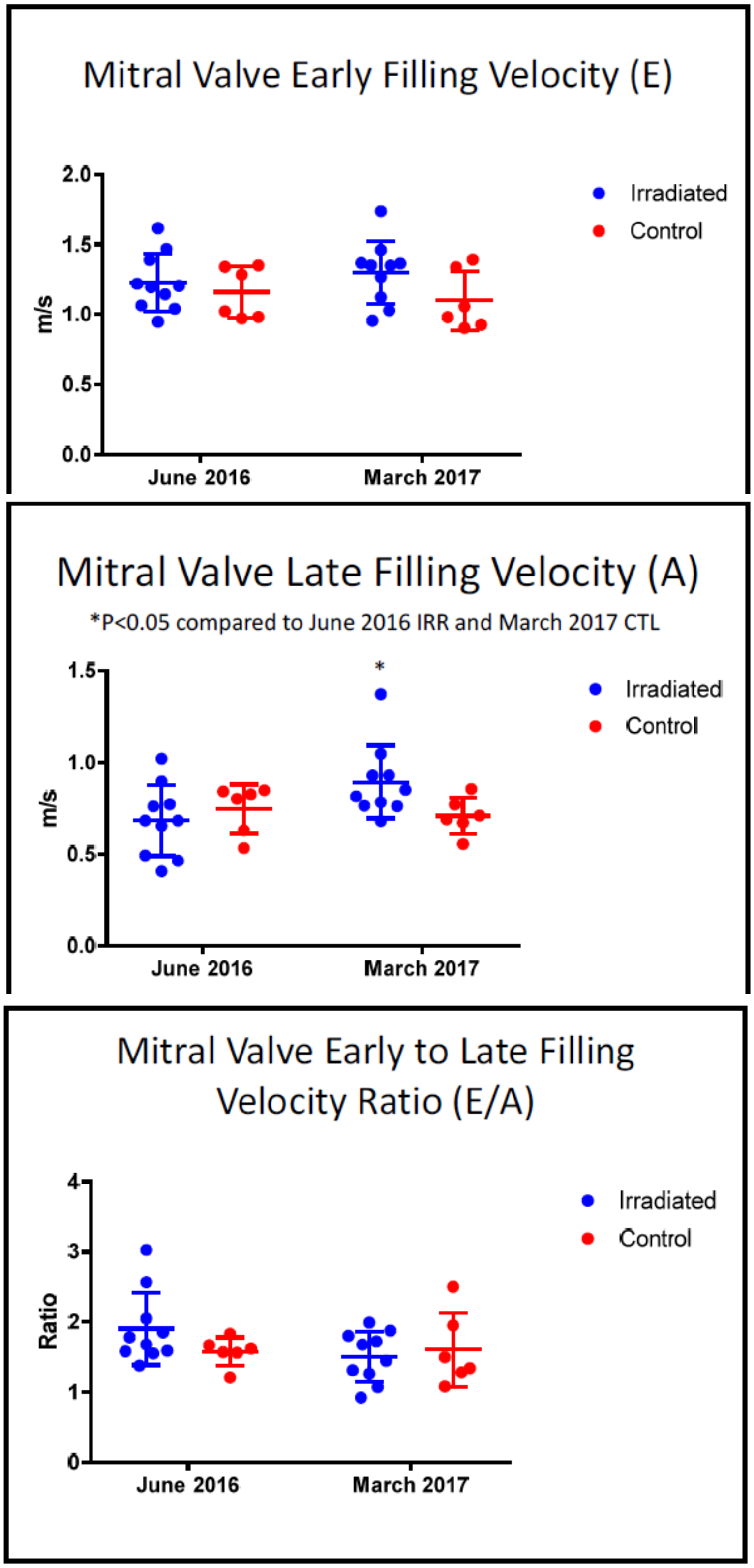

Figure 2.2. Echocardiographic Measures of Diastolic Filling of the Left Ventricle. Early filling velocity of the left ventricle did not change over time and there was no difference between groups. Irradiated monkeys experienced a significant increase in the late filling velocity (A) across the mitral valve ($p<0.05$), and the E/A ratio showed a non-significant trend towards a reduction ($p=0.11$), which would be indicative of impairment on LV relaxation, though the numbers technically appear to be within the normal range.

Manuscript development: *Evaluation of a Superoxide Dismutase Mimetic as a Mitigator of Acute and Delayed Responses of the Lung and Heart to Thoracic Gamma Irradiation* Ryne J. DeBo, Kris T. Michalson, Gregory O. Dugan, Cynthia J. Lees, David B. Hanbury, David L. Caudell, Rachel N. Andrews, Zeljko Vujaskovic, Ines Batinic-Haberle, J. Daniel Bourland, J. Mark Cline, Thomas C. Register

We have been evaluating the effects of a potential mitigators of radiation effects on the heart in a study initially designed to assess the effects of a superoxide dismutase mimetic ((MnTnHex-2-Pyp5+, Hexyl) to mitigate radiation induced lung injury in rhesus monkeys. Subjects were 18 male rhesus macaques receiving a 10 Gy dose of gamma radiation to the thorax, followed by treatment with either saline (control, n = 9) or Hexyl (0.125 mg/kg, in saline, n = 9) initiated 24 hours post-exposure. Respiratory and pulmonary health primary outcomes in the study. Cardiovascular function was also monitored. Pulmonary and cardiovascular tissues were examined histologically and collagen content was quantified. Left ventricular myocardial transcript expression profiles were determined by microarray analysis. Hexyl did not significantly improve survival or physiological indices of pulmonary and cardiovascular health. Hexyl treated animals had greater proportional collagen present in their right ventricles (26%, +/- 2) compared to saline-treated controls (17%, +/- 1.9) ($p = 0.006$). Myocardial expression of 53 different genes was different between Hexyl and controls (t-test, FDR < 0.05). Myocardial expression of matrix genes (collagen type 1 alpha 1, collagen type 1 alpha 2, collagen type IV alpha 1) was 1.6-fold higher in animals dying prior to day 100 post irradiation compared to those surviving beyond 100 days, irrespective of treatment group. Expression of B-type natriuretic peptide (BNP) was more than 2-fold-up-regulated in hexyl treated animals dying prior to day 100 post-radiation exposure (ANOVA, $p < 0.05$) compared to treated animals surviving more than 100 days, as well as untreated animals dying before and after 100 days post-irradiation. These results indicate that while Hexyl treatment influenced myocardial gene expression, it did not improve survival, physiological outcomes, or reduce collagen burden in lungs or heart. Alternative dosing regimens or approaches may be needed to increase the efficacy of Hexyl in preserving lung and heart health post radiation exposure. New data on circulating troponin-I and BNP have been collected and will be incorporated into the manuscript .

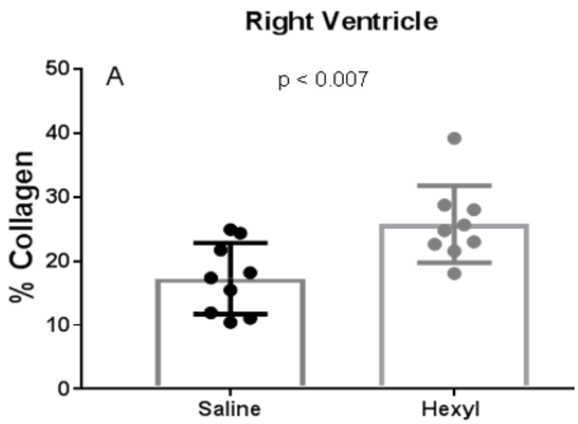

Figure 2.3 Effects of Hexyl on indices of cardiac fibrosis. Panel A: The RV of animals treated with Hexyl had significantly increased collagen content compared to the RV of control animals (p = 0.007, t-test)

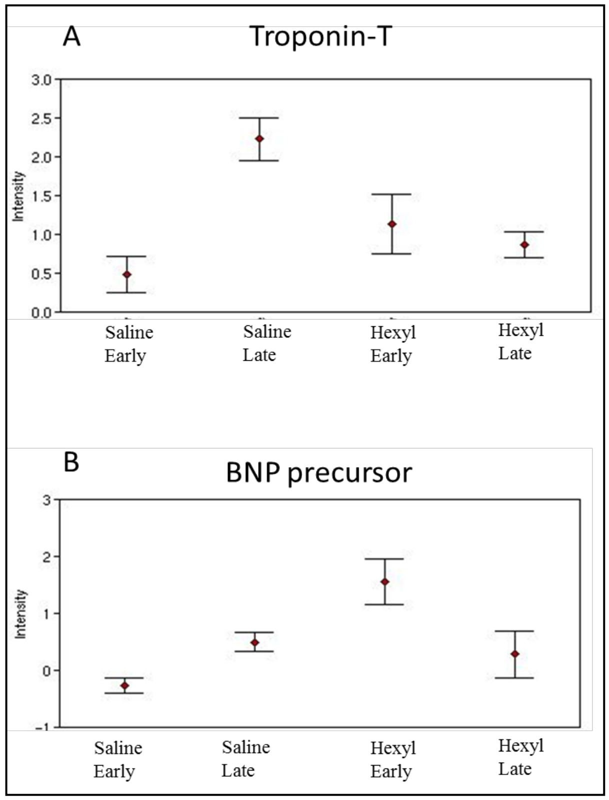

Figure 2.4 Effect of Hexyl and survival duration on myocardial expression of markers of cardiovascular damage. Panel A: Expression of troponin-T was greatest in control animals surviving longer than 100 post-radiation exposure. Panel B: Expression of BNP was greatest in Hexyl treated animals dying prior to day 100 post-radiation exposure. Intensity is log base 2. Data are +/- SEM

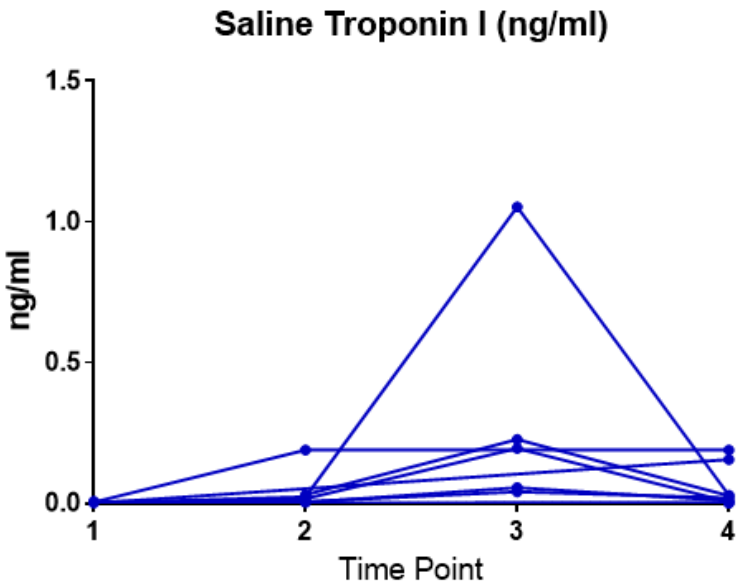

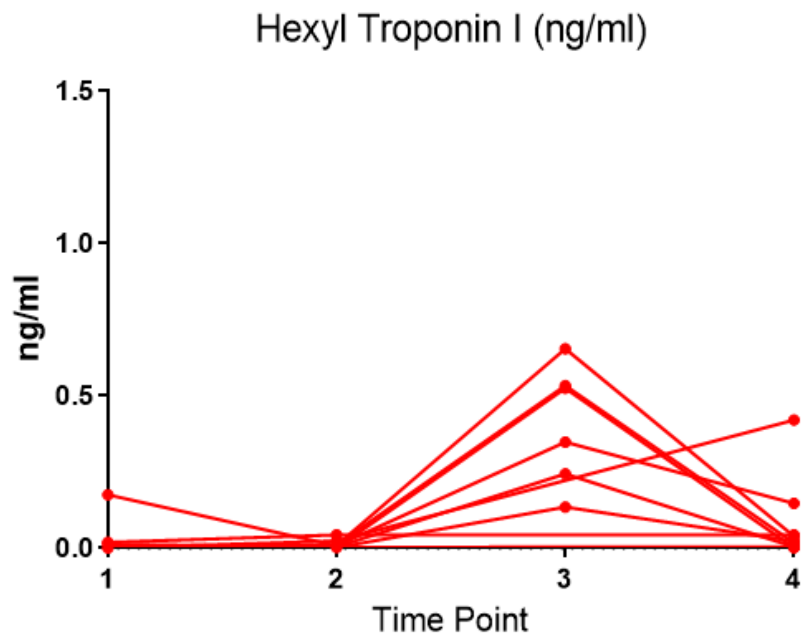

Figure 2.5 Effects of thoracic irradiation on circulating biomarkers of cardiac injury (serum troponin I) over time in Saline Controls and Hexyl treated monkeys. Time point 1 is baseline; subsequent time points 2-4 are 2, 4, and 6 months post-irradiation.

Serum troponin I was largely undetectable at baseline, with the exception of 1 monkey in the hexyl group. Increases in troponin were observed in most subjects, although this did not consistently occur until ~4 months after irradiation. Pulmonary injury can place strain on the heart and produce subclinical injury, so we looked at potential relationships between respiratory rate (RR) and serum troponin I levels at the point which troponins showed a significant increase (time point 3 @ 4 months (Figure 2.6). Troponin I and RR showed a trend towards a significant positive relationship (r=0.41, p=0.1).

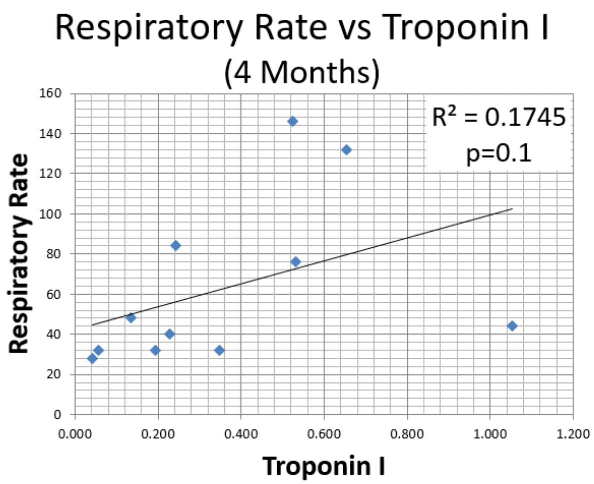

Figure 2.6 Respiratory rate (breaths per minute) and troponin 1 concentrations in serum (in ng/ml), showing a weak but potentially relevant relationship.

Relationships between final respiratory rates and myocardial collagen content are shown in Figure 2.7. Significant associations were observed between RR and collagen content in the right ventricle, the interventricular septum, and average collagen across all chambers of the heart (all $p<0.05$), and there was a trend in the left ventricle ($p=0.06$).

Taken together, these results suggest cardio-pulmonary interactions which may be due in part to radiation injury to both organs as well as subsequent interactions by which lung injury may damage the heart and vice versa. This area merits further investigation.

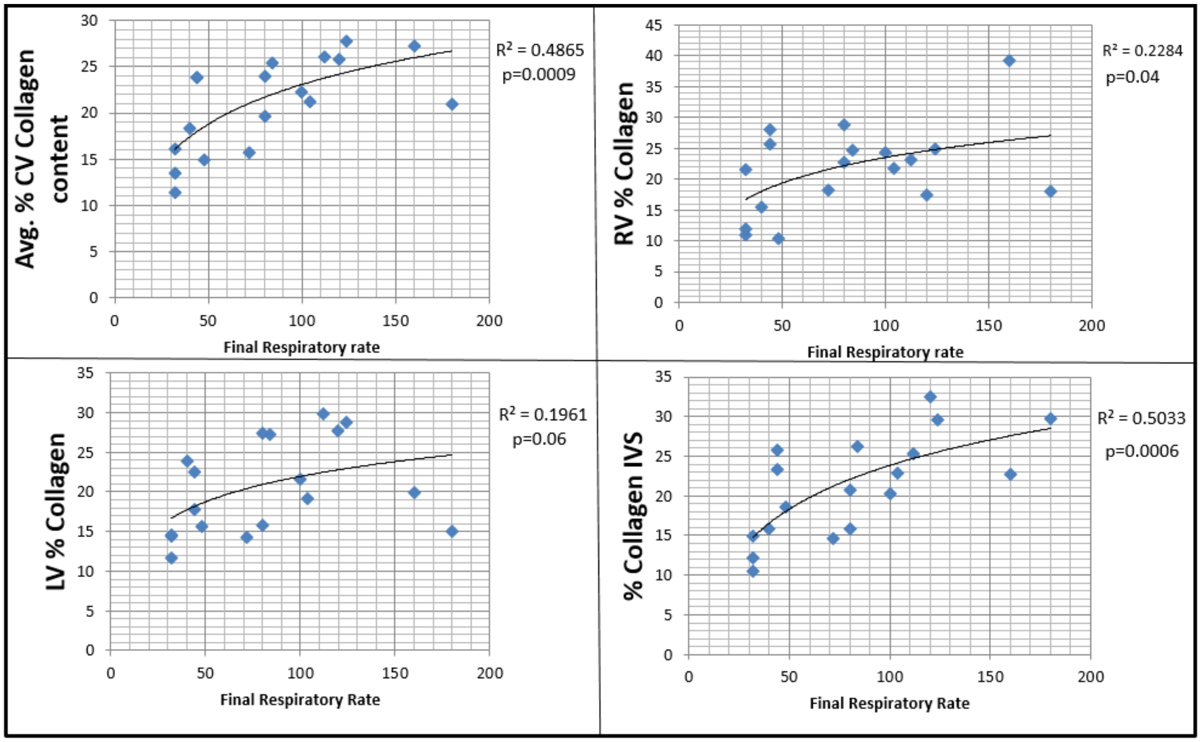

Figure 2.7 Myocardial collagen content (percentage of sections positive by Masson's trichrome stain), plotted against respiratory rate (breaths per minute).

4) Other Achievements:

Grants: We leveraged the availability of the PRC to conduct further explorations of radiation effects through an institutional pilot grant, which led to submission of a large pilot grant to the Center for Medical Countermeasures Program entitled *"Monocyte Polarization in Acute & Delayed Responses to Total Body Irradiation in Nonhuman Primates"* which was funded and is now underway.

Abstracts: Two abstracts were submitted and accepted for the 2017 Radiation Research Meeting, one a standard abstract containing data on the effects of radiation on circulating cell populations from the RSC in collaboration with Project 3, the second a late-breaking abstract reporting some of the echocardiographic outcomes 5 months after radiation exposure in the PRC. Dr. Kris Michalson received a travel award from the Radiation Research Society to attend the meeting. (see products below)

Awards: Our manuscript describing radiation induced heart disease in the RSC which appeared in Radiation Research in 2016 and for which a key figure was selected for the cover, was selected for the 2017 Radiation Research Editor's Choice Award for scholar-in-training Dr. Ryne DeBo, who received his PhD earlier this year and is now a post-doctoral fellow in the lab. He also received a travel award for the meeting.

5) Changes/Problems:

None

6) Products:

An abstract describing the effects of radiation on monocyte polarization was accepted for presentation at the 2017 Radiation Research Meeting. ABSTRACT: Evaluation of monocyte polarization in long term non-human primate survivors of acute ionizing radiation exposure AUTHORS: Kristofer T. Michalson, Andrew N. McIntyre, Ryne J. DeBo, Gregory D. Sempowski, J. Mark Cline, Thomas C. Register
(See Attachment 4)

An abstract describing the subacute effects of radiation on cardiac structure and function was accepted for presentation as a late breaking abstract at the 2017 Radiation Research Meeting. ABSTRACT: Effects of Total Body Irradiation on Echocardiographic Phenotypes in Male Rhesus Macaques. AUTHORS: Kristofer T. Michalson, Gregory Dugan, Ryne J. DeBo, Dalane Kitzman, J. Mark Cline, Thomas C. Register
(See Attachment 5)

Project 3: Immune Recovery (Sempowski/Chen)

1) Major Activities (Year 2)

- **A.** Received and processed NHP blood from the X-10-12 long-term survivor cohort (two time points: Nov. 2016 and fall 2017 (ongoing)). Performed immunophenotyping and froze viable PBMC and plasma for future batch molecular analysis and multiplex cytokine profiling, respectively. Continued to develop a RedCap database for project-specific NHP data generated at Duke to facilitate comprehensive statistical analysis of the data.
- **B.** Received and processed NHP blood from the X-15-03 prospective cohort (two time points: 4 months and 9 months post irradiation with 4Gy vs sham). Performed immunophenotyping and froze viable PBMC and plasma for future batch molecular analysis and multiplex cytokine profiling, respectively. Continued to develop a RedCap database for project-specific NHP data generated at Duke to facilitate comprehensive statistical analysis of the data.
- **C.** Continued to optimize flow cytometry staining panels so as to incorporate additional monocyte and T cell markers while reducing number of stains required per sample.
- **D.** Researched and wrote a discussion of NHP Blood immunophenotyping for Mark Cline's Late Effects Methods chapter.
- **E.** An amendment to add new personnel to the existing mouse animal protocol was approved by Duke IACUC and to ACURO.
- **F.** We studied the roles of thymopoiesis and peripheral expansion in overall T cell recovery in a classic mouse radiation injury model. This experiment includes more animals per group and also additional control groups (see details below). In addition, we have monitored these animals for more than 6 months after irradiation in order to determine whether TBI induces permanent quantitative immune defects. Total T, B, and T cell subsets are monitored in peripheral blood overtime.

2) Specific Objectives (Year 2)

SA1: Define the roles of thymopoiesis and peripheral expansion in overall T cell reconstitution after radiation-induced injury based on radiation dose.

Major Task 1: NHP Studies

Phenotypic analyses in prospective and long-term cohorts

Major Task 2: Murine Studies

Determine the roles of thymopoiesis and peripheral expansion in overall T cell recovery in two mouse radiation injury models

3) Results/Key Outcomes

SA1 Major Task 1: NHP Studies (Sempowski, Duke)

Long-term cohort (X-10-12):

The X-10-12 Long-term Survivor cohort of 108 NHP (control and irradiated) will be cross-sectionally analysed at distinct dates over the five year study to monitor immune recovery and correlate with radiation dose and age. The first set of 108 samples were shipped and processed in November 2016. The shipping and processing of the second set of samples started in late August 2017 and is being staggered across the fall to ensure the process remains manageable as the cohort increases in size.

The sample collection and shipment schedule is coordinated by the WF Primate Core team. On each shipment day, fresh NHP blood (two 10 mL GTT sodium heparin tubes) from the long-term survivor NHP cohort is packaged and shipped via first overnight Federal Express shipment (room temp) to the Sempowski lab at Duke. Blood receipt is confirmed with WF and processed by standard ficoll separation to isolate peripheral blood mononuclear cells (PBMC) and plasma. Aliquots of PBMC are retained for a fresh immunophenotype and viability assessment. The remainder of the PBMC are cryopreserved using standard DMSO freeze medium and stored in liquid nitrogen for batch processing for sjTREC, sharing with Project 4 and possible TCR sequencing. Aliquots of Plasma are also crypopreserved for potential add on studies, such as multiplex cytokine profiling in collaboration with Project 2.

All samples and aliquots are inventoried in the Sempowski group FreezerPro lab inventory control system. All freezers are on 24/7 emergency power back up and 24/7 remote temperature monitoring (Minus 80 Inc.) with alarm notifications via phone, text and email. An empty backup -80°C freezer is kept at the ready in case a freezer fails. The Sempowski lab is housed in the Duke Regional Biocontaiment laboratory, which has an external bulk liquid nitrogen (LN2) storage tank containing sufficient LN2 to supply all storage tanks for one month without refill.

Phenotypic analyses of NHP in long-term cohort (X-10-12):
Flow cytometry-based immunophenotyping of peripheral blood populations from the November 2016 sample set was performed as described above and the FCS 3.0 files were analyzed for a number of distinct cell subsets using FloJo software. The frequency of specific cell populations was determined as % and recorded in a Sempowski Lab central data set for the Long-term cohort. CBC with differential data were obtained on matched fresh blood samples at Wake Forest and the data were forwarded to Duke for inclusion into our central data repository. Data reference the monkey unique ID, dose and date irradiated, sex, date of birth and sample collection date.

Figure 3.1 shows select plots of the November 2016 peripheral blood immuophenotype performed on the 108 NHP in the long-term cohort. Using the demographic meta-data about the individual animals we are able to look at difference in peripheral blood cell subsets (e.g. T and B cells) with respect to the time in years since irradiation **(Figure 3.1 A, C, E, G)** and radiation dose group **(Figure 3.1 B, D, F, H)**. **Figure 3.2** shows a more detailed look specifically at the Naïve CD4 and CD8 T cell subsets in these animals. Again, the data are shown with respect to time in years since irradiation **(Figure 3.2 A, C)** and radiation dose group **(Figure 3.1 B, D). Figure 3.3** shows a more detailed look at the CD4 effector memory and central memory populations. These data suggest that the percentage of peripheral blood CD4 central memory T cells drops significantly after irradiation (as a proportion of total CD4 T cells) but that the effector memory population does not show the same decrease.

It is clear from this analysis that age (at time of radiation and time of sample) and sex may be important co-variates in the observed specific damage to the T cell compartment with radiation. We are exploring comprehensive statistical models to determine the relative interaction of age, sex, dose on ALL peripheral blood measures.

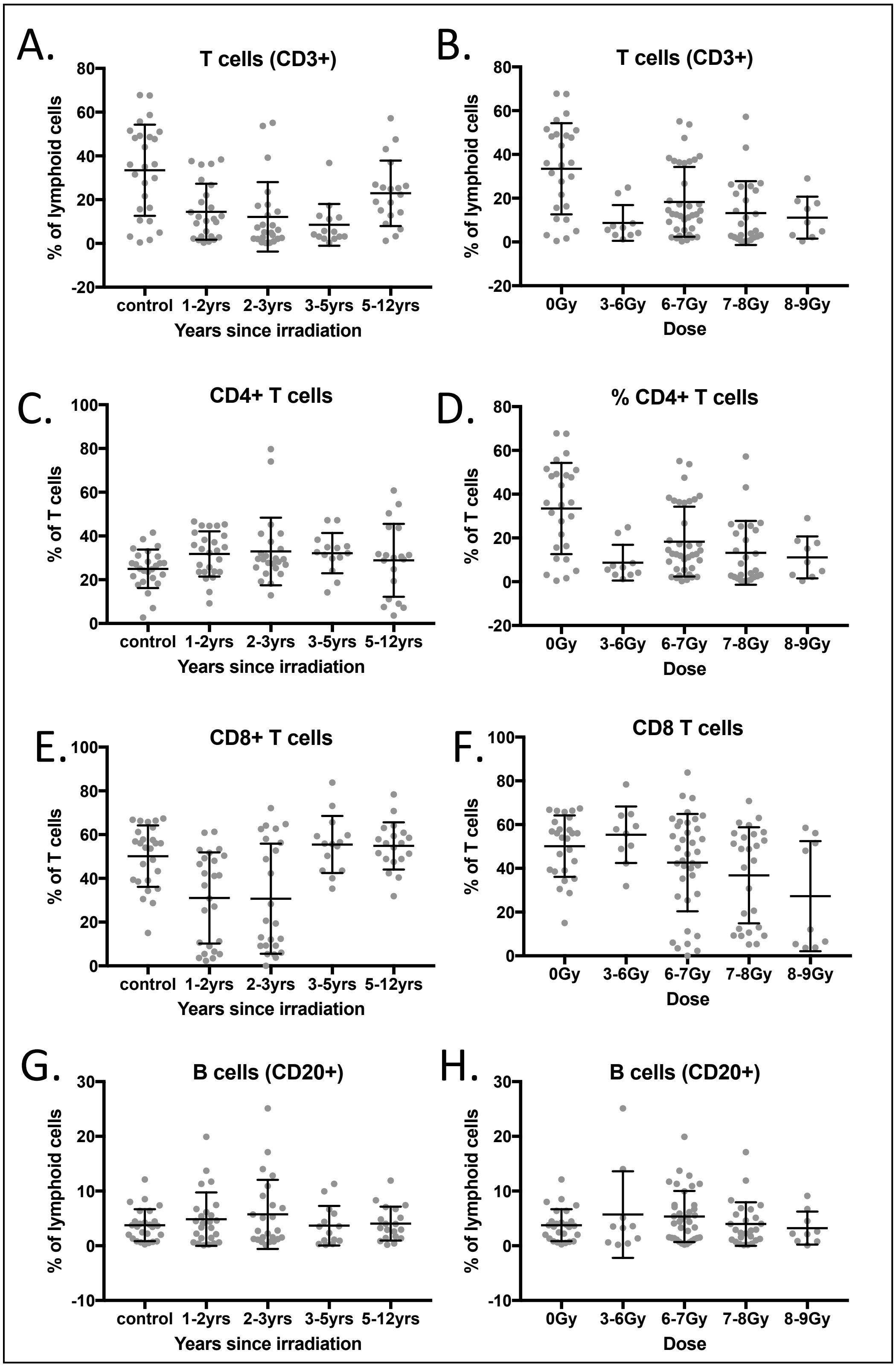

Figure 3.1: Total T and B cell recovery in peripheral blood after irradiation in NHP Long-term cohort

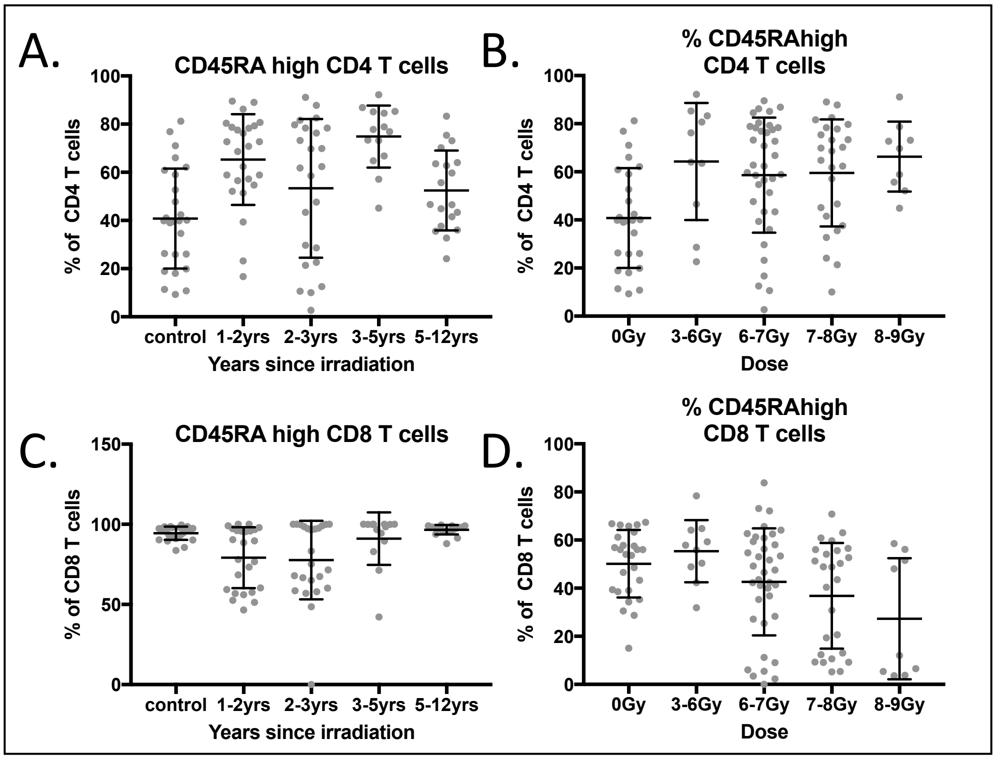

Figure 3.2: Naive T cell recovery in peripheral blood after irradiation in NHP Long-term cohort

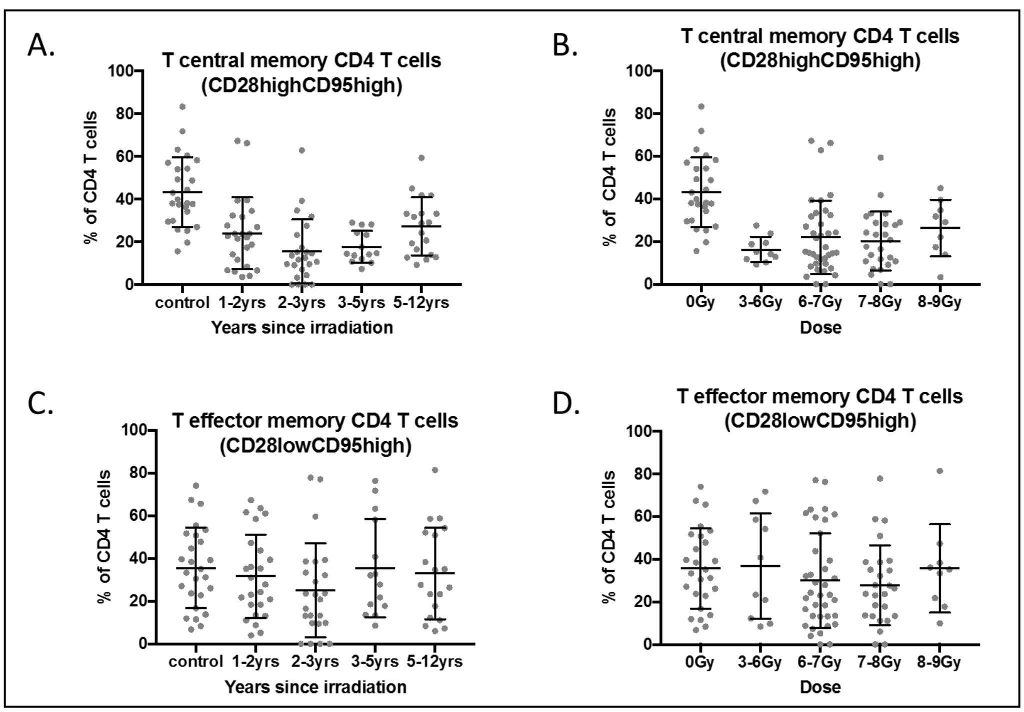

Figure 3.3: CD4 memory T cell populations in peripheral blood after irradiation in NHP Long-term cohort

Prospective cohort (X-15-03):
In Y1Q4, 14 of the 20 NHP in the X-15-03 prospective cohort were irradiated with 4Gy and six were subject to sham irradiation. Four of the irradiated animals were removed due to health reasons before the four-month time point was reached.

At the baseline (Year 1), four- and nine-month time points (both Year 2), fresh NHP blood (two 10 mL GTT sodium heparin tubes) was packaged and shipped for first overnight Federal Express shipment (room temp) to the Sempowski lab at Duke, based on a pre-determined sample collection and shipment schedule coordinated by the WF NHP Core team. Blood receipt was confirmed to WF and processed by standard ficoll separation to isolate peripheral blood mononuclear cells (PBMC) and plasma. Aliquots of PBMC were retained for a fresh immunophenotype and viability assessment. The remainder of the PBMC were cryopreserved using standard DMSO freeze medium and stored in liquid nitrogen for batch processing for sjTREC, sharing with project 4 and potential TCR sequencing. Aliquots of Plasma were also cryopreserved for potential add on studies, such as multiplex cytokine profiling in collaboration with Project 2. All samples and aliquots were inventoried and stored as described above for the long-term cohort.

Phenotypic analyses of NHP in prospective cohort (X-15-03):
Flow cytometry-based immunophenotyping of peripheral blood populations was performed as described above and the FCS 3.0 files were analyzed for a number of distinct cell subsets using FloJo software. The frequency of specific cell populations is determined as % and recorded in a Sempowski Lab central data set for the NHP cohort. CBC with differential data were obtained on matched fresh blood samples at Wake Forest and the data are forwarded to Duke for inclusion into our central data repository. Data reference the monkey unique ID, dose and date irradiated, sex, date of birth and sample collection date. Analyses of the data from the baseline and four-month time point are complete. Analysis of the data from the nine-month time point will be completed by Y3Q1.

Shown below is the peripheral blood analysis four months (130 days) post irradiation in comparison to baseline. Based on clinical CBC the absolute numbers of platelets, red cells, white cells, basophils, neutrophils, monocytes, eosinophils, and lymphocytes per µL whole blood are shown in **Figure 3.4**. Total lymphocyte levels appear to be normal at this time point. CBC hematology measures (mean corpuscular Hb, HCT, Hemoglobin, mean corpuscular volume and mean corpuscular Hb concentration) were all normal on day 130 (**Figure 3.5**).

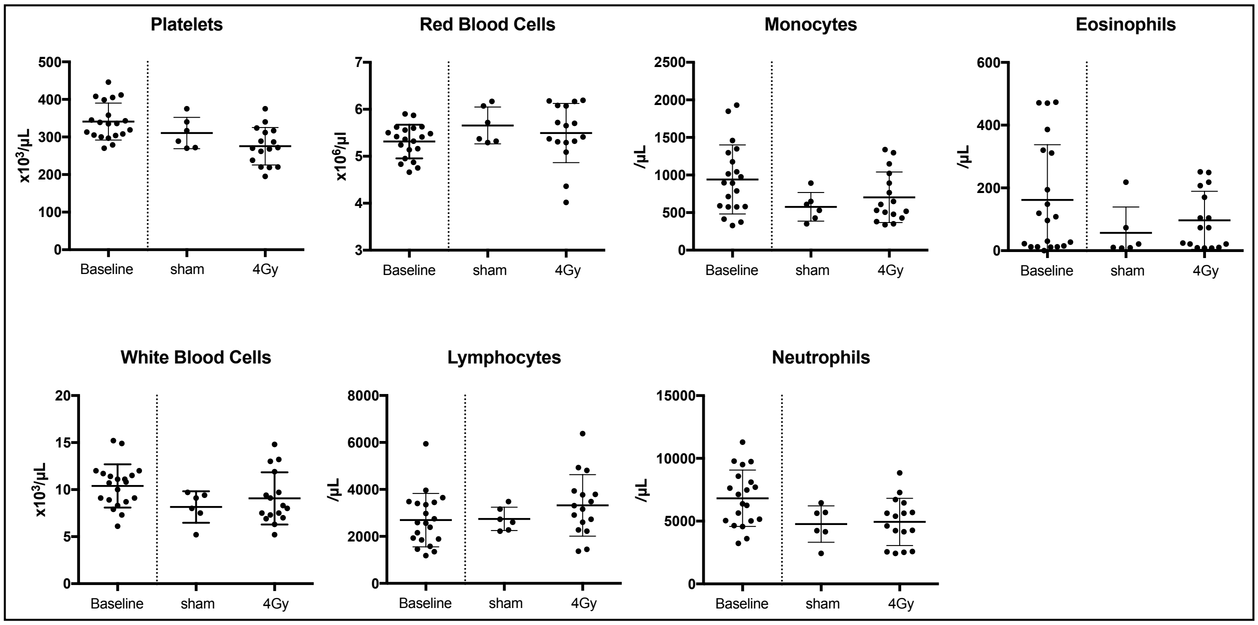

Figure 3.4: CBC at baseline and Day 130 in the prospective cohort.

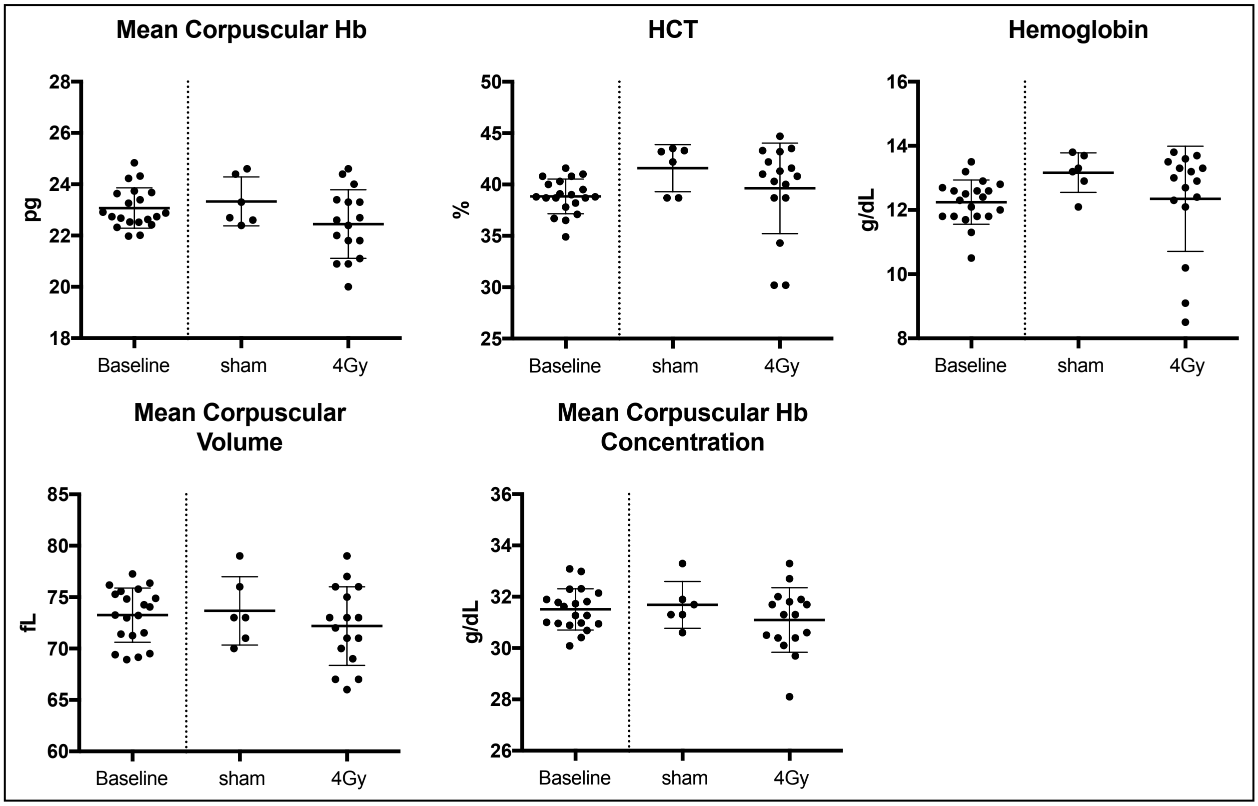

Figure 3.5: Hemoglobin analysis at baseline and Day 130 in the prospective cohort.

Baseline % of white cell subsets (differential) is shown in **Figure 3.6.** A significant drop in proportion of neutrophils persists 130 days post irradiation; however, the proportion of lymphocytes appears to be increased. This is most likely a compensatory recover of the compartment. No changes were seen in monocytes, basophils and eosinophils at day 130.

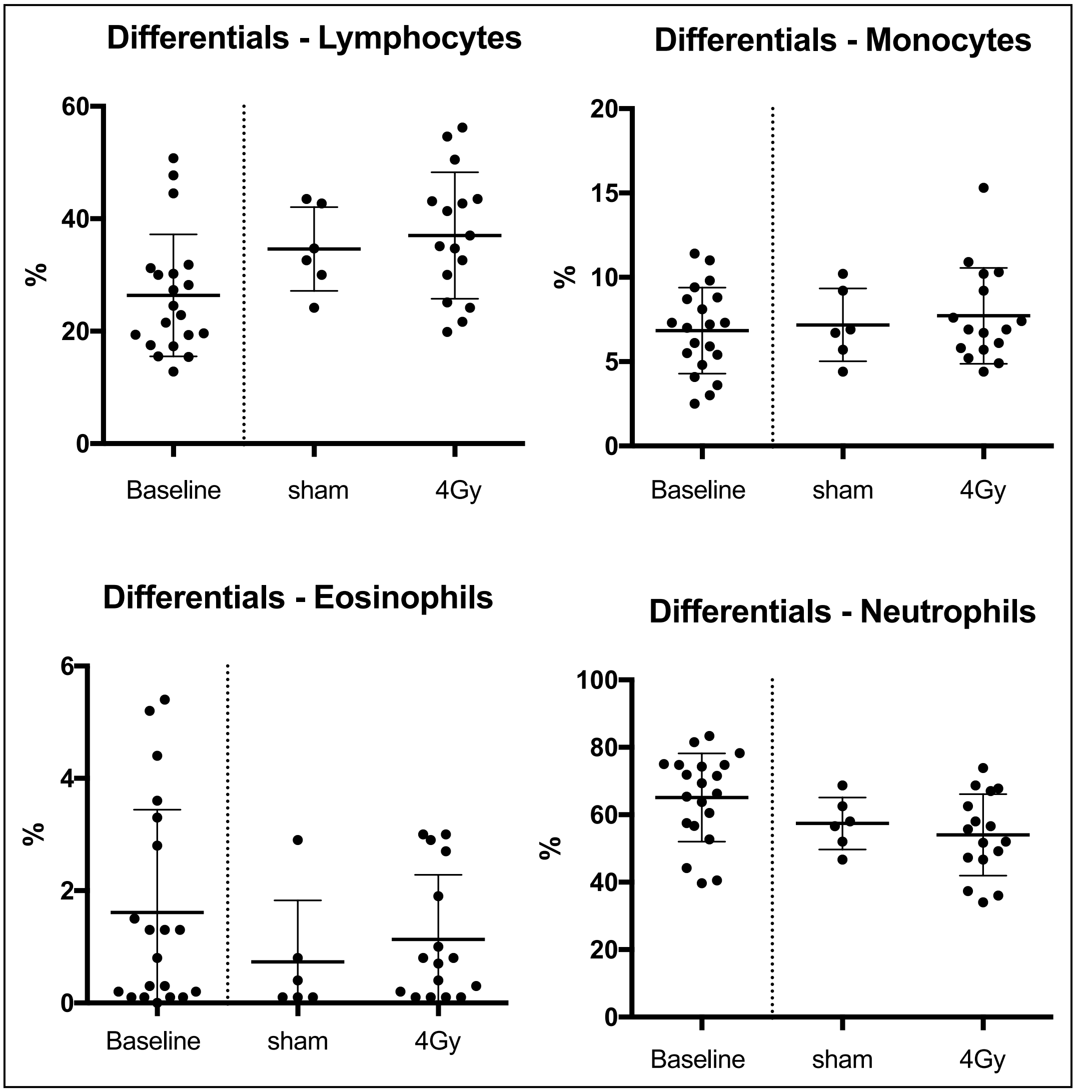

Figure 3.6: White cell differential at baseline and day 130 in the prospective cohort.

Using our immunophenotype panel we have defined the percentage or frequency of our target peripheral blood cell subsets 130 days post irradiation. These results are shown in figures below compared to the baseline reference data.

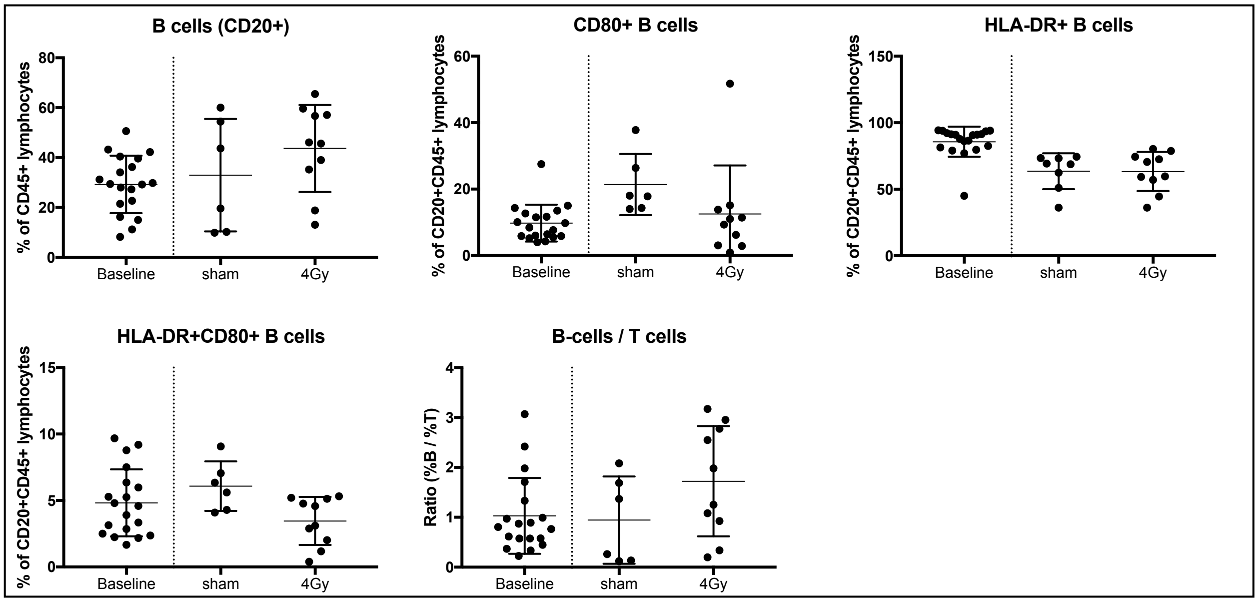

Figure 3.7: Frequency at baseline and day 130 in the prospective cohort of B cell subsets.

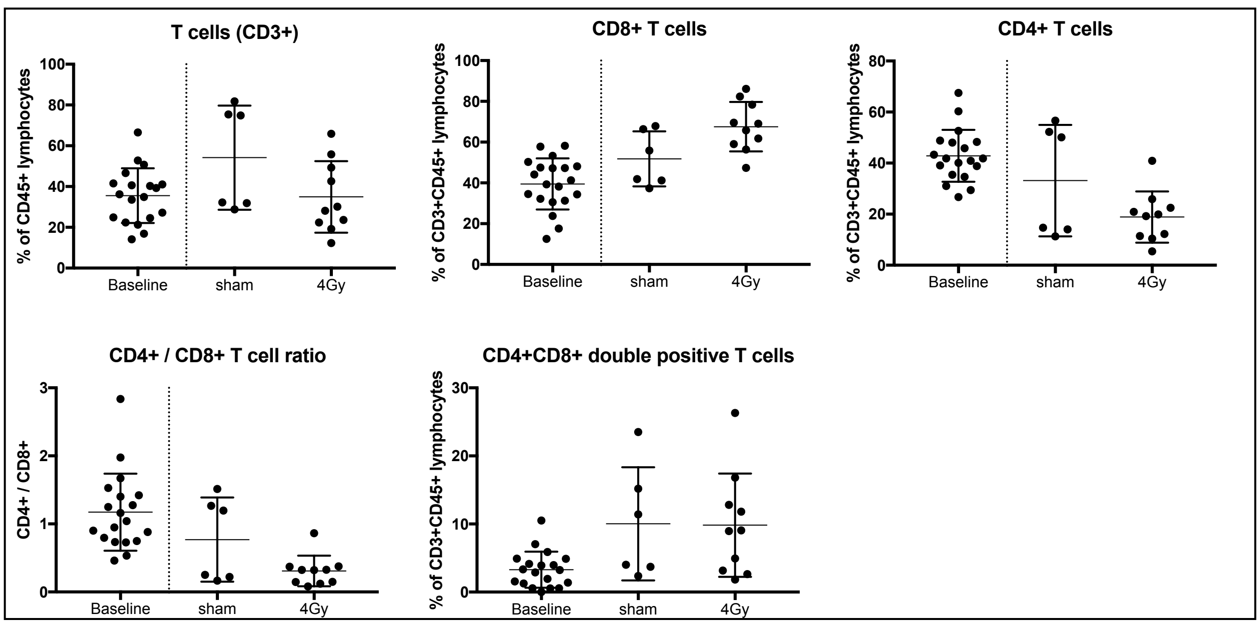

Figure 3.8: Frequency at baseline and day 130 in the prospective cohort of T cell subsets.

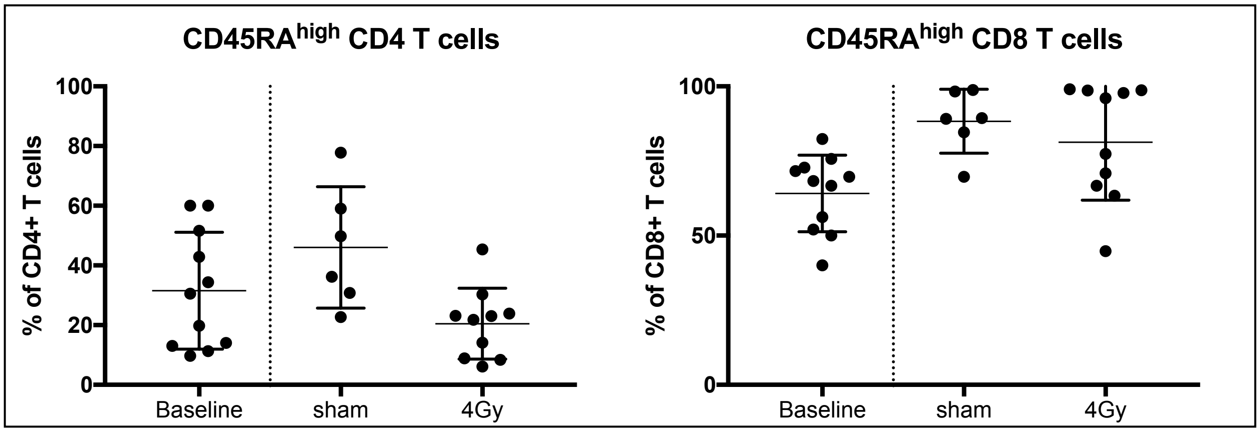

Figure 3.9: Frequency at baseline and day 130 in the prospective cohort of Naïve T cell subsets.

Molecular analysis of samples from both prospective and long-term cohorts

T cell receptor rearrangement analysis (sjTREC) will be batch run on PBMC cryopreserved from both cohorts of NHP for analysis starting in Y3Q1 (scheduled to begin week of 10/23/2017). sjTREC sample processing will be coordinated with sample preparation for **Project 4** to maximize use of each cryopreserved PBMC aliquot. We are continuing to work with Adaptive Biotech to develop a T cell receptor deep sequencing assay. If unavailable by Y3 close we will work with Dave Project 4, or others, to pull TCR sequences for repertoire analysis from RNAseq of selected samples.

NHP-Immunophenotyping / Flow Cytometry Panel Development

Based on the analysis of the prospective and long-term cohorts by flow cytometry, a review of the immune recovery literature in year 1 and requests from Project 2, we developed an enhanced immunophenotype panel (Version 2.1). The improved NHP phenotyping staining panel (**Table 3.1**) was used for staining of the prospective cohort 9-month time point and the second sample set from the long-term cohort. This more comprehensive panel will be used to analyze samples from both cohorts moving forward. The new v2.1 panel allows us to further define the frequency of the following cell types: Memory B cells, Plasmacytoid and myeloid DC, Central and effector memory T cells, cytolytic and non-cytolytic NK, classical/non-classical monocytes etc.

Table 3.1: Enhanced NHP Immunophenotyping Panel for Project 3 – v2.1

Target Populations	FITC	PerCP-Cy5.5	PE	PE-Cy5	PE-Cy7	APC	APC-H7	BV421	live/dead aqua	BV605	BV650	BV711
Plasmacytoid and myeloid DC	CD1c		CD11c		CD123	CD3 & CD20	HLA-DR		live/dead aqua	CD45		CD14
NK, NK-T, T cells, classical & nonclassical monocytes, granulocytes	CD56	HLA-DR	CD16		CD8	CD3	CD20		live/dead aqua	CD45		CD14
Naïve, Central Memory and Effector Memory CD4 and CD8 T cells	CD3		CD45RA	CD95	CD8	CD28		CD4	live/dead aqua	CD45	CCR7	
Naïve and memory B cells	CD27		CD3		CD80		CD20		live/dead aqua	CD45		

Molecular analysis of samples from Prospective Cohort

T cell receptor rearrangement analysis (sjTREC) will be batch run on PBMC cryopreserved from all NHP for analysis in Y3Q1 (scheduled to begin week of 10/23/2017). sjTREC sample processing will be coordinated with PBMC sample preparation for Project 4 to maximize use of each cryopreserved PBMC aliquot. We are continuing to work with Adaptive Biotech to develop a T cell receptor deep sequencing assay. If unavailable by Y3 we will work with Dave Project, or

others, to pull TCR sequences for repertoire analysis from RNA seq of selected samples. Alternatively we will utilize an antibody panel reactive against a distribution of surface TCRa/b families.

Major Task 2: Murine Studies (Chen, Duke)

In Year 1, we performed the initial experiment to determine the roles of thymopoiesis and peripheral expansion in overall T cell recovery in the classic mouse radiation injury model. The results suggested that T cell recovery post-irradiation is radiation dose-dependent (see Y1 annual report). We are currently repeating this experiment using more animals per group to increase statistical power. Since the recovery of total T and B cells and T cell subsets in spleen followed a similar pattern as that in peripheral blood, we are measuring T cell recovery in peripheral blood only in this experiment.

8-12 week-old C57BL/6 mice were irradiated with three different doses of radiation (2, 5, 7 Gy), Two additional control groups were added in this experiment. The first control is age-matched non-irradiated mice. The second control group was irradiated with 7 Gy and transplanted with 1x10e5 Lin- bone marrow cells from normal C57BL/6 mice. Total T, B, and T cell subsets are monitored in peripheral blood by flow cytometry overtime.

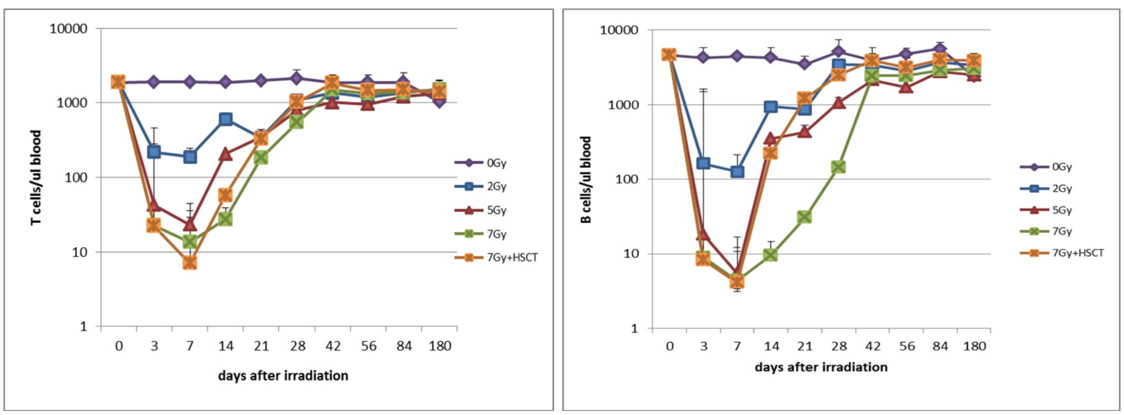

Figure 3.10. Total T and B cell recovery in peripheral blood after irradiation

After irradiation, total T cells (CD3+) and B cells (B220+) were measured in peripheral blood over time post-irradiation. As shown in **Figure 3.10**, the numbers of both T and B cells in all irradiated groups were no longer lower than those in the non-irradiated control group. In fact, T cells were even higher in 2 Gy, 5 Gy, and 7 Gy when compared with those in non-irradiated control mice.

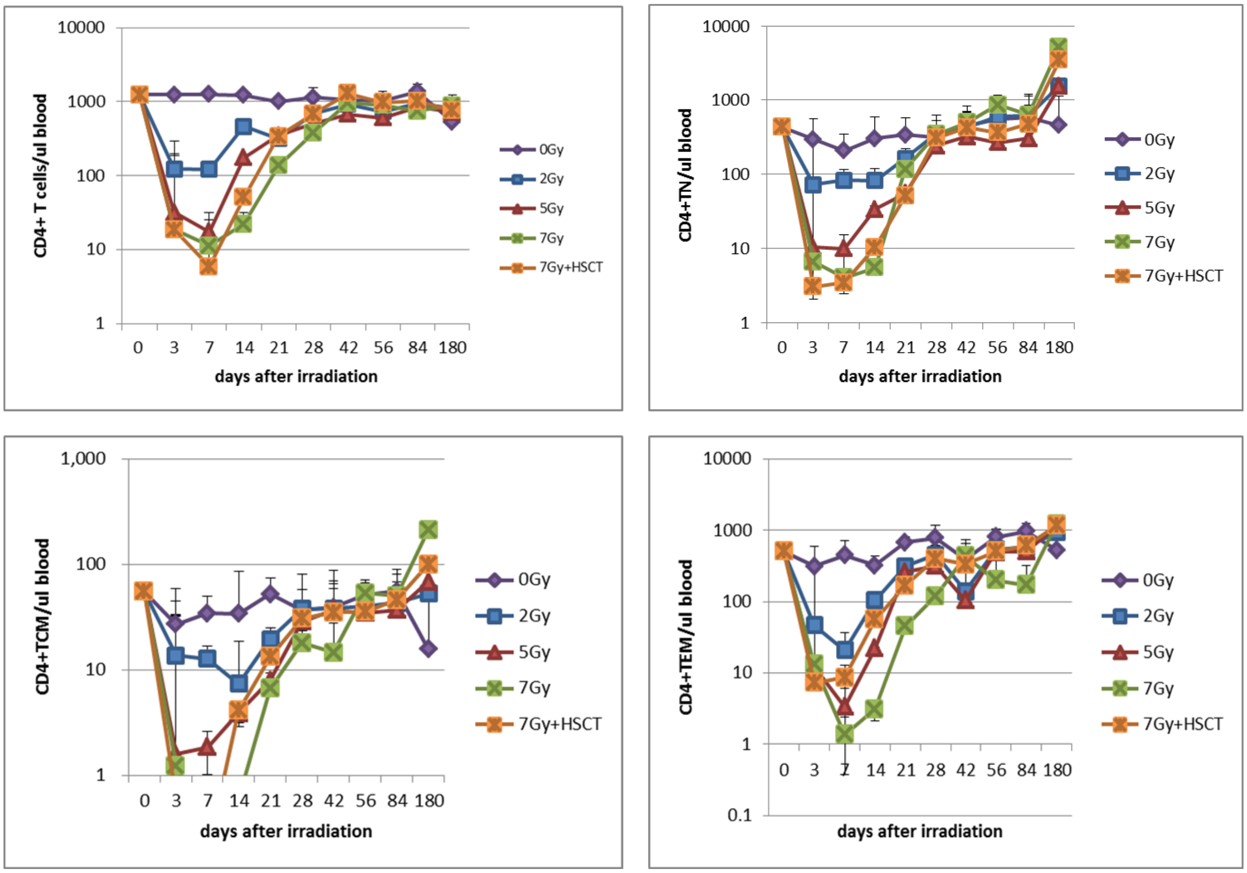

Figure 3.11. CD4 T cell recovery in peripheral blood after irradiation

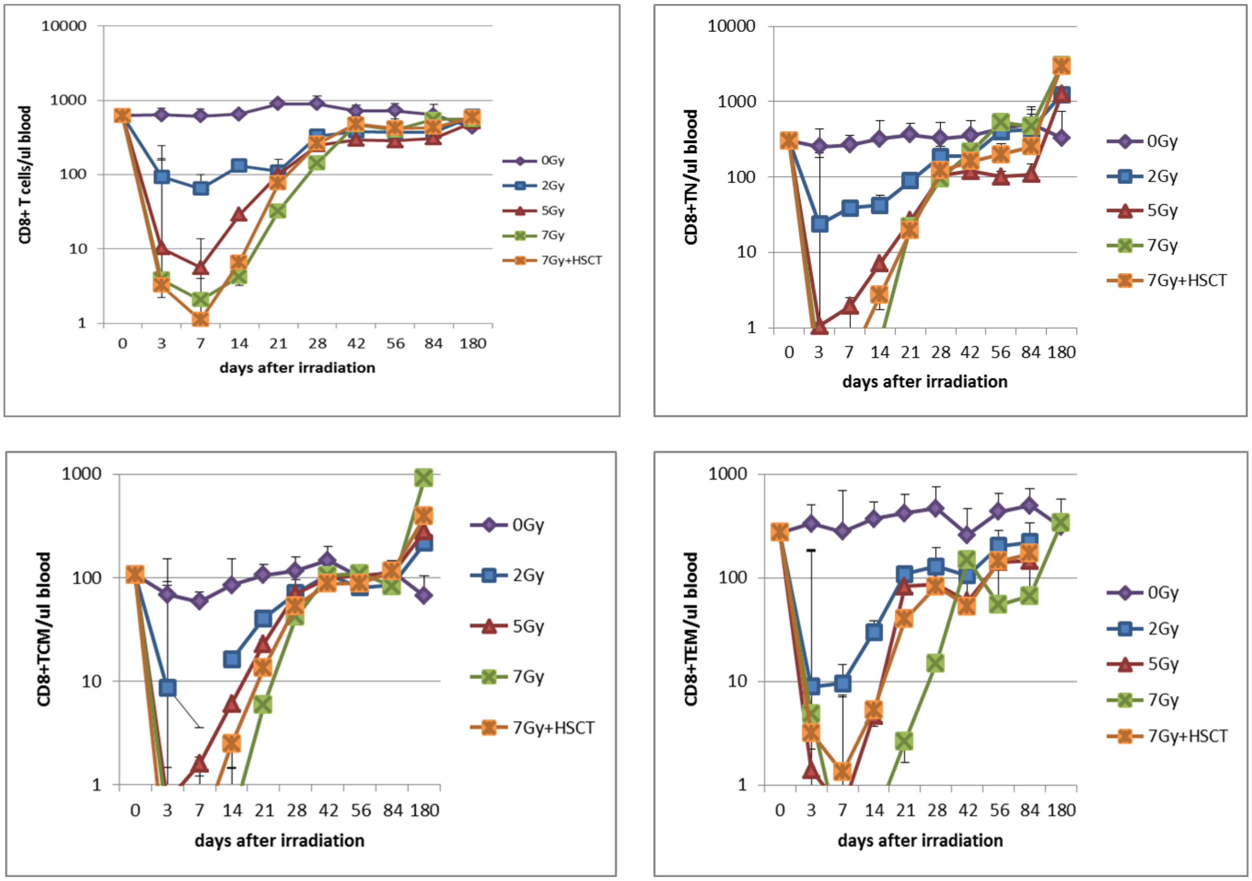

Figure 3.12. CD8 T cell recovery in peripheral blood after irradiation

As shown in **Figures 3.11 and 3.12**, the recovery of total CD4 and CD8 T cells followed a very similar pattern as that of total T cells (**Figure 3.10**). Similar results were obtained for both CD4+ and CD8+ naive (TN), central memory (TCM), and effector memory (TEM) T cells despite some minor differences.

We also measured the numbers of Qa2+CD24+ recent thymic emigrants in peripheral blood. As shown in **Figure 3.13**, both CD4+Qa2+CD24+ and CD8+Qa2+CD24+ cells dropped significantly in non-irradiated mice at day 180. In contract, both CD4+Qa2+CD24+ and CD8+Qa2+CD24+ cells in all irradiation groups recovered back to the normal level.

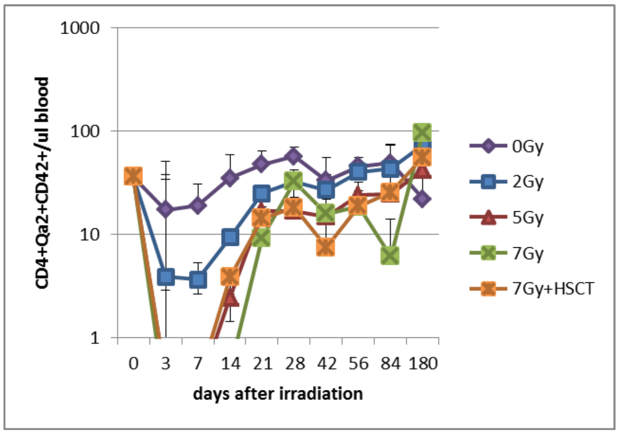

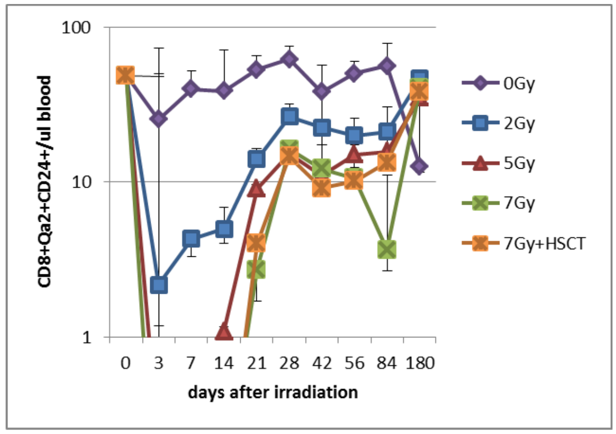

Figure 3.13. Recent thymic emigrant recovery in peripheral blood after irradiation

We also monitored the recovery of CD4+CD25+ regulatory T cells. As shown in **Figure 3.14**, Treg cells dropped significantly in non-irradiated controls mice at day 180. Treg cells did not recover back to the pre-irradiation level in all irradiated groups at day +180.

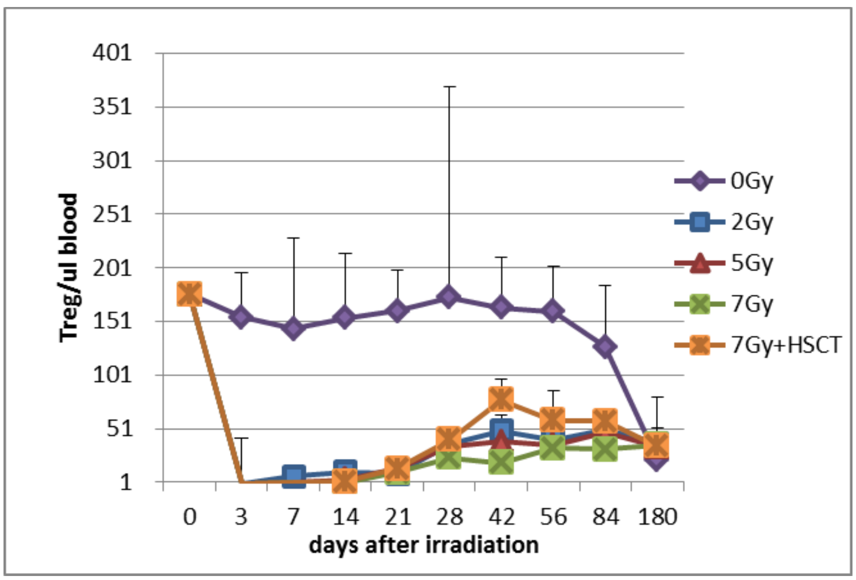

Figure 3.14. Regulatory T cell recovery in peripheral blood after irradiation

Due to the unexpected observations that T and B cell numbers are able to recover back to normal level post-irradiation, we have postponed the experiment using a second radiation injury model. This delay has affected this milestone. We are waiting to determine whether this is also true in NHPs. If it is true, we will focus our efforts on early phenotypic recovery, repertoire, and functional changes. If the results in NHPs are different, we will focus our efforts on studies using NHP model. In addition, we may consider performing the study in middle-aged mice. **We will obtain prior written approval if significant changes in objectives and scope will need to be made.**

Project 4 - Genomic Sequencing and Stem Cell Lines (Dr. Dave)

Major Activities

a) Collection and processing of blood samples in the prospective cohort during the subacute post-radiation phase for planned genomic analyses.

b) Method development for reliable mutation and expression identification from NHPs for which no standard methods currently exist.

c) Continued discussions with Duke and Wake Forest investigators on cross-project technical collaboration on cell collections, processing, and analysis.

d) Analysis of RNAseq data from NHPs: We continue to improve the analytical approaches for gapped alignments in NHPs that is important to measure expression from the RNA sequencing reads while skipping the introns in the NHP reference genomes.
e) Development of metrics for concordance between variants identified from RNAseq and DNA sequencing. While genetic variants can be identified from RNAseq data, the degree to which they recapitulate those from DNA sequencing, which is regarded as the “gold standard” is unknown. Our study provides the unique opportunity to examine this in NHPS.
f) Development of stem cell regeneration model that provides a functional approach to validation of genetic alterations. We performed ex vivo studies of iPS differentitation and have developed in vivo approaches to overcome the limitations of the ex vivo approaches.
g) Monthly DOD Conference calls

There were two main goals of the study. First, to define the genetic mutations and gene expression signatures induced by radiation. Second, define the molecular basis of immune deficiency and hematologic abnormalities induced by radiation.

Define genetic mutations induced by radiation (Aim #1)
In the past year, we continued to develop and have now finalized our methodologies for DNA whole exome sequencing n order to define the genetic mutations in rhesus macaques, we had to fully develop the methodologies for next generation sequencing and bioinformatics analysis. In the past year, we completed the development of methodologies for whole exome sequencing from rhesus macaque DNA and developed the methodology for transcriptome sequencing from rhesus macaque RNA.

Summary of work from DNA sequencing
Briefly, genomic DNA was sheared to 250 bp and size/concentration were verified using Bioanalyzer (Agilent Technologies). Sheared DNA was end-repaired, A-tailed, and ligated to Illumina paired-end adapters. The resulting libraries were amplified using Illumina PE specific primers. Samples were column purified and the size and quantity of the final libraries was determined using Bioanalyzer (Agilent Technologies).

The critical new element that was added this year custom-design of exome-capture baits that collectively span the entire gene coding region of rhesus macaques (35 million bases). To our knowledge, this is the first design of rhesus-macaque specific probes for whole exome sequencing.

Separately, we refined our analytical pipelines to account for statistical variations in the measured allele frequency. Thus, our method reliably identifies variants that appear to vary in allele frequency owing to statistical variation in sequencing coverage that inevitably occurs owing to the stochastic nature of sequencing data generation.
Separately, we have also applied this updated method to human data from patients with diffuse large B cell lymphoma and found a 10% improvement in the sensitivity and specificity of identifying genetic variants. We recently published those results in Cell (Reddy et al, 2017).

We are in the process of sequencing 40 NHPs and controls with data estimated to be returned in January 2018 from the core facility. Data analysis will commence immediately with these established methods.

Development of RNA sequencing pipeline for rhesus macaques
In the pat year, we began to fully develop our analytical methods for RNA sequencing from rhesus macaques. We took RNA from four samples and generated RNA sequencing libraries. These were aligned to the macaque genome.

We carefully generated quality control scores as a function of base-position in the sequencing read. We found that the Phred-like quality scores were uniformly over 20. We also found that the distribution of the different sequenced bases matched the expected frequencies from the macaque genome in terms of A, C, G and T frequencies. The non-called bases were an exceedingly low fraction of the overall bases (Figure 1).

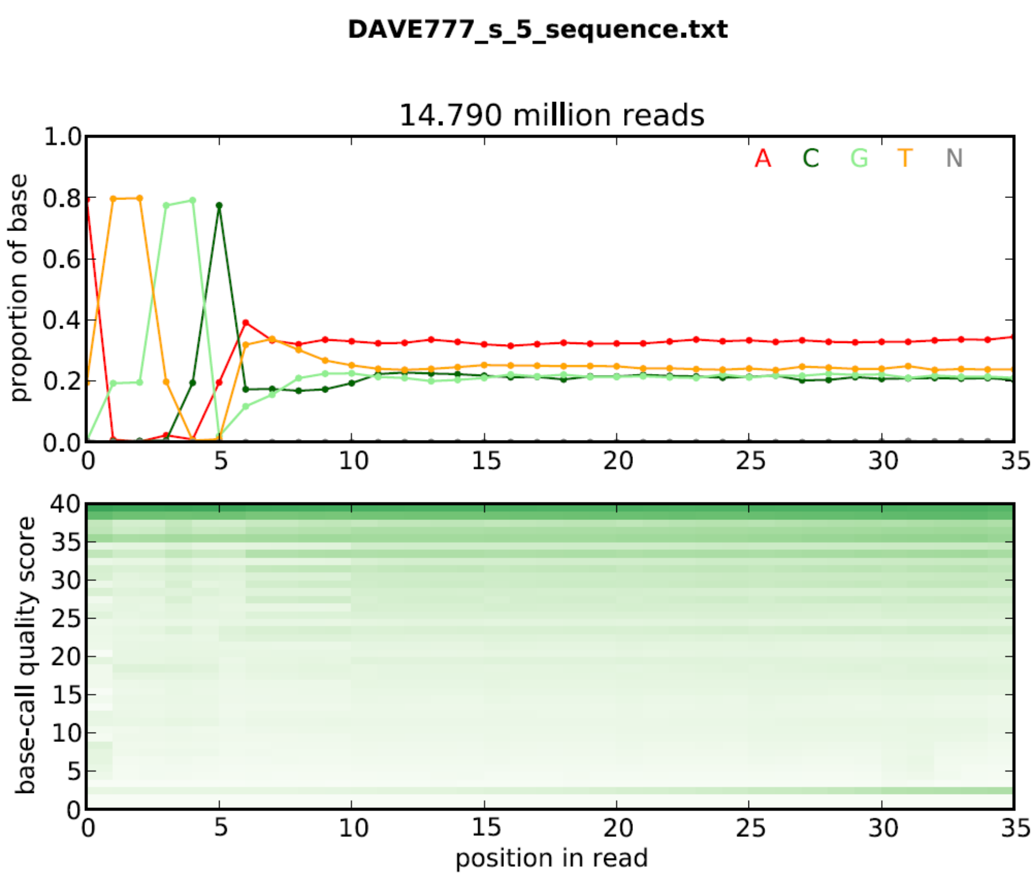

Figure 1: Base-level quality control reads as a function of position in read. The first seven

bases are reserved for sequencing bar codes.

An example of the aligned reads with gapped alignments to skip over introns is shown in figure 2.

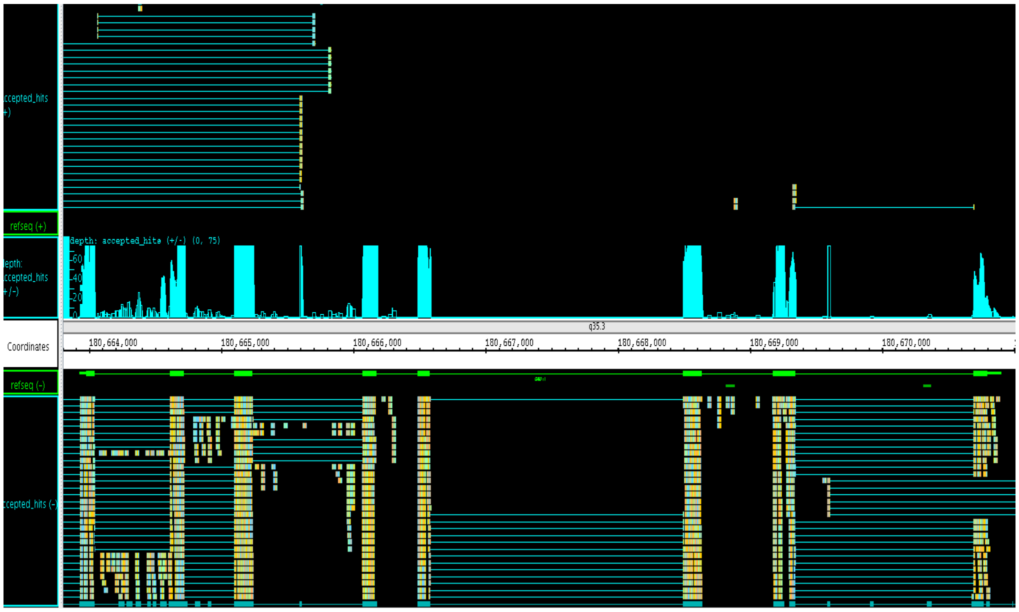

Figure 2: Example of mapping RNAseq reads for Base-level quality control reads as a function of position in read. The first seven bases are reserved for sequencing bar codes.

The sequencing reads mapped to the exons with clear skipping of the introns indicating that RNAseq is working well. The alignment patterns of specific exons will allow us to discern whether particular transcripts are favored in particular genes.
We also found that the sequencing reads generated from multiple barcodes aligned well to the gene coding exons. An example of the aligned reads is shown in the figure 3 below.

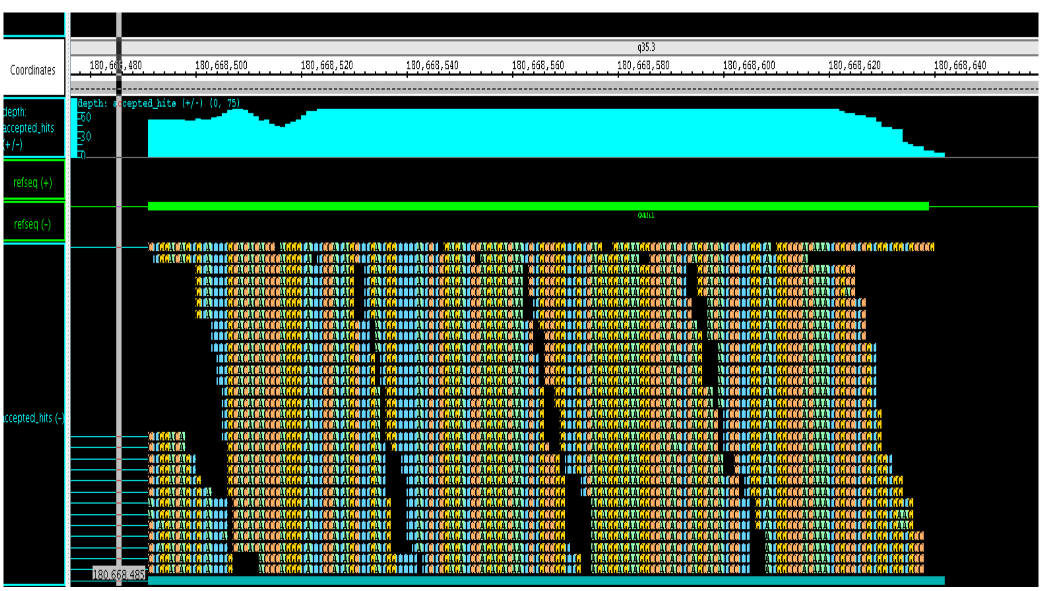

Figure 3: Alignment of RNAseq reads to exons.

These data indicate that the RNAseq approach can allow us to accurately estimate gene expression in our cases.

<u>Develop a stem-cell based model to generate immune B cells in vitro (AIM #2)</u>

Given the potential multigenic nature of genetic variation and the emerging role for B cell receptor signaling and other immune functions, we proposed to differentiate stem cells from irradiated macaques (or human stem cells with the genetic modifications present in irradiated macaques) into B cells to better understand their function and the long-term effects of radiation on immune function.

We have previously developed the schema shown in Figure 4 below to differentiate B cells from stem cells.

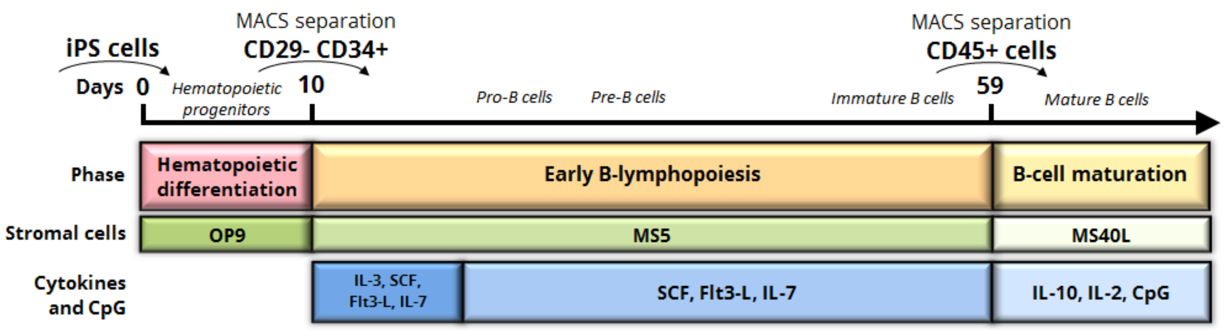

Figure 4: Schema for generating B lymphoid cells.

The yields of B cells from three consecutive experiments at at 90 days are shown below, and were on-average, less than 1% (Figure 5). Two additional experiments with new reagents yielded no measurable B cells.

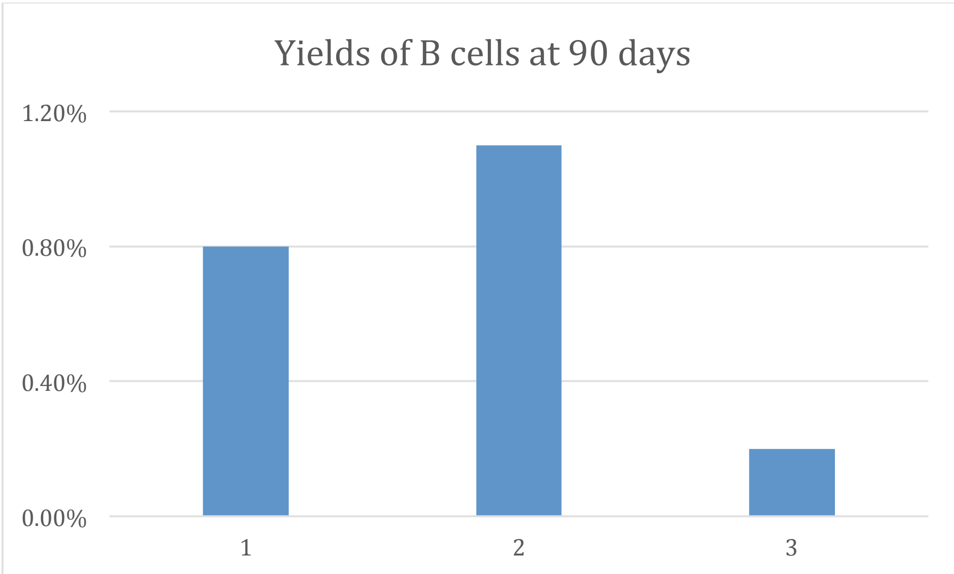

Figure 5: Yields of B cells after in vitro differentiation; the Y axis represents B cell yield; the X axis indicates experimental replicate number.

Recognizing these critical limitations, we utilized **Duke institutional funds** to initiate experiments using a humanized mouse model that transplants human stem cells to regenerate intact and functional human immune cells into an immune compromised mouse.

Generation of humanized mouse model:

We used the the NOD,B6.SCIDIl2rγ$^{-/-}$kit$^{W41/W41}$ (NBSGW) mice as the base model to generate a humanized mouse. NBSGW mice are ideal for this type of project as they contain a polymorphism in the *Sirpa* gene providing for phagocytic tolerance of human cells, PRKDC^{scid} mutation and Il2rγ$^{-/-}$ mutations which lead to absence of T, B, and NK cells thus preventing xenoreactivity, and a c-kit mutation resulting in impairment of hematopoiesis of the mouse cells, providing a competitive advantage to transplanted cells.We have comprehensively tested this system in experiments transplanting CD34+ hematopoietic stem cells from anonymized human donors.

Figure 6 shows our success with generation complete human lineages in mice by implanting as few as 125,000 human stem cells. As shown, we were able to identify substantial numbers of human derived circulating B cells (CD19+), T cells (CD3+) and myeloid cells (CD33+) in blood, spleen, bone marrow and thymus of the mice. Importantly, these humanized mice have an essentially unlimited supply of B and T cells for future experiments.

Interestingly, stem cell dosage did not have a large impact on the recovery of mature human immune cells by the time mice were 10 weeks old. Thus, we can reliably generate humanized mouse models by injecting human stem cells.
This model will be used as a starting point for comparing the immune phenotypes in cells arising from different genetic alterations observed from the DEARE data generated in Aim #1.

We will formally request using this new mouse model to be included as part of Aim 2, including IACUC and ACURO approvals as requred prior to funding new mouse studies from this program.

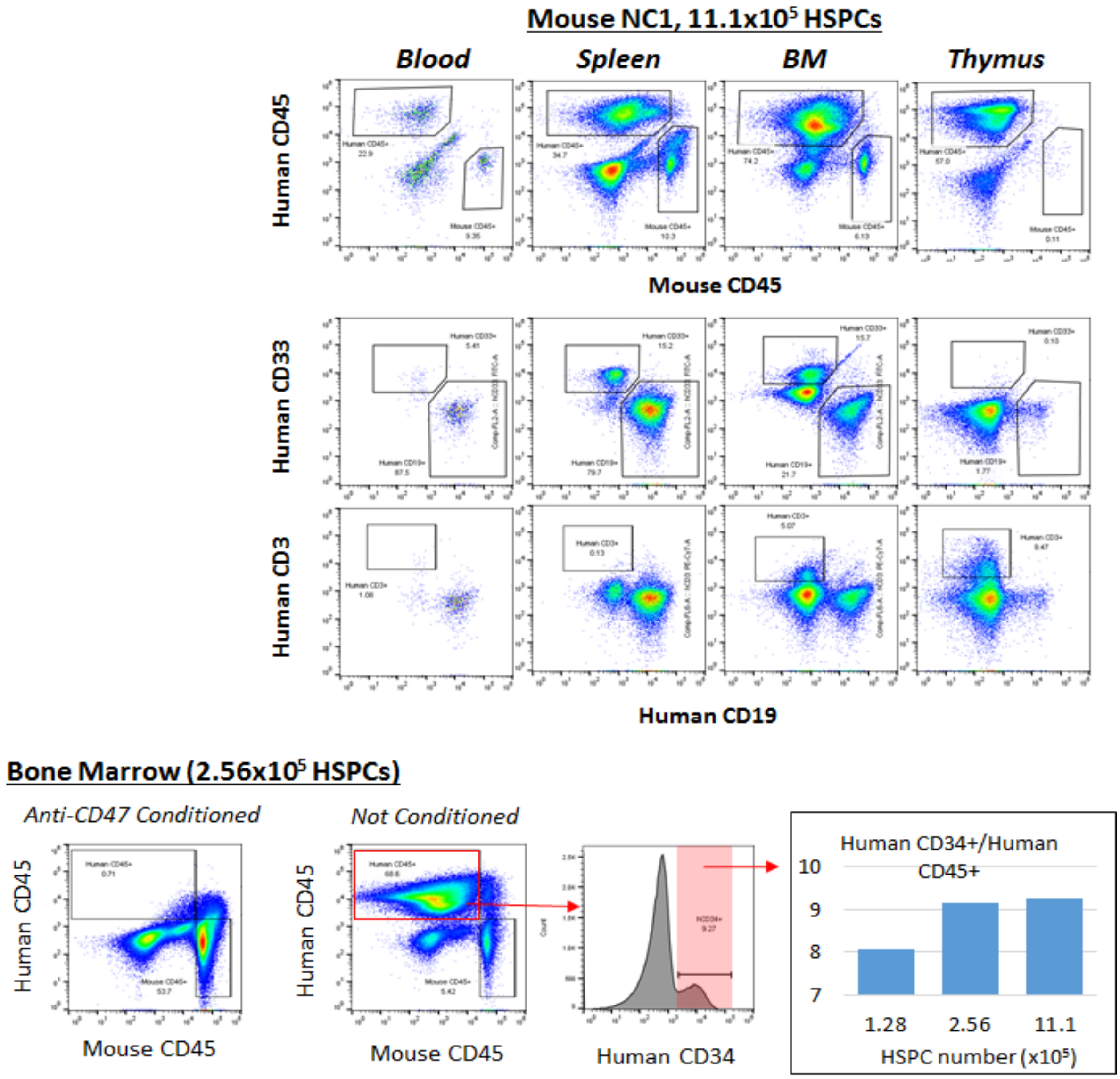

Figure 6: Presence of B cells (CD19+), T cells (CD3+), and myeloid cells (CD33+) in blood, spleen, bone marrow, and thymus at 10 weeks post transplantation. [Note, this preliminary data was funded by Duke development funds in preparation fof potential use in our program].

Apart from the planned change in model that will utilize an *in vivo* rather than *in vitro* approach, Aim 2 is unchanged. We will evaluate B and T cell activation, Ig secretion, and cell proliferation and compare in the context of genetic alterations data from Aim 1. B and T cells will be isolated by flow sorting and the rate of proliferation over 2 weeks will be measured by a BrdU assay. Cell viability will be measured by activated caspase 3 and 7-AAD staining.

We will then use shRNAs and/or CRISPR constructs targeting the gene of interest to knock down its expression in stem cells prior to generating the humanized mouse model from those cells. We will then perform identical experiments as above to characterize B and T cell function in that context. These experiments will establish the viability of the humanized mouse model as a nearly unlimited source of cells for experimentation and for modeling the effects of other genes identified in Aim #1.

Expected Outcomes: At the end of this revised Aim, we will have generated and characterized hematopoietic lineages from genetic alterations observed in DEARE macaques and demonstrated the feasibility of our approach for modeling complex genetic interactions.

4) Other Achievements

What opportunities for training and professional development has the project provided?

Overall (PI Cline)

1. All investigators attended a Radiation Countermeasures Retreat (28th of July 2017) which provided an opportunity for professional interaction.
2. All investigators participated in an in-depth discussion of this program's goals and objectives on August 9th, 2017 hosted by the PI's team at Wake Forest School of Medicine.
3. Investigators and Fellows attended the 2016 and 2017 Radiation Research Society meetings, which provided education and professional development.

Project 1 Diabetes (PI Kavanagh).

1. This project has led to training of the technical staff in data management and analysis.
2. Dr. Kavanagh attended a DOD-focused research retreat (9th of August 2017) to share research progress and discuss collaborative opportunities.
3. Dr. Fanning attended the World Congress of Gerontology and Geriatrics (23-27th of July 2017, San Francisco) to present an abstract and further the concept of radiation exposure as an accelerant to aging.
4. A post-graduate, pre-doctorate (DVM) student Catherine Si from North Caroline State University spent the summer doing research at Wake Forest University. She was trained in histomorphometry and analyzed the skeletal muscle structure from the RSC.
5. All staff have participated in radiation dosimetry training to enable conduct of the mouse study.
6. The PI is part of the PhD dissertation committee for a graduate student in Dr. Furdui's laboratory, and whose work relates to redox proteomics relating to Akt2 regulation.

Project 2 RIHD (PI Register)

1. Image Analysis Software, Cardiac Ultrasound, Cardiac MRI, and RNAseq analysis
2. Tissues: VisioPharm, programmable, working to develop semi-automated programs to assess myocardial, arterial, and other phenotypes including fibrosis and atherosclerosis.
3. Cardiac Ultrasound: CV ultrasound applications and measurements being optimized through interactions with Cardiology faculty and vendors, establishing new SOPs for prospective cohort.
4. Cardiac MRI: Register and Michalson have had interactive discussion sessions with Clinical Cardiology staff and faculty
5. Gene expression analyses: Day-long tutorial on the use of Ingenuity Pathways software from applications specialists attended by Drs. Michalson and Register, ½ day session on utilization of Bioconductor and R to conduct RNAseq and other genomics analyses.

Project 3 (Immune Recovery) PI Sempowski and Chen

1. Dr. Xinhua Che is a visiting scholar with Dr. Chen at Duke. He has performed work in *in vitro* flow cytometric studies and was mentored by Dr. Chen.

Project 4 (Genomics) PI Dave - Nothing to Report

How were the results disseminated to communities of interest?

Overall Program (Cline)
Study design, public health and strategic relevance, and opportunities for collaboration were presented by Dr. Cline at several venues:

- Wake Forest Department of Pathology Grand Rounds, Winston-Salem, NC
- The NIH/NIAID Centers for Medical Countermeasures Against Radiation (Annual meeting 12/7/16, monthly teleconferences with the CMCR Steering Committee)
- Comparative Medicine Research Strategy Meetings
- Wake Forest Animal Resources Program Continuing Education Seminar

Project 1 - Diabetes (Kavanagh)

- Comparative Medicine Research Strategy Meetings

Project 2 - Radiation-Induced Heart Disease (Register)

- Comparative Medicine Research Strategy Meetings
- Presentations at the annual Radiation Research meeting, at the annual RADCCORE meeting at Duke University, in Departmental and other seminars at Wake Forest, along with special presentations and discussion with visiting Cardiologists from other institutions.

Project 3 - (Immune Recovery) (Semposki/Chen)

- Nothing to report.

Project 4 - Genomics (Dave)

- Nothing to report.

What do you plan to do during the next reporting period to accomplish the goals?
If this is the final report, state "Nothing to Report."

Describe briefly what you plan to do during the next reporting period to accomplish the goals and objectives.

Overall (PI Cline):

No Change from Statement of Work.

For all projects we anticipate continued local and national presentations of results at relevant scientific meetings, and publications of results in the peer-reviewed literature.

Project 1 (Diabetes, PI Kavanagh):

No Change from Statement of Work.

Project 2 (RIHD, PI Register):

No Change from Statement of Work.

During the next year, we will be

1) Collecting fasted blood samples from the PRC and the RSC.
2) Remeasuring cardiac ultrasound images from baseline using the TOMTEC analysis to verify cross platform reproducibility of measures obtained on the GE instrument and by the stand alone package.
3) Continuing statistical analyses of the effects of radiation exposure on echocardiographic outcomes in the RSC.
4) Continuing image analysis of cardiac MR images in the PRC.
5) Statistical analysis of data collected to date from the cardiac MRI conducted in the PRC at baseline and 24 weeks after ARE.
6) Continuing plans for analysis of ECM and other biomarkers.
7) Planning for MR assessments of the PRC and the RSC
8) Ongoing molecular and cellular phenotyping of the monocytes in the PRC and the RSC (ancillary study funded through Center for Medical Countermeasures Program).

Project 3 (Immune Recovery, PI Sempowski/Chen):

Presentations, abstracts, meetings and manuscripts as studies mature

Project 4 (Genomics, PI Dave): Abstracts/meetings and manuscripts as studies mature.

In the coming year, we will scale up the sequencing. We will sequence 30 whole exomes and 30 transcriptomes to preliminarily define the genomic signatures associated with DEARE. For AIM #2, we will repeat our experiments to generate B cells from stem cells. We will increase the exposure to CD40L, which is known to stimulate B cell production and differentiation. We will carefully monitor these experiments for increased efficiency of lymphoid differentiation.

4. **IMPACT:** Describe distinctive contributions, major accomplishments, innovations, successes, or any change in practice or behavior that has come about as a result of the project relative to:

What was the impact on the development of the principal discipline(s) of the project?

Overall (PI Cline):

The findings produced by this program have increased awareness of the multi-systemic nature of late radiation effects, in the domains of radiation biology, radiation mitigation, and medical management of affected individuals post-exposure.

Project 1 (Diabetes, PI Kavanagh):

The work described in this report indicates that radiation exposure produces systemic dysregulation of metabolic functions, leading to altered protein signaling pathways, impaired tissue blood flow and deranged metabolic activity, including overt diabetes mellitus.

Project 2 (Radiation Induced Heart Disease, PI Register):

The project has produced new data on the effects of radiation on myocardial fibrosis and cardiac function, producing evidence of restrictive cardiomyopathy, as well as chronic persistent whole-body increases in circulating inflammatory signals, years after exposure.

Project 3 (Immune Recovery, PI Sempowski/Chen):

Our findings indicate that total body irradiation produces both acute and long-term impairment of immune function.

Project 4 (Genomics, PI Dave): Abstracts/meetings and manuscripts as studies mature.

Nothing to report. Future elucidation of the underlying genomic, transcriptomic and functional consequences is anticipated as Project 4 (Genomics/Dave) progresses into the analytic phase in year 3.

What was the impact on other disciplines?

The impact of our findings is broad, and spans multiple groups and agencies working to understand and mitigate delayed effects of acute radiation exposure, including the DOD, BARDA, NIH, FDA, and NASA. We anticipate that our data will influence response strategies, biomarker development, and re-adjustment of regulatory assumptions regarding the modeling, prediction and treatment of the long-term consequences described herein.

What was the impact on technology transfer?

Nothing to Report

What was the impact on society beyond science and technology?

Nothing to Report

5. CHANGES/PROBLEMS: The Project Director/Principal Investigator (PD/PI) is reminded that the recipient organization is required to obtain prior written approval from the awarding agency Grants Officer whenever there are significant changes in the project or its direction. If not previously reported in writing, provide the following additional information or state, "Nothing to Report," if applicable:

Changes in approach and reasons for change

We have made no substantial changes in any Project during Year 2 of this Program.

Minor changes are listed below:

Overall (Cline, PI):

Nothing to report.

Project 1 (Diabetes, PI Kavanagh):

No changes in overall approach occurred within this year.
Within the proteomics analysis strategy, we have added tissue section staining for oxidation (**Figure 1.18**). We will stain histological sections of skeletal muscle and subcutaneous fat with marker BP1 which is able to separate radiation sensitive and resistant cell cultures. We hypothesize that staining will differ in RSC monkeys that track towards diabetes or maintain good health. A secondary hypothesis is that the oxidant burden visualized will associate with level of redox modifications of Akt2.

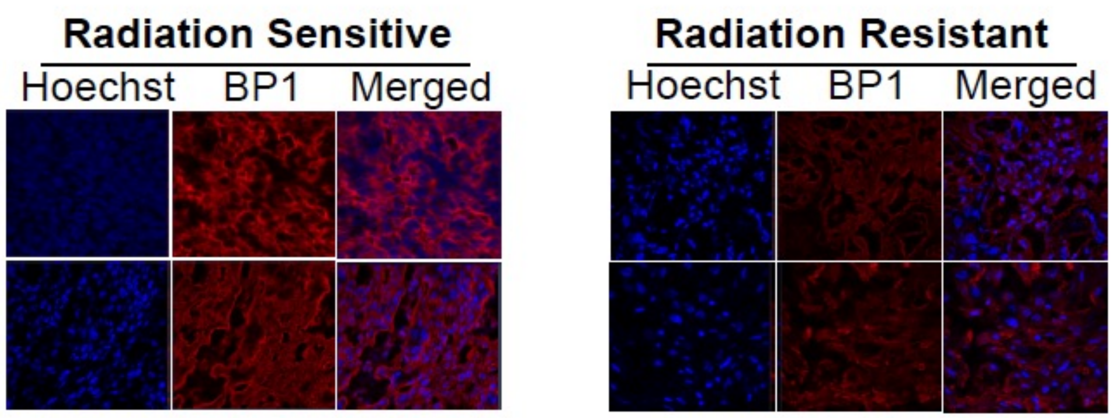

Figure 1.18. Cell cultures stained with BP1 showing brighter staining in radiation sensitive cells as compared to radiation resistant cells.

Project 2 (RIHD, PI Register):

Nothing to Report.

Project 3 (Immune Recovery, PI Sempowski/Chen):

Nothing to Report.

Project 4 (Genomic, PI Dave):

As stated above, we anticipate a change in iPSC gene expression experimental strategy.

Actual or anticipated problems or delays and actions or plans to resolve them

Overall:

The unanticipated mortality caused by infection with the opportunistic commensal pathogen *Spironucleus* (**Figure 8** above) reduced our animal numbers, but we are still within the range of numbers sufficient to address the experimental questions planned. We do not anticipate any need to repeat experimental work or acquire any additional animals.

Project 1 (Diabetes, PI Kavanagh):

We have experienced unexpected deaths in irradiated mice treated with both Tadalafil and IPW-5371. We have taken steps to resolve this adverse effect by decreasing the IPW-5371 dose (30 mg/kg/d reduced to 10 mg/kg/d). Since dose reduction no further deaths have been recorded. The number of mice affected was in the range of a priori expected adverse event rate described in the original animal use protocol.

The differential weight gain and insulin sensitivity in the control and irradiated monkeys of the PRC was not expected. This may delay our ability to detect insulin resistance as a result of radiation exposure. We have considered calorically restricting the obese control monkeys however this would change the biology of the control group and increase variability. We have opted to allow the next 6 months for the irradiated monkeys to fully recover and gain weight, with re-assessment of responses and tissues at 12 months post-radiation. This time point will reflect approximately 3 years human equivalent and is a reasonable time course for when delayed effects of radiation manifest clinically.

Project 2 (Radiation Induced Heart Disease, PI Register)

Nothing to Report.

Project 3 (Immune Recovery, PI Sempowski/Chen)

BD Biosciences (antibody provider for immunophenotyping) recalled the majority of their fluor-conjugated human/NHP antibodies used in our Y2Q1/2 immunophenotyping studies due to loss of fluorescent signal. We re-analyzed all the flow data to accommodate these shifts in fluorescent signature and have re-optimized all our stain panels to accommodate substitute reagents.

Due to the unexpected observations that T and B cell numbers are able to recover back to normal level post-irradiation, we have postponed the experiment using a second radiation injury model in

mice. This delay has affected this milestone. We are waiting to determine whether this is also true in NHPs. If it is true, we will focus our efforts on early phenotypic recovery, repertoire, and functional changes. If the results in NHPs are different, we will focus our efforts on studies using NHP model. In addition, we may consider performing the study in middle-aged mice. We will obtain prior written approval if significant changes in objectives and scope will need to be made.

Project 4 - Genomic Sequencing and Stem Cell Lines (PI Dave)

The expected yield of B cells from differentiation experiments was roughly 10%. However, the actual yields that we observed at 90 days was on-average, less than 1%. Repeating these experiments did with new reagents did not improve the yields of B cells. Therefore, in the coming year we will propose to differentiate the stems cells in vivo using a Nod-Scid-gamma (NSG) mouse model. ***We will confer with our program officer prior to implementing any changes in experimental approaches, and will obtain all necessary regulatory IACUC and ACURO approvals before supporting this work from DOD funds.***

Changes that had a significant impact on expenditures

Overall: Nothing to report.

Project 1 (Diabetes, PI Kavanagh): Nothing to report.

Project 2 (Radiation-Induced Heart Disease, PI Register): Nothing to report.

Project 3 (Immune Recovery, PI Sempowski/Chen):

1. We had a visiting scholar (Dr. Xinhua Chen) working on this project. He was supported by his home institute and did not charge to the project.
2. The mouse experiment using a second radiation injury model was postponed. The funds allocated for this experiment have thus not been spent yet.

Project 4 (Genomics, PI Dave): Nothing to report.

Significant changes in use or care of human subjects, vertebrate animals, biohazards, and/or select agents

Significant changes in use or care of human subjects

Not applicable - No human subjects

Significant changes in use or care of vertebrate animals.

Overall (PI Cline; All Projects)

In our overarching cross-project Nonhuman Primate Protocols - A variety of minor protocol amendments were made throughout the year, reflecting personnel changes and minor procedural changes.

Core Primate Studies (Cline)

Protocol 1 of 4 total: [ACURO Assigned Number]: PR141508.04

Title: Radiation Countermeasures Long Term Response of Rhesus Macaques

Target required for statistical significance: 120

Target approved for statistical significance: 132

Submitted to and Approved by:

Wake Forest IACUC (9/17/13; WF IACUC no. A13-117; Renewed/reapproved 6/23/16 as A16-094 as part of routine full renewal every 3 years as per IACUC policy)

Amendments since our prior annual report are shown below.

Protocol # A16-094 - Radiation Survivor Core

Amendment No.	Reason for amendment	Wake Forest IACUC approval date	ACURO approval date
6	Personnel; removal of summer students	10/19/16	10/21/16
7	Personnel; addition of new employee	11/17/16	11/21/16
8	Personnel change request	3/17/2017	3/20/2017
9	Adding Midazolam as an alternate to Diazepam	3/16/2017	3/24/2017
10	Personnel change request	6/19/2017	7/5/2017
11	Personnel change request	7/14/17	7/20/17

Status

This long-term cohort is under study as planned.

Protocol 2 of 4 total [ACURO Assigned Number]: PR141508.01

Title: Prospective Radiation Cohort: Cardiac and Metabolic Studies

Target required for statistical significance: 20

Target approved for statistical significance: 28

Submitted To And Approved By:

Wake Forest IACUC (Protocol #A15-083, approved 7/6/15)

ACURO approval (9/3/15, ACURO no. PR141508.01)

Amendments since last annual progress report.

Amendment No.	Reason for amendment	Wake Forest IACUC approval date	ACURO approval date
15	Personnel; addition of new employee	8/30/16	10/18/16
16	Addition of bone marrow collection	9/14/16	10/18/16
17	Adding drugs (sucralfate famotidine) for post radiation. Midazolam as alternate drug for Diazepam.	10/18/16	10/25/16
18	Personnel; removal of employees	10/19/16	10/25/16
19	Requesting an additional 10 animals on the protocol	11/10/16	11/15/16
20	We are adding blood culture and alternative antibiotics when signs of sepsis are present despite prophylactic antibiotics	12/14/16	12/16/16
AE	Bleed animal use for a transfusion 3 days early	12/1/16 note to ACURO & eIACUC	12/13/16 via David Lyons
21	Personnel change request	3/17/2017	3/20/2017
22	Personnel change request	Withdrawn 5/1/17	NA
23	Personnel change request (summer students added)	6/19/2017	7/5/17
24	Personnel change request (departing employee removed)	7/14/17	7/20/17

Status

Animals are undergoing irradiation and studies as planned including acute supportive care.

Protocol 3 of 4 total: ACURO Assigned Number PR141508.02

Title: **Prospective Evaluation of Diabetogenesis Post-irradiation in Mice (Metabolic Effects of Radiation Exposure)**

Target required for statistical significance: 200

Target approved for statistical significance: 200

Submitted To And Approved By:

Wake Forest IACUC (A15-068, Approved 5/20/15

ACURO (PR141508.02, Approved 10/19/15)

Amendments since prior annual report:

Amendment No.	Reason for amendment	Wake Forest IACUC approval date	ACURO approval date
4	Personnel change	7/11/16	1/4/17
5	Refinements to procedures (ear tagging, irradiation source, dose, location, addition of physical function testing, changed monitoring plan, post-irradiation antibiotic dose)	10/11/16	1/6/17
6	Personnel change	10/4/16	1/4/17
7	Use of tadalafil as agent to improve muscle perfusion	12/5/16	1/6/17
8	Use of IPW5371 to inhibit fibrosis	12/15/16	1/6/17
9	Withdrawn	NA	NA
10	Personnel change	4/28/17	5/12/17
11	Addition of microCT imaging methodology as an alternative to standard CT imagine (improve image quality) and Dose reduction in IPW-5371.	7/27/17	8/2/117

Status:

Approved studies are in progress.

Protocol 4 of 4 total:
Protocol [ACURO Assigned Number]: PR141508.03
Title: IMMUNOLOGICAL INJURY AND RECOVERY AFTER RADIATION INJURY
Target required for statistical significance: 4184 mice
Target approved for statistical significance: 4184 mice

Submitted to and approved by:
Duke IACUC (A142-15-05, Approved on 5/28/15)
ACURO (PR141508.03, Approved on 3/3/16)

Amendments:

Amendment No.	Reason for amendment	Duke IACUC approval date	ACURO approval date
1	Personnel change	9/12/17	10/13/17

Status - Approved, work in progress.

Significant changes in use of biohazards and/or select agents

Nothing to report

6. **PRODUCTS:** List any products resulting from the project during the reporting period. If there is nothing to report under a particular item, state "Nothing to Report."

- **Publications, conference papers, and presentations**

Report only the major publication(s) resulting from the work under this award.

Journal publications.

Overall (Cline): Nothing to Report.

Project 1 (Diabetes, PI Kavanagh):

Fanning KM, Pfisterer B, Davis AT, Presley TD, Williams IM, Wasserman DH, Cline JM, **Kavanagh K**. Changes in microvascular density differentiate metabolic health outcomes in monkeys with prior radiation exposure and subsequent skeletal muscle ECM remodeling. American Journal of Physiology – Regulatory, Integrative and Comparative Biology 2017 313(3): R290-297.
Federal Support was acknowledged.

Project 2 (Radiation-Induced Heart Disease, PI Register):

DeBo RJ, Lees CJ, Dugan GO, Caudell DL, Michalson KT, Hanbury DB, Kavanagh K, Cline JM, Register TC. Late Effects of Total-Body Gamma Irradiation on Cardiac Structure and Function in Male Rhesus Macaques. Radiat Res. 2016;186:55-64. doi: 10.1667/RR14357.1. Epub 2016 Jun 22. PubMed PMID:27333082. **(http://www.ncbi.nlm.nih.gov/pubmed/27333082)**
Federal Support was acknowledged.

DeBo RJ, Michalson KT, Lees CJ, Dugan GO, Hanbury DB, Caudell DL, Andrews RN, Vujaskovic Z, Batinic-Haberle I, Bourland JD, Cline JM, Register TC. SOD mimetic (MnTnHex-2-PyP5+) alters cardiovascular gene expression profiles in the absence of phenotypic improvement in NHP's following 10Gy irradiation to the thorax. *(In preparation, 2017).*
Federal Support will be acknowledged.

Project 3 (Immune Recovery, PI Sempowski/Chen):

Nothing to Report.

Project 4 (Genomics, PI Dave):

Reddy A, Zhang J, Davis NS, Moffitt AB, Love CL, Waldrop A, Leppa S, Pasanen A, Meriranta L, Karjalainen-Lindsberg ML, Nørgaard P, Pedersen M, Gang AO, Høgdall E, Heavican TB, Lone W, Iqbal J, Qin Q, Li G, Kim SY, Healy J, Richards KL, Fedoriw Y, Bernal-Mizrachi L, Koff JL, Staton AD, Flowers CR, Paltiel O, Goldschmidt N, Calaminici M, Clear A, Gribben J, Nguyen

E, Czader MB, Ondrejka SL, Collie A, Hsi ED, Tse E, Au-Yeung RKH, Kwong YL, Srivastava G, Choi WWL, Evens AM, Pilichowska M, Sengar M, Reddy N, Li S, Chadburn A, Gordon LI, Jaffe ES, Levy S, Rempel R, Tzeng T, Happ LE, Dave T, Rajagopalan D, Datta J, Dunson DB, Dave SS. Genetic and Functional Drivers of Diffuse Large B Cell Lymphoma. Cell. 2017 Oct 5;171(2):481-494.e15. doi: 10.1016/j.cell.2017.09.027. PubMed PMID: 28985567; PubMed Central PMCID: PMC5659841.
This paper utilized methods developed for this project.
Federal Support was acknowledged.

Books or other non-periodical, one-time publications.

Overall (PI Cline): Nothing to report.

Project 1 (Diabetes, PI Kavanagh): Nothing to report.

Project 2 (Radiation Induced Heart Disease, PI Register):

PhD Dissertation

Ryne DeBo, MS, PhD. Non-Human Primate Models of Ionizing Radiation Exposure and Evaluation of the Effects of a Potential Radiation Mitigator. Molecular Medicine and Translational Sciences Graduate Program, Wake Forest School of Medicine, May 2017.
Federal Support was acknowledged.

Abstracts

Effects of Total Body Irradiation on Echocardiographic Phenotypes in Male Rhesus Macaques Kristofer T. Michalson, Gregory Dugan, Ryne J. DeBo, Dalane Kitzman, J. Mark Cline, Thomas C. Register. Wake Forest School of Medicine, Winston-Salem, NC.
Accepted, Radiation Research Society Meeting, October 2017
Federal Support was acknowledged.

Evaluation of Monocyte Polarization in Long Term Non-Human Primate Survivors of Acute Ionizing Radiation Exposure Kristofer T. Michalson1, Andrew N. McIntyre2, Ryne J. DeBo1, Gregory D. Sempowski2, J. Mark Cline1, Thomas C. Register1, Wake Forest School of Medicine, Winston-Salem, NC1 and Duke University, Durham, NC2.
Accepted for presentation at the 2017 Radiation Research Society Meeting October 2017
Federal Support was acknowledged.

Evaluation of a superoxide dismutase mimetic as a potential mitigator of acute and delayed responses of the lung and heart to thoracic x-ray irradiation. Ryne J. DeBo1, Kristofer T. Michalson1, Gregory O. Dugan1, Cynthia J. Lees1, David B. Hanbury1, David L. Caudell1, Rachel N. Andrews1, Zeljko Vujaskovic2, Ines Batinic-Haberles2, J. Daniel Bourland1, J. Mark Cline1, Thomas C. Register1, Wake Forest School of Medicine, Winston-Salem, NC1 and Duke University, Durham, NC2
Federal Support was acknowledged.

“Serum IL-10 and IL-15 Levels are Increased with Prior Exposure to Gamma Irradiation and are Associated with Radiation Sensitive Cardiac Phenotypes” Thomas C. Register1; Ryne J. DeBo1; Kris Michalson, DVM1; Cynthia J. Lees, DVM, PhD1; Greg Dugan, DVM1; Greg Sempowski, PhD2; Kylie Kavanagh, DVM1; David Caudell, DVM, PhD1; and J. Mark Cline, DVM, PhD1, Wake Forest School of Medicine, Winston-Salem, NC1 and Duke University, Durham, NC2, Radiation Research Society Meeting October 2016
Federal Support was acknowledged.

Project 3 (Immune Recovery, PI Sempowski/Chen):

Xinhua Chen, Ying Huang, Yiqun Jiao, Xiaoli Nie, and Benny J. Chen. T cell reconstitution following ionizing irradiation

Division of Cellular Therapy/BMT, Duke University Medical Center, Durham, NC
Abstract accepted; 63rd Radiation Research Society Annual Meeting 2017
Federal support acknowledged

Project 4 (Genomics, PI Dave):

Nothing to report.

Other publications, conference papers, and presentations.

Overall: (PI Cline):

Rotating monthly presentations of project progress via WebEx to Progam Team.

Overview Presentation, Annual Retreat, Wake Forest School of Medicine, August 9th 2017.

Multisystemic late effects of radiation exposure in nonhuman primates
J Mark Cline[1]; Greg Dugan[1]; Rachel Andrews[1]; Kylie Kavanagh[1]; Daniel Bourland[1]; David Hanbury[1]; Ann Peiffer[1]; Thomas Register[1]; Ryne DeBo[1]; David Caudell[1]; and Nelson Chao[2]
Wake Forest University School of Medicine, Winston-Salem, NC[1] and Duke University Medical Center, Durham, NC[2]
Radiation Research Society, Invited Presentation, 2016
Federal Support was acknowledged.

Primate Radiation Survivor Core
J Mark Cline1; John Olson1; Greg Dugan1; Rachel Andrews1; Kylie Kavanagh1; Daniel Bourland1; David Hanbury1; Ann Peiffer1; Thomas Register1; Ryne DeBo1; David Caudell1; Greg Sempowski2 and Nelson Chao2
Centers for Medical Countermeasures against Radiation Annual Meeting, Rockville, MD, December 6-7, 2016
Federal Support was acknowledged.

Project 1 (Diabetes, PI Kavanagh):

Rotating monthly presentations of project progress via WebEx to Progam Team.

Project 1 Presentation, Program Annual Retreat, Wake Forest School of Medicine, August 9th 2017.

Project 2 (Radiation-Induced Heart Disease, PI Register):

Rotating monthly presentations of project progress via WebEx to Progam Team.

Project 3 Presentation, Program Annual Retreat, Wake Forest School of Medicine, August 9th 2017.

Thomas C. Register. “Radiation Induced Heart Disease” Radiation Countermeasures Center of Research Excellence, J. B. Duke Conference Center, Duke University, July 2017

Federal Support was acknowledged.

Kristofer T. Michalson and Thomas C Register. “Monocyte Programming and Fibrotic Responses to Total Body Irradiation”, Third Annual Comparative Medicine Research Symposium, Wake Forest Bowman Gray Center for Medical Education, July 2017
Federal Support was acknowledged.

DeBo RJ, Lees CJ, Dugan GO, Caudell DL, Michalson KT, Hanbury DB, Kavanagh K, Cline JM, Register TC. “Late Effects of Total Body Gamma Irradiation on Cardiac Structure and Function in Male Rhesus Macaques” Third Annual Comparative Medicine Research Symposium, Wake Forest Bowman Gray Center for Medical Education, July 2017
Federal Support was acknowledged.

Ryne J DeBo, “Effects of a Potential Radiation Mitigator on Nonhuman Primate Heart and Lung” Comparative Medicine Research Strategy Meeting, Wake Forest School of Medicine, February 2017
Federal Support was acknowledged.

Ryne J DeBo “Molecular, Cellular and Cardiovascular Effects of Total Body Irradiation and the Investigation of a Potential Radiation Mitigator in Non-Human Primate Models” Molecular Medicine and Translational Sciences Seminar Series, Wake Forest School of Medicine, December 2016
Federal Support was acknowledged.

Kristofer T. Michalson “Monocyte Programming and Fibrotic Responses to Total Body Irradiation in Nonhuman Primates” Comparative Medicine Research Strategy Meeting, Wake Forest School of Medicine, September 2017
Federal Support was acknowledged.

Ryne J. DeBo 2017 Radiation Research Editors' Award Lecture for the publication: *DeBo RJ, Lees CJ, Dugan GO, Caudell DL, Michalson KT, Hanbury DB, Kavanagh K, Cline JM, Register TC. “Late Effects of Total Body Gamma Irradiation on Cardiac Structure and Function in Male Rhesus Macaques.”* 2017 Radiation Research Society Scholars in Training Workshop, Cancun, Mexico, October 2017
Federal Support was acknowledged.

Project 3 (Immune Recovery, PI Sempowski/Chen):

Rotating monthly presentations of project progress via WebEx to Progam Team.

Project 3 Presentation, Program Annual Retreat, Wake Forest School of Medicine, August 9th 2017.

Project 4 (Genomics, PI Dave):

Rotating monthly presentations of project progress via WebEx to Progam Team.

Project 4 Presentation, Program Annual Retreat, Wake Forest School of Medicine, August 9th 2017.

- **Website(s) or other Internet site(s)**

Nothing to report

- **Technologies or techniques**

Nothing to report

- **Inventions, patent applications, and/or licenses**

Nothing to report

- **Other Products**

Overall (PI Cline):

Nothing to report.

Project 1 (Diabetes, PI Kavanagh):

Nothing to report.

Project 2 (Radiation Induced Heart Disease, PI Register):

Grants submitted and funded

Pathology Internal Pilot Grant Application (funded) $25,000 Thomas C. Register, PhD. “In Situ Molecular Profiling of Myocardial Responses to Ionizing Radiation in Rhesus Macaques” July 2017

RADCCORE Pilot Grant Application (funded)
5U19AI067773-13 (Register-PI) $100,000 (Year 1) 08/01/17-07/31/18
“Monocyte Polarization in Acute and Delayed Responses to Total Body Irradiation in Nonhuman Primates” This project is designed to determine the effect of total body irradiation on circulating monocyte polarization and transcriptional programming in the acute and chronic phases post irradiation, and to explore relationships of these monocyte phenotypes with radiation induced conditions in male rhesus macaques.

Project 3 (Immune Recovery, PI Sempowski/Chen):

Nothing to report.

Project 4 (Genomics, PI Dave):

Nothing to report.

7. PARTICIPANTS & OTHER COLLABORATING ORGANIZATIONS

What individuals have worked on the project?

Core Primate Studies (Cline)

Name: J. Mark Cline
No change

Name: Daniel Bourland
No change

Name: David Caudell
No change

Name: Janet Tooze
No change

Name: Jean Gardin
No change

Name: Matt Dwyer
No change

Name: Russell O'Donnell
No change

Name: Chrystal Bragg
No change

Name: Renae Hall
No change

Name: Patricia Warren
No change

Project 1 – Diabetes (Kavanagh)

Name: Kylie Kavanagh
No change

Name: Ashley Davis
No change

Name: Christina Sherrill
No change

Name: Cristina Furdui
No change

Name: Xiaofei Chen
No change

Project 2 – Radiation/Heart Disease (Register)

Name: Thomas Register
No change

Name: Sujethra Vasu
No change

Name: Craig Hamilton
No change

Name: Kris Michalson, DVM
Project Role: Graduate Student
Researcher Identifier: N/A
Nearest person month worked: 6 months (supported from NIH T32 training grant funds)
Studies of monocyte/macrophage differentiation, echocardiography, and myocardial fibrosis.

Name: Ryan DeBo, PhD
Project Role: Research Fellow
Researcher Identifier: N/A
Nearest person month worked: 4.0 (effort began 06/01/17)
Dr. DeBo was the first author on the manuscript: "Late Effects of Whole Body Gamma Irradiation on Cardiac Structure and Function in Male Rhesus Macaques" which was awarded the 2017 Editor's Choice Award by the journal Radiation Research. He received his PhD this spring after being supported by RADCCORE, and began receiving support to continue work on Project 2.

Name: James Bottoms
No change

Name: Maryanne Post
No change

Project 3 – Immune Recovery (Chen & Sempowski)

Name: Benny Chen
No change

Name: Gregory Sempowski
No change

Name: Lesslee Arwood

No change

Name:	Xinhua Chen
Project Role:	Visiting Scholar
Researcher Identifier (e.g. ORCID ID):	N/A
Nearest person month worked:	6
Contribution to Project:	Dr. Chen has performed flow cytometry experiments and data analyses

Name: Laura Hale
No change

Name: Yiqun Jiao
No change

Name: Andrew Macintyre, PhD
No Change

Name:	Xiaoli Nie
Project Role:	Visiting Scholar
Researcher Identifier (e.g. ORCID ID):	N/A
Nearest person month worked:	1
Contribution to Project	Dr. Nie has performed flow cytometry experiments and data analyses

Name:	Brittany Sanders, MS
Project Role:	Research Analyst
Researcher Identifier (e.g. ORCID ID):	N/A
Nearest person month worked:	1
Contribution to Project:	NEW HIRE. Ms Sanders performs tissue processing And flow cytometry experiments.

Project 4 - Genomic Sequencing and Stem Cell Lines (Duke Consortium – Dave)

Name: Sandeep Dave
No change

Name: Anupama Reddy
No change

Name: Cassandra Love
No change

Name:	Guojie Li
Project Role:	Research Fellow
Researcher Identifier (e.g. ORCID ID):	N/A
Nearest person month worked:	6
Contribution to Project:	Sequencing and bioinformatics analysis.

Has there been a change in the active other support of the PD/PI(s) or senior/key personnel since the last reporting period?

J. Mark Cline (PI)

Changes in *Current* Support as reported in the original application:

Project Title: Oxygen, Gastrin-Releasing Peptide & Radiation-induced Pulmonary Fibrosis
Change: Project Complete

Project Title: Assessment Study to Evaluate CCL2 Clearance in a Tumor- Bearing Non-human Primate
Change: New Award

Daniel Bourland (Co-Investigator)

Changes in *Current* Support as reported since the last reporting period (annual report):

Project Title: Planimetry for Assessment of Vessicant Chemical-induced Skin Injury (subcontract GTS 44511)
Change: Project complete

Project Title: Biodosimetry after Radiological and Nuclear Events (subcontract GTS 43942)
Change: Project complete

David Caudell (Co-Investigator)

Changes in *Current* Support as reported since the last reporting period (annual report):

Project Title: Development of Radiation Dosage Parameters for Lymphodepletion with Minimal Myeloablation in Cynomolgus Maraques
Change: Project Complete

Project Title: Immunophenotyping of the Intestinal Muscosal Immune System in Irradiated Monkeys
Change: New Award

Christina Furdui (Co-Investigator)

Project Title: 2016 Thiol-based Redox Regulation & Signaling GRC and GRS (R13 AG053038)
Change: Project Complete

Project Title: Model-based Prediction of Redox-Modulated Responses to Cancer Treatments
Change: New Award

Project Title: Cancer Center Support
Grant Change: New Award

Project Title: Modified Ketogenic Diet Effects on Alzheimer's Disease Biomarkers and Cognition in Mild Cognitive Impairment
Change: New Award

Project Title: Oxidative Stress and the Development of
Osteoarthritis Change: New Award

Project Title: Isoform-specific Roles of AMPK in Synaptic Failure and Memory Deficit in Alzheimer's Disease
Change: New Award

Kylie Kavanagh (Co-Investigator)

No changes to report

Thomas Register (Project 3 PI)

Project Title: Monocyte Polarization in Acute and Delayed Responses to Totla Body Irradiation
Change: New award

Project Title: In Situ Molecular Profiling of Myocardial Responses to Ionizing Radiation in Rhesus Macaques
Change: New award

Janet Tooze (Co-Investigator)

Changes in *Current* Support as reported since the last reporting period (annual report):

Project Title: Untangling Sodium, Energy, and Blood Pressure in Whites and African Americans
Change: Project Complete

Project Title: Prepare to Care: A Supported Self-Management Intervention for Head and Neck Cancer Caregivers
Change: Project Complete

Project Title: Quantitative CT and MRI-based Assessment of Dynamic Vertebral Strength and Injury Risk Following Long-Duration Spaceflight
Change: New Award

Project Title: EHealth Mindful Movement and Breathing to Improve Gynecologic Cancer Surgery Outcomes
Change: New Award

Greg Sempowski (Project 3 Co-PI - Duke)

Project Title: Harrison Influenza P01 - Virology P01-AI089618 (NIAID)
Change: New award

Project Title: Human Thymus P01 - Human Translation and Verification (NIA)
Change: New award

Project Title: Duke DARPA Pandemic Prevention Platform (P3) HR0011-17-2-0069 (DoD - DARPA)
Change: New award

Benny Chen (Project 3 Co-PI - Duke)

Project Title: Endothelial Cell-Derived Extracellular Vesicles Mitigate Hematopoietic Injury Following Ionizing Radiation
Change: New award

Project Title: Mitigators of Radiation-Induced Endovascular Injury: Targeting Tie2 and Thrombocytopenia
Change: New award

Project Title: Advanced Development of Medical Countermeasures for Platelet Regeneration Following Radiation Exposure from a Radiological/Nuclear Incident
Change: Project Complete

<u>Sandeep Dave (Project 4 PI - Duke)</u>

Project Title: 5P30-CA14236-40: Cancer Center Program Leadership

Change: New appointment

Project Title: R01CA193655-01: Defining the functional role of mutations in diffuse large B cell lymphoma

Change: New award

Project Title: Leukemia and Lymphoma Society Study 6492-16.

Change: Project ended.

What other organizations were involved as partners?

Nothing to report

8. SPECIAL REPORTING REQUIREMENTS

COLLABORATIVE AWARDS: For collaborative awards, independent reports are required from BOTH the Initiating PI and the Collaborating/Partnering PI. A duplicative report is acceptable; however, tasks shall be clearly marked with the responsible PI and research site. A report shall be submitted to **https://ers.amedd.army.mil** for each unique award.

Not Applicable

QUAD CHARTS: If applicable, the Quad Chart (available on https://www.usamraa.army.mil) should be updated and submitted with attachments.

See attachment 1.

9. APPENDICES: Attach all appendices that contain information that supplements, clarifies or supports the text. Examples include original copies of journal articles, reprints of manuscripts and abstracts, a curriculum vitae, patent applications, study questionnaires, and surveys, etc.

Attachments:

1 Quad Chart

2 Katie Fanning, Christina Sherrill, Ashley Davis, Kylie Kavanagh.
Healthspan Measures in a Western Diet Conditioned, Irradiated Rodent Model of Accelerated Aging.
World Congress of Gerontology and Geriatrics (23-27th of July 2017, San Francisco).
Federal support acknowledged.

3 Kristofer T. Michalson, Andrew N. McIntyre, Ryne J. DeBo, Gregory D. Sempowski, J. Mark Cline, Thomas C. Register
Evaluation of monocyte polarization in long term non-human primate survivors of acute ionizing radiation exposure
Radiation Research Society 2017, Cancun, Mexico
Federal support was acknowledged.

4 Kristofer T. Michalson, Gregory Dugan, Ryne J. DeBo, Dalane Kitzman, J. Mark Cline, Thomas C. Register.
Effects of total body irradiation on echocardiographic phenotypes in male rhesus macaques
Radiation Research Society, 2017, Cancun, Mexico
Federal support was acknowledged.

5 Fanning KM¬, Pfisterer B, Davis AT, Presley TD, Williams IM, Wasserman DH, Cline JM, Kavanagh K. **Changes in microvascular density differentiate metabolic health outcomes i monkeys with prior radiation exposure and subsequent skeletal muscle ECM remodeling**
American Journal of Physiology – Regulatory, Integrative and Comparative Biology 2017 313(3) R290-297.
Radiation Research Society, October 14-19, 2017, Cancun, Mexico
Federal support was acknowledged.

6 Reddy A, Zhang J, Davis NS, Moffitt AB, Love CL, Waldrop A, Leppa S, Pasanen A, Meriranta L, Karjalainen-Lindsberg ML, Nørgaard P, Pedersen M, Gang AO, Høgdall E, Heavican TB, Lone W, Iqbal J, Qin Q, Li G, Kim SY, Healy J, Richards KL, Fedoriw Y, Bernal-Mizrachi L, Koff JL, Staton AD, Flowers CR, Paltiel O, Goldschmidt N, Calaminici M, Clear A, Gribben J, Nguyen E, Czader MB, Ondrejka SL, Collie A, Hsi ED, Tse E, Au-Yeung RKH, Kwong YL, Srivastava G, Choi WWL, Evens AM, Pilichowska M, Sengar M, Reddy N, Li S, Chadburn A, Gordon LI, Jaffe ES, Levy S, Rempel R, Tzeng T, Happ LE, Dave T, Rajagopalan D, Datta J, Dunson DB, Dave SS. **Genetic and Functional Drivers of Diffuse Large B Cell Lymphoma.** Cell. 2017 Oct 5;171(2):481-494.e15. doi: 10.1016/j.cell.2017.09.027. PubMed PMID: 28985567; PubMed Central PMCID: PMC5659841.
This paper utilized methods developed for this project.
Federal Support was acknowledged.

Long Term Follow-up of the Late Effects of Acute Radiation Exposure in Primates

Proposal Log Number PR141508

PI: J Mark Cline, DVM, PhD **Org:** Wake Forest Health Sciences **Award Amount:** $9,999,998

Study/Product Aim(s)

To study delayed effects of acute radiation exposure (DEARE) with a focus on our newly-described radiation-induced pathologies, through phenotypic and mechanistic studies, including:

1. Type 2 diabetes mellitus
2. Radiation-induced heart disease (RIHD)
3. Chronic immune impairment with restriction of the antigenic response repertoire; and
4. Radiation-specific genomic signatures underlying 1-3.

Approach

We will use unique nonhuman primate (NHP) resources, including a pre-existing long-term (10+ year) radiation-exposed survivor cohort and development of a prospective cohort allowing baseline pre-exposure assessments and 4 years of follow-up. Complementary immune, metabolic, and interventional studies to be done in mice. Priority will be given to pathways and strategies with high potential for translation to human exposures and outcomes.

Platforms \ Projects	Project 1: Diabetes Body composition, Redox Injury	Project 2: Radiation Induced Heart Disease Cardiac function and biomarkers	Project 3: Immune Recovery Thymopoiesis and immune function	Project 4: Genomic signatures Genomic basis for observed injury
NHP Survivor cohort Long-term outcomes	✓	✓	✓	✓
NHP Prospective Cohort Baseline-controlled	✓	✓	✓	✓
Mouse Studies and Treatments	✓		✓	
NHP Study Archives Tncluding Treatments		✓		

Figure 1. Schematic overview of the matrix relationship between populations of irradiated animals studied and investigative approaches used.

Accomplishments: NHP and mouse irradiation studies under way. Data collection and analysis in progress. Methods development in progress for some novel outcomes, as planned. Initial publications and abstracts, data presented at national meetings.

Timeline and Cost

Activities CY	15	16	17	18	19	20
Oversight/Core Primate Studies						
Proj 1 Diabetes						
Proj 2 Radiation/Heart Disease						
Proj 3 Immune Recovery						
Proj 4 Genomic sequencing and stem cell lines						
Estimated Budget ($K) ***Based on budget period 09/30/15 – 09/29/20. Budget period in ( ) after dollar amounts.***	1	2	3	4	5	

$2,150,541 (1)
$1,975,657 (2)
$2,030,283 (3)
$1,979,721 (4)
$1,863,796 (5)

Updated: July 14, 2017

Goals/Milestones

CY15 Goal – Program/Project "Kickoff"

☑ Regulatory approvals, establishment of admin structure, scheduling/ planning

☑ Animal acquisition and NHP quarantine & sampling/analysis, both cohorts

CY16 Goals – Prospective NHP studies begin, preliminary results presented nationally

☑ Exome sequencing and IPSCs from NHP studies (in progress)

☑ Irradiation of NHP prospective cohort and post-irradiation sampling/analysis for cardiac, redox, tissue composition, RNA profiling, and biomarker studies; presentation of early results (in progress)

☑ Mouse radiation studies: classic model

CY17 Goal – Continued NHP and mouse studies

☐ Mouse radiation studies: secondary model

☑ Continued analysis of NHP composition/biomarkers as above based on preliminary results; presentation of data

CY18 Goal – Continued NHP and mouse studies

☐ Mouse intervention study of HGH and IGF-1 (phenotypic)

☐ Continued analysis of NHP composition/biomarkers as above; publication

☐ Preliminary cell lineage data from NHPs presented nationally

CY19 Goal – Continued NHP and mouse studies

☐ Mouse intervention study of HGH and IGF-1 (functional)

☐ Primate studies as above continue; publication

CY20 Goal – Analysis and publication of results

☐ Mouse intervention study of HGH and IGF-1 (mechanistic)

☐ Necropsy of prospective cohort, analysis of terminal outcomes; publication

Comments/Challenges/ Issues/Concerns

- No changes to timeline at this time
- No changes in quarterly expenditures at this time

Budget Expenditure to Date

Projected Expenditure:
$2,150,541
GY 2015/2016
$1,975,657
GY 2017
$2,030,283
GY 2017

Attachment 2 - Abstract, World Congress of Gerontology and Geriatrics 2017

CONTROL ID: 2724125
TITLE: **Healthspan Measures in a Western Diet Conditioned, Irradiated Rodent Model of Accelerated Aging**
CURRENT CHOOSE A SESSION TOPIC: Biology of Aging | Chronic Conditions
AUTHORS (FIRST NAME, LAST NAME): Katie Fanning1, Christina Sherrill1, Ashley Davis1, Kylie Kavanagh1
INSTITUTIONS (ALL):
1. Pathology, Wake Forest School of Medicine, Winston-Salem, NC, United States.
ABSTRACT BODY:
Abstract Body (Required; Limit 250 words) : Deteriorating metabolic and physical function play significant roles in declining healthspan, however most animal models of aging rely on single gene mutations and few demonstrate translationally relevant multi-system decline. This study is the first to compare healthspan measures (metabolic and physical function) in rodents on a high-fat diet exposed to sub-lethal doses of whole body irradiation (IR). Four week old male and female C57/BL6 mice consuming a western diet (17% protein, 35% fat, 48% carbohydrate) were randomized as IR or control (CTL). At 8 weeks, IR mice received 7 Gy total body irradiation (Cobalt60, divided as 2 fractions delivered at 357 rad/min), with metabolic assessments evaluated at early (4 weeks) and late (12-16 weeks) post-exposure time-points (n=6/group/time-point). Delayed effects of irradiation included significantly higher fasting glucose at both time-points ($p \leq 0.01$) and worse insulin sensitivity (AUC_{ITT}; $p=0.10$) with comparable body weights between groups. Physical function outcomes were assessed late, with IR resulting in functional deficits that were 23% lower on average across 6 function tests (n=8-12/group). IR mice scored significantly worse on the 4-limb hang time test measuring muscular endurance ($p=0.02$) and on a composite performance score ($p<0.05$). Measures were covaried by body weight which was comparable between groups. As hypothesized, IR mice demonstrated poorer glucose metabolism and physical function relative to control non-irradiated mice. This work adds support to the use of IR mice as a model of accelerated aging. Objective 1: (Required) "After attending this session participants will be able to..." : Describe a battery of physical function tests for a rodent model of aging. Objective 2: (Required) "After attending this session participants will be able to..." : Identify the strengths and weaknesses of mice fed a Western diet plus non-lethal whole body irradiation as a model of accelerated aging. Statement of timeliness. Explain why your abstract is considered late breaking.: Our study describes a novel animal model of aging and outcomes relevant to the assessment of healthspan relevant to translational geroscience.

Supported by DOD W81XWH-15-1-0574 and NIH T32 OD010957

Attachment 3 - Radiation Research Society Abstract 2017

Evaluation of monocyte polarization in long term non-human primate survivors of acute ionizing radiation exposure

Kristofer T. Michalson, Andrew N. McIntyre, Ryne J. DeBo, Gregory D. Sempowski, J. Mark Cline, Thomas C. Register

Radiation induced fibrosis (RIF) is an incompletely understood, multi-organ, chronic adverse effect of ionizing radiation. Monocyte-macrophages may play a key role in the pathogenesis of RIF. Monocytes can become programmed into classical, intermediate, or non-classical phenotypes, classical monocytes are linked to pro-inflammatory responses, while intermediate monocytes have been linked to pro-fibrotic signaling and systemic pathologic fibrotic disorders. The role of classical and intermediate monocytes in RIF is currently unclear.

We evaluated the effects of prior total body irradiation (TBI) on monocyte polarization in male rhesus macaques. Subjects were 25 non-irradiated controls (9.63 ± 0.90 yrs old) and 67 irradiated macaques (8.69 ± 0.50 yrs old) exposed to a single dose of TBI (6.81± 0.12 Gy) at 4.25 ± 0.25 years old and were 1.72 to 11.3 years post-irradiation (mean interval 4.44 ± 0.41 years). Classical (CD14++, CD16-) and intermediate (CD14++, CD16+) monocyte percentages were quantified from gated total monocytes using flow cytometry. Total monocytes were not influenced by time since irradiation or dose, and proportions of classical and intermediate monocyte subsets did not differ by dose. However, the monocyte fractions obtained from monkeys 1-2 years post-irradiation had higher classical and intermediate monocyte percentages (15.08 ± 3.41%, 2.01 ± 0.36%) relative to controls (3.58 ± 1.10%, 1.02 ± 0.27%), and to monocytes 2-3 years (6.80 ± 2.31%, 1.23 ± 0.38%) and 3-5 years (5.63 ± 1.97%, 0.84 ± 0.17%) post-irradiation (ANOVA, $p < 0.05$). These data suggest that post-radiation recovery phenotypes of circulating monocytes may be initially shifted towards classical and intermediate pathways, later tapering towards more normal proportions. Prospective studies evaluating monocyte-macrophage polarization and co-localization with organ fibrosis are needed to confirm and extend these data. Ultimately, monocytes may shape the inflammatory and fibrotic response in RIF and monocyte programming presents a novel target opportunity for preventative therapies.

Supported by NIH/NIAID U19 AI67798, NIH T32 OD010957, and DOD W81XWH-15-1-0574

Attachment 4 - Radiation Research Society Abstract 2017

Effects of total body irradiation on echocardiographic phenotypes in male rhesus macaques

Kristofer T. Michalson, Gregory Dugan, Ryne J. DeBo, Dalane Kitzman, J. Mark Cline, Thomas C. Register.

Radiation induced heart disease is a serious delayed effect of acute radiation exposure (DEARE). The effects of total body irradiation on the heart are being evaluated longitudinally in a cohort of male rhesus macaques. Subjects are young adult (ages 6-8 years) male rhesus monkeys randomized to receive no radiation (Control, n=6) or 4 Gy total body irradiation (TBI, n=10) with longitudinal assessments of cardiac structure and function using echocardiography and Cardiac Magnetic Resonance Imaging (CMRI). Echocardiographic data from baseline and 20 week follow-up examinations are presented here. There were no significant differences between groups in any of the baseline echocardiographic measures of CV structure or function. At 20 weeks post TBI, no significant changes over time or differences between groups were observed in chamber diameters, fractional shortening, ejection fraction, cardiac output, aorta/left atrium ratio. Mitral annular tissue velocity parameters (e', a', or E/e', or e'/a') did not appear to change over time or differ by group. Early left ventricular diastolic filling velocity (E) was unchanged over time and there was no difference between groups. However, irradiated monkeys showed a significant increase in the late filling velocity (A) across the mitral valve ($p<0.05$ vs baseline) which differed from controls at 20 weeks ($p<0.01$), and the E/A ratio showed a non-significant trend ($p=0.12$) towards reduction, potentially indicative of impairment of LV relaxation. Color flow doppler echo indicated mitral regurgitation in one of the irradiated monkeys which was evident at 20 weeks post TBI but not at baseline. These preliminary results, ongoing evaluations of CMRI data, and planned evaluations of key biomarkers should provide useful insights into early stage intermediate phases in the development of RIHD phenotypes.
Supported by DOD W81XWH-15-1-0574, NIH U19 AI67798, and NIH T32 OD10957-36.

Am J Physiol Regul Integr Comp Physiol 313: R290–R297, 2017.
First published July 12, 2017; doi:10.1152/ajpregu.00108.2017.

RESEARCH ARTICLE | *Obesity, Diabetes and Energy Homeostasis*

Changes in microvascular density differentiate metabolic health outcomes in monkeys with prior radiation exposure and subsequent skeletal muscle ECM remodeling

K. M. Fanning,[1] B. Pfisterer,[1] A. T. Davis,[1] T. D. Presley,[2] I. M. Williams,[3] D. H. Wasserman,[3] J. M. Cline,[1] and K. Kavanagh[1]

[1]*Department of Pathology, Wake Forest University School of Medicine, Winston-Salem, North Carolina;* [2]*Department of Chemistry, Winston Salem State University, Winston-Salem, North Carolina; and* [3]*Department of Molecular Physiology and Biophysics, Vanderbilt University, Nashville, Tennessee*

Submitted 30 March 2017; accepted in final form 27 June 2017

Fanning KM, Pfisterer B, Davis AT, Presley TD, Williams IM, Wasserman DH, Cline JM, Kavanagh K. Changes in microvascular density differentiate metabolic health outcomes in monkeys with prior radiation exposure and subsequent skeletal muscle ECM remodeling. *Am J Physiol Regul Integr Comp Physiol* 313: R290–R297, 2017. First published July 12, 2017; doi: 10.1152/ajpregu.00108.2017.—Radiation exposure accelerates the onset of age-related diseases such as diabetes, cardiovascular disease, and neoplasia and, thus, lends insight into in vivo mechanisms common to these disorders. Fibrosis and extracellular matrix (ECM) remodeling, which occur with aging and overnutrition and following irradiation, are risk factors for development of type 2 diabetes mellitus. We previously demonstrated an increased incidence of skeletal muscle insulin resistance and type 2 diabetes mellitus in monkeys that had been exposed to whole body irradiation 5–9 yr prior. We hypothesized that irradiation-induced fibrosis alters muscle architecture, predisposing irradiated animals to insulin resistance and overt diabetes. Rhesus macaques (*Macaca mulatta*, $n = 7–8$/group) grouped as nonirradiated age-matched controls (Non-Rad-CTL), irradiated nondiabetic monkeys (Rad-CTL), and irradiated monkeys that subsequently developed diabetes (Rad-DM) were compared. Prior radiation exposure resulted in persistent skeletal muscle ECM changes, including a relative overabundance of collagen IV and a trend toward increased transforming growth factor-β1. Preservation of microvascular markers differentiated the irradiated diabetic and nondiabetic groups. Microvascular density and plasma nitrate and heat shock protein 90 levels were lower in Rad-DM than Rad-CTL. These results are consistent with a protective effect of abundant microvasculature in maintaining glycemic control within radiation-induced fibrotic muscle.

irradiation; type 2 diabetes; monkey; muscle; fibrosis; microvasculature

LONG-TERM EFFECTS OF IONIZING IRRADIATION include an increased risk of type 2 diabetes mellitus (T2DM), which is documented in patients exposed to radiation as children (16, 30) and patients treated with abdominal radiation for Hodgkin's lymphoma (33). After nuclear disasters such as Chernobyl and Hiroshima, increased rates of diabetes mellitus are reported, but the distribution of type 1 and type 2 diabetes is generally not clear (17, 46). Metabolic disturbance as a delayed effect of acute whole body irradiation (WBI) has also recently been documented in mice (34) and nonhuman primates (25).

The hallmark of metabolic decline and T2DM is peripheral insulin resistance in tissues such as skeletal muscle, which is responsible for the vast majority of insulin-stimulated peripheral glucose metabolism (7). While musculoskeletal damage has been described postirradiation, physical function has generally been the clinically studied outcome (41). Because of the importance of muscle metabolism and the pronounced effects of irradiation, it is imperative that the link between prior irradiation and the pathogenesis of metabolic disease be defined. There has been little attention to this important area of study.

Well-known biological effects of radiation exposure include the induction of reactive oxygen species and resulting inflammatory cascades, mediated by transforming growth factor-β1 (TGFβ1), which lead to tissue fibrosis (28, 36, 45). Fibrosis in skeletal muscle, defined as the accumulation of collagen and other extracellular matrix (ECM) components, is linked to overall metabolic dysfunction in humans (2, 37). Furthermore, mechanistic studies in rodent models demonstrate that skeletal muscle ECM expansion contributes to the development of insulin resistance (19–22). It is possible that fibrosis of skeletal muscle plays a role in the increased incidence of metabolic disease following WBI.

Balanced ECM synthesis and degradation are required for capillary bed maintenance (13). Radiation may disturb this balance, effectively decreasing accessible muscle metabolic surface area. Radiation causes a decrease in capillary density in cardiac muscle (39) and brain tissue (10); thus we hypothesized that skeletal muscle was likely similarly affected. Human studies have demonstrated that increased capillary density in skeletal muscle is associated with better health status (32), while loss of capillary density has been associated with disease states such as T2DM (11). Of particular importance in the development of metabolic disease, perhaps including that after radiation exposure, are dysfunctional microvascular responses to insulin, as extensively reviewed by Keske and others (26).

Taken together, current evidence suggests that skeletal muscle is an underappreciated organ for determination of metabolic health outcomes following irradiation. The relative importance

Address for reprint requests and other correspondence: K. Kavanagh, Dept. of Pathology, Section on Comparative Medicine, Wake Forest University Health Sciences, Medical Center Blvd., Winston-Salem, NC 27127 (e-mail: kkavanag@wakehealth.edu).

of architectural changes in muscle following irradiation and the ultimate progression of T2DM are not fully understood. Our previous work demonstrated that radiation exposure was associated with muscle tissue insulin resistance, even in objectively healthy, nondiabetic monkeys many years after exposure (25). Our aim for this study was to evaluate whether the architectural properties of skeletal muscle could explain why some irradiated animals with skeletal muscle insulin resistance differentiate into overt diabetes, while others do not. We tested the hypothesis that impaired muscle insulin action corresponds to remodeling of skeletal muscle architecture following radiation exposure.

MATERIALS AND METHODS

Animals

Rhesus macaques (*Macaca mulatta*) are part of the animal core within the consortium termed Radiation Countermeasures Centers of Research Excellence (RadCCORE), an animal resource used to collectively and collaboratively increase possible agents to detect, mitigate, and treat acutely people exposed to deterministic doses of radiation (www.radccore.org). As previously reported, these animals originated from different institutions and are survivors of exposure to a single sublethal 6.5- to 8.4-Gy dose of gamma WBI before their arrival at Wake Forest University (25). The radiation exposure occurred 5–9 yr before this study (Table 1). Animals (n = 7–8/group) that were nonirradiated controls (Non-Rad-CTL), irradiated nondiabetic monkeys (Rad-CTL), and irradiated monkeys that subsequently developed diabetes (Rad-DM) were further characterized for skeletal muscle architecture changes (see below). All animals were housed equivalently and had limited opportunities to exercise. All monkeys have been maintained since 2010 on a diet similar in nutritional profile to that typically consumed by people of Westernized nations (monkey diet 5L0P, LabDiet, St. Louis, MO), with the exception of the diabetic monkeys, which were switched to a standard laboratory chow diet (monkey diet 5038, LabDiet) immediately following diagnosis. Food was available ad libitum, and consumption was not quantitated.

Monkeys were diagnosed with diabetes according to the current American Diabetes criteria (1a) ranging from 1–4 yr before the start of this investigation All combination insulin administration was withdrawn from animals with diabetes for ≥24 h and regular insulin was withdrawn for ≥12 h before assessment. The monkeys were fasted for ≥12 h before assessment. Animals were anesthetized with intramuscular ketamine (10–15 mg/kg) to allow for sample and data collection. Each animal was weighed. Blood samples were obtained by percutaneous venipuncture of the femoral vein and collected in ethylenediaminetetraacetic acid (EDTA)-containing tubes. The blood was held on ice until it could be processed. After processing was completed, samples were stored at −80°C until analysis. Fasting blood glucose was determined by the glucose oxidase method and fasting plasma insulin concentration was determined by enzyme-linked immunosorbent assay (ELISA; Mercodia, Uppsala, Sweden) of the plasma sample. Whole blood was used to determine glycated hemoglobin (HbA1c) using high-performance liquid chromatography methodology (Primus PDQ, Primus Diagnostics, Kansas City, MO). Triglyceride (TG), high-density lipoprotein cholesterol, and total plasma cholesterol concentrations were measured enzymatically. Muscle biopsies were collected from the biceps femoris, fixed in 4% paraformaldehyde for 24 h, and then transferred to 70% ethyl alcohol until processing and embedding for histology or frozen in liquid nitrogen for protein extractions.

All animal procedures were performed according to the protocol approved by the Wake Forest University Institutional Animal Care and Use Committee in compliance with the US Department of Agriculture Animal Welfare Act and Animal Welfare Regulations (Animal Welfare Act as Amended; Animal Welfare Regulations) and according to recommendations in the *Guide for Care and Use of Laboratory Animals* (Institute for Laboratory Animal Research).

Extracellular Matrix

Collagens. Collagen I, III, and IV were assessed in formalin-fixed paraffin-embedded sections of muscle. Slides were stained using the BOND-MAX immunohistochemistry stainer (Leica). For heat-induced antigen retrieval, slides were incubated for 20 min in Epitope Retrieval Solution 2 (Leica). Slides were then incubated in anti-collagen I (1:100 dilution; ab138492, Abcam), anti-collagen III (1:100 dilution; ab6310, Abcam), or anti-collagen IV (1:600 dilution; ab6586, Abcam) antibody for 1 h. The Bond Polymer Refine Detection system was used to produce localized, visible 3,3′-diaminobenzidine (DAB) staining. Slides were finally dehydrated and cleared, and coverslips were mounted. Images were captured at ×200 total magnification using a camera (model DS-Ri2, Nikon) mounted on an upright, wide-field microscope (model AZ100M, Nikon). Image analysis was performed using a custom, automated macro in ImageJ. Briefly, DAB staining was isolated using color deconvolution, and then a variation of the isodata algorithm was used for automatic thresholding. Finally, the percent area of the section occupied by DAB staining was measured. An investigator blinded to group identity performed all image acquisition and analyses.

Table 1. *Demographic information and cardiometabolic end points for Non-Rad-CTL, Rad-CTL, and Rad-DM rhesus macaques*

	Group			*P* Value		
	Non-Rad-CTL	Rad-CTL	Rad-DM	Overall	Radiation effect	Diabetes effect
Age, yr	12.6 ± 0.4	13.1 ± 0.9	13.9 ± 1.0	0.52	N/A	N/A
Age at exposure, yr	N/A	4.24 ± 0.67	5.04 ± 0.76	0.44	N/A	N/A
Radiation dose, Gy	N/A	7.14 ± 0.21	6.98 ± 0.20	0.57	N/A	N/A
Time since irradiation, yr	N/A	8.9 ± 0.2	9.0 ± 0.3	0.76	N/A	N/A
Body wt, kg	14.1 ± 1.3[a]	8.9 ± 0.6[b]	14.2 ± 0.9[a]	<0.001	0.10	0.08
Waist circumference, cm	45.3 ± 3.1[a,b]	35.1 ± 2.5[a]	46.7 ± 3.6[b]	0.03	0.31	0.13
Blood glucose, mg/dl	62 ± 6[a]	66 ± 4[a]	237 ± 31b	<0.001	0.02	<0.001
Insulin, μIU/ml	35.3 ± 9.6[a,b]	14.8 ± 5.0[a]	62.7 ± 31.3[b]	0.02	0.37	0.09
Hemoglobin A1c, %	4.5 ± 0.8[a]	4.6 ± 0.7[a]	9.5 ± 0.7[b]	<0.001	0.11	0.0002
Blood TG, mg/dl	45.6 ± 3.7[b]	37.0 ± 2.9[b]	154.1 ± 26.5[a]	<0.001	0.35	<0.001
HDL cholesterol, mg/dl	72.9 ± 4.4[a,b]	78.8 ± 4.3[a]	57.1 ± 5.8[b]	0.02	0.55	0.005
Systolic blood pressure, mmHg	139.9 ± 7.5	153.1 ± 13.4	141.5 ± 10.1	0.69	0.58	0.72
Diastolic blood pressure, mmHg	73.8 ± 3.4	72.7 ± 5.4	70.0 ± 3.7	0.80	0.61	0.51

Values are means ± SE. Non-Rad-CTL, nonirradiated nondiabetic, Rad-CTL, irradiated nondiabetic, Rad-DM, irradiated type 2 diabetic; TG, triglycerides. Different superscripted letters (a, b) indicate significant difference between groups (P < 0.05).

TGFβ. TGFβ1 in monkey muscle was measured by ELISA. Quantities in muscle lysates were determined using the human TGFβ1 ELISA (Quantikine kit, R & D Systems) according to the manufacturer's instructions. Samples were acid-activated using a protocol provided by the manufacturer. Quantities were estimated based on a standard curve generated with recombinant TGFβ1.

Matrix metalloproteinase activity. Gelatin zymography was performed to measure matrix metalloproteinase 9 (MMP9) activity. Monkey skeletal muscle samples were mechanically homogenized (Bullet Blender, Next Advance) in a pH 7.5 buffer containing 100 mM Tris·HCl, 10 mM EDTA, and 0.5% Triton X-100. Homogenates were centrifuged at 13,000 rpm for 20 min at 4°C. Supernatants (500 μg of protein) were incubated with gelatin-Sepharose beads for 2 h at 4°C to purify and concentrate gelatinases. After three washes, gelatin-Sepharose beads were resuspended in nonreducing Laemmli buffer and loaded onto 10% zymogram gels for electrophoresis. Conditioned medium from HT-1080 cells was used as a positive control. After electrophoresis, gels were washed in a renaturing buffer (Invitrogen, Carlsbad, CA) to restore gelatinolytic activity. Gels were then incubated in a developing buffer (Invitrogen) overnight at 4°C. Finally, the gels were stained with SimplyBlue SafeStain (Thermo Fisher, Waltham, MA) to reveal areas of gelatin digestion, which appear clear against a blue background. The gels were then imaged, and digestion band intensity was quantified by densitometry.

Skeletal muscle TGs. Muscle TG content was measured as previously described (24).

Microvasculature-Related Parameters

$CD31^+$ endothelial cells. Slides of muscle tissue were embedded for immunohistochemistry. $CD31^+$ endothelial cells were stained with PECAM-1 (M-20) goat anti-mouse polyclonal antibody (Santa Cruz Biotechnology). Blinded assessors counted in duplicate the total number of cells that stained positively for CD31 in 20 fields at × 20 magnification. Representative images are shown in Fig. 2, *C–E*.

Plasma nitrate. Nitrate (NO_3) levels were measured in the plasma samples using an NOx analyzer (model eNO-20, Eicom) according to the manufacturer's instructions, as previously described (40).

Vascular endothelial growth factors. Vascular endothelial growth factor (VEGF) and tumor necrosis factor-related ligand 1A (TNFR1A) in muscle tissue were measured using ELISA (MyBioSource, San Diego, CA) according to the manufacturer's protocols.

Endothelial nitric oxide synthase. Quantification of nitric oxide (NO) synthase [endothelial NO synthase (eNOS)] mRNA in muscle was measured by quantitative real-time polymerase chain reaction (qRT-PCR). Primer sequences for eNOS were as follows: 5′-gaaggctggcatctggaa-3′ (forward) and 5′-cagagccctggccttttc-3′ (reverse). Data are expressed in arbitrary units normalized by the qRT-PCR signal obtained in the same cDNA preparation for glyceraldehyde 3-phosphate dehydrogenase (GAPDH) mRNA. The primer sequences used for GAPDH were as follows: 5′-caccaactgcttagcacccc-3′ (forward) and 5′-tggtcatgagtccttccacg-3′ (reverse).

Heat shock protein. Heat shock protein (HSP) 90 (HSP90) in muscle homogenate was quantified in duplicate using a sandwich ELISA with the HSP90 Alpha ELISA kit (StressMarq Biosciences, Victoria, BC, Canada) according to the manufacturer's instructions.

Data Analysis

Data were first inspected for significant outliers and winsorized as necessary to three standard deviations. Data were also inspected for deviations from normality. Nonnormal parameters were log-transformed if required to achieve statistical assumptions of normality. Values are means ± SE. Group differences were analyzed using one-way ANOVA with α-level set at 0.05 for statistical significance and $P = 0.10$ for trends. We additionally examined for the main effects of radiation and diabetes by ANOVA. Outcome measures were covaried by the monkeys' body weights at assessment. Post hoc analyses were conducted using Tukey's honest significant differences testing. Correlation coefficients were determined by Pearson's R statistics for association. All statistical testing was performed using Statistica v10 (StatSoft, Carlsbad, CA).

RESULTS

Demographic and metabolic characteristics of Non-Rad-CTL, Rad-CTL, and Rad-DM monkeys are shown in Table 1. There were no significant differences in age between groups. Among irradiated monkeys there were no significant differences in irradiation dose, age at irradiation, and years since irradiation. The mean post-WBI delay to assessment was 9.0 yr, which is the human equivalent of ~20 yr, a significant period of life that would span childhood to adulthood. In all subsequent analyses, dose of irradiation, time since irradiation, and age at irradiation were not related to any outcome measures. No results violated the outlier criterion.

Rad-DM monkeys were neither overweight nor obese, and their body weight was comparable to that of Non-Rad-CTL animals. Rad-CTL monkeys were significantly leaner (~40%) than the other groups. Waist circumference showed a pattern similar to body weight (Table 1), as did body fat percentage, which was previously documented by computed tomography (25). No differences in systolic or diastolic blood pressure were noted between groups. Other related health and inflammatory markers within this cohort have been previously published (6, 25).

Diabetic monkeys were hyperglycemic and hyperinsulinemic, as expected. The degree of hyperinsulinemia was highly variable within the diabetic group, reflecting different stages of compensatory insulin secretion. As expected, HbA1C and plasma TG levels were significantly higher in diabetic than nondiabetic monkeys. Circulating insulin levels were significantly lower in Rad-CTL than Rad-DM monkeys likely due to their decreased adiposity (18). Previous work within this cohort included mixed meal tolerance testing, intravenous glucose tolerance testing, and skeletal muscle insulin signaling. Briefly, as expected, tolerance test results were significantly worse in diabetic than nondiabetic animals. Interestingly, all irradiated animals showed poorer skeletal muscle insulin signaling response, as evidenced by decreased phosphorylation of protein kinase B and insulin receptor substrate-1 in insulin-stimulated muscle biopsies (25).

Years after radiation exposure, monkeys had a relative overabundance of collagen IV deposition, as reflected by a significantly greater ratio of collagen IV to collagen I (Fig. 1*A*; $P = 0.04$) and a trend toward an increase in TGFβ1 (Fig. 1*B*; $P = 0.10$). There were no differences between groups in ECM breakdown as measured by MMP9 activity (Table 2). Muscle TG content and absolute collagen IV deposition were greater in skeletal muscle of Rad-DM than nondiabetic monkeys (Table 2).

$CD31^+$ cells were more abundant (Fig. 2*A*; $P = 0.02$) and plasma NO_3 levels were higher (Fig. 2*B*; $P = 0.04$) in Rad-CTL than Rad-DM animals. Abundance of $CD31^+$ cells was 150% greater and NO_3 levels were 160% higher in Rad-CTL than Non-Rad-CTL animals. The NO_3 results were repeated in an additional cohort of monkeys consistently demonstrating higher values in Rad-CTL than Non-Rad-CTL animals (data not shown). VEGF and TNFR1A showed no significant differences between groups (Table 3). In addition, there were no

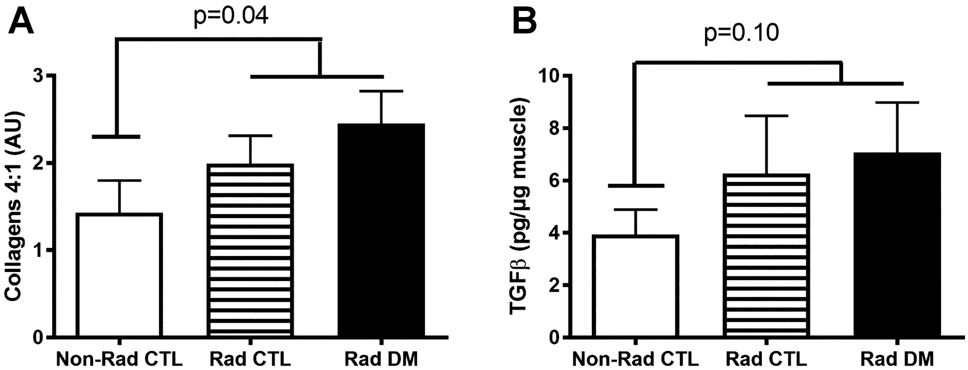

Fig. 1. *A*: radiation exposure leads to relative overabundance of collagen IV in skeletal muscle of rhesus macaques exposed to radiation years earlier. Non-Rad-CTL, control nonirradiated nondiabetic; Rad-CTL, irradiated nondiabetic; Rad-DM, irradiated type 2 diabetic; AU, arbitrary units. *B*: levels of the master signaling molecule transforming growth factor-β (TGFβ) tend to be higher (P = 0.1) in muscle with prior radiation exposure, consistent with altered collagen deposition in *A*. Values are means ± SE; n = 8 in each group.

significant differences in the quantity of eNOS mRNA (Table 3). HSP90 levels were significantly lower in muscle from irradiated monkeys (Fig. 3*A*). Both HSP90 and TNFR1A positively correlated with plasma NO_3 [$r = 0.44$, $P = 0.04$ (Fig. 3*B*) and $r = 0.44$, $P = 0.05$ (Fig. 3*C*)].

The relationship between groups with respect to MMP9 activity and TNFR1A is similar to the group pattern for $CD31^+$ endothelial cells and NO_3. In Rad-CTL monkeys, mean MMP9 activity was 1.8-fold greater and mean TNFR1A level was 1.7-fold greater, which is similar to the 2- to 4-fold greater abundance of $CD31^+$ cells and NO_3 level, than in Rad-DM.

Evidence of an interaction between ECM and microvasculature-related indexes is demonstrated as TGFβ1 correlated negatively with both proangiogenic VEGF and the eNOS chaperone HSP90 [$r = -0.42$, $P = 0.04$ (Fig. 4*A*) and $r = -0.51$, $P = 0.01$ (Fig. 4*B*)]. Additionally, greater muscle lipid content was associated with increased fibrotic signaling and increased collagen IV deposition [$r = 0.48$, $P = 0.018$ (Fig. 4*C*) and $r = 0.49$, $P = 0.019$ (Fig. 4*D*)].

DISCUSSION

Our study is the first to examine the late effects of irradiation-induced changes in skeletal muscle architecture and their relationship with metabolic health. It is unique in the description of these changes in nonhuman primates, a model that very closely matches the pathogenesis of human metabolic disease (44). The preservation of microvascular abundance in nondiabetic monkeys exposed to radiation is consistent with previous studies showing a link between capillary density and metabolic disease (1, 11, 35). We also demonstrate that radiation is associated with changes in muscle ECM and leads to suppression of HSP90 levels many years after radiation exposure. This reduction in HSP90 may reduce skeletal muscle perfusion through decreased eNOS activity in response to insulin (42).

Microvasculature

Staining for the endothelial cell marker CD31 showed that microvascular abundance differentiated diabetic and nondiabetic irradiated animals, as Rad-DM had significantly fewer $CD31^+$ cells than Rad-CTL. Surprisingly, there were no significant differences in VEGF and TNFR1A between groups, suggesting a similar balance of vascular remodeling between groups. Studies evaluating delayed effects of irradiation on skeletal muscle microvascular abundance are limited. Mouse studies suggest that the response is dependent on dose. In mouse cardiac muscle, capillary density decreased following exposure to radiation at doses comparable to the level used in our study (≥8 Gy) (39). Conversely, Mathias et al. found an increase in $CD31^+$ cells in mouse cardiac muscle following exposure to a low (2-Gy) dose of radiation (29).

There is evidence that T2DM is associated with reduced insulin-mediated muscle capillary recruitment even without changes in capillary density (4). Therefore, indicators of endothelial function were further examined in this study. Capillary endothelial cells contain an enzyme, NO synthase (NOS), that produces NO in response to shear stress and growth factors. Insulin increases eNOS activity in endothelial cells to promote microvascular recruitment, which subsequently improves hormone (e.g., insulin) and nutrient (e.g., glucose) delivery to tissues (5). There were no significant differences in eNOS gene expression between groups. There was, however, a significant decrease in plasma NO_3, an NO metabolite, in Rad-DM monkeys. This may suggest decreased function of eNOS in Rad-DM animals, which is in agreement with the

Table 2. *Effects of radiation and diabetes on mean abundance of collagen, TG levels, and MMP activity in skeletal muscle of Non-Rad-CTL, Rad-CTL, and Rad-DM rhesus macaques*

	Group			*P* Value		
	Non-Rad-CTL	Rad-CTL	Rad-DM	Overall	Radiation effect	Diabetes effect
Collagen IHC, %stained						
Type I	5.79 ± 0.72	4.50 ± 0.34	4.48 ± 0.83	0.27	0.09	0.50
Type III	3.47 ± 0.58	4.44 ± 0.59	3.44 ± 0.61	0.38	0.50	0.46
Type IV	8.78 ± 0.67	8.29 ± 0.43	9.86 ± 0.64	0.19	0.75	0.04
MMP9 activity, AU	0.90 ± 0.34	1.35 ± 0.37	0.74 ± 0.26	0.39	0.80	0.32
Muscle TG, μg/mg protein	64.55 ± 12.7[a]	32.12 ± 3.54[a]	90.18 ± 25.19[b]	0.04	0.87	0.04

Values are means ± SE. MMP9, matrix metalloproteinase 9; AU, arbitrary units. Different superscripted letters (a and b) indicate significant difference between groups ($P < 0.05$).

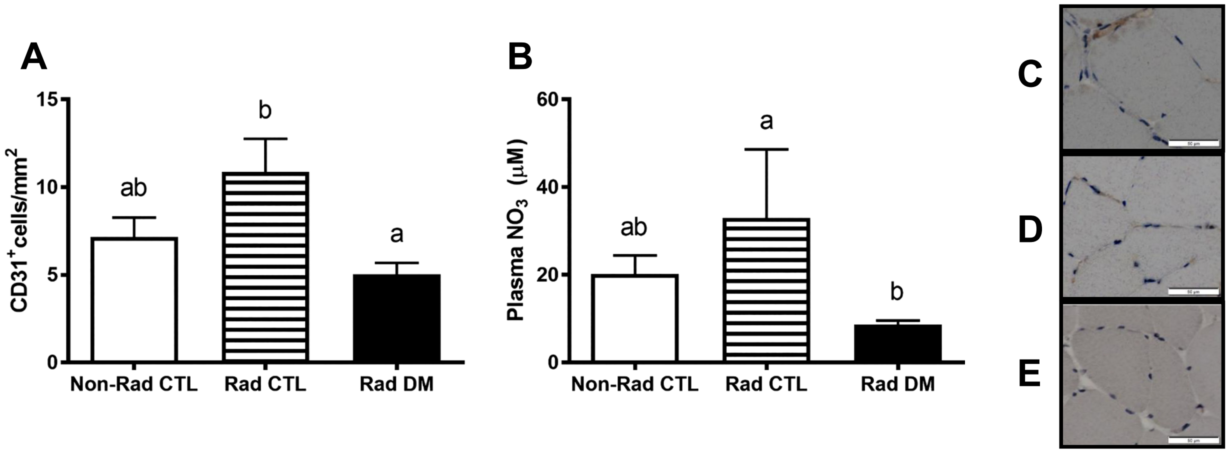

Fig. 2. *A*: CD31$^+$ endothelial cell counts per high-powered field were used as a biomarker of capillary density in skeletal muscle. Data show that protection from type 2 diabetes after radiation exposure was accompanied by greater capillary density in muscle. *B*: plasma nitrate (NO_3) was significantly lower in monkeys with type 2 diabetes than nondiabetic monkeys. Values are means ± SE; $n = 8$ in each group. Different superscript letters (a and b) denote significant difference between groups ($P < 0.05$). *C, D,* and *E*: representative images of CD31$^+$ endothelial cell immunohistochemistry in Non-Rad-CTL, Rad-CTL, and Rad-DM, respectively. Magnification ×10; scale bar = 100 μm.

finding of Kashyap et al. that NOS activity increased 2.5-fold in controls in response to insulin; however, insulin failed to stimulate NOS activity in humans with diabetes (23).

HSP90 influences perfusion by associating with eNOS and augmenting the production of NO (9). HSP90 levels were significantly lower in muscle tissue of irradiated than nonirradiated monkeys and also significantly lower in Rad-DM monkeys than both groups without diabetes. In rats that developed fibrosing alveolitis following irradiation, HSP90 levels decreased >90% in lung parenchymal cells (14). One mechanism for decreased amounts of HSP90 in irradiated tissues could be repressed gene expression by p53, as noted in UV-irradiated cells (47). Microvascular function is impaired in proinflammatory states such as obesity and aging (26). Here we provide evidence of reduced HSP90 as a possible mechanism of endothelial impairment and predisposition to insulin resistance following radiation exposure. A limitation to our study is lack of direct measurement and comparison of microvascular responsiveness between groups.

Extracellular Matrix

TGFβ1 is widely recognized as a major regulating cytokine involved in tissue wound healing and fibrosis. It is involved in the deposition of fibrotic products through proliferation of fibroblasts and enhanced collagen synthesis and negatively influences the breakdown of these products (28). We observed a trend toward increased amounts of TGFβ1 in the irradiated monkeys, which suggests an ongoing initiation of fibrosis, consistent with documented ongoing inflammatory stimuli previously reported in this same cohort of monkeys (6).

Collagen IV is associated with the pericapillary basement membrane (BM) in tissues (27). We found significantly greater collagen IV deposition in the muscle of diabetic than nondiabetic monkeys. This is not surprising, as collagen IV deposition and BM thickening are known microvascular characteristics of patients with chronic diabetes, most clinically notable as diabetic retinopathies and nephropathies (43). Suggestive of ECM remodeling, all irradiated monkeys had a relative overabundance of collagen IV, consistent with previous findings acutely with low doses of radiation in mouse cardiac muscle (29) and chronically in lung tissue following larger doses of radiation (31). Kang et al. demonstrated that inflammatory effects from a high-fat diet lead to greater collagen IV deposition and subsequent insulin resistance in mice (19). Additionally, a genetic deletion of MMP9, a collagen-degrading enzyme, exacerbates collagen IV deposition and insulin resistance in the skeletal muscle in these mice (21).

BM thickening in skeletal muscle is also seen with advancing age and senescence (3). For example, key BM molecules (collagen IVa1, collagen IVa2, and laminin 2) were increased approximately twofold in myofibroblasts differentiated from 32-mo-old rats compared with those from 3-mo-old rats (48). As age is the greatest risk factor for diabetes development, the parallels in these muscle changes are of note. Radiation is considered a model for aging, as it accelerates the onset of many age-related diseases such as heart failure and cancer (38),

Table 3. *Effect of radiation and diabetes on mean perfusion-related parameters in skeletal muscle*

	Group			*P* Value		
	Non-Rad-CTL	Rad-CTL	Rad-DM	Overall	Radiation effect	Diabetes effect
VEGF, pg/μg muscle protein	11.45 ± 2.11	10.05 ± 1.18	11.49 ± 1.52	0.78	0.74	0.71
TNFR1A, pg/μg muscle protein	7.39 ± 0.98	13.2 ± 3.68	7.85 ± 2.91	0.13	0.34	0.53
ln eNOS, AU	1.012 ± 0.28	1.069 ± 0.30	1.634 ± 0.69	0.90	0.93	0.67

Values are means ± SE. VEGF, vascular endothelial growth factor; TNFR1A, tumor necrosis factor-related ligand 1A; eNOS, endothelial nitric oxide synthase; ln, natural log.

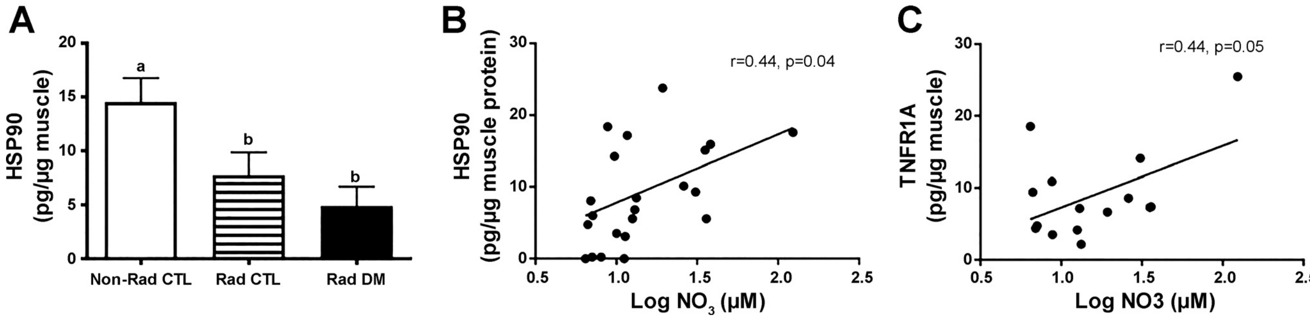

Fig. 3. Heat shock protein (HSP) 90 associates with endothelial nitric oxide synthase (eNOS) to improve its function. *A*: HSP90 levels were suppressed by radiation eposure ($P = 0.01$ for Non-Rad-CTL vs. Rad-CTL and RAD-DM), which were most reduced in T2DM monkeys ($P = 0.03$ for Non-Rad-CTL and Rad-CTL vs. Rad-DM). Values are means ± SE; $n = 8$ in each group. Different superscript letters (a and b) denote significant difference between groups ($P < 0.05$). *B* and *C*: HSP90 significantly correlated with plasma nitrate (NO_3) and tumor necrosis factor-related ligand 1A (TNFR1A).

thereby possibly further broadening the scope of relevance of our findings to the natural aging processes and associated age-related metabolic dysfunction. Illustrative of this accelerated aging is the average age of T2DM diagnosis of 13 yr in our cohort vs. 19 yr in other colonies (15).

High-dose therapeutic radiation is prevalent, and the persistent threat of malicious or accidental radiation exposure continues to exist; therefore, results of this study are of significant public health interest. The monkeys in our study are long-term survivors of WBI and, as such, present a survivor bias that may provide particular relevance to humans who survive to develop delayed late effects following radiation exposures. Additionally, the accelerated phenotype of metabolic disease noted in clinical trials is evident within our cohort. It is likely that our model shares relevant pathogenesis, perhaps an exaggerated version, of radiation therapy-associated increased T2DM risk.

This study is particularly novel, in that it utilizes a nonhuman primate model of delayed adverse effects of radiation. This model is superior, in that it has more humanlike muscle architecture than rodent models (8). The translatability of our findings is further bolstered by the dietary environment of the monkeys, which is similar to the diets consumed by people in Westernized nations. Our study is limited by the variability of individual monkey's histories, small sample size, lack of quantification of food intake and physical activity, and unavailability of a nonirradiated diabetic control group for comparison. The possibility of other subclinical disease, such as cardiac fibrosis, which has been described in animals within this cohort (6), exists in our irradiated monkeys. It is possible that fibrosis of other metabolically active tissues, such as fat, could influence T2DM disease risk of the monkeys within this study.

Perspectives and Significance

Our study provides evidence that irradiation leads to persistent ECM muscle changes many years after radiation exposure.

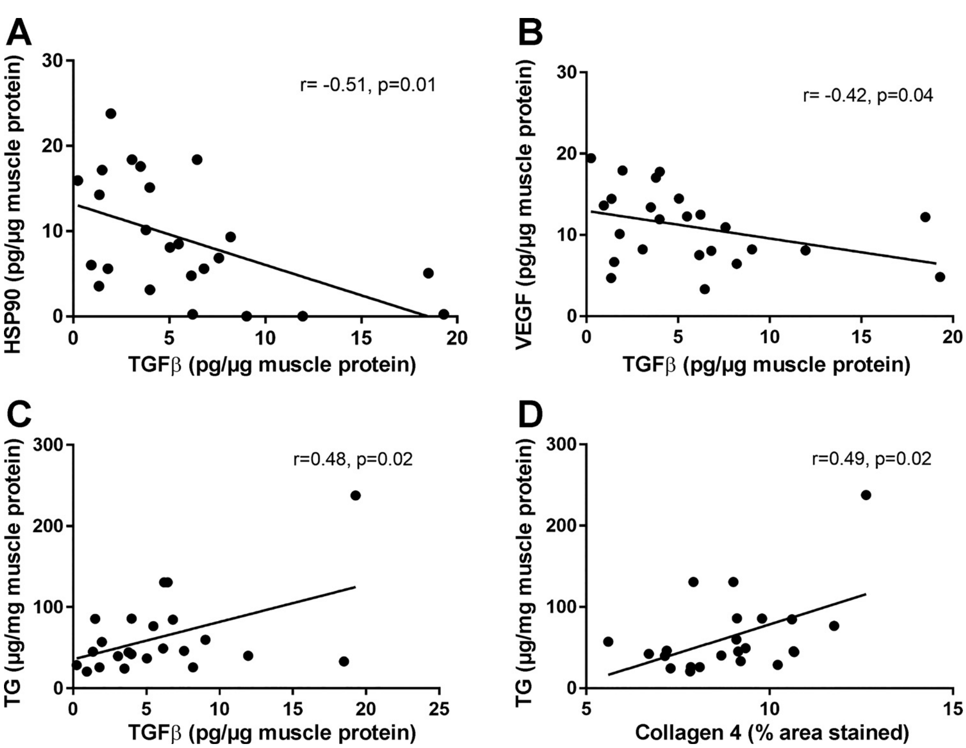

Fig. 4. *A* and *B*: greater fibrotic signaling, as indicated by TGFβ levels in skeletal muscle, correlated with less-abundant HSP90 and vascular endothelial growth factor (VEGF). *C* and *D*: increasing abundance of TGFβ1 and resultant collagen IV deposition in skeletal muscle were associated with greater muscle lipid, as measured by muscle triglyceride (TG) content.

This remodeling is associated with muscle lipid content and variable microvascular abundance. Maintained or enhanced microvascular abundance in muscle appears to protect against radiation-induced metabolic disease in the face of ECM changes and decreased HSP90 levels. Future studies will include prospective monitoring and evaluation of irradiated monkeys to determine when and how the trend for muscle metabolic defects progresses to eventually overwhelm the ability to metabolize glucose. These studies will include functional measurements of perfusion to build on the noteworthy architectural differences in skeletal muscle microvasculature between groups within this study. Additionally, elucidation of potential therapeutic targets, such as HSP induction and other avenues, to enhance muscle perfusion or decrease fibrosis will be pursued with an aim to alleviate the predisposition for and prevent the progression to overt T2DM following radiation exposure.

ACKNOWLEDGMENTS

We are grateful for the valuable contributions of colleagues at Radiation Countermeasures Centers of Research Excellence (RadCCORE) and for the donations of irradiated nonhuman primates from our colleagues at the Armed Forces Radiobiology Research Institute, the University of Maryland, and the University of Chicago. We also thank Mickey Flynn.

GRANTS

This study was supported by National Institute of Allergy and Infectious Diseases Grant U19 AI-67798 through RadCCORE to Principal Investigator N. Chao (Duke University). Additional support to authors was provided by National Institutes of Health Grants T32 OD-010957 (to K. M. Fanning) and T35 OD-010946 (to B. Pfisterer).

DISCLOSURES

No conflicts of interest, financial or otherwise, are declared by the authors.

AUTHOR CONTRIBUTIONS

D.H.W. and K.K. conceived and designed research; K.M.F. and K.K. analyzed data; K.M.F. and I.M.W. prepared figures; K.M.F. and I.M.W. drafted manuscript; K.M.F., I.M.W., D.H.W., J.M.C., and K.K. edited and revised manuscript; K.M.F. and K.K. approved final version of manuscript; B.P., A.T.D., T.D.P., I.M.W., and K.K. performed experiments; K.K. interpreted results of experiments.

REFERENCES

1. **Akerstrom T, Laub L, Vedel K, Brand CL, Pedersen BK, Lindqvist AK, Wojtaszewski JFP, Hellsten Y.** Increased skeletal muscle capillarization enhances insulin sensitivity. *Am J Physiol Endocrinol Metab* 307: E1105–E1116, 2014. doi:10.1152/ajpendo.00020.2014.

1a. **American Diabetes Association.** 2. Classification and diagnosis of diabetes. *Diabetes Care* 38 *Suppl* 1: S8–S16, 2015. doi:10.2337/dc15-S005.

2. **Berria R, Wang L, Richardson DK, Finlayson J, Belfort R, Pratipanawatr T, De Filippis EA, Kashyap S, Mandarino LJ.** Increased collagen content in insulin-resistant skeletal muscle. *Am J Physiol Endocrinol Metab* 290: E560–E565, 2006. doi:10.1152/ajpendo.00202.2005.
3. **Bigler M, Koutsantonis D, Odriozola A, Halm S, Tschanz SA, Zakrzewicz A, Weichert A, Baum O.** Morphometry of skeletal muscle capillaries: the relationship between capillary ultrastructure and ageing in humans. *Acta Physiol (Oxf)* 218: 98–111, 2016. doi:10.1111/apha.12709.
4. **Clerk LH, Vincent MA, Barrett EJ, Lankford MF, Lindner JR.** Skeletal muscle capillary responses to insulin are abnormal in late-stage diabetes and are restored by angiotensin-converting enzyme inhibition. *Am J Physiol Endocrinol Metab* 293: E1804–E1809, 2007. doi:10.1152/ajpendo.00498.2007.
5. **Coggins M, Lindner J, Rattigan S, Jahn L, Fasy E, Kaul S, Barrett E.** Physiologic hyperinsulinemia enhances human skeletal muscle perfusion by capillary recruitment. *Diabetes* 50: 2682–2690, 2001. doi:10.2337/diabetes.50.12.2682.
6. **DeBo RJ, Lees CJ, Dugan GO, Caudell DL, Michalson KT, Hanbury DB, Kavanagh K, Cline JM, Register TC.** Late effects of total-body gamma irradiation on cardiac structure and function in male rhesus macaques. *Radiat Res* 186: 55–64, 2016. doi:10.1667/RR14357.1.
7. **DeFronzo RA, Tripathy D.** Skeletal muscle insulin resistance is the primary defect in type 2 diabetes. *Diabetes Care* 32 *Suppl* 2: S157–S163, 2009. doi:10.2337/dc09-S302.
8. **Feng X, Zhang T, Xu Z, Choi SJ, Qian J, Furdui CM, Register TC, Delbono O.** Myosin heavy chain isoform expression in the vastus lateralis muscle of aging African green vervet monkeys. *Exp Gerontol* 47: 601–607, 2012. doi:10.1016/j.exger.2012.05.007.
9. **García-Cardeña G, Fan R, Shah V, Sorrentino R, Cirino G, Papapetropoulos A, Sessa WC.** Dynamic activation of endothelial nitric oxide synthase by Hsp90. *Nature* 392: 821–824, 1998. doi:10.1038/33934.
10. **Greene-Schloesser D, Robbins ME, Peiffer AM, Shaw EG, Wheeler KT, Chan MD.** Radiation-induced brain injury: a review. *Front Oncol* 2: 73, 2012. doi:10.3389/fonc.2012.00073.
11. **Groen BBL, Hamer HM, Snijders T, van Kranenburg J, Frijns D, Vink H, van Loon LJC.** Skeletal muscle capillary density and microvascular function are compromised with aging and type 2 diabetes. *J Appl Physiol (1985)* 116: 998–1005, 2014. doi:10.1152/japplphysiol.00919.2013.
13. **Gustafsson T.** Vascular remodelling in human skeletal muscle. *Biochem Soc Trans* 39: 1628–1632, 2011. doi:10.1042/BST20110720.
14. **Haase MG, Geyer P, Fitze G, Baretton GB.** Down-regulation of heat shock protein HSP90ab1 in radiation-damaged lung cells other than mast cells. *J Histochem Cytochem* 62: 355–368, 2014. doi:10.1369/0022155414529133.
15. **Hansen BC, Newcomb JD, Chen R, Linden EH.** Longitudinal dynamics of body weight change in the development of type 2 diabetes. *Obesity (Silver Spring)* 21: 1643–1649, 2013. doi:10.1002/oby.20292.
16. **Holmqvist AS, Olsen JH, Andersen KK, de Fine Licht S, Hjorth L, Garwicz S, Moëll C, Anderson H, Wesenberg F, Tryggvadottir L, Malila N, Boice JD Jr, Hasle H, Winther JF; ALiCCS Study Group.** Adult life after childhood cancer in Scandinavia: diabetes mellitus following treatment for cancer in childhood. *Eur J Cancer* 50: 1169–1175, 2014. doi:10.1016/j.ejca.2014.01.014.
17. **Ito C.** Trends in the prevalence of diabetes mellitus among Hiroshima atomic bomb survivors. *Diabetes Res Clin Pract* 24, *Suppl*: S29–S35, 1994. doi:10.1016/0168-8227(94)90224-0.
18. **Kahn SE, Hull RL, Utzschneider KM.** Mechanisms linking obesity to insulin resistance and type 2 diabetes. *Nature* 444: 840–846, 2006. doi:10.1038/nature05482.
19. **Kang L, Ayala JE, Lee-Young RS, Zhang Z, James FD, Neufer PD, Pozzi A, Zutter MM, Wasserman DH.** Diet-induced muscle insulin resistance is associated with extracellular matrix remodeling and interaction with integrin-$\alpha_2\beta_1$ in mice. *Diabetes* 60: 416–426, 2011. doi:10.2337/db10-1116.
20. **Kang L, Lantier L, Kennedy A, Bonner JS, Mayes WH, Bracy DP, Bookbinder LH, Hasty AH, Thompson CB, Wasserman DH.** Hyaluronan accumulates with high-fat feeding and contributes to insulin resistance. *Diabetes* 62: 1888–1896, 2013. doi:10.2337/db12-1502.
21. **Kang L, Mayes WH, James FD, Bracy DP, Wasserman DH.** Matrix metalloproteinase 9 opposes diet-induced muscle insulin resistance in mice. *Diabetologia* 57: 603–613, 2014. doi:10.1007/s00125-013-3128-1.
22. **Kang L, Mokshagundam S, Reuter B, Lark DS, Sneddon CC, Hennayake C, Williams AS, Bracy DP, James FD, Pozzi A, Zent R, Wasserman DH.** Integrin-linked kinase in muscle is necessary for the development of insulin resistance in diet-induced obese mice. *Diabetes* 65: 1590–1600, 2016. doi:10.2337/db15-1434.
23. **Kashyap SR, Roman LJ, Lamont J, Masters BSS, Bajaj M, Suraamornkul S, Belfort R, Berria R, Kellogg DL Jr, Liu Y, DeFronzo RA.** Insulin resistance is associated with impaired nitric oxide synthase activity in skeletal muscle of type 2 diabetic subjects. *J Clin Endocrinol Metab* 90: 1100–1105, 2005. doi:10.1210/jc.2004-0745.
24. **Kavanagh K, Davis MA, Zhang L, Wilson MD, Register TC, Adams MR, Rudel LL, Wagner JD.** Estrogen decreases atherosclerosis in part by reducing hepatic acyl-CoA:cholesterol acyltransferase 2 (ACAT2) in monkeys. *Arterioscler Thromb Vasc Biol* 29: 1471–1477, 2009. doi:10.1161/ATVBAHA.109.191825.
25. **Kavanagh K, Dendinger MD, Davis AT, Register TC, DeBo R, Dugan G, Cline JM.** Type 2 diabetes is a delayed late effect of whole-body irradiation in nonhuman primates. *Radiat Res* 183: 398–406, 2015. doi:10.1667/RR13916.1.

26. **Keske MA, Premilovac D, Bradley EA, Dwyer RM, Richards SM, Rattigan S.** Muscle microvascular blood flow responses in insulin resistance and ageing. *J Physiol* 594: 2223–2231, 2014.
27. **LeBleu VS, Macdonald B, Kalluri R.** Structure and function of basement membranes. *Exp Biol Med (Maywood)* 232: 1121–1129, 2007. doi:10.3181/0703-MR-72.
28. **Lieber RL, Ward SR.** Cellular mechanisms of tissue fibrosis. 4. Structural and functional consequences of skeletal muscle fibrosis. *Am J Physiol Cell Physiol* 305: C241–C252, 2013. doi:10.1152/ajpcell.00173.2013.
29. **Mathias D, Mitchel REJ, Barclay M, Wyatt H, Bugden M, Priest ND, Whitman SC, Scholz M, Hildebrandt G, Kamprad M, Glasow A.** Correction: Low-dose irradiation affects expression of inflammatory markers in the heart of ApoE$^{-/-}$ mice. *PLoS One* 11: e0157616, 2016. doi:10.1371/journal.pone.0157616.
30. **Meacham LR, Sklar CA, Li S, Liu Q, Gimpel N, Yasui Y, Whitton JA, Stovall M, Robison LL, Oeffinger KC.** Diabetes mellitus in long-term survivors of childhood cancer. Increased risk associated with radiation therapy: a report for the Childhood Cancer Survivor Study. *Arch Intern Med* 169: 1381–1388, 2009. doi:10.1001/archinternmed.2009.209.
31. **Miller GG, Kenning JM, Dawson DT.** Radiation-induced changes in collagen isotypes I, III, and IV in the lung of LAF1 mouse: effects of time, dose, and WR-2721. *Radiat Res* 115: 515–532, 1988. doi:10.2307/3577301.
32. **Nicklas BJ, Leng I, Delbono O, Kitzman DW, Marsh AP, Hundley WG, Lyles MF, O'Rourke KS, Annex BH, Kraus WE.** Relationship of physical function to vastus lateralis capillary density and metabolic enzyme activity in elderly men and women. *Aging Clin Exp Res* 20: 302–309, 2008. doi:10.1007/BF03324860.
33. **van Nimwegen FA, Schaapveld M, Janus CP, Krol AD, Raemaekers JM, Kremer LC, Stovall M, Aleman BM, van Leeuwen FE.** Risk of diabetes mellitus in long-term survivors of Hodgkin lymphoma. *J Clin Oncol* 32: 3257–3263, 2014. doi:10.1200/JCO.2013.54.4379.
34. **Nylander V, Ingerslev LR, Andersen E, Fabre O, Garde C, Rasmussen M, Citirikkaya K, Bæk J, Christensen GL, Aznar M, Specht L, Simar D, Barrès R.** Ionizing radiation potentiates high-fat diet-induced insulin resistance and reprograms skeletal muscle and adipose progenitor cells. *Diabetes* 65: 3573–3584, 2016. doi:10.2337/db16-0364.
35. **Prior SJ, Goldberg AP, Ortmeyer HK, Chin ER, Chen D, Blumenthal JB, Ryan AS.** Increased skeletal muscle capillarization independently enhances insulin sensitivity in older adults after exercise training and detraining. *Diabetes* 64: 3386–3395, 2015. doi:10.2337/db14-1771.
36. **Reisz JA, Bansal N, Qian J, Zhao W, Furdui CM.** Effects of ionizing radiation on biological molecules—mechanisms of damage and emerging methods of detection. *Antioxid Redox Signal* 21: 260–292, 2014. doi:10.1089/ars.2013.5489.
37. **Richardson DK, Kashyap S, Bajaj M, Cusi K, Mandarino SJ, Finlayson J, DeFronzo RA, Jenkinson CP, Mandarino LJ.** Lipid infusion decreases the expression of nuclear encoded mitochondrial genes and increases the expression of extracellular matrix genes in human skeletal muscle. *J Biol Chem* 280: 10290–10297, 2005. doi:10.1074/jbc.M408985200.
38. **Richardson RB.** Ionizing radiation and aging: rejuvenating an old idea. *Aging (Albany NY)* 1: 887–902, 2009. doi:10.18632/aging.100081.
39. **Seemann I, Gabriels K, Visser NL, Hoving S, te Poele JA, Pol JF, Gijbels MJ, Janssen BJ, van Leeuwen FW, Daemen MJ, Heeneman S, Stewart FA.** Irradiation induced modest changes in murine cardiac function despite progressive structural damage to the myocardium and microvasculature. *Radiother Oncol* 103: 143–150, 2012. doi:10.1016/j.radonc.2011.10.011.
40. **Silverstein MG, Ordanes D, Wylie AT, Files DC, Milligan C, Presley TD, Kavanagh K.** Inducing muscle heat shock protein 70 improves insulin sensitivity and muscular performance in aged mice. *J Gerontol A Biol Sci Med Sci* 70: 800–808, 2015. doi:10.1093/gerona/glu119.
41. **Stubblefield MD.** Radiation fibrosis syndrome: neuromuscular and musculoskeletal complications in cancer survivors. *PM R* 3: 1041–1054, 2011. doi:10.1016/j.pmrj.2011.08.535.
42. **Takahashi S, Mendelsohn ME.** Synergistic activation of endothelial nitric-oxide synthase (eNOS) by HSP90 and Akt: calcium-independent eNOS activation involves formation of an HSP90-Akt-CaM-bound eNOS complex. *J Biol Chem* 278: 30821–30827, 2003. doi:10.1074/jbc.M304471200.
43. **Tsilibary EC.** Microvascular basement membranes in diabetes mellitus. *J Pathol* 200: 537–546, 2003. doi:10.1002/path.1439.
44. **Wagner JE, Kavanagh K, Ward GM, Auerbach BJ, Harwood HJ Jr, Kaplan JR.** Old World nonhuman primate models of type 2 diabetes mellitus. *ILAR J* 47: 259–271, 2006. doi:10.1093/ilar.47.3.259.
45. **Yarnold J, Brotons MC.** Pathogenetic mechanisms in radiation fibrosis. *Radiother Oncol* 97: 149–161, 2010. doi:10.1016/j.radonc.2010.09.002.
46. **Zalutskaya A, Bornstein SR, Mokhort T, Garmaev D.** Did the Chernobyl incident cause an increase in type 1 diabetes mellitus incidence in children and adolescents? *Diabetologia* 47: 147–148, 2004. doi:10.1007/s00125-003-1271-9.
47. **Zhang Y, Wang JS, Chen LL, Zhang Y, Cheng XK, Heng FY, Wu NH, Shen YF.** Repression of hsp90β gene by p53 in UV irradiation-induced apoptosis of Jurkat cells. *J Biol Chem* 279: 42545–42551, 2004. doi:10.1074/jbc.M314213200.
48. **Zwetsloot KA, Nedergaard A, Gilpin LT, Childs TE, Booth FW.** Differences in transcriptional patterns of extracellular matrix, inflammatory, and myogenic regulatory genes in myofibroblasts, fibroblasts, and muscle precursor cells isolated from old male rat skeletal muscle using a novel cell isolation procedure. *Biogerontology* 13: 383–398, 2012. doi:10.1007/s10522-012-9382-7.

Cell

Genetic and Functional Drivers of Diffuse Large B Cell Lymphoma

Graphical Abstract

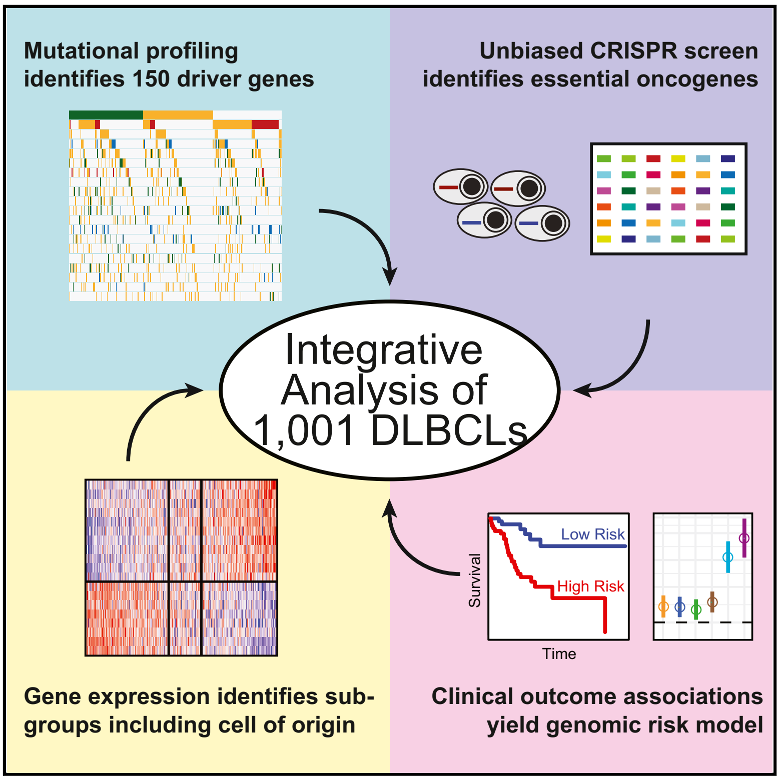

Highlights

- Exome sequencing in 1,001 DLBCL patients comprehensively identifies 150 driver genes
- Unbiased CRISPR screen in DLBCL cell lines identifies essential oncogenes
- Integrative analysis connects genomics, CRISPR hits, and clinical outcome
- A genomic risk model of survival outperforms existing risk-assessment methods

Authors

Anupama Reddy, Jenny Zhang, Nicholas S. Davis, ..., Jyotishka Datta, David B. Dunson, Sandeep S. Dave

Correspondence

sandeep.dave@duke.edu

In Brief

An integrative analysis in 1,001 newly diagnosed DLBCL patients identifies 150 genetic drivers with functional characterization using an unbiased CRISPR screen in DLBCL cell lines and connects with clinical outcome.

Reddy et al., 2017, Cell *171*, 481–494
October 5, 2017
https://doi.org/10.1016/j.cell.2017.09.027

Cell

Genetic and Functional Drivers of Diffuse Large B Cell Lymphoma

Anupama Reddy,[1,2,22] Jenny Zhang,[1,2,22] Nicholas S. Davis,[1,22] Andrea B. Moffitt,[1,22] Cassandra L. Love,[1] Alexander Waldrop,[1] Sirpa Leppa,[3] Annika Pasanen,[3] Leo Meriranta,[3] Marja-Liisa Karjalainen-Lindsberg,[3] Peter Nørgaard,[4] Mette Pedersen,[4] Anne O. Gang,[4] Estrid Høgdall,[4] Tayla B. Heavican,[5] Waseem Lone,[5] Javeed Iqbal,[5] Qiu Qin,[1] Guojie Li,[1] So Young Kim,[1] Jane Healy,[1] Kristy L. Richards,[6] Yuri Fedoriw,[6] Leon Bernal-Mizrachi,[7] Jean L. Koff,[7] Ashley D. Staton,[7] Christopher R. Flowers,[7] Ora Paltiel,[8] Neta Goldschmidt,[8] Maria Calaminici,[9] Andrew Clear,[9] John Gribben,[9] Evelyn Nguyen,[10] Magdalena B. Czader,[10] Sarah L. Ondrejka,[11] Angela Collie,[11] Eric D. Hsi,[11] Eric Tse,[12] Rex K.H. Au-Yeung,[12] Yok-Lam Kwong,[12] Gopesh Srivastava,[12] William W.L. Choi,[12] Andrew M. Evens,[13] Monika Pilichowska,[13] Manju Sengar,[14] Nishitha Reddy,[15] Shaoying Li,[16] Amy Chadburn,[17] Leo I. Gordon,[18] Elaine S. Jaffe,[19] Shawn Levy,[20] Rachel Rempel,[1] Tiffany Tzeng,[1] Lanie E. Happ,[1] Tushar Dave,[1] Deepthi Rajagopalan,[1] Jyotishka Datta,[1] David B. Dunson,[21] and Sandeep S. Dave[1,2,23,*]
[1]Duke Cancer Institute and Center for Genomic and Computational Biology, Duke University, Durham, NC, USA
[2]Department of Medicine, Duke University Medical Center, Durham, NC, USA
[3]Helsinki University Hospital Cancer Center and University of Helsinki, Helsinki, Finland
[4]Herlev and Gentofte Hospital, Copenhagen University, Herlev, Denmark
[5]Department of Pathology and Microbiology, University of Nebraska Medical Center, Omaha, NE, USA
[6]Pathology and Laboratory Medicine, University of North Carolina, Chapel Hill, NC, USA
[7]Winship Cancer Institute, Emory University, Atlanta, GA, USA
[8]Hadassah-Hebrew University Medical Center, Jerusalem, Israel
[9]Barts Cancer Institute of Queen Mary University of London, London, UK
[10]Pathology, Indiana University, Indianapolis, IN, USA
[11]Pathology and Laboratory Medicine Institute, Cleveland Clinic, Cleveland, OH, USA
[12]Queen Mary Hospital, University of Hong Kong, Hong Kong
[13]Tufts University Medical Center, Boston, MA, USA
[14]Tata Memorial Center, Mumbai, India
[15]Vanderbilt University Medical Center, Nashville, TN, USA
[16]MD Anderson Cancer Center, Houston, TX, USA
[17]Columbia-Presbyterian Hospital, New York, NY, USA
[18]Northwestern University Medical School, Chicago, IL, USA
[19]National Cancer Institute, Bethesda, MD, USA
[20]Hudson Alpha Institute for Biotechnology, Huntsville, AL, USA
[21]Department of Statistical Science, Duke University, Durham, NC, USA
[22]These authors contributed equally
[23]Lead Contact
*Correspondence: sandeep.dave@duke.edu
https://doi.org/10.1016/j.cell.2017.09.027

SUMMARY

Diffuse large B cell lymphoma (DLBCL) is the most common form of blood cancer and is characterized by a striking degree of genetic and clinical heterogeneity. This heterogeneity poses a major barrier to understanding the genetic basis of the disease and its response to therapy. Here, we performed an integrative analysis of whole-exome sequencing and transcriptome sequencing in a cohort of 1,001 DLBCL patients to comprehensively define the landscape of 150 genetic drivers of the disease. We characterized the functional impact of these genes using an unbiased CRISPR screen of DLBCL cell lines to define oncogenes that promote cell growth. A prognostic model comprising these genetic alterations outperformed current established methods: cell of origin, the International Prognostic Index comprising clinical variables, and dual *MYC* and *BCL2* expression. These results comprehensively define the genetic drivers and their functional roles in DLBCL to identify new therapeutic opportunities in the disease.

INTRODUCTION

Diffuse large B cell lymphoma (DLBCL) is the most common hematologic malignancy, with an annual incidence of over 100,000 cases worldwide. Although more than half of these patients may achieve long-term remission, the majority of the remaining patients succumb to DLBCL. Application of next-generation sequencing has revealed a striking degree of molecular and clinical heterogeneity in DLBCL (Zhang et al., 2013).

The heterogeneity of DLBCL has imposed several major limitations on previous genetic studies (Lohr et al., 2012; Morin et al.,

2011; Pasqualucci et al., 2011; Zhang et al., 2013). First, sample-size limitations of earlier studies have hampered the discovery of low-frequency but pathogenetically important mutations. Systematic pan-cancer analysis has indicated that 400 tumor-normal DLBCL pairs would be needed to comprehensively discover all the genes mutated at a frequency of 5% or higher with greater than 90% power (Lawrence et al., 2014). Second, defining the link between genetic mutations and clinical outcome has been challenging. Third, even as the genetic alterations are being defined, the functional impact of these mutations and their role in promoting the growth of lymphoma cells remains unclear, even though these are critical considerations for exploring therapeutics.

In this study, we sought to comprehensively define the genetic drivers of DLBCL and their association with functional and clinical outcomes through whole-exome and transcriptome sequencing of tumors from 1,001 newly diagnosed patients treated uniformly with rituximab-containing regimens. We further characterized the downstream functional impact of genes using an unbiased CRISPR screen in DLBCL cell lines.

RESULTS

Discovery of Genetic Drivers in DLBCL

We started with a discovery phase of identifying genes mutated in DLBCL through whole-exome sequencing of 1,001 DLBCL and 400 paired germline DNAs. The clinical characteristics of these patients are described fully in Table S1. The sample size of 400 tumor-normal pairs provided nearly 100% power for the discovery of genes mutated in 10% of patients and over 90% power to detect genes mutated in 5% of DLBCL patients (Lawrence et al., 2014). To increase the sensitivity and robustness of our discovery of driver-gene mutations, we added 102 previously described tumor-germline pairs (Lohr et al., 2012; Morin et al., 2011; Pasqualucci et al., 2011; Zhang et al., 2013) to our set of 400 paired cases. These 502 paired tumor-germline cases represented a primary discovery set for identifying genetic drivers in DLBCL, with the remaining cases serving as a validation set to ensure the reproducibility of the findings and to characterize the frequency of genetic events and clinical associations in these driver genes. In addition to single nucleotide variants (SNVs) and insertions/deletions (indels), we also characterized copy number alterations from whole-exome sequencing data (Magi et al., 2013). A comprehensive exome sequencing quality summary is presented in STAR Methods, Table S1 and Figures S1 and S2. We verified the accuracy of our variant identification through Sanger sequencing of 1,130 events, representing 61 genes with 90% concordance (Table S1).

The distribution of somatic alterations in tumor-normal pairs were used to identify (Lawrence et al., 2013) 150 putative driver genes that were recurrently mutated in DLBCL. We then defined genetic alterations for all 1,001 DLBCLs corresponding to these 150 genes, identifying variants that meet the criteria for driver mutations as described (Lawrence et al., 2013; Papaemmanuil et al., 2016). The mean number of mutations per DLBCL case was 7.75. The individual variants identified by patient are listed in Table S1, with copy number and gene-level alterations summarized in Table S1.

The top 60 most frequently mutated genes are shown in the mutational heatmap in Figure 1A. Genes frequently exhibited a pattern of either predominant missense and/or copy number gains consistent with an oncogene (e.g., *BCL2*, *CARD11*, and *IRF4*) or truncating mutations and/or copy number losses consistent with a tumor suppressor gene (e.g., *SPEN*, *CDKN2A*, and *TNFAIP3*).

Figure 1B summarizes the international prognostic index (IPI) (Shipp, 1993) score, initial response to therapy (complete response or not), and the cell-of-origin subsets of DLBCL, activated B cell-like (ABC), and germinal center B cell-like (GCB) DLBCL. When the cases were ordered in descending order by gene-mutation frequency, there were no obvious patterns detectable in the corresponding clinical data. The large sample size in our study enabled not only the identification of driver genes in DLBCLs but also provided clarity on the types of mutations in known driver genes.

Cell-of-Origin Effects in DLBCL

We defined the lineage-based subgroups of DLBCL using RNA-seq (RNA sequencing) to generate expression data in 775 patients for whom adequate material was available. Using gene expression to distinguish cell of origin (Wright et al., 2003), we identified 313 ABC DLBCLs and 331 GCB DLBCLs, while the rest were unclassified DLBCLs (Figure 2A; Table S2).

We validated the efficacy of the RNA-seq-based classifier through two complementary approaches. First, we performed Nanostring assays (Scott et al., 2014) in 200 of these cases to determine cell of origin. We found excellent agreement between the expression data and the cell-of-origin calls generated by RNA-seq and Nanostring (Figure 2B, top, $R^2 = 0.87$, $p < 10^{-6}$). We also compared the RNA-seq classifier with the immunohistochemistry-based Hans algorithm (Hans et al., 2004) commonly used to distinguish cell of origin. In 654 cases (Figure 2B, bottom, $p < 10^{-6}$) that we tested using immunohistochemistry for IRF4, BCL6, and CD10, we found that the RNA-seq classifier score was significantly different between the two Hans algorithm classes. As expected, ABC DLBCLs had worse overall survival compared to GCB DLBCLs in our study ($p = 0.004$, logrank test). These data indicate that RNA-seq can be reliably used to distinguish the DLBCL cell-of-origin subsets.

The Connectivity of DLBCL Driver Genes

We further examined the differences in mutational frequencies among the ABC and GCB DLBCL subgroups. We found that these two subgroups shared the vast majority of driver genes at statistically indistinguishable frequencies. However, 20 genes were differentially mutated among the two groups (Figure 2C; Table S2) including *EZH2*, *SGK1*, *GNA13*, *SOCS1*, *STAT6*, and *TNFRSF14*, which were more frequently mutated in GCB DLBCLs, while *ETV6*, *MYD88*, *PIM1*, and *TBL1XR1* were more frequently mutated in ABC DLBCLs.

We examined pairwise overlaps using Fisher's test and mutual exclusion (Leiserson et al., 2016) among the 150 DLBCL driver genes. 61 genes had statistically significant relationships with other driver genes ($p < 0.01$, Table S2), depicted in the network in Figure 2D. We noted a number of interesting features, including subnetworks associated with cell of origin in DLBCL

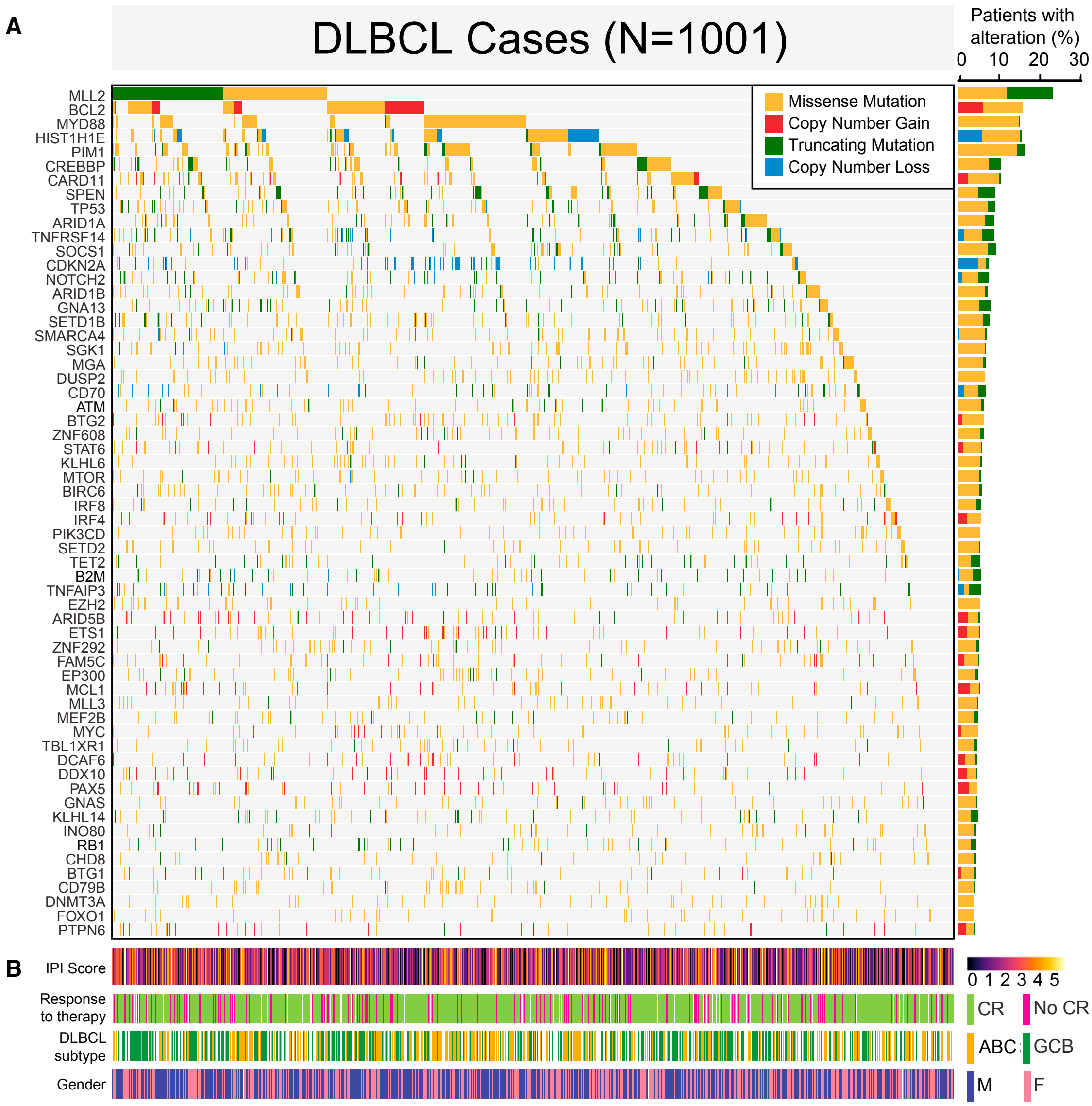

Figure 1. The Landscape of Genetic Drivers in 1,001 DLBCLs

(A) The mutational heatmap indicates the most recurrently altered genes in 1,001 DLBCL cases with frequency >5%, color coded by four genetic alteration types: missense mutation (yellow), copy number gain (red), truncating mutation (green), and copy number loss (blue). To the right of the mutational heatmap, the stacked bargraph indicates the gene-level alteration type breakdown using the same four-color scheme.

(B) Clinical features of the corresponding 1,001 patients are indicated below the mutational heatmap, including the international prognostic index (IPI) score, response to therapy (complete response or not), activated B cell-like (ABC) versus germinal center B cell-like (GCB) DLBCL subtype, and gender.

See also Figures S1 and S2 and Table S1.

that generally exhibited mutually exclusive mutation patterns, as well as a larger network of genes shared between the subgroups. For instance, *MLL2* mutations occurred in a largely exclusive fashion with *MYC*, while *TP53* mutations occurred in a mutually exclusive fashion with *KLHL6*, implicating biologically relevant models for DLBCL.

Functional Genomics through CRISPR Screening

CRISPR screening has emerged as a powerful method for identifying critical functional dependencies *in vitro* (Koike-Yusa et al., 2014; Shalem et al., 2014). We selected a total of six cell lines including three ABC DLBCLs (LY3, TMD8, and HBL1), two GCB DLBCLs (SUDHL4 and Pfeiffer), and one Burkitt lymphoma cell line (BJAB) that phenotypically resembles GCB DLBCLs.

We utilized the GeCKO v2 genome-wide human single guide (sgRNA) library (Shalem et al., 2014), containing over 120,000 sgRNAs targeting 19,050 protein coding genes, to transduce three replicate populations from each cell line with the complete sgRNA library. The schematic for our CRISPR screen is shown in Figure 3A. Each gene was targeted by six distinct sgRNAs in Cas9-expressing DLBCL cells with cell growth allowed to proceed for 14 population doublings. At the end of these

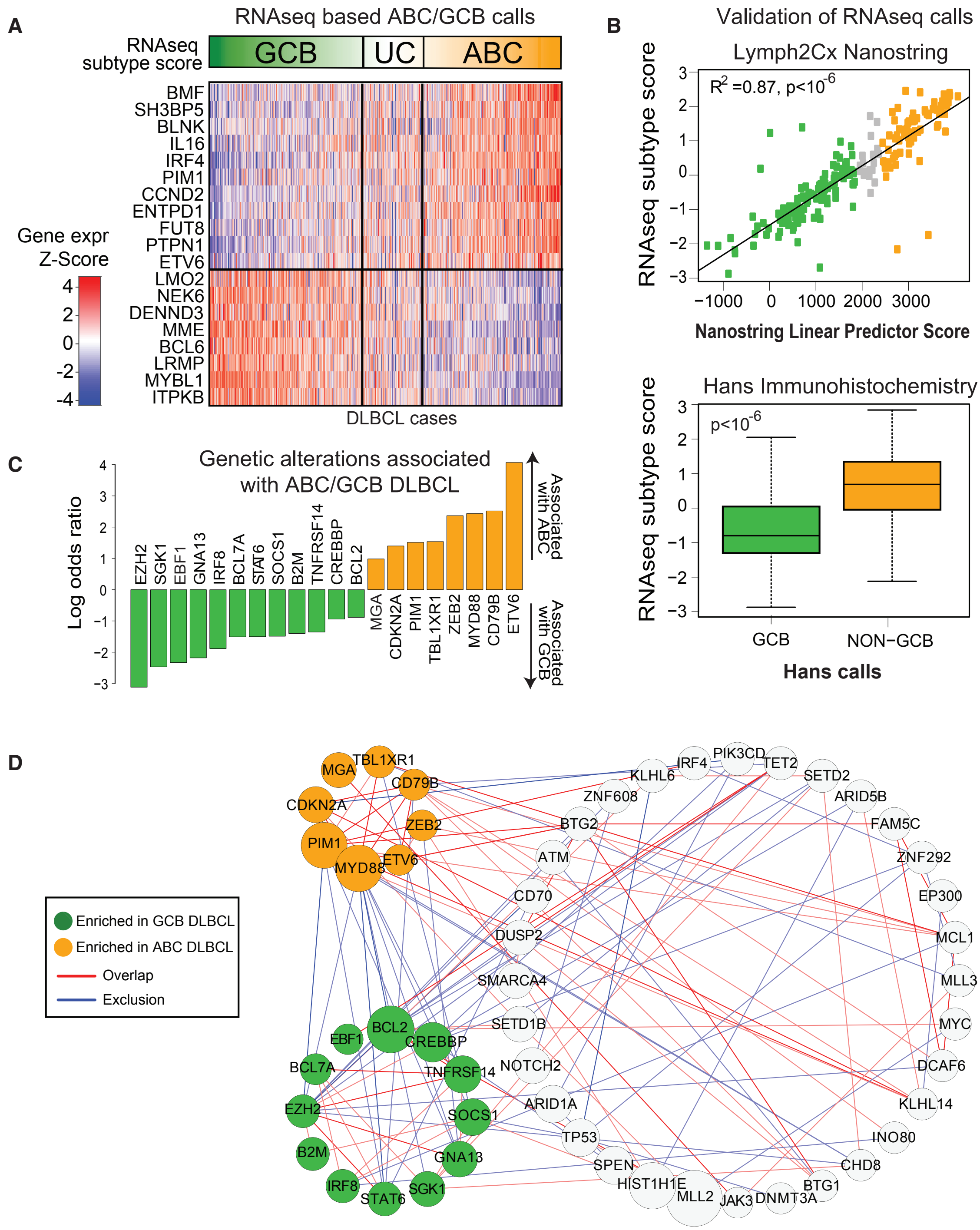

Figure 2. ABC/GCB-Based Classification of DLBCL

(A) RNA-seq gene expression classifier distinguishes germinal center B cell-like DLBCL (GCB), unclassified DLBCL (UC), and activated B cell-like DLBCL (ABC).

(B) Comparison of RNA-seq subtype score versus the Nanostring linear predictor score (using Pearson's correlation R^2 = 0.87, p < 10^{-6}) (top) and by immunohistochemistry Hans GCB versus non-GCB classification (Wilcoxon test p < 10^{-6}) (bottom).

(C) Genetic alterations that are enriched in ABC versus GCB DLBCL (Fisher's test FDR < 0.1).

(D) Network of genes with statistically significant (p < 0.01) overlap or co-occurrence (red edges) and mutational exclusion (blue edges). Stronger associations are indicated with thicker and darker colored lines between nodes (p < 0.001). Genes significantly enriched in GCB or ABC DLBCL are colored in green and orange, respectively, or gray otherwise.

See also Table S2.

Cell

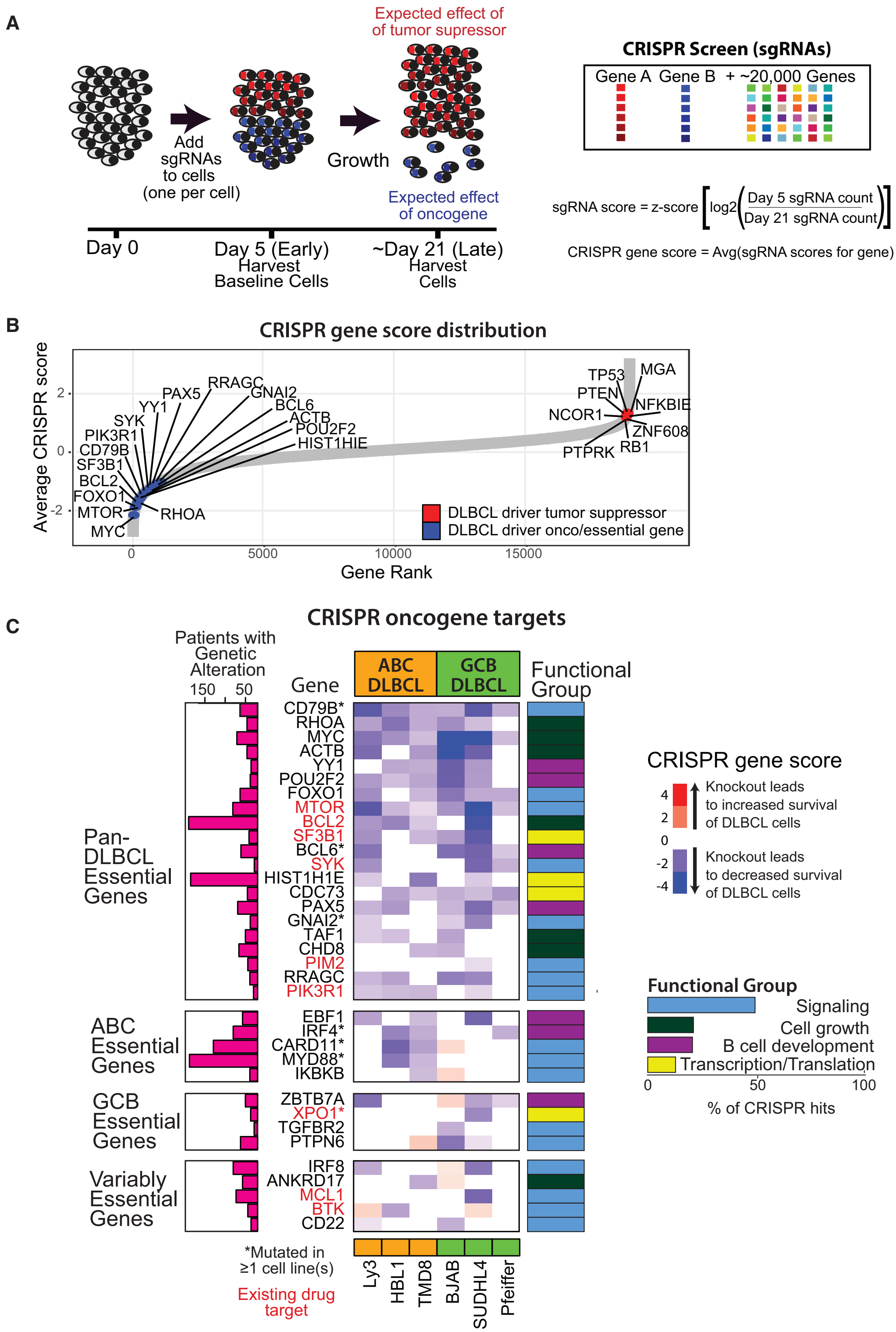

(legend on next page)

experiments, we expected that cells expressing sgRNAs that target oncogenes promoting cell growth and proliferation would be selectively depleted from the cell population, whereas cells expressing sgRNAs that target tumor-suppressor genes inhibiting cell growth and proliferation would be selectively enriched in the cell population.

We sequenced replicate populations at two time points (Figure 3A; Early: after transduction, Late: after 14 population doublings) to observe changes in sgRNA frequency over time. The resulting changes were then used to infer the magnitude and directionality of fitness effects associated with targeted gene knockout in DLBCL cell lines, with the ultimate goal of broadly identifying genes essential to the development and/or maintenance of DLBCL. High-throughput sequencing of sgRNA libraries amplified from plasmid sequences was used to determine sgRNA abundance for populations at each time-point. Summary statistics of sgRNA sequencing library quality are detailed in the STAR Methods and Figure S3.

We identified 1,956 "essential genes" whose silencing resulted in significantly decreased cell fitness in at least one cell line (see Table S3 for exhaustive list). We ranked all the genes based on their CRISPR score, a measure of the degree of alteration in each gene as a function of altered abundance of the guide RNAs targeting that gene (Figure 3B). We found that the genetic drivers identified through whole-exome sequencing were disproportionately at the extremes of the distribution ($p = 3 \times 10^{-5}$). The genes that were depleted in the screen and therefore implicated as oncogenes critical to cell growth across the majority of DLBCLs included *MYC*, *RHOA*, *SF3B1*, *MTOR*, and *BCL2.* Among genes that were enriched in the screen and therefore implicated functionally as tumor-suppressor genes, we noted *TP53*, *MGA*, *PTEN*, and *NCOR1*. Separately, we examined the association of genomic copy number and the guide RNAs that were significantly altered in our screen (Figure S3) to rule out copy number alterations as a source of artifactual results (Aguirre et al., 2016). None of the essential driver genes were found within genomic regions identified by our analysis as potentially influenced by copy number amplification. Thus, we concluded that the decreased fitness resulting from essential driver gene knockout reflects the functional importance of these genes in the context of DLBCL.

In all, there were 35 driver genes whose knockout resulted in decreased viability of DLBCL cells, identifying them as functional oncogenes (Figure 3C). Nine of these driver genes were found to be important in a subtype-specific fashion. Knockout of *EBF1*, *IRF4*, *CARD11*, *MYD88*, and IKBKB was selectively lethal in ABC DLBCL, whereas knockout of *ZBTB7A*, *XPO1*, *TGFBR2*, and *PTPN6* was selectively lethal in GCB DLBCL. These data provide critical clues to the functional dependence of DLBCL on particular oncogenes and suggest that small molecule inhibitors of these oncogenes may provide therapeutic benefit in affected DLBCL patients. All of these genes were well expressed in DLBCLs. Of the 35 CRISPR driver gene hits, 9 genes are direct targets of the therapeutic drug targets either in human clinical trials or already in use for another indication. Importantly, 36% of the DLBCL patients have genetic alterations in these nine drug targets and would potentially benefit from targeted therapy.

Gene set enrichment analysis of the significant driver genes (Table S3) identified four functional groups, including signaling (e.g., *MTOR*, *PIK3R1*, *PIM2*, *BTK*), cell growth (e.g., *MYC*, *CHD8*, *BCL2*), B cell development (e.g., *EBF1*, *IRF4*, *PAX5*, *POU2F2*, *YY1*), and transcription/translation (e.g., *SF3B1*, *XPO1*, *HIST1H1E*). Importantly, we observed that the lethal effects of knocking down these genes were not limited to cell lines that harbored alterations in these genes, suggesting that these driver genes represent favored pathways for promoting proliferation in DLBCL.

Gene Expression Signature Associations with Genetic Alterations and Outcome

Gene expression profiling has long been used to define subtypes and understand the heterogeneity within DLBCL. Microarray-based gene expression studies have identified cell-of-origin subgroups (Alizadeh et al., 2000), as well as gene expression signatures derived from host inflammatory response (Monti et al., 2005) and stromal tissues (Lenz et al., 2008), as well as other biological processes. However, the connections between these gene expression signatures and genetic alterations is largely unknown.

We first sought to comprehensively define the relevant gene expression signatures across our DLBCL cohort by performing RNA-seq on all tumors for which RNA was available (N = 775). From these cases, we defined a core set of 624 samples (STAR Methods) for integrative analysis.

Figure 4A provides an overview of the integrative expression analysis. We began the analysis with a comprehensive universe of nearly 9,500 annotated gene sets from widely used gene set databases (Kegg, Reactome, MSigDB), as well as several lymphoma-specific gene signature sources (Lenz et al., 2008; Monti et al., 2005; Shaffer et al., 2006). We first identified annotated gene sets that showed a pattern of high correlation among the constituent genes in our dataset, indicating that these gene sets represented processes that are co-regulated, as well as variable, across DLBCL tumors. We found that 1,228 gene sets exhibited such patterns of co-regulation.

In addition to the observed high correlation among their constituent genes, the vast majority of these 1,228 gene sets were strongly correlated with each other. The high inter-gene set correlation indicated a high degree of redundancy between these gene sets, likely reflecting their origin from shared biological processes. To reduce this observed redundancy and focus on distinct gene expression sets that described the underlying

Figure 3. Defining the Functional Role of Genetic Drivers through CRISPR Screen

(A) Schematic of CRISPR screen performed for six cell lines in triplicate.

(B) A ranked list of CRISPR scores for the 19,032 genes targeted in the screen. Illustrative driver genes are shown in blue (likely oncogenes) or red (likely tumor suppressor genes).

(C) CRISPR scores for 35 DLBCL oncogenes are shown alongside the frequency of genetic alterations and functional group.

See also Figure S3 and Table S3.

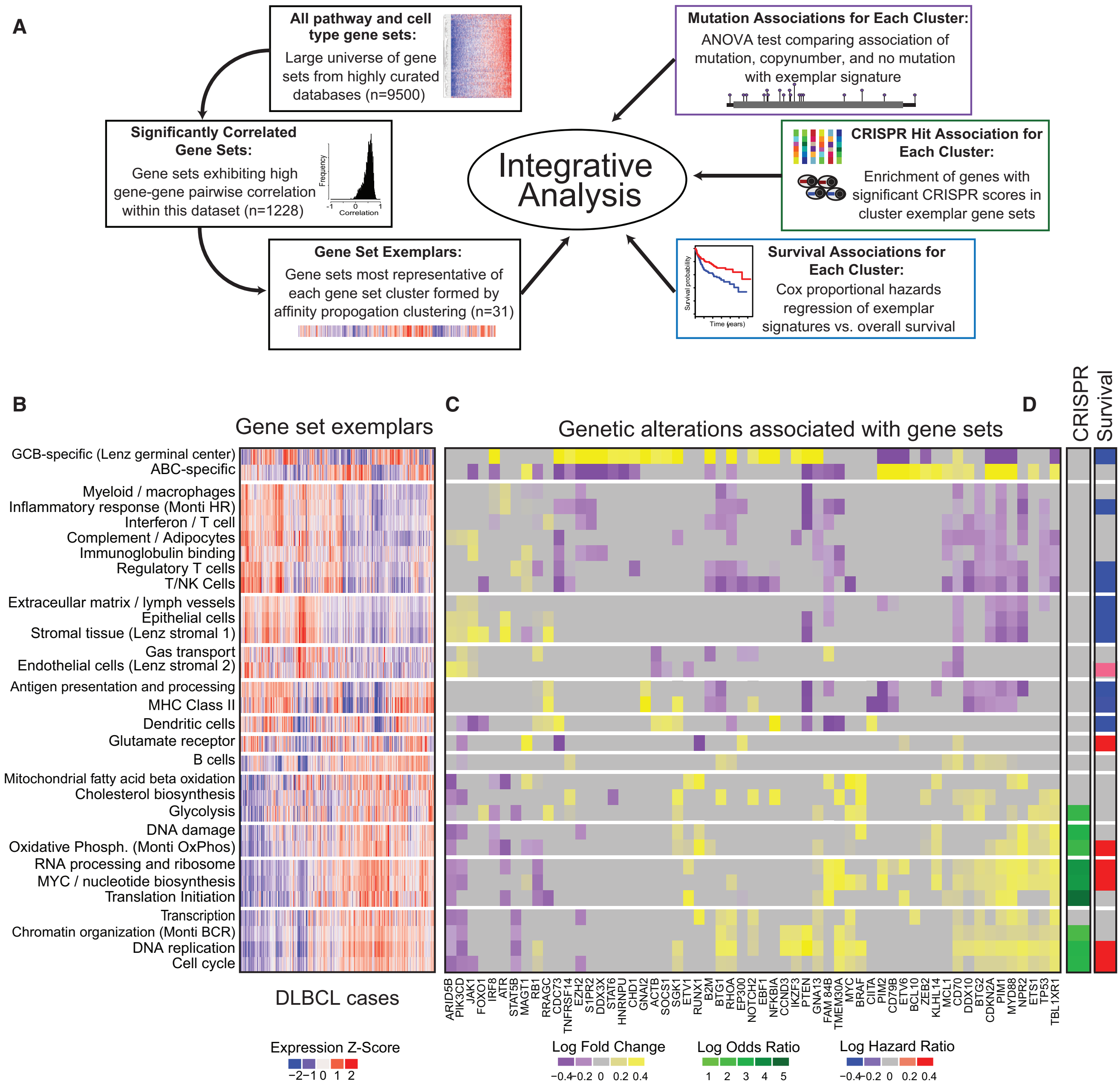

Figure 4. Integrative Analysis of Gene Expression, Genetic Alterations, and Outcome

(A) Schematic depicting the integrative analysis.

(B) Heatmap of expression of significantly correlated gene set exemplars across DLBCL samples (N = 624).

(C) Heatmap of fold-change associations of significant genetic alterations with gene set exemplars. Fold-changes for significant associations (ANOVA test, $p < 0.05$) are shown in yellow-purple color scales, while insignificant associations are colored gray.

(D) Left: Enrichment of CRISPR hits within the cluster exemplar gene sets (Fisher's test, $p < 0.05$). Right: Survival association with cluster exemplar signature (logrank test, $p < 0.05$).

See also Table S4.

biology, we applied affinity propagation clustering (Frey and Dueck, 2007) to define the exemplars that essentially replicated the patterns of the members of the cluster. Application of affinity propagation clustering resulted in 31 unique clusters with cluster assignments for all gene sets. This analysis identified 31 non-redundant gene clusters that each comprised highly correlated gene sets (Table S4), as well as exemplar gene sets that represent each cluster (Figure 4B). Our results recapitulated a number of described patterns underlying DLBCL gene expression. The cell-of-origin-derived ABC-high and GCB-high signatures were

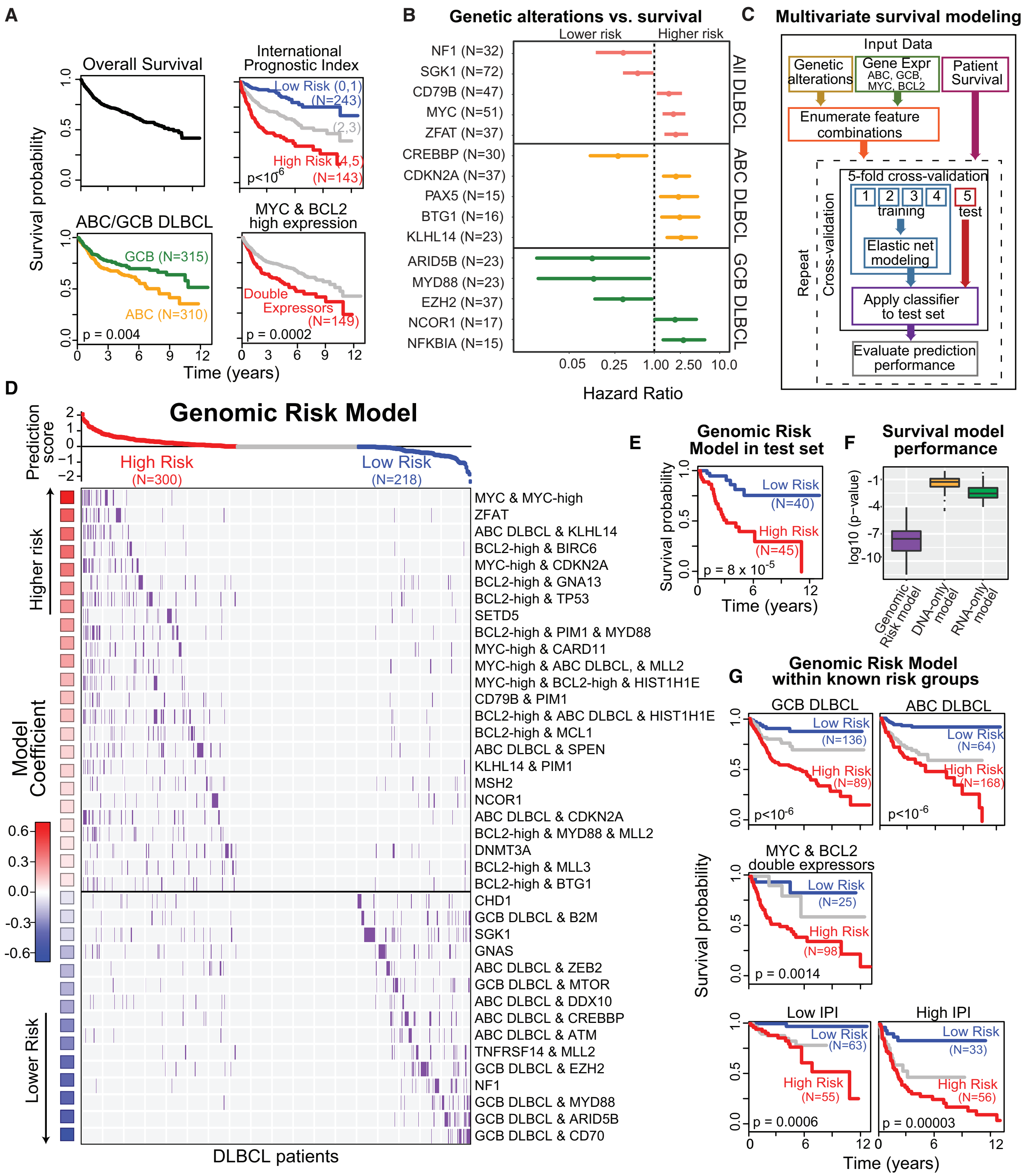

Figure 5. Genomic Risk Model Stratifies DLBCL Survival

(A) Overall survival of 1,001 DLBCL cases, cases stratified by IPI groups, ABC/GCB DLBCL, and *MYC* and *BCL2* expression.

(B) Hazard ratios and 95% confidence intervals of selected survival-associated genetic alterations ($p < 0.05$).

(C) Schematic depicting multivariate survival modeling.

(D) Combinations of genetic and expression features that comprise the genomic risk model in DLBCL patients.

(legend continued on next page)

generally expressed in a mutually exclusive fashion. In addition, the signature clustering analysis also revealed two broad classes of gene sets. The first class included signatures representing many immune-cell types (regulatory T cells, myeloid cells, NK cells) and stromal connective tissue (epithelial and endothelial cells). This group included the Monti Host Response signature (Monti et al., 2005), as well as the Lenz Stromal 1 and Stromal 2 signatures (Lenz et al., 2008). The second class included signatures related to tumor cell processes including proliferation, transcription, translation, DNA replication, and cell cycle, as well as the Monti BCR and Oxidative Phosphorylation signatures (Monti et al., 2005).

For each of these gene set exemplars, we identified the genetic alterations associated with high and low expression. Figure 4C shows a heatmap of signatures versus mutated genes (mutations and copy number alterations). These associations demonstrate a number of interesting patterns including the association of *RHOA* and *MYC* with proliferation-related signatures. The expression of many signaling pathways such as PI3 kinase did not reliably associate with specific mutations in *PIK3R1*, *PIK3CD*, or *PTEN*, suggesting that expression patterns from non-malignant cells may confound the effective measurement of these associations. There was no association between the expression of stromal signatures and overall mutational burden ($p = 0.4$).

We further investigated the relationship of our CRISPR hits and these gene sets. We found that gene sets related to cancer-related processes (e.g., oxidative phosphorylation, DNA replication, cell-cycle progression, RNA processing) demonstrated significant enrichment of the CRISPR-identified driver genes. Strikingly, no enrichment of CRISPR hits were found in the immune and stromal gene sets. Finally, we tested each of the cluster exemplar signatures for associations with overall patient survival. Figure 4D annotates the significant associations for all gene expression clusters. As expected, the GCB DLBCL signature was associated with better overall survival. Interestingly, the signatures in the stromal and immune response group (e.g., regulatory T cells) tended to associate with better survival, while the signatures in the proliferation and B cell group tended to associate with worse survival (e.g., MYC/Nucleotide Biosynthesis). The complete list of associations can be found in Table S4.

Clinical Characteristics of DLBCL Driver Genes

Overall survival following diagnosis and initial treatment is shown in Figure 5A. The clinical risk groups of the IPI was highly prognostic in our patients ($p < 10^{-6}$), with clear distinctions in survival for the low-, intermediate-, and high-risk groups. The cell of origin distinction was found to be prognostic in our data (Figure 5A).

High expression of *MYC* and *BCL2* has been associated with worse prognosis (Green et al., 2012; Johnson et al., 2012). High expressors were defined from RNA-seq data as *MYC*-high and *BCL2*-high and were significantly associated with survival (Figure S4). Double expressors were defined as samples that have both high expression of *MYC* and high expression of *BCL2* (Figure 5A). We assessed the independence of ABC/GCB subgrouping and double expressors (high *MYC* and *BCL2*) and found that ABC/GCB status does not further stratify the double expressors (Figure S4).

We separately examined the association of translocations in *MYC* and *BCL2* with mutations and expression by performing fluorescent *in situ* hybridization (FISH) using both genes to define translocations involving the immunoglobulin locus and *MYC* and *BCL2* (performed separately). *MYC* translocations are associated with mutations and high expression of MYC, while translocations in *BCL2* were associated with mutations and amplifications (Figure S4).

The potential association of mutations with clinical outcome has largely been unexplored. We first examined the association of specific mutations and survival among all DLBCLs. We found that *MYC* mutations were strongly associated with poorer survival, as were mutations in *CD79B* and *ZFAT*. Mutations in *NF1* and *SGK1* were associated with more favorable survival. We further examined the association of different mutations and survival within ABC and GCB DLBCL. Genetic alterations in *KLHL14*, *BTG1*, *PAX5*, and *CDKN2A* were associated with significantly poorer survival in ABC DLBCL. Alterations in *CREBBP* were associated with favorable survival in ABC DLBCLs. In the GCB DLBCL group, genetic alterations in *NFKBIA*, *NCOR1* were associated with poorer prognosis, while alterations in *EZH2*, *MYD88*, and *ARID5B* were all associated with significantly better prognosis (Figure 5B). The complete list of genes associated with survival is in the Table S5.

We have developed an interactive webtool (https://dlbcl.davelab.org) for survival analysis using clinical and genomic features. Our large dataset provided the opportunity to directly examine the combinatorial and potential confounding effects of *MYC*, *BCL2*, and cell of origin, along with other genetic alterations.

We developed a multivariate supervised learning approach for defining the association of survival with combinations of genetic markers (150 genetic driver genes) and gene expression markers (cell of origin, *MYC*, and *BCL2*). Our method is summarized in Figure 5C and STAR Methods. We first enumerated all 313 possible combinations, which involved up to three separate genetic and gene expression markers and affected a minimum of 20 patients, as inputs for predictive model for survival (Zou and Hastie, 2005).

The individual components of the model are depicted in descending order of their association with poor survival in Figure 5D. *MYC* genetic alterations combined with *MYC* expression defined the subset with the least favorable prognosis in DLBCLs, while GCB DLBCLs with *CD70* alterations had the most favorable prognosis. Each component in the model was defined so

(E) Survival of the predicted risk groups in the test set (logrank test, $p = 8 \times 10^{-5}$).

(F) Cross-validation performance of the genomic risk model compared to that with only genetic alterations (DNA-only), and gene expression (RNA-only).

(G) The genomic risk model significantly stratifies survival within known risk groups (logrank test).

See also Figure S5 and Table S5.

as to be prognostically independent from all others to collectively identify subgroups that cover the entire set of DLBCL cases. These features were combined into a Cox proportional hazards model to generate a prediction score, and the DLBCL cases were divided into three subgroups based on their predicted risk. The full list of these combinatorial features along with sample-level information and model coefficients is provided in Table S5.

We validated our predictive modeling approach using an independent test set (20% of the data). The genomic model was highly significant in distinguishing patients with high versus low risk of death in the test set ($p = 8 \times 10^{-5}$; Figure 5E; Table S5). In addition, we also used 5-fold cross-validation repeated 100 times to gain a robust estimation of model performance, finding that it was highly statistically significant in distinguishing the survival groups (median logrank $p = 8 \times 10^{-6}$). The integrative model strongly outperformed the other models based on genetic alterations (DNA only) or expression (RNA only) alone (Figure 5F). The genomic risk model, which used combinatorial features, also strongly outperformed a model with the same input features (DNA+RNA) but with no combinations used (Figure S5), underscoring the importance of examining interactions between different genomic features for evaluating a patient's risk.

We further examined the performance of the genomic model in the known risk groups that are known to influence survival: cell of origin, double expression of *MYC* and *BCL2*, and IPI. Our genomic model was able to discern patients with significantly distinct outcomes within each group (Figure 5G, $p < 10^{-3}$ in all cases). These data indicate that our genomic predictor provides robust prognostic information that is not currently captured by widely used clinical and expression-based models.

Comparison of Clinical versus Genomic Risk

The hazard ratios of the different survival models in DLBCL are compared in Figure 6A for cell of origin and *MYC* and *BCL2* separately and together, as well as the clinical risk (IPI) and genomic risk models. The genomic risk model outperformed all of these existing risk predictors in DLBCL. Next, we examined the time-dependent effects of the genomic model and IPI for DLBCL patients who survived for at least 1, 3, or 5 years (Figure 6B). We found that while IPI was highly prognostic in early years, its effect waned as a function of time. In contrast, the genomic risk model had significant prognostic value for predicting longer-term mortality. These data indicate that the effects of IPI are strongest in predicting early mortality, whereas genomic risk is effective in predicting both early and late mortality.

We separately examined the survival effects of response to initial therapy. We found that response to initial therapy was significantly associated with survival, with median survival for complete responses being >12 years, while the median survival for partial (2 years) and no responses (1 year) were drastically lower (Figure 6C). We also observed a pattern of continued mortality in patients achieving a complete remission, suggesting that for a large proportion of patients, achieving a complete remission does not necessarily indicate a cure. Both IPI and genomic risk models are significantly associated with response to initial therapy (Figure 6D), with IPI being more predictive. The genomic risk model has a higher percentage of high-risk patients in the complete response group compared to IPI. We hypothesized that while the complete responders have a generally favorable prognosis as a group, this group still harbors a significant fraction of patients with early mortality that can be identified by the genomic risk model. To test our hypothesis, we examined survival for the predicted risk models stratified by clinical responses (Figure 6E). The genomic risk model was highly prognostic within each of the clinical response groups, indicating that the genomic profile of a patient strongly influences their prognostic risk, regardless of their initial response to therapy.

DISCUSSION

The genetic heterogeneity of DLBCL has led to diverse approaches to classification and prognostication and presented challenges in the development of effective new therapies. By enrolling 1,001 DLBCL patients, we designed a study that is adequately powered to identify genetic drivers and their clinical significance. CRISPR screening provided a powerful approach to probing the functional role of the genetic drivers, identifying the driver genes that directly affect cell survival.

Of the 150 driver genes that we identified, 27 genes including *SPEN*, *KLHL14*, and *MGA* have not been previously implicated in DLBCL to our knowledge. In addition, a number of genes such as *CDKN2A* and *RB1* that were thought to be altered in DLBCLs through copy number alterations were also revealed to be recurrent targets for function-altering mutations. While there is considerable interest in nominating genes for therapeutic targeting using mutational and ontology data, our data indicate a considerable need for caution. For instance, CRISPR-based knockout of several therapeutically targetable *NOTCH2*, *PIK3CD*, and *JAK2* did not have a significant impact in the growth of DLBCL cells. These findings suggest that such oncogenes may play a role in early pathogenesis or another cancer-related function that may not be easy to target directly in DLBCL. On the other hand, functional screening established a role for a number of genetic drivers as potentially targetable genes in DLBCL.

Our study informs therapeutic development in several ways. First, our data provide a comprehensive approach to risk stratification, distinguishing DLBCL patients who benefit from standard therapy from those who are expected to experience poor outcomes. Second, our data indicate that nearly 36% of DLBCL patients have a genetic alteration that may inform sensitivity to currently available therapies. Our genomic risk model can be applied clinically using existing assays, through the measurement of cell of origin, *BCL2* and *MYC* expression, and targeted sequencing of a panel of DLBCL driver genes. Our data also provide the context for understanding outcomes in clinical trials of targeted therapy. For instance, while *MTOR* mutations are prevalent in DLBCL, those patients tend to have generally good outcomes, especially in the GCB subtype. Since patients with relapsed DLBCL comprise the vast majority of patients who are enrolled in clinical trials, many such trials may be missing the DLBCL population that harbors the target (e.g., *MTOR*) but respond well to standard therapy, potentially contributing

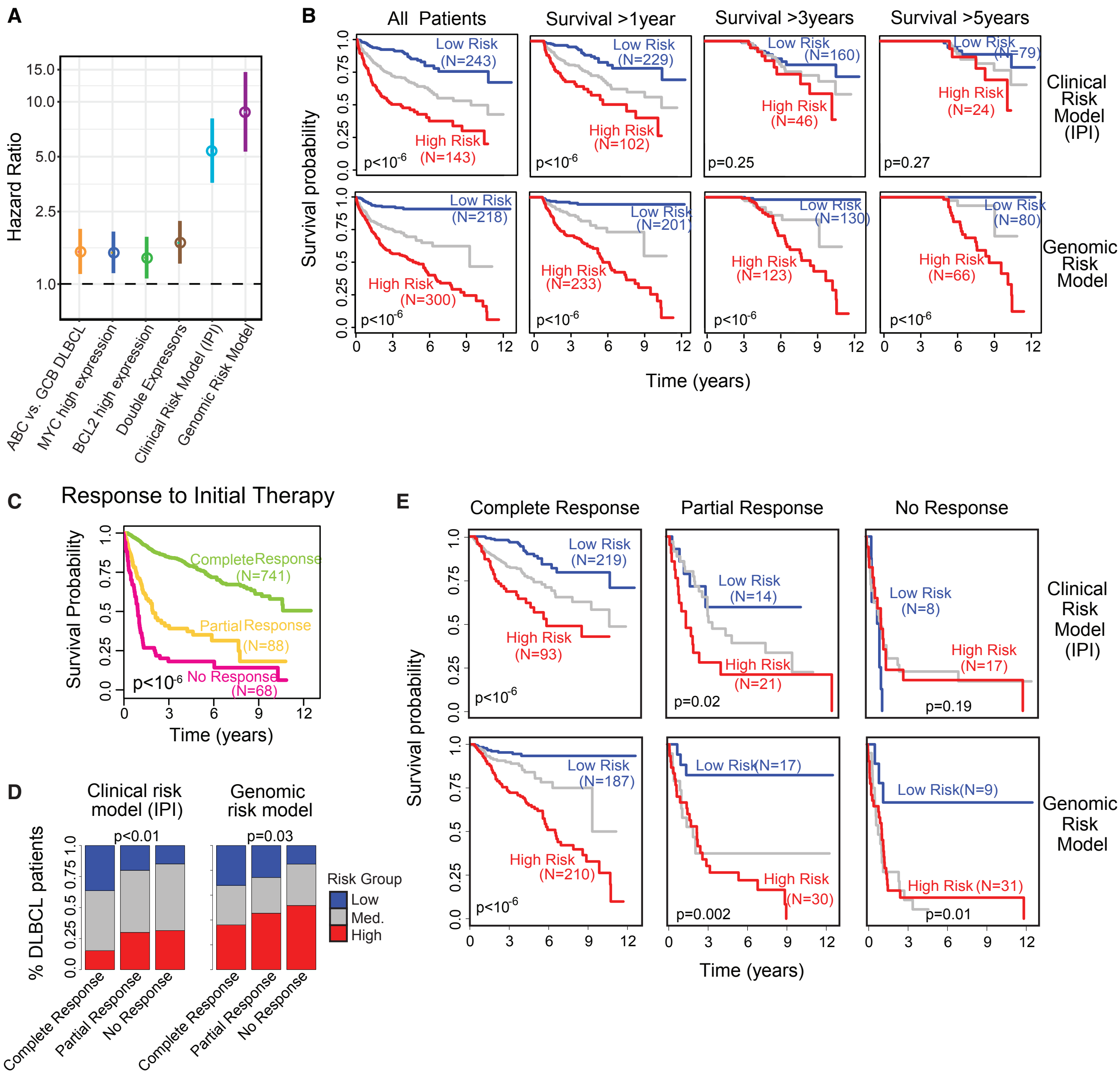

Figure 6. Comparison of Clinical Risk Model with Genomic Risk Model

A. Comparison of hazard ratios (high- versus low-risk groups) and 95% confidence intervals for various DLBCL risk models, including our genomic risk model.

B. The matrix of Kaplan-Meier survival plots indicates risk stratification by clinical risk model (IPI) versus genomic risk model for all patients and patients stratified by minimum overall survival of 1, 3, and 5 years (logrank test).

C. Survival plot for response to initial therapy (logrank test, $p < 10^{-6}$).

D. Prediction of response to initial therapy using clinical risk model (left) and genomic risk model (right) (chi-square test).

E. Survival plots showing the stratification of genomic and clinical risk models for each of the individual responses to therapy (logrank test).

to a negative trial that fails to show efficacy of these agents. Finally, we anticipate that our work will provide a starting point for hypothesis-driven biological modeling of different gene combinations that contribute to poor-risk DLBCLs to better understand their combined effects and aid in developing new therapeutic approaches.

Genetic heterogeneity is a defining feature of DLBCL. Our study demonstrates the benefits of applying genomic methodologies to large, well-characterized cohorts of cancers to discern patterns that are not possible with smaller studies. Our approach has identified clinical and functional drivers of DLBCL that are prerequisites to improving outcomes in the disease.

STAR★METHODS

Detailed methods are provided in the online version of this paper and include the following:

- KEY RESOURCES TABLE
- CONTACT FOR REAGENT AND RESOURCE SHARING
- EXPERIMENTAL MODEL AND SUBJECT DETAILS
  - DLBCL patients
  - Cell lines for CRISPR screening
- METHOD DETAILS
  - Sample processing
  - High-throughput exome library preparation
  - Exome Sequence Alignment
  - Variant and gene filtering, analysis of significantly mutated genes
  - Copy Number Analysis
  - Comparing FFPE versus fresh frozen samples in matched patients
  - Comparing tumors with matched normal versus unpaired tumors
  - CRISPR Screen
  - Normalized sgRNA abundance quantification for CRISPR screen
  - Statistical Estimation of Gene Knockout Fitness Effects on Cell Lines
  - Accounting for genomic copy number in CRISPR screen
  - CRISPR screen quality control
  - Identification of "essential" DLBCL genes
  - RNA sequencing library preparation and analysis
  - Defining correlated gene signatures
  - Clustering gene signatures
  - Association of genetic alterations with gene expression signatures
  - Association of gene expression signatures with CRISPR hits and survival
  - Classification of DLBCL into ABC and GCB subtypes
  - Validation of the RNaseq ABC/GCB classifier
  - MYC and BCL2 expression and translocations
  - Genomic risk model
- QUANTIFICATION AND STATISTICAL ANALYSIS
- DATA AND SOFTWARE AVAILABILITY

SUPPLEMENTAL INFORMATION

Supplemental Information includes five figures and five tables and can be found with this article online at https://doi.org/10.1016/j.cell.2017.09.027.

AUTHOR CONTRIBUTIONS

The following authors contributed to the design of the study: J.Z., A.R., N.S.D., A.B.M., C.L.L., A.W., and S.S.D. The following authors contributed to sample or data collection: J.Z., A.R., N.S.D., A.B.M., C.L.L., A.W., S. Leppa, A.P., L.M., M.-L.K.-L., P.N., M. Pedersen, A.O.G., E.H., T.B.H., W.L., J.I., G.L., S.Y.K., J.H., K.LR., Y.F., L.B.-M., J.L.K., A.S., C.R.F., O.P., N.G., M.C., A. Clear, J.G., E.N., M.B.C., S.L.O., A. Collie, E.D.H., E.T., R.K.H.A.-Y., Y.-L.K., G.S., W.L.C., A.M.E., M. Pilichowska, M.S., N.R., S. Li, A. Chadburn, L.I.G., E.S.J., R.R., T.T., L.E.H., T.D., S.Levy., and S.S.D. The following authors contributed to data analysis: J.Z., A.R., N.S.D., A.B.M., C.L.L., A.W., G.L., S.Y.K., J.H., R.R., T.T., L.E.H., T.D., D.R., Q.Q., J.D., D.B.D., and S.S.D. The following authors contributed to manuscript preparation: J.Z., A.R., N.S.D., A.B.M., A.W., and S.S.D.

ACKNOWLEDGMENTS

This work was partly funded through the Leukemia Lymphoma Society, Department of Defense, and the National Institutes of Health. We gratefully acknowledge the generous support of C. Stiefel and D. Stiefel.

Received: July 31, 2017
Revised: September 5, 2017
Accepted: September 18, 2017
Published: October 5, 2017

REFERENCES

Adiconis, X., Borges-Rivera, D., Satija, R., DeLuca, D.S., Busby, M.A., Berlin, A.M., Sivachenko, A., Thompson, D.A., Wysoker, A., Fennell, T., et al. (2013). Comparative analysis of RNA sequencing methods for degraded or low-input samples. Nat. Methods *10*, 623–629.

Aguirre, A.J., Meyers, R.M., Weir, B.A., Vazquez, F., Zhang, C.-Z., Ben-David, U., Cook, A., Ha, G., Harrington, W.F., Doshi, M.B., et al. (2016). Genomic copy number dictates a gene-independent cell response to CRISPR/Cas9 targeting. Cancer Discov. *6*, 914–929.

Alizadeh, A.A., Eisen, M.B., Davis, R.E., Ma, C., Lossos, I.S., Rosenwald, A., Boldrick, J.C., Sabet, H., Tran, T., Yu, X., et al. (2000). Distinct types of diffuse large B-cell lymphoma identified by gene expression profiling. Nature *403*, 503–511.

Andrews, S. (2010). FastQC: a quality control tool for high throughput sequence data. Available online at: http://www.bioinformatics.babraham.ac.uk/projects/fastqc.

Cibulskis, K., Lawrence, M.S., Carter, S.L., Sivachenko, A., Jaffe, D., Sougnez, C., Gabriel, S., Meyerson, M., Lander, E.S., and Getz, G. (2013). Sensitive detection of somatic point mutations in impure and heterogeneous cancer samples. Nat. Biotechnol. *31*, 213–219.

Cieslik, M., Chugh, R., Wu, Y.-M., Wu, M., Brennan, C., Lonigro, R., Su, F., Wang, R., Siddiqui, J., and Mehra, R. (2015). The use of exome capture RNA-seq for highly degraded RNA with application to clinical cancer sequencing. Genome Research *25*, 1372–1381.

Cock, P.J., Fields, C.J., Goto, N., Heuer, M.L., and Rice, P.M. (2010). The Sanger FASTQ file format for sequences with quality scores, and the Solexa/Illumina FASTQ variants. Nucleic Acids Res. *38*, 1767–1771.

Frey, B.J., and Dueck, D. (2007). Clustering by passing messages between data points. Science *315*, 972–976.

Green, T.M., Young, K.H., Visco, C., Xu-Monette, Z.Y., Orazi, A., Go, R.S., Nielsen, O., Gadeberg, O.V., Mourits-Andersen, T., Frederiksen, M., et al. (2012). Immunohistochemical double-hit score is a strong predictor of outcome in patients with diffuse large B-cell lymphoma treated with rituximab plus cyclophosphamide, doxorubicin, vincristine, and prednisone. J. Clin. Oncol. *30*, 3460–3467.

Hans, C.P., Weisenburger, D.D., Greiner, T.C., Gascoyne, R.D., Delabie, J., Ott, G., Müller-Hermelink, H.K., Campo, E., Braziel, R.M., Jaffe, E.S., et al. (2004). Confirmation of the molecular classification of diffuse large B-cell lymphoma by immunohistochemistry using a tissue microarray. Blood *103*, 275–282.

Hart, T., Brown, K.R., Sircoulomb, F., Rottapel, R., and Moffat, J. (2014). Measuring error rates in genomic perturbation screens: gold standards for human functional genomics. Mol. Syst. Biol. *10*, 733.

Hart, T., Tong, A., Chan, K., van Leeuwen, J., Seetharaman, A., Aregger, M., Chandrashekhar, M., Hustedt, N., Seth, S., and Noonan, A. (2017). Evaluation and design of genome-wide CRISPR/Cas9 knockout screens. bioRxiv. http://dx.doi.org/10.1101/117341.

Johnson, N.A., Slack, G.W., Savage, K.J., Connors, J.M., Ben-Neriah, S., Rogic, S., Scott, D.W., Tan, K.L., Steidl, C., Sehn, L.H., et al. (2012). Concurrent expression of MYC and BCL2 in diffuse large B-cell lymphoma treated with rituximab plus cyclophosphamide, doxorubicin, vincristine, and prednisone. J. Clin. Oncol. *30*, 3452–3459.

Koike-Yusa, H., Li, Y., Tan, E.-P., Velasco-Herrera, Mdel.C., and Yusa, K. (2014). Genome-wide recessive genetic screening in mammalian cells with a lentiviral CRISPR-guide RNA library. Nat. Biotechnol. *32*, 267–273.

Lawrence, M.S., Stojanov, P., Mermel, C.H., Robinson, J.T., Garraway, L.A., Golub, T.R., Meyerson, M., Gabriel, S.B., Lander, E.S., and Getz, G. (2014). Discovery and saturation analysis of cancer genes across 21 tumour types. Nature *505*, 495–501.

Lawrence, M.S., Stojanov, P., Polak, P., Kryukov, G.V., Cibulskis, K., Sivachenko, A., Carter, S.L., Stewart, C., Mermel, C.H., Roberts, S.A., et al. (2013). Mutational heterogeneity in cancer and the search for new cancer-associated genes. Nature *499*, 214–218.

Leiserson, M.D., Vandin, F., Wu, H.-T., Dobson, J.R., Eldridge, J.V., Thomas, J.L., Papoutsaki, A., Kim, Y., Niu, B., McLellan, M., et al. (2015). Pan-cancer network analysis identifies combinations of rare somatic mutations across pathways and protein complexes. Nat. Genet. *47*, 106–114.

Leiserson, M.D.M., Reyna, M.A., and Raphael, B.J. (2016). A weighted exact test for mutually exclusive mutations in cancer. Bioinformatics *32*, i736–i745.

Lenz, G., Wright, G., Dave, S.S., Xiao, W., Powell, J., Zhao, H., Xu, W., Tan, B., Goldschmidt, N., Iqbal, J., et al.; Lymphoma/Leukemia Molecular Profiling Project (2008). Stromal gene signatures in large-B-cell lymphomas. N. Engl. J. Med. *359*, 2313–2323.

Li, H. (2011). A statistical framework for SNP calling, mutation discovery, association mapping and population genetical parameter estimation from sequencing data. Bioinformatics *27*, 2987–2993.

Li, H., and Durbin, R. (2010). Fast and accurate long-read alignment with Burrows-Wheeler transform. Bioinformatics *26*, 589–595.

Li, H., Handsaker, B., Wysoker, A., Fennell, T., Ruan, J., Homer, N., Marth, G., Abecasis, G., and Durbin, R.; 1000 Genome Project Data Processing Subgroup (2009). The sequence alignment/map format and SAMtools. Bioinformatics *25*, 2078–2079.

Li, W., Köster, J., Xu, H., Chen, C.-H., Xiao, T., Liu, J.S., Brown, M., and Liu, X.S. (2015). Quality control, modeling, and visualization of CRISPR screens with MAGeCK-VISPR. Genome Biology *16*, 281.

Lohr, J.G., Stojanov, P., Lawrence, M.S., Auclair, D., Chapuy, B., Sougnez, C., Cruz-Gordillo, P., Knoechel, B., Asmann, Y.W., Slager, S.L., et al. (2012). Discovery and prioritization of somatic mutations in diffuse large B-cell lymphoma (DLBCL) by whole-exome sequencing. Proc. Natl. Acad. Sci. USA *109*, 3879–3884.

Love, C., Sun, Z., Jima, D., Li, G., Zhang, J., Miles, R., Richards, K.L., Dunphy, C.H., Choi, W.W., Srivastava, G., et al. (2012). The genetic landscape of mutations in Burkitt lymphoma. Nat. Genet. *44*, 1321–1325.

Magi, A., Tattini, L., Cifola, I., D'Aurizio, R., Benelli, M., Mangano, E., Battaglia, C., Bonora, E., Kurg, A., Seri, M., et al. (2013). EXCAVATOR: detecting copy number variants from whole-exome sequencing data. Genome Biol. *14*, R120.

Martin, M. (2011). Cutadapt removes adapter sequences from high-throughput sequencing reads. EMBnetjournal *17*, 10–12.

McKenna, A., Hanna, M., Banks, E., Sivachenko, A., Cibulskis, K., Kernytsky, A., Garimella, K., Altshuler, D., Gabriel, S., Daly, M., and DePristo, M.A. (2010). The Genome Analysis Toolkit: a MapReduce framework for analyzing next-generation DNA sequencing data. Genome Res. *20*, 1297–1303.

Meyer, M., and Kircher, M. (2010). Illumina sequencing library preparation for highly multiplexed target capture and sequencing. Cold Spring Harb Protoc. *6*, pdb.prot5448.

Monti, S., Savage, K.J., Kutok, J.L., Feuerhake, F., Kurtin, P., Mihm, M., Wu, B., Pasqualucci, L., Neuberg, D., Aguiar, R.C., et al. (2005). Molecular profiling of diffuse large B-cell lymphoma identifies robust subtypes including one characterized by host inflammatory response. Blood *105*, 1851–1861.

Morin, R.D., Mendez-Lago, M., Mungall, A.J., Goya, R., Mungall, K.L., Corbett, R.D., Johnson, N.A., Severson, T.M., Chiu, R., Field, M., et al. (2011). Frequent mutation of histone-modifying genes in non-Hodgkin lymphoma. Nature *476*, 298–303.

Papaemmanuil, E., Gerstung, M., Bullinger, L., Gaidzik, V.I., Paschka, P., Roberts, N.D., Potter, N.E., Heuser, M., Thol, F., Bolli, N., et al. (2016). Genomic classification and prognosis in acute myeloid leukemia. N. Engl. J. Med. *374*, 2209–2221.

Pasqualucci, L., Trifonov, V., Fabbri, G., Ma, J., Rossi, D., Chiarenza, A., Wells, V.A., Grunn, A., Messina, M., Elliot, O., et al. (2011). Analysis of the coding genome of diffuse large B-cell lymphoma. Nat. Genet. *43*, 830–837.

Quinlan, A.R., and Hall, I.M. (2010). BEDTools: a flexible suite of utilities for comparing genomic features. Bioinformatics *26*, 841–842.

Sanjana, N.E., Shalem, O., and Zhang, F. (2014). Improved vectors and genome-wide libraries for CRISPR screening. Nat Meth *11*, 783–784.

Scott, D.W., Wright, G.W., Williams, P.M., Lih, C.-J., Walsh, W., Jaffe, E.S., Rosenwald, A., Campo, E., Chan, W.C., Connors, J.M., et al. (2014). Determining cell-of-origin subtypes of diffuse large B-cell lymphoma using gene expression in formalin-fixed paraffin-embedded tissue. Blood *123*, 1214–1217.

Sehn, L.H., Berry, B., Chhanabhai, M., Fitzgerald, C., Gill, K., Hoskins, P., Klasa, R., Savage, K.J., Shenkier, T., Sutherland, J., et al. (2007). The revised International Prognostic Index (R-IPI) is a better predictor of outcome than the standard IPI for patients with diffuse large B-cell lymphoma treated with R-CHOP. Blood *109*, 1857–1861.

Shaffer, A.L., Wright, G., Yang, L., Powell, J., Ngo, V., Lamy, L., Lam, L.T., Davis, R.E., and Staudt, L.M. (2006). A library of gene expression signatures to illuminate normal and pathological lymphoid biology. Immunol Rev *210*, 67–85.

Shalem, O., Sanjana, N.E., Hartenian, E., Shi, X., Scott, D.A., Mikkelson, T., Heckl, D., Ebert, B.L., Root, D.E., Doench, J.G., and Zhang, F. (2014). Genome-scale CRISPR-Cas9 knockout screening in human cells. Science *343*, 84–87.

Shipp, M.; International Non-Hodgkin's Lymphoma Prognostic Factors Project (1993). A predictive model for aggressive non-Hodgkin's lymphoma. N. Engl. J. Med. *329*, 987–994.

Stewart, S.A., Dykxhoorn, D.M., Palliser, D., Mizuno, H., Yu, E.Y., An, D.S., Sabatini, D.M., Chen, I.S.Y., Hahn, W.C., Sharp, P.A., et al. (2003). Lentivirus-delivered stable gene silencing by RNAi in primary cells. RNA *9*, 493–501.

Trapnell, C., Pachter, L., and Salzberg, S.L. (2009). TopHat: discovering splice junctions with RNA-Seq. Bioinformatics *25*, 1105–1111.

Trapnell, C., Roberts, A., Goff, L., Pertea, G., Kim, D., Kelley, D.R., Pimentel, H., Salzberg, S.L., Rinn, J.L., and Pachter, L. (2012). Differential gene and transcript expression analysis of RNA-seq experiments with TopHat and Cufflinks. Nat. Protoc. *7*, 562–578.

Wang, K., Li, M., and Hakonarson, H. (2010). ANNOVAR: functional annotation of genetic variants from high-throughput sequencing data. Nucleic Acids Res. *38*, e164.

Wang, T., Wei, J.J., Sabatini, D.M., and Lander, E.S. (2014). Genetic screens in human cells using the CRISPR-Cas9 system. Science *343*, 80.

Wang, T., Yu, H., Hughes, N.W., Liu, B., Kendirli, A., Klein, K., Chen, W.W., Lander, E.S., and Sabatini, D.M. (2017). Gene essentiality profiling reveals gene networks and synthetic lethal interactions with oncogenic Ras. Cell *168*, 890–903.e15.

Wright, G., Tan, B., Rosenwald, A., Hurt, E.H., Wiestner, A., and Staudt, L.M. (2003). A gene expression-based method to diagnose clinically distinct subgroups of diffuse large B cell lymphoma. Proc. Natl. Acad. Sci. USA *100*, 9991–9996.

Yang, H., and Wang, K. (2015). Genomic variant annotation and prioritization with ANNOVAR and wANNOVAR. Nat. Protoc. *10*, 1556–1566.

Zhang, J., Grubor, V., Love, C.L., Banerjee, A., Richards, K.L., Mieczkowski, P.A., Dunphy, C., Choi, W., Au, W.Y., Srivastava, G., et al. (2013). Genetic heterogeneity of diffuse large B-cell lymphoma. Proc. Natl. Acad. Sci. USA *110*, 1398–1403.

Zhang, J., Jima, D., Moffitt, A.B., Liu, Q., Czader, M., Hsi, E.D., Fedoriw, Y., Dunphy, C.H., Richards, K.L., Gill, J.I., et al. (2014). The genomic landscape of mantle cell lymphoma is related to the epigenetically determined chromatin state of normal B cells. Blood *123*, 2988–2996.

Zou, H., and Hastie, T. (2005). Regularization and variable selection via the elastic net. J. R. Stat. Soc. Series B Stat. Methodol. *67*, 301–320.

STAR★METHODS

KEY RESOURCES TABLE

REAGENT or RESOURCE	SOURCE	IDENTIFIER
Chemicals, Peptides, and Recombinant Proteins		
Mirus TransIT-LT1	Mirus	MIR2305
Takara Ex Taq DNA Polymerase	Takara	RR001A
puromycin	Sigma Aldrich	P8833
blasticidin	Invivogen	Anti-bl-1
polybrene	Sigma Aldrich	H9268
Critical Commercial Assays		
AlamarBlue Cell Viability Reagent	ThermoFisher Sci	DAL1100
KAPA Stranded RNA-Seq Library Preparation Kit Illumina Platforms	KAPA Biosystems	KR0934 – v2.16
QIAamp DNA Blood Maxi kit	QIAGEN	51194
Surveyor Assay	IDT	706020
TOPO TA Cloning Kit	ThermoFisher	450641
Deposited Data		
Exome and RNA sequencing files	European Genome-Phenome Archive	EGA: EGAS00001002606
Experimental Models: Cell Lines		
OCI-LY3	DSMZ	ACC 761; RRID: CVCL_8800
Pfeiffer	ATCC	CRTL-2632; RRID: CVCL_3326
SU-DHL-4	ATCC	CRL-2957; RRID: CVCL_0539
BJAB	DSMZ	ACC 757; RRID: CVCL_5711
TMD8	Laboratory of Dr. Shuji Tohda	RRID: CVCL_A442
HBL-1	Laboratory of Dr. Richard E. Davis	RRID: CVCL_4213
Oligonucleotides		
AAVS1-forward: ccccgttctcctgtggattc	Wang et al., 2014	N/A
AAVS1-reverse: atcctctctggctccatcgt	Wang et al., 2014	N/A
rRNA removal Oligo	Listed in STAR Methods	N/A
Recombinant DNA		
LentiCas9-blast	Shalem et al., 2014	Addgene: 52962
GeCKO v2 Addgene Human sgRNA library	Sanjana et al., 2014	Addgene: 1000000049
psPAX2	Didier Trono	Addgene: 12260
pCMV-VSVG	Stewart et al., 2003	Addgene: 8454
Lentiguide-puro	Sanjana et al., 2014	Addgene: 52963
Software and Algorithms		
GATK v3.2	McKenna et al., 2010	https://software.broadinstitute.org/gatk/download/; RRID: SCR_001876
Burrows-Wheeler Aligner (BWA) v 0.7.7	Burrows-Wheeler Aligner (BWA)	http://bio-bwa.sourceforge.net/; RRID: SCR_010910
MuTect version 1.1.4	Cibulskis et al., 2013	http://archive.broadinstitute.org/cancer/cga/mutect; RRID: SCR_000559
Annovar	Wang et al., 2010	http://annovar.openbioinformatics.org/en/latest/user-guide/download/; RRID: SCR_012821
MutsigCV	Lawrence et al., 2013	http://software.broadinstitute.org/cancer/software/genepattern/modules/docs/MutSigCV

(*Continued on next page*)

Continued		
REAGENT or RESOURCE	SOURCE	IDENTIFIER
EXCAVATOR	Magi et al., 2013	https://sourceforge.net/projects/excavatortool/; RRID: SCR_012766
MAGeCK-VISPR v0.5.3	Li et al., 2015	https://bitbucket.org/liulab/mageck-vispr
TopHat	Trapnell et al., 2009	https://ccb.jhu.edu/software/tophat/index.shtml; RRID: SCR_013035
Cufflinks	Trapnell et al., 2012	http://cole-trapnell-lab.github.io/cufflinks/; RRID: SCR_014597
affinity propagation clustering	Frey and Dueck, 2007	CRAN: apcluster
elastic net regression	Zou and Hastie, 2005	CRAN: glmnet

CONTACT FOR REAGENT AND RESOURCE SHARING

Further information and requests for resources and reagents should be directed to and will be fulfilled by the Lead Contact, Sandeep Dave (sandeep.dave@duke.edu).

EXPERIMENTAL MODEL AND SUBJECT DETAILS

DLBCL patients

Diffuse Large B Cell Lymphoma (DLBCL) tumors (N = 1001) and paired-normal tissue (N = 400), along with patient clinical information, were obtained from the institutions listed in the affiliations section. All cases were required to be *de novo* (i.e., not relapsed or transformed disease) and treated with a rituximab-containing standard regimen. All cases were reviewed by experienced hematopathologists. These cases were anonymized, shipped to Duke University, and processed in accordance with a protocol approved by the Institutional Review Board at Duke University. Clinical data including initial response to therapy, overall survival, gender, age, stage, performance status and number of extranodal sites were collected on nearly all cases.

Cell lines for CRISPR screening

OCI-LY3 were grown in RPMI 1640 (GIBCO) with 20% HI-Fetal bovine serum and 1% Penicillin-Streptomycin (5,000 U/mL) (ThermoFisher). Pfeiffer, SU-DHL-4, BJAB, TMD8, and HBL-1 were grown in RPMI 1640 (GIBCO) with 10% HI-Fetal bovine serum and 1% Penicillin-Streptomycin (5,000 U/mL) (ThermoFisher). All cell lines were grown at 37C. OCI-LY3, TMD8, SU-DHL-4, Pfeiffer, and HBL-1 are derived from males, and BJAB is derived from a female. Cell lines were authenticated through whole exome sequencing (Zhang et al., 2013).

METHOD DETAILS

Sample processing

Total RNA and DNA was extracted from samples using the AllPrep DNA/RNA FFPE kit (QIAGEN, Cat. # 80234) per manufacturers guidelines. Briefly, paraffin was removed with Xylene, and the resulting tissue was washed once with 100% ethanol, and digested with PKD and proteinase K for 15 minutes at 56 C. The tissue was spun at full speed in a microcentrifuge, and the supernatant containing the RNA was bound to a column, washed with FRN buffer, treated with DNase I, washed with RPE buffer and eluted in 30 ul of water. The pellet was further digested in ATL and proteinase K for 1 hour at 56 C followed by 2 hours at 90 C. The DNA was bound to a column, washed and eluted in 100 ul of EB.

High-throughput exome library preparation

Genomic DNA was sheared to 250 bp using the Covaris S2 platform. A custom, in-house exome library preparation process based on the Agilent XT2 pooled exome capture method was designed to meet the need to create over 1400 sequencing libraries within a reasonable time frame. To increase the throughput of exome library preparation, a custom 96-well barcode system was designed based on the Illumina sequencing system whereby a separate sequencing read is used to identify the barcode of a particular library. Custom barcodes of length 8, compatible with the 3-read Illumina hiseq v2 platform, were designed using scripts available at https://bioinf.eva.mpg.de/multiplex/ (Meyer and Kircher, 2010). The barcodes were designed to maximize capture efficiency, edit distance among one another, and sequence quality. An edit distance of 3 or greater was enforced, as well as standard channel balancing for optimal base diversity at each sequencing cycle.

Oligonucleotides were ordered with standard Illumina barcode modifications of 5′ phosphorylation, a phosphorothioate bond between the last two bases on the 3′ end, and HPLC purification. Oligonucleotides were annealed by standard protocols and diluted to a 15 μM working concentration in EB. The barcode sequences that we utilized are shown below.

Sequences for the 96 custom barcodes used in high-throughput library preparation.

CTATGCTG	GGATTCGT	AGCGGATA	TCGCTTAA	TCATACGC	AACGATGA
CAATCGAA	GCGAACTA	GGTCGTTA	GTTCAAGC	CCTAACTC	ATCTGACG
ACCATGCA	CTCGCTAT	GTTGAGGT	GGTAAGAC	AAGCGAAG	CGTACTAG
TGCAATCG	AGGCTACT	TCTAGCAA	ACGGTTGA	GAGCATCA	ATCCGAAC
AGCTCATC	GTCTATCC	ACCTGCTT	AGAGCGAA	AGAGCTCT	CAACTACC
GATCAGTC	GTTATGCG	GTTGCCTA	TATCAAGA	AAGAGCTT	ACTTCCAT
CTACTCCT	TCGTTAGA	GTCATTAT	GAACGAGT	TGATGCAA	TGGCAGTA
TAGATACC	GACGTCAA	TTGATAGG	CGTAAGGT	CTAGTCAG	TCTTCTGA
CAACCTCA	CTACCATG	TAGTCTAC	ACTAGAGG	AGAACCGT	TACGCGTA
CTTATCTT	AAGGTCCA	CCAGTAAT	CGCTATAG	CCATGGTT	AACTGCAG
ACGCATTG	ACCAGTTC	TGACCTAG	TATGATGG	AGGTTGCA	TAATGCGT
TGATCTGC	CCTGATCT	ACCAAGGT	GAAGGATA	GCATCGTA	GGAACGTT
TAGCGATA	CATCGCAT	TGACTAGC	TGCTTACC	AAGCCGTA	TCTTGGAC
TCCGATTG	TATCTGCG	ACTGGATC	ACTACTCT	CTCTTGCT	CTCGAAGT
GATACTCG	TCGATCTG	TGGATTGC	GGAAGTAC	GATGGTAG	ACGTACGT
CATGAGGA	GCTCTATC	TTAAGCGC	CTGAGCAA	CGCCTATA	CTGGACTT

Pre-capture libraries were prepared with standard library preparation protocols using the KAPA Hyper kit (Kapa Biosystems, Wilmington, MA), and then pooled at equal volume and sequenced on the Illumina platform at low depth to determine exact relative abundances. Based on these abundances, libraries were balanced optimally for exome using the Agilent All Exon V5 human bait set. Library sequencing was performed to an average of 75X coverage on Illumina Hiseq 2500 platform.

Exome Sequence Alignment

Reads in fastq format (Cock et al., 2010) were pre-processed with GATK (McKenna et al., 2010) version 3.2 to remove Illumina adaptor sequences (analysis type –T ClipReads, -XF <illumina.adapters.fa>) and Phred-scaled base qualities of 10 and below (-QT 10) similarly to described previously (Sehn et al., 2007; Zhang et al., 2013; Zhang et al., 2014). The adapter sequences are provided below.

```
>Adapter 1
AGATCGGAAGAGCACACGTCTGAACTCCAGTCAC
>Adapter 2
AGATCGGAAGAGCGTCGTGTAGGGAAAGAGTGTA
>Adapter 3
GATCGGAAGAGCTCGTATGCCGTCTTCTGCTTG
>Adapter 4
ACACTCTTTCCCTACACGACGCTCTTCCGATCT
>Adapter 5
AGATCGGAAGAGCGGTTCAGCAGGAATGCCGAG
>Adapter 6
AGATCGGAAGAGCGTCGTGTAGGGAAAGAGTGTA
>Adapter 7
AATGATACGGCGACCACCGAGATCTACACTCTTTCCCTACACGACGCTCTTCCGATCT
>Adapter 8
CAAGCAGAAGACGGCATACGAGATCGGTCTCGGCATTCCTGCTGAACCGCTCTTCCGATCT
```

After GATK processing, reads were mapped to hg19 using Burrows-Wheeler Aligner (BWA) (Li and Durbin, 2010) version 0.7.7 with the mem algorithm. Reads were sorted with Novoalign V2.08.03 novosort. SAMtools (Li et al., 2009) flagstat was used to compute the number and percent of reads that mapped to the genome. Both depth and breadth of coverage for each exome were computed using BEDTools (Quinlan and Hall, 2010). PCR/optical duplicates were marked by Picard. Base quality recalibration and indel realignment was performed using GATK (McKenna et al., 2010).

Variant and gene filtering, analysis of significantly mutated genes

Joint variant calling was performed on all 1001 DLBCL samples together using Samtools (Li, 2011) mpileup v. 0.1.19 and somatic variant calling was performed using MuTect version 1.1.4 (Cibulskis et al., 2013) for the tumor/normal pairs. This resulted in a total of ~1.1 million variants. The variant functions and population statistics were annotated using Annovar (Wang et al., 2010; Yang and Wang, 2015). The MuTect somatic mutations were used as a high-quality discovery dataset for identifying mutated genes. Variant filtering was performed using the following criteria: select exonic, not synonymous variants, somatic variants, rare and damaging variants, exclude duplicate frameshifts that were found in multiple samples, variants found in repetitive regions, variants found in regions with poor coverage. Additionally, each variant was required to have an instance of genotype quality greater than 30 and read depth greater than 5.

Driver gene analysis was performed using a combination of three approaches: (i) MutsigCV (Lawrence et al., 2013) which identifies driver genes with point mutations above the background mutation rate; and (ii) Hotnet2 (Leiserson et al., 2015) which identifies subnetworks of genes based on protein interactions; and (iii) the model we have applied previously (Love et al., 2012) to factor in copy number alterations, gene variability and the enrichment of rare (EXAC frequency less than 0.001), functional variants (CADD score greater than 10), as well as the proximity of SNVs to each other. Gene with very low expression levels across samples were excluded.

Copy Number Analysis

We estimated copy number aberrations in the 1001 DLBCLs using EXCAVATOR (Magi et al., 2013) in the pooled mode, against a set of 15 high quality normal samples. Normals were also run against normals to control for normal variation and population artifacts. Copy number segmentation is performed to smooth the exon-level counts. This resulted in the sample x gene copy number matrix. Integrative analysis of mutations and copy number variations was performed to identify driver genes. Amplifications and deletions were defined using thresholds of +1 and −1 respectively on log ratios.

Comparing FFPE versus fresh frozen samples in matched patients

We performed parallel whole-exome sequence analysis of 34 sets of paired FFPE and frozen tumors, with each pair obtained from the same patient. The cases ranged in age from 4 years to 16 years, allowing us to determine the effect of sample age. We evaluated our overall mutation discovery sensitivity compared to previous DLBCL studies utilizing fresh-frozen biopsies by preparing paired FFPE and frozen biopsies from the same DLBCL case prepared and whole exome sequenced identically. The similarity metric between any two sequencings was computed with the Jaccard similarity metric, or the number of variants shared as fraction of the union of the variants in the two samples being compared. With the frozen case as the gold standard in any given pair, the Jaccard metric is sensitive to both false positives (increases denominator) and false negatives (decreases the numerator). An overall score of 0 equates to no overlap, and an overall score of 1 equates to complete overlap. We found that the similarity coefficient between the genomic profiles from the same patient derived from FFPE versus frozen biopsies was completely preserved regardless of the age of the specimen. The results are summarized in the heatmap in Figure S1, with an adjoining bar graph indicating sample age. These data indicate that, at least for specimens that are less than 16 years of age, we can reliably identify mutations from FFPE cases at the same rate as frozen cases.

We also examined a potential concern with respect to FFPE samples is that the preservation method may cause some regions of the genome to be sequenced unevenly, resulting in poor sensitivity to somatic mutation detection in some portions of the genome. The violin plots in Figure S1 (right panel) show that the total variant distribution is equivalent between FFPE and frozen samples and that the recovery of somatic variants was equivalent ($p = 0.49$, Wilcoxon rank-sum test). These results demonstrate that with appropriate processing and analysis, FFPE cases can be used to generate mutational data that are equivalent to those generated from frozen cases.

Comparing tumors with matched normal versus unpaired tumors

To check for biases between tumors with paired normal ($N = 400$) and the unpaired tumors ($N = 601$), we have directly compared their mutational patterns and frequency for the set of 150 driver genes. The heatmap of genetic alterations for the paired and unpaired samples is shown in Figure S2A, which shows very similar patterns for the two groups. The scatterplot of mutational frequency for these two set of samples is shown in Figure S2B. The mutational frequencies are essentially identical ($R^2 = 0.94$, $p < 10^{-6}$).

CRISPR Screen

To generate GeCKO.v2 library virus, 293T cells were seeded in 15 cm dishes at 12 million cells per dish. The following day, cells were transfected using TransIT-LT1 (Mirus) according to manufacturer's instructions with 10 μg lentivector, 10 μg psPAX2 and 1 μg pCMV-VS. 16 hours post transfection, media was changed. Virus was harvested at 48 and 72 hours post transfection, pooled, filtered, aliquoted and stored at −80 until needed for screening.

DLBCL cells stably expressing Cas9 were generated by transduction of cells with lentiCas9-blast virus at multiplicity of infection (MOI) < 1. Forty-eight hours post transduction, cells were selected with 10 ug/ml blasticidin for four or five days and expanded. Cas9 activity in each stable cell line was confirmed by transduction with a control sgRNA targeting the AAVS1 locus (ggggccactagggacaggat) (3), followed by Surveyor assay (IDT) and Sanger sequencing of AAVS1 to assess editing rates. Sanger sequencing was performed on AAVS1 PCR product after cloning into the pCR 2.1 TOPO TA vector. For the TMD8 and HBL1 cell lines, single cell cloning was needed to isolate Cas9-expressing cells with > 80% editing efficiency after testing with the AAVS1 sgRNA.

Cas9-expressing cells were transduced with the human GeCKO.v2 library virus pools with 8 μg /ml polybrene using conditions to obtain MOIs between 0.3-0.5 and 1000-fold representation of the library after selection. Subpools A and B of the GeCKO library were transduced into cells and screened separately in triplicate. 24-48 hours post transduction, cells were selected with 2 μg /ml puromycin for 72 hours. Some cells were harvested after puromycin selection to serve as the initial time point sample as well as after 14 population doublings. 1000-fold representation of the library was maintained at each passage.

Genomic DNA was harvested from each time point sample using the QIAamp Blood Maxi Kit according to manufacturer's instructions. The sgRNA cassettes from each sample were amplified and barcoded for multiplexing from 50-100 μg of genomic DNA with two rounds of PCR with Takara Ex Taq DNA polymerase as previously described. PCR products were gel purified and isopropanol precipitated for sequencing on the HiSeq2500.

Normalized sgRNA abundance quantification for CRISPR screen

Guide RNA (sgRNA) amplicon sequencing reads for each library were downloaded from Hudson Alpha as de-multiplexed FASTQ files. Raw reads were then trimmed using CutAdapt v1.8.3 (Martin, 2011) to remove 5′ barcoded adaptor sequences (33-38bp) specific to each library and 3′ PCR primer sequences (20bp). Reads were discarded if both barcode sequences could not be identified or if the resulting trimmed read was longer than 25bp or shorter than 15bp (cutadapt -g^ < 5primeadapter > -a < 3primeadapter > -e 0.25 -m 15 -M 25). Successfully trimmed reads were aligned to the GeCKO v2 (Sanjana et al., 2014) sgRNA library using MAGeCK-VISPR v0.5.3 (Li et al., 2015) under default settings (no mismatches allowed) to produce a raw count table of sgRNAs across cell line replicates. The resulting count table was then normalized to account for sampling differences using the variance-stabilizing transformation implemented in the MAGeCK count module.

Statistical Estimation of Gene Knockout Fitness Effects on Cell Lines

CRISPR gene scores were used to quantify the magnitude and directionality of fitness effects from normalized sgRNA counts as in (Aguirre et al., 2016). Briefly, under a scenario in which there are m total genes being screened in cell line j, the CRISPR gene score for gene i targeted by n sgRNAs is given by the following equation:

$$crisprgenescore_{ij} = \frac{\sum_{k=1}^{n} sgRNA\ score_{ijk}}{n}$$

where $sgRNA\ score_{ijk}$ is given as the z-score transformation of the log-fold change between early and late samples in cell line j for a sgRNA k targeting gene i:

$$sgRNAscore_{ijk} = log2\left(\frac{Latecount_{ijk}}{earlycount_{ijk}}\right)$$

$$sgRNAscore_{ijk} = \frac{sgRNAscore_{ijk} - \overline{sgRNAscore_j}}{sd(sgRNAscorej)}$$

Accounting for genomic copy number in CRISPR screen

In lieu of cell line-level copy number data, we used the sliding window method used by (Wang et al., 2017) to identify suspect genomic regions where CRISPR scores might reflect genomic amplification. Briefly, we computed a neighborhood score for each gene by counting the number of low CRISPR scores (< 5^{th} percentile for a cell line) in the 40 gene genomic window surrounding the gene (20 "upstream genes," 20 "downstream" genes). Genes were removed from further consideration if their genomic neighborhood score was > 12 to minimize the confounding influence of genomic copy number on our analysis of essential DLBCL genes.

CRISPR screen quality control

Basic sequencing quality statistics were computed for both raw and trimmed libraries using FastQC (Andrews, 2010). Basic count table quality metrics, including alignment rate and two measures of sgRNA evenness (zero count sgRNAs, Gini Index) were determined using MAGeCK-VISPR. Pairwise Pearson correlation coefficients were used to measure the degree of correlation between cell line replicates. To further investigate the concordance among biological replicates, Principal Components Analysis (PCA) was performed using log-transformed normalized sgRNA counts.

We generated an average of 26.9 million reads per time-point (range: 14.2 million to 49.3 million), yielding an average of 224 reads/sgRNA for each library. After filtering and trimming reads to remove adaptor sequences and low-quality reads, an average of 57.6% of reads aligned with perfect identity to the GeCKO sgRNA reference (range: [42.8% – 64.4%]), resulting in an median effective sgRNA coverage of 121.8 mapped reads/sgRNA (range: [65.5 – 228.9]). Broadly, the depth and quality of sequence data generated for sgRNA amplicon libraries falls within acceptable levels sufficient for differential abundance testing between early and late cell populations.

As shown in Figure S3, sequencing reads appeared to be uniformly distributed across sgRNAs in early time point libraries (median Gini index = 0.12; range [0.10 – 0.132]; ~0.1 typically acceptable for early time points) with an acceptably small percentage of sgRNAs

absent from each library (median zero count sgRNAs = 657; 0.5% of total sgRNAs; range [496 – 1559]). As expected, the distribution of sequencing reads across sgRNAs was significantly more uneven in late time point samples (median Gini Index = 0.21; range [0.16 – 0.42]), with significantly more sgRNAs missing from these sequencing libraries altogether (median zero count sgRNAs = 4654 sgRNAs; 3.7% of total sgRNAs; range [1901 – 16835]). Critically, we found no relationship between sequencing depth and the number of missing sgRNAs ($R^2 = 0.012$, $p = 0.64$), suggesting a biological explanation for their absence (i.e., negative selection). Though these results fall within acceptable ranges (Gini Index < 0.2) for the majority of late samples, the uneven sgRNA distribution among late samples was especially pronounced in TMD8 and Pfeiffer cell lines. Because of this we were careful to interpret downstream patterns of sgRNA abundance driven primarily by TMD8 and Pfeiffer.

Changes in sgRNA abundance over the course of the experiment were largely consistent within cell lines and—to a lesser degree—across cell lines. GuideRNA abundance was sufficiently correlated among late time point libraries for most cell lines. The median pairwise correlation between late samples for each cell line was 0.72 (Pearson's r; range [0.56 – 0.80]). This pattern was supported by Principal Component Analysis (PCA), which shows sgRNA abundance in late populations cluster by cell line along the first two PCs (Variation explained: PC1 = 18.7%, PC2 = 13.1%). Notably, sgRNA abundances from late time point TMD8 and Pfeiffer samples form distinct clusters along these axes apart from the primary cluster containing other cell lines.

To assess the degree to which previously known fitness effects were recapitulated by our CRISPR screen, Mann-Whitney U-tests were used to test whether the mean CRISPR score of previously described universally essential genes was significantly less than 0. Two sets of universally essential genes were chosen from the literature (Hart et al., 2014; Hart et al., 2017) on the basis of experimentally demonstrated essentiality across multiple human cell lines in previous CRISPR screens (downloaded from http://tko.ccbr.utoronto.ca/). Additionally, we used a permutation test to determine whether the mean CRISPR score of universally essential genes was significantly less than could be expected for a set of randomly chosen genes (NPERM = 9999).

Broad patterns of gene fitness inferred from sgRNA abundance changes were largely consistent with biological expectation and results from previous CRISPR screens. Shown in Figure S3, we found that sgRNAs with significantly decreased abundance were more likely to be members of KEGG genes sets for critical cellular functions including ribosomal biosynthesis, DNA replication, transcription, and translation, indicating negative selection against the loss of these genes in cells. Additionally, sgRNAs targeting genes that had been previously demonstrated to be essential across multiple human cell types resulted in significantly decreased cell fitness relative to randomly chosen sgRNAs (avg. CRISPR score = −0.153; CRISPR $score_{essential}$ = CRISPR $score_{random}$: p = 0; NPERM = 9999). By contrast, non-targeting control sgRNAs showed a significant increase in cell fitness relative to randomly chosen sgRNAs (avg. CRISPR score = 1.15; CRISPR $score_{control}$ = CRISPR $score_{random}$: p = 0; NPERM = 9999). Collectively, these results suggest that changes in sgRNA frequency over the course of the experiment likely reflect real changes in cell fitness induced by targeted gene silencing via the CRISPR/Cas9 complex.

Identification of "essential" DLBCL genes

Paired Mann-Whitney U tests were used to determine whether there was a significant ($\alpha = 0.05$) difference between the average sgRNA counts at early and late time points for each gene in each cell line. Early and late sgRNA counts from the same replicate population were considered as pairs. Normalized sgRNA counts were log-transformed (log2 [1 + sgRNA count]) prior to significance testing to minimize the effects of outliers. Additionally, p values were adjusted for multiple comparisons using the FDR method implemented in the R statistical environment.

Genes were assessed for significance at the pan-DLBCL and disease subtype-level (ABC/GCB) only if a significant effect was observed in at least one cell line. If observed, replicates from multiple cell lines were considered as a single cell line and assessed for significance using paired Mann-Whitney U tests as above.

Essential DLBCL genes were identified from the set of ~21,000 screen genes using two sets of criteria. Under the most stringent criteria, a gene was considered significant if (i) its' FDR was < 0.05 at the DLBCL, GCB, or ABC-level and (ii) a significant effect was observed in at least 2 cell lines. A more relaxed set of criteria was used to identify essential driver genes among the 161 most commonly mutated genes in DLBCL cases. These genes were considered significant if (i) a significant effect (p < 0.05) was observed in at least one cell line and (ii) an extreme CRISPR score (absolute value > 1) was observed in at least two cell lines.

RNA sequencing library preparation and analysis

We removed rRNA from total RNA by hybridization to homologous rRNA DNA oligonucleotides (IDT, 200pmol Ultramer DNA oligos) by incubating in a thermocycler at 95 C for 2 minutes, followed by ramping down the temperature −0.1 C every 1 s until the temperature reached 45 C (Adiconis et al., 2013). The rRNA and DNA oligos that formed double stranded DNA/RNA complexes were then digested with RNase H (New England Biolabs, Cat. # M0297) for 30 minutes at 45 C. The remaining DNA oligos were then digested with DNase I (New England Biolabs, Cat. # M0303) for 30 minutes at 37 C.

RNA libraries were prepared using the Stranded mRNA-seq kit (Kapa Biosystems, Cat. # KK8401) per manufacturers guidelines. Briefly, cDNA was generated using random hexamer primers followed by A-tailing. The P5 and P7 universal sequencing adaptors containing specific 8-mer index sequences were ligated to the A-tailed cDNA. For this, we generated adaptors containing the P5 and P7 sequencing primers with 96 specific index sequences (Supplementary Appendix). The resulting libraries were PCR amplified and pools of 96 were quantified using the Bioanalyzer (Agilent). To identify the breakdown of indexes within the pools,

they were run on the MiSeq instrument using the Miseq reagent kit V2 50 cycles (Illumina, Cat. #MS-102-2001). Using the percent index value, the approximate concentration was normalized and calculated.

To improve the sensitivity and specificity of RNaseq in FFPE cases, RNaseq libraries were hybridized to Human All Exon V6 + 3′ UTR capture baits (Agilent, Cat. #5190-9306) as described previously (Cieslik et al., 2015). Each capture pool contained 24 libraries at 50 ng each for a total of 1200 ng of DNA. The pools were lyophilized using the speed vacuum technique. The libraries were first denatured and blocked at 95 C for 5 minutes, followed by holding at 65 C. The capture baits were mixed with RNase OUT and incubated for 2 minutes at 65 C. Hybridization buffer was mixed with the baits, followed by addition of the denatured libraries. The hybridization reaction was held at 65 C for 24 hours, followed by washing and amplification. These sequencing libraries were assessed for quality with the Bioanalyzer 2100 (Agilent) using the Agilent DNA 1000 Kit per manufacturer's instructions. Libraries of high quality (e.g., with size distribution between 120-400bp and sufficient quantity for sequencing) were subjected to high throughput sequencing using the Illumina HiSeq 2500 platform per manufacturer's instructions using HiSeq V4 125 PE, to generate an average of 10 million reads per sample.

The sequencing reads were aligned using TopHat, a spliced read aligner which allows for sequencing reads to span multiple exons (Trapnell et al., 2009). On average, we were able to align 80% of the sequencing reads for each sample to the reference genome. The Cufflinks software package was then used for reference-based transcript assembly and quantification of gene and transcript level expression (Trapnell et al., 2012). Using the Cufflinks package, we quantified the number of reads mapping to each exonic locus as exon fragments per kilobase of exon per million fragments mapped (FPKM) (Trapnell et al., 2012).

Gene expression measurements were FPKM normalized. To enable broad gene expression signature discovery and validation, we omitted 151 samples with expression of fewer than 12,000 genes owing potentially to either technical or biological artifacts. The remaining 624 cases were designated as the core set for the integrative analysis (Table S2). Additionally, quantile normalization was performed to remove the effects due to technical variation, and the data was log2 normalized.

Defining correlated gene signatures

We define gene signatures using a collection of widely used annotated gene set databases (Kegg, Reactome, Biocarta, Gene Ontology, MSigDB), as well as several lymphoma-specific gene signature sources (Lenz et al., 2008; Monti et al., 2005, and SigDB from Staudt et al.). We then test these signatures for significant correlation in our expression dataset by utilizing a permutation test that compares these gene sets to random gene sets of the same size. With n = 500 permutations, we randomly sample without replacement from the universe of genes in the dataset. Then the pairwise correlation between all genes is calculated and the average of that matrix across the whole gene set is used as the test statistic. This test statistic is calculated for each gene set of interest and compared to the appropriate null distribution, given the number of genes in the set. Significant gene sets are those whose p value when compared to the null distribution is less than $5x10^{-3}$, whose test statistic is > 0.1, and whose proportion of gene-gene correlations above 0.5 is greater than 5%.

Sources for gene sets.

Pathway Collection	Abbreviation	Original Pathway Source
Biocarta	BIOCARTA	http://www.biocarta.com/
Kegg	KEGG	http://www.genome.jp/kegg/
Reactome	REACTOME	http://www.reactome.org/
NCI Pathway Interaction Database	PID	http://www.ndexbio.org/
Sigma Aldrich	SA	http://www.sigmaaldrich.com/
Signaling Gatemway	SIG	http://www.signalinggateway.org/
Signaling Transduction	ST	http://stke.sciencemag.org/
Matrisome	NABA	http://matrisome.org/
Gene Ontology	GO	http://www.geneontology.org/
MSigDB Oncogenic Signatures	ONCO	MSigDB, Various publications
MSigDB Hallmark Signatures	HALLMARK	http://doi.org/10.1016/j.cels.2015.12.004
Panther Pathway Database	PANTHER	http://www.pantherdb.org/
Netpath Database	NETPATH	http://www.netpath.org/
HumanCyc Pathways	HUMANCYC	https://humancyc.org/
Institute of Bioinformatics Pathways	IOB	http://www.ibioinformatics.org/
Xcell Algorithm Genesets	XCELL	http://xcell.ucsf.edu/
Cibersort Algorithm Genesets	CIBERSORT	https://cibersort.stanford.edu/
Lenz et al., 2008 signatures	LENZ	http://doi.org/10.1073/pnas.0804295105
Staudt lab Signature DB	SIGDB	https://lymphochip.nih.gov/signaturedb/
Monti et al., 2005 signatures	MONTI	http://doi.org/10.1182/blood-2004-07-2947

Clustering gene signatures

We clustered the significantly correlated gene sets using affinity propagation clustering (Frey and Dueck, 2007). Affinity propagation is a clustering algorithm that simultaneously identifies clusters and exemplars (cluster representatives) in the data without the user specifying the number of clusters (k) to be identified. The algorithm starts by considering all samples to be exemplars, and then by iteratively exchanging messages between data points until it converges to an optimal set of exemplars and clusters.

Using affinity propagation on the 1228 significantly correlated gene sets we obtained 31 clusters. Exemplar names were manually curated to best represent the gene signatures that were part of the cluster.

Association of genetic alterations with gene expression signatures

Genetic alterations were encoded as missense mutations, truncating mutations, copy number gains and copy number deletions. We tested for associations between genetic alterations and gene expression signature using ANOVA. Multiple hypothesis correction was performed using Benjamini-Hochberg test.

Association of gene expression signatures with CRISPR hits and survival

We identified significantly enriched genesets associated with CRISPR hits using Fisher's test ($p < 0.05$ & Odds ratio > 1). Exemplar genesets related to proliferation and cell cycle exemplar were significantly associated with CRISPR hits.

We identified exemplar genesets associated with survival using logrank test ($p < 0.05$). Interestingly, 16 out of the 31 exemplars were significantly associated with survival. Exemplars related to stromal signatures were associated with better prognosis, while exemplar genesets related to proliferation were associated with worse prognosis.

Classification of DLBCL into ABC and GCB subtypes

Genes previously associated with ABC/GCB classification were used to classify samples into ABC/GCB subgroups (Wright et al., 2003) (table below). Gene expression data used for this analysis are shown in Table S2.

ensembl_ID	gene_name	Subtype associated with gene
ENSG00000143772	*ITPKB*	GCB
ENSG00000196549	*MME*	GCB
ENSG00000113916	*BCL6*	GCB
ENSG00000185697	*MYBL1*	GCB
ENSG00000105339	*DENND3*	GCB
ENSG00000119408	*NEK6*	GCB
ENSG00000135363	*LMO2*	GCB
ENSG00000118308	*LRMP*	GCB
ENSG00000170054	*SERPINA9*	GCB
ENSG00000131370	*SH3BP5*	ABC
ENSG00000137265	*IRF4*	ABC
ENSG00000137193	*PIM1*	ABC
ENSG00000138185	*ENTPD1*	ABC
ENSG00000095585	*BLNK*	ABC
ENSG00000118971	*CCND2*	ABC
ENSG00000139083	*ETV6*	ABC
ENSG00000033170	*FUT8*	ABC
ENSG00000104081	*BMF*	ABC
ENSG00000172349	*IL16*	ABC
ENSG00000196396	*PTPN1*	ABC

Quantile normalized and log2 transformed gene expression measurements were z-normalized across the genes. The ABC and GCB-specific scores were computed for each sample by taking the average of the z-scores for ABC, GCB genes respectively. A combined RNAseq subtype score was then computed by taking the difference in the ABC-specific score to the GCB-specific score. A sample was classified as ABC if the RNAseq subtype score was > 0.25 and its GCB score was < 0.75; and it was classified as GCB if the combined score was < -0.25 and its ABC score < 0.75. The rest of the samples belonged to the unclassified group. The classification schema is described in detail below.

$$E_{ij} = \text{sample x gene expression matrix for samples } i = 1, \ldots, |\text{samples}| \text{ and } j = 1, \ldots, |\text{genes}|$$

$$\text{ABCscore}_i = \frac{\sum_{j=1,\ldots,|\text{ABC\_genes}|} E_{ij}}{|\text{ABC\_genes}|}$$

$$\text{GCBscore}_i = \frac{\sum_{j=1,\ldots,|GCB\_genes|} E_{ij}}{|GCB\_genes|}$$

$$\text{RNAseqSubtypeScore}_i = \text{ABCscore}_i\text{-GCBscore}_i$$

$$\text{RNAseqSubtype}_i = \left\{ \begin{array}{c} \text{ABC if RNAseqSubtypeScore}_i > 0.25 \\ \text{GCB if RNAseqSubtypeScore}_i < -0.25 \\ \text{Unclassified otherwise} \end{array} \right\}$$

This results in 313 samples being classified as ABC DLBCL, 331 samples being classified as GCB DLBCL and 131 as Unclassified. The gene expression data for this classification is included in Table S2.

Validation of the RNaseq ABC/GCB classifier

NanoString Lymph2Cx ABC/GCB

In order to validate the RNaseq based subtype calls, we profiled 200 samples using the NanoString-based Lymph2Cx assay(Scott et al., 2014). We obtained NanoString linear predictor score (LPS) as well ABC/GCB calls from the Lymph2Cx assay. The RNaseq subtype scores are highly correlated to the NanoString LPS score ($R2 = 0.87$, $p < 10^{-6}$).

Hans GCB/non-GCB calls

Additionally, we obtained immunohistochemistry-based Hans GCB/non-GCB calls (Hans et al., 2004) for 522 samples. There is also a high degree of concordance between the Hans calls and the RNaseq-based subtypes ($p < 10^{-6}$).

MYC and BCL2 expression and translocations

In our study, we used log2 transformed RNaseq expression data for *MYC* and *BCL2* and defined high expressors based on cutoffs trained from immunohistochemistry (IHC) data. We ran IHC for *MYC* (N = 284) and *BCL2* (N = 404) and defined positive and negative IHC groups based on a cutoff of 40% and 50% respectively (Table S1). High expressors were defined from RNAseq data as *MYC*-high and *BCL2*-high and were significantly associated with survival (*MYC* p = 0.0025 and *BCL2* p = 0.01). Double expressors were defined as samples that have both high expression of *MYC* and high expression of *BCL2* (N = 149, p = 0.0002).

We assessed the independence of ABC/GCB subgrouping and double expressors (high *MYC* and *BCL2*) by stratifying for ABC/GCB within the double expressors (N = 154). Survival plot in Figure S4 shows that ABC/GCB status does not further stratify the double expressors (p = 0.415).

We separately examined the association of translocations in *MYC* and *BCL2* with mutations and expression by performing fluorescent *in situ* hybridization using both genes to define translocations involving the immunoglobulin locus and *MYC* and *BCL2* (performed separately).

We profiled these translocation events using FISH for *MYC* and *BCL2* in 126 DLBCLs. We found that *MYC* had a total of 14 translocations, while *BCL2* has 26 translocations. We examined the associations between translocations and expression, mutations and copy number events (Figure S4). *MYC* translocations are associated with high expression (p = 0.027). We found that nearly 80% of the cases with *MYC* mutations also had a translocation in *MYC*, whereas only 10% cases with wild-type *MYC* also had a translocation of the gene (p = 0.005), while we don't see an association with copy number amplifications. *BCL2* mutations are strongly associated with translocations (p = 4E-6) and amplifications are also associated with translocation events (p = 0.03). BCL2 translocations have a trend toward higher expression, but the association is not statistically significant.

Survival plots of *MYC*, *BCL2* translocations and double hits – *MYC* and *BCL2* or *BCL6* translocations do not show significant differences in the translocated cases (Figure S4).

Genomic risk model

We developed a supervised learning approach for defining the association of survival with combinations of the following genetic and molecular features: (a) known expression subgroups (ABC, GCB subgroups, *MYC*, and *BCL2* high expression), (b) the mutations/copy number events in the 150 DLBCL-associated genes identified in this study. We use a comprehensive approach by first defining combinatorial features derived from genetic and molecular features.

A schematic of our predictive modeling workflow is shown in Figure 5C. The first step of our method involves enumerating all possible combinations that involved up to 4 separate genetic and molecular features (degree $\leq$ 3) and affected a minimum of 20 patients (coverage > = 20). This approach identified 313 combinatorial features, which includes 95 singletons, 166 pairs, 52 triplets. These combinatorial features formed the input for the survival predictive model.

We used elastic net regression (Zou and Hastie, 2005) with a Cox proportional hazards model. Elastic net is a regularized regression framework that is a linear combination of the L1 (Lasso regression) and L2 (Ridge regression) penalties. Ridge regression tends to favor lower coefficients and to keep correlated features in the model, while lasso regression tends to shrink the number of features in the model. Elastic net combines the advantages of these two methods, and allows for the flexibility of choosing the combination in a dataset-specific manner by tuning parameters using cross-validation within the training data.

The performance of the model was rigorously evaluated using 5-fold cross-validation which was repeated 100 times. Briefly, the data was randomly split into 5 parts, of which one of the part was designated test set and the remaining was used for training. The elastic net model was trained only on the training data, and then applied to the test set to get predictions. The predictions were then evaluated using a logrank test. The methods were implemented in R using glmnet library.

QUANTIFICATION AND STATISTICAL ANALYSIS

All statistical analyses were performed using R v3.3.0. Kaplan-Meier survival curves were used for survival analysis. Statistical analyses used for each of the figures is specified in the legend. Ns for the different groups are provided in the figures.

DATA AND SOFTWARE AVAILABILITY

The exome and RNA sequencing files are uploaded to European Genome-Phenome Archive (https://www.ega-archive.org/) and can be accessed using the accession number EGA: EGAS00001002606. Clinical data and all data used for this study are provided in the Supplementary tables. We have developed an interactive webtool (https://dlbcl.davelab.org) for survival analysis using clinical and genomic features.

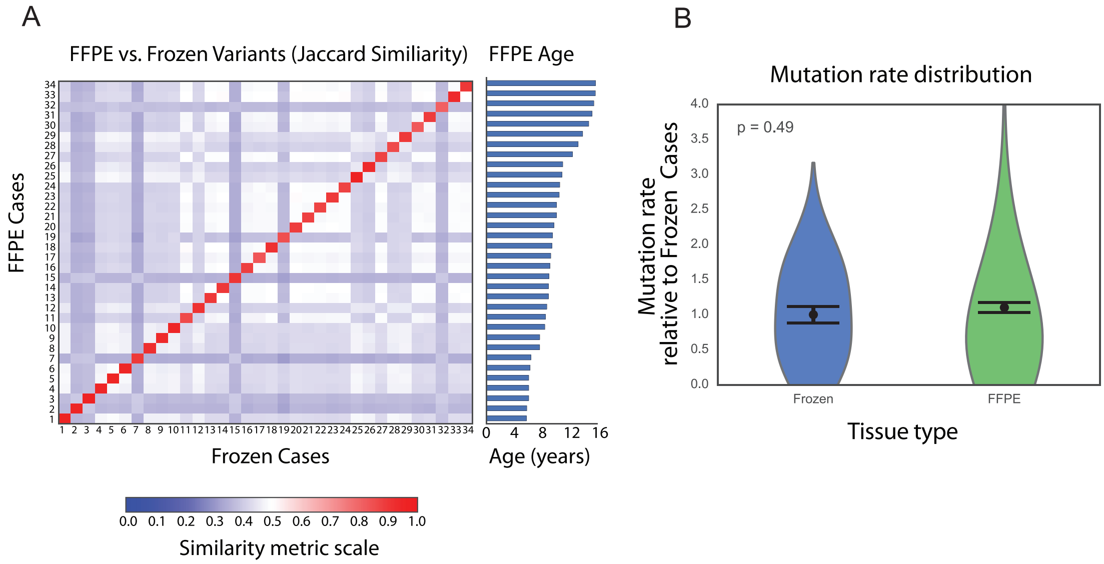

Figure S1. Comparing Variants in FFPE versus Frozen Samples, Related to Figure 1

(A) The heatmap indicates all-pairs Jaccard similarity distance between variants measured from 34 paired FFPE and frozen DLBCL tumors obtained from the same patient. On the diagonal, the similarity for FFPE and Frozen cases from the same individual can be seen. The cases are sorted by sample age, indicated on the horizontal bar graph.

(B) We compared the somatic mutation distribution of 30 frozen tumor/normal pairs, and 400 FFPE tumor/normal cases. There is no difference in the distribution ($p = 0.49$, Wilcoxon Rank test). The mean and standard error of the mean of the frozen cases, as well as that of FFPE cases, are super-imposed on the violin plots.

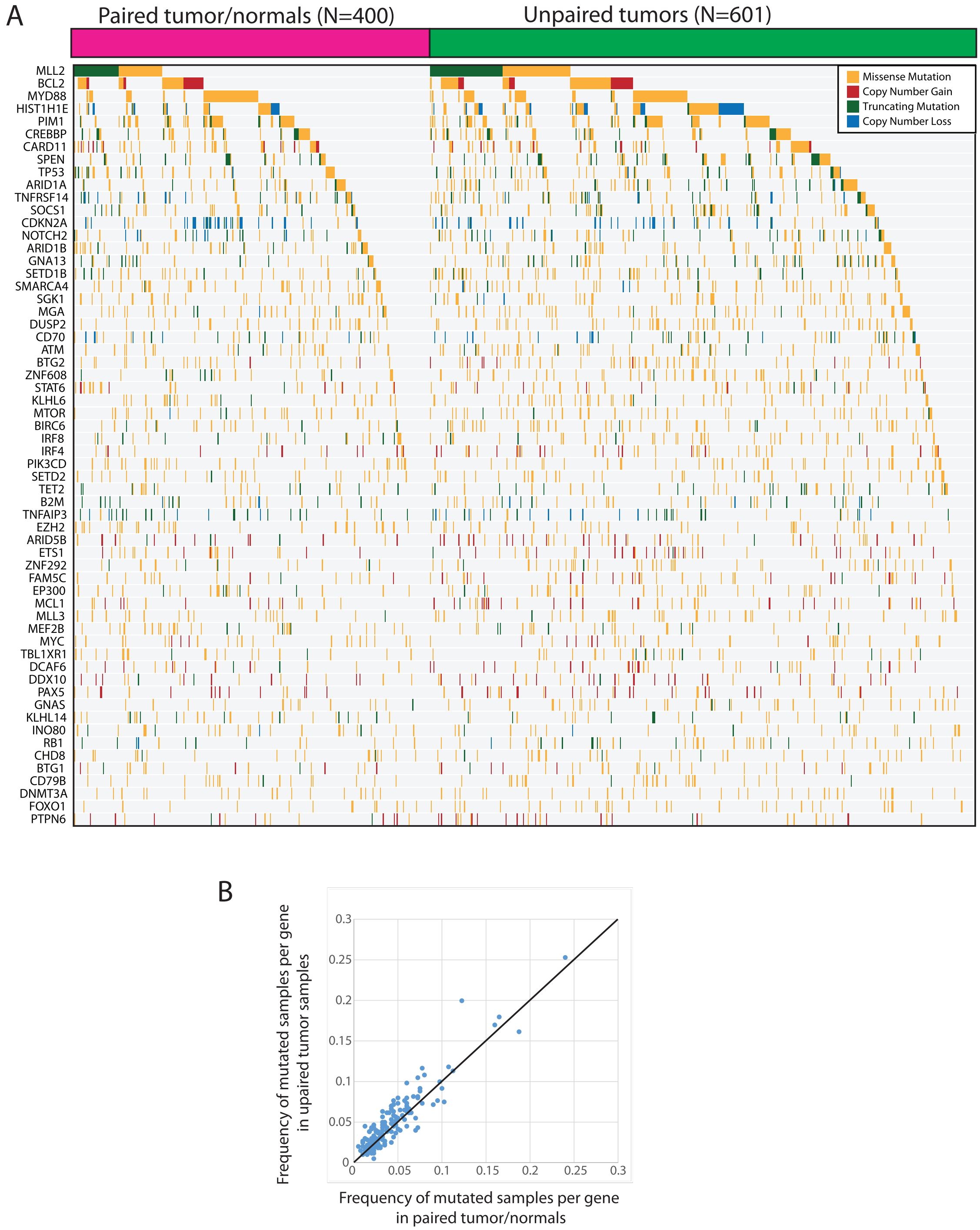

Figure S2. Comparison of Tumors with Paired Normal versus Unpaired Tumors, Related to Figure 1

(A) Heatmap of genetic alterations for the paired tumors compared to the unpaired group shows very similar patterns of overlaps and exclusions.

(B) Scatterplot of the mutational frequency for the paired and unpaired samples shows a high degree of similarity ($R^2 = 0.94$, $p < 10^{-6}$).

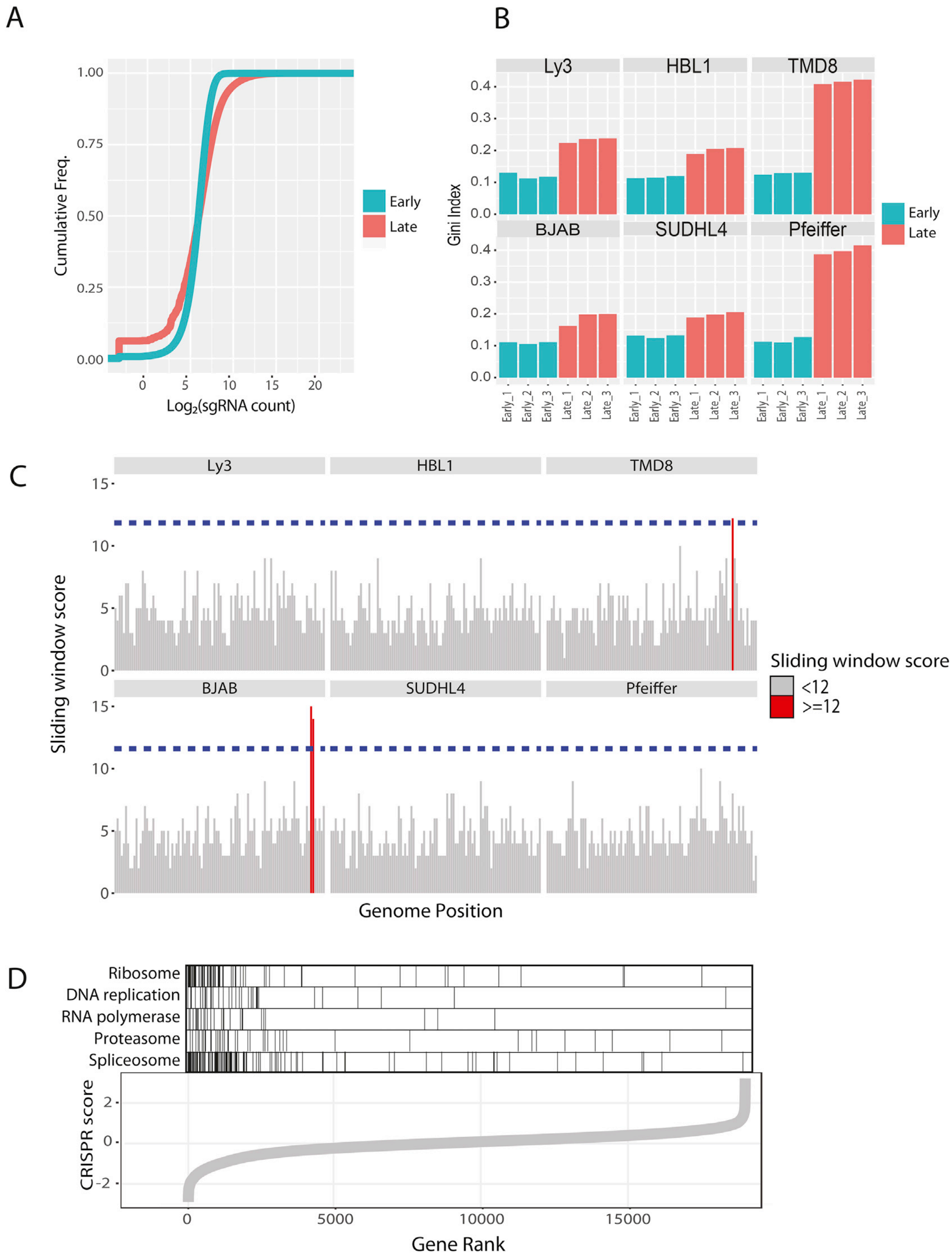

Figure S3. CRISPR Screen QC Summary, Related to Figure 3

(A) Cumulative frequency distribution of normalized sgRNA counts among early and late cell line replicates.

(B) Gini evenness indices computed from normalized sgRNA counts for all cell line replicates.

(C) Sliding window copy number peak plot with y axis displaying genes counts in each genomic region with CRISPR scores < 5th percentile CRISPR score for a cell line. Red bars indicate genomic regions significantly enriched for genes with negative CRISPR scores (> 12) as would be expected in amplified regions. Genes in these regions were discarded from consideration for essential gene status in DLBCL.

(D) Gene set membership of genes ranked by CRISPR score. Genes with lower CRISPR scores are significantly more likely to be involved in fundamental cellular processes such as ribosome biosynthesis, DNA replication, transcription and translation.

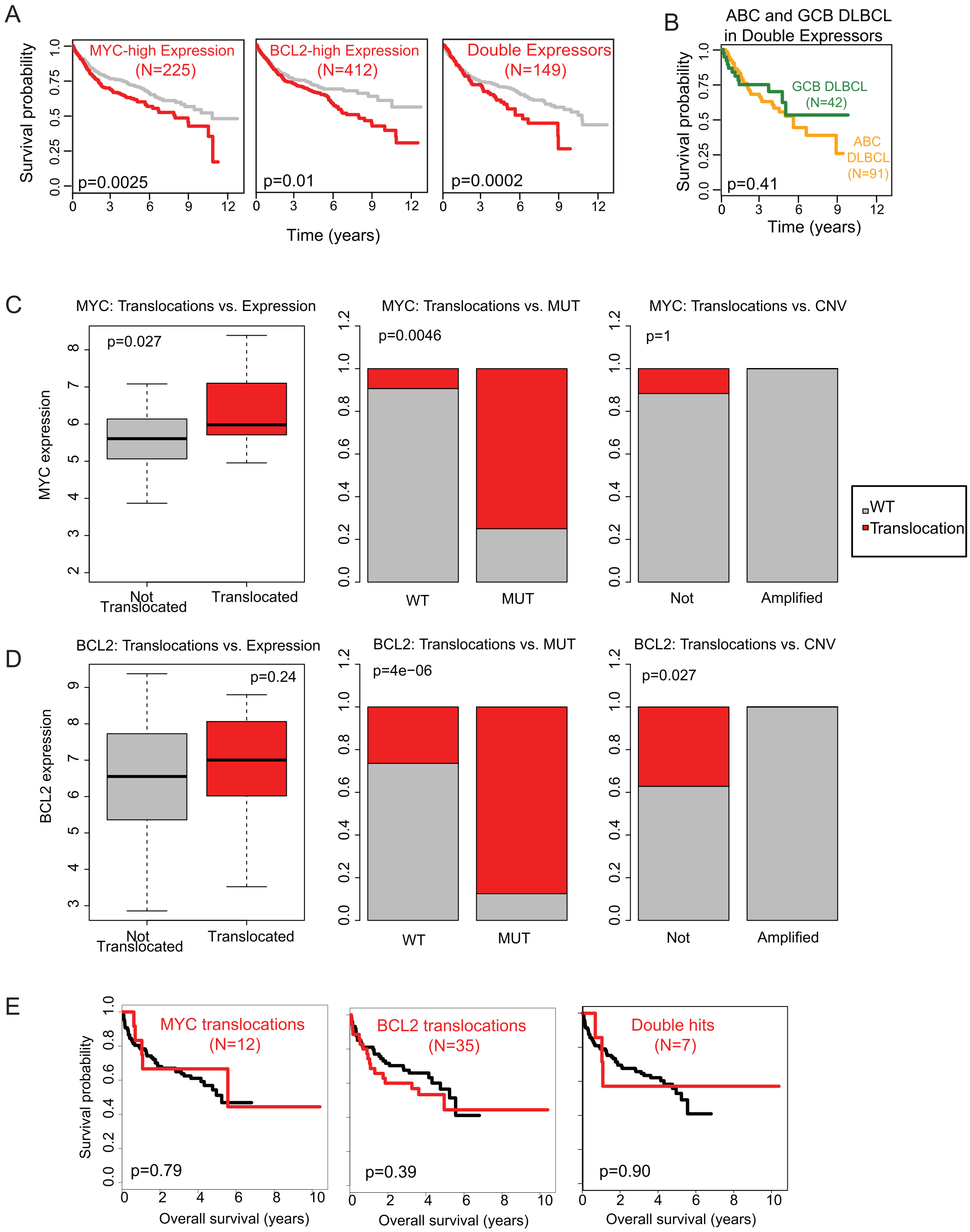

Figure S4. MYC and BCL2 High Expression and Translocations, Related to Figure 5

(A) Survival of DLBCL cases with high expression in *MYC*, *BCL2* and their combination - double expressors, show significant survival differences. All tests are logrank tests.

(B) Double expressors (*MYC* and *BCL2* high expression) stratified by ABC and GCB DLBCL subgroups are not associated with survival differences (p = 0.41).

(C and D) Association of translocations of *MYC* (C) and *BCL2* (D) with expression, mutations and copy number amplifications were tested in 126 DLBCLs.

(E) Survival plots for *MYC*, *BCL2* translocations and double hits (*MYC* & *BCL2* or *BCL6* translocations).

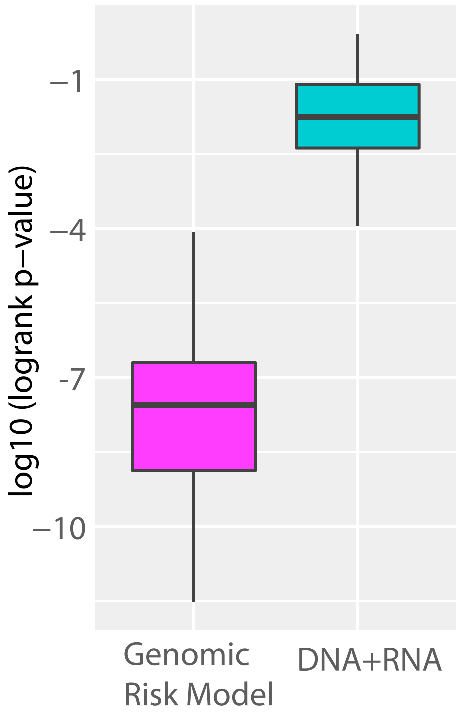

Figure S5. Performance of Genomic Risk Model, Related to Figure 5

The cross-validation performance of the genomic risk model comprised of combinations of DNA and RNA features, is compared to a model with the same features used individually (not in combinations) shows that combinations, i.e., interactions contribute to the superior performance of the genomic risk model.